Universiteit Antwerpen
Faculteit Wetenschappen

Fluctuations
in
multicomponent quantum fluids

Gaussian trajectories, spin mixing and the analog Hawking effect

Proefschrift voorgelegd tot het behalen van de graad van doctor in de Wetenschappen aan de Universiteit Antwerpen te verdedigen door

Lennart Fernandes

Promotoren:
Prof. Dr. Michiel Wouters
Prof. Dr. Jacques Tempere

Antwerpen, 2024

Jury

Chair:

Prof. Dr. Sofie Cambré – Universiteit Antwerpen

Supervisors:

Prof. Dr. Michiel Wouters – Universiteit Antwerpen

Prof. Dr. Jacques Tempere – Universiteit Antwerpen

Members:

Prof. Dr. Iacopo Carusotto – Università degli Studi di Trento

Prof. Dr. Jean Dalibard – Collège de France

Prof. Dr. François Damanet – Université de Liège

Prof. Dr. Johan Verbeeck – Universiteit Antwerpen

Public defence: January 10th, 2024

The research presented in this thesis was performed at the *Theory of Quantum Systems and Complex Systems* research group, which is part of the Physics department of the University of Antwerp. It was funded by the Research Foundation – Flanders (FWO) through a predoctoral fellowship Fundamental Research, project 11E8120N.

Cover image:
Pierre-Auguste Renoir, Seascape (1879),
Potter Palmer Collection, Art Institute of Chicago

Preface

While the cover of this thesis carries my name, I could not have completed it without the help of colleagues, friends and family, and the happiness to count many of them among more than one of these categories. As they are the ones who will involuntarily receive a copy of this work, I want to thank them all.

First and foremost on this list are my supervisors. Jacques, for taking me on as a master student and offering me to join his group for a PhD – though cunningly converting me to the quantum side of things. Thanks for being a truly great teacher, creating a pleasant work environment, and being the voice of reason in many nonsensical lunch discussions. Michiel, for being the most supportive supervisor I could have imagined. Thanks for always being available and never afraid to dive into rabbit holes so deep to leave us confused by the simplest of physics, before dragging us out again with an elegant back-of-the-envelope calculation. Thanks for always treating me as an equal, even when my input to your ideas was often limited to hesitant nodding. By encouraging me to spend time on summer schools and side projects, you have made these four years an exciting and enriching period in my life. Having supervisors who value interesting activities and well-being over output has been a privilege I won't easily forget.

As the people you work with are at least as important as the work itself, a heartfelt thanks goes to all other TQC members I've had the pleasure of working alongside: Robbe, Matthew, Timour, Filippo, Wouter, Wouter, Wout, Lucas, Jago, Laura, Dietrich, Senne, Dolf, Laurent, Denise, Hadrien, Mathias, Michiel (the Younger), Ingvar and Mister Delonghi. Among this lovely bunch of people, a few in particular deserve an additional word of thanks. Firstly to Mathias, Wouter and Hadrien, whose shoulders much of this work stands on and who, especially in the early parts of my trajectory, were very helpful in explaining calculations and providing code of their own work. Secondly, an additional shout-out goes to Michiel (the Elder), Robbe, Matthew and Timour for being great travel companions to wherever physics took us. Outside our research group, I

want to thank the entire *Fusieshow* team for dragging me along in what has turned out to be an incredibly fun adventure.

In 2022, part of this work brought me to Trento, an experience which broadened my horizon in a very literal sense. Thank you Iacopo for welcoming me in the BEC group, for letting me join a project which I had no previous experience in, for being as supportive as you are jovial and – to my slight shame – for often helping me with line-by-line debugging. Your bucolic metaphors from banana skins to Cherenkov ducks have clarified more physics than I dare to admit. During my months in Trento, I had the pleasure of collaborating with and learning from some very talented people. Many thanks to Anna, Alessio, Giulio and Luca for being patient teachers and all-round great colleagues. Even more so than scientifically interesting, my stay in Trento was simply a lot of fun, not in the least thanks to Alberto, Daniele, Sergio, Matheus, the *Kanarini* and everyone in the Erasmus group. Thank you all for the unforgettable trips, hikes and *notti brave* spent in the few bars and many streets of this charming town. Thanks Francesca for giving me a warm home to stay in, teaching me some Italian and motivating me to experience local life to the fullest.

At home I want to thank my brother Vincent, my parents and grandparents, who have loved and supported me unwaveringly, and who always assumed things would work out fine, long before I believed it myself. Thanks for everything, far too much to list. Thanks also to Ann, Dirk, Greet and Thijs, my in-law family who I have come to regard as a second home. Another big thanks goes to all friends who have illuminated the past years. Thanks to Arseny for all the nights of pseudobohemian idealism and unbridled enthusiasm, here's to many more! Thanks to Francesco, Hendrik and Mees for less frequent but all the more appreciated encounters, may our paths continue to cross much and often! Thanks to all the *Unifriendo's* for countless fun activities, and to Marnicq and Yente for going *way back* and remaining great friends ever since.

Lastly, none of this would have been worthwhile without the love of my girlfriend Marjan. Thanks for sharing all moments of joy and for being there when things got difficult. Thanks for tolerating my inhuman work schedule, thanks for always putting a smile on my face and most of all thanks for being you, *oh you*.

Finally, I want to thank all members of the jury for their careful reading of this manuscript and for making valuable suggestions to improve its final version.

Lennart
21/12/2023

Nederlandstalige samenvatting

In deze thesis wordt het gedrag bestudeerd van kwantumfluïda uit evenwicht. Dit zijn ultrakoude gassen waarin kwantummechanische effecten – doorgaans slechts zichtbaar op atomaire schaal – het macroscopische gedrag bepalen. Het werk is opgebouwd uit enkele aan elkaar gerelateerde projecten, waarin de centrale rol van *kwantumfluctuaties* in de dynamica van deze fluïda wordt belicht.

In het eerste deel wordt de algemene context geschetst van ultrakoude fluïda en hun toepassing voor het bestuderen van veeldeeltjes-kwantummechanica. In het bijzonder belichten we de *Bose-Einstein condensatie* die aanleiding geeft tot macroscopisch waarneembare kwantumeffecten, en introduceren we *spinorcondensaten* als voorbeeld van *multicomponent* kwantumfluïda. Vervolgens behandelen we theoretische methodes om het gedrag van deze fluïda bij benadering te beschrijven. Naast de Gross-Pitaevskii vergelijking en de Bogoliubov theorie voor elementaire excitaties introduceren we hier de Gaussische variationele theorie, die kwantumfluctuaties tot op laagste orde in rekening brengt als kleine correcties op een klassieke beschrijving van het fluïdum.

Voortbouwend op de beperkingen van de Gaussische methode, wijden we Deel II aan de ontwikkeling van de methode van *Gaussische kwantumtrajecten*. Met een klassiek chaotische Bose-Hubbard keten als modelsysteem illustreren we het falen van de Gaussische methode voor kwantumtoestanden met grote, niet-lineaire fluctuaties. Geïnspireerd door de studie van open kwantumsystemen introduceren we een mechanisme voor *decoherentie* door de toevoeging van een virtuele omgeving aan de theoretische beschrijving. Deze onderdrukt de groei van kwantumfluctuaties door het voortdurend meten van het systeem. De geldigheid van de Gaussische theorie wordt hierdoor sterk uitgebreid ten koste van de introductie van klassieke ruis, waardoor de evolutie van het systeem moet worden afgeleid uit

de simulatie van een groot aantal *kwantumtrajecten*. De haalbaarheid van deze aanpak wordt aangetoond door de ontwikkeling van een concreet algoritme voor kunstmatige dissipatie.

In Deel III passen we deze Gaussische-trajectenmethode verder toe op de *spin mixing* dynamica in een fluïdum van spin-1 atomen. Bij een plotse verandering van het externe magneetveld werd in dit systeem recent de evolutie waargenomen naar een *gefragmenteerd condensaat*, een niet-evenwichts-toestand gekarakteriseerd door een hoge mate van kwantumverstrengeling tussen de atomen van het gas. We bestuderen de snelle groei van fluctuaties in een Gaussische benadering van dit fenomeen, en besluiten dat ook hier de Gaussische-trajectenmethode een grote verbetering oplevert in de overeenkomst met experimentele resultaten. Gemotiveerd door de cruciale rol van behoudswetten in de evolutie van het spin-1 condensaat, bestuderen we de dynamica van een dissipatief condensaat, waarin de koppeling met een reële omgeving leidt tot een breking van het behoud van magnetisatie. In een zwak-dissipatief fluïdum voorspellen we het verval van een pre-thermale niet-evenwichtstoestand naar thermisch evenwicht op een universele tijdsschaal bepaald door de koppelingssterkte met de omgeving. We brengen dit in verband met een *multimode* model, waarvan het kwalitatieve gedrag op gelijkaardige wijze afhangt van de koppelingssterkte tussen verschillende modes. In het sterk-dissipatieve regime onthult de Gaussische-trajectenmethode een dissipatieve faseovergang in de uiteindelijke verdeling van spintoestanden in het condensaat, geïnterpreteerd als een manifestatie van het kwantum *Zeno effect*.

Tot slot zetten we in Deel IV de verkenning van niet-evenwichtsdynamica in spinorcondensaten verder door hun toepassing als platform voor analoge zwaartekracht te bestuderen. We introduceren Hawkingstraling van zwarte gaten en tonen hoe dit fenomeen tot stand komt als een algemene eigenschap van kwantumvelden in een achtergrond die sneller stroomt dan de voortplantingssnelheid van kwantumfluctuaties. We passen deze analogie toe op spingolven in een spinorcondensaat, waar coherente koppeling leidt tot een effectief massief veld van excitaties onderhevig aan het Hawking-effect. Door ons te richten op externe stimulatie van de anders zwakke spontane Hawkingstraling, tonen we hoe alle spectrale eigenschappen ervan kunnen worden afgeleid uit de verstrooiing van golfpakketten op een *spin-sonische horizon*. We bestuderen hoe de Hawkingtemperatuur van de uitgezonden straling afhangt van het ruimtelijke profiel van de horizon en koppelen deze waarnemingen aan de oppervlaktezwaartekracht van het analoge zwarte gat.

"Belief, like fear or love, is a force to be understood as we understand the theory of relativity and principles of uncertainty. Phenomena that determine the course of our lives.

[...]

Our lives and our choices, like quantum trajectories, are understood moment to moment. At each point of intersection, each encounter suggests a new potential direction."

– David Mitchell, *Cloud Atlas*

Contents

1 | Introduction

A world out of equilibrium

This thesis concerns quantum fluids out of equilibrium and the development of theoretical tools to predict their evolution. This may seem rather trivial, given that most properties of liquids and gases can be summarized in simple quantities as volume, pressure and temperature. Indeed, the development of statistical mechanics by Boltzmann, Maxwell and Gibbs in the second half of the 19th century has shown that *microscopic* details of a physical system can largely be neglected. Instead, physical properties are extracted by taking suitable averages over the ensemble of *macroscopically* discernable configurations, assigning to each one a probability $\mathcal{P}[E]$ given by the *Boltzmann* distribution,

$$\mathcal{P}[E] \sim \exp\left\{-\frac{E}{k_B T}\right\},$$

where E is the energy of a configuration and $k_B T$ the temperature multiplied by the Boltzmann constant. As the theoretical nephew of the more practically oriented field of thermodynamics, statistical mechanics stands as one of the pillars on which modern physics is built.

A caveat of statistical mechanics, however, is that its results hold only in *thermal equilibrium*, a situation defined as that in which all possible microscopic configurations of a system are equally probable. This assumption is a useful approximation for everyday liquids and gases, but it remains an idealization which is strictly only satisfied at infinite times. Before the eventual *heat death* of the universe, we are thus faced with a fundamentally *out-of-equilibrium* world which refuses to follow the rules of equilibrium statistical mechanics, and where microscopic details of particles and their interactions may crucially determine the behaviour of physical systems.

The curse of quantum mechanics

To make matters worse, the development of quantum theory in the early 20th century uncovered the fact that Boltzmann's classical configurations are merely the basis vectors of a space containing all *quantum states* of a physical system. While measurements force the collapse into a classical configuration, the unobserved system may reside in any linear combination of classical states. This is the *superposition principle* which allows atoms to be in two places at once, and famously enables cats to be dead and alive at the same time. Unfortunately, it also implies that the exact solution of a quantum system is fundamentally inaccessible, as it requires us to account for superpositions of all possible configurations, the number of which scales exponentially with the size of the system.

A focal point in theoretical physics has therefore become the development of approximate theories, which generally come in two flavours. In *perturbative* theories one starts from a simplified system for which a solution is available, and adds particularly challenging complications as a small perturbation to the simplified system, assuming its effect to be relatively weak. In *variational* theories, on the other hand, one is not bound by the relative magnitude of different processes happening in the system. Instead, the state $|\psi\rangle$ of the system is assumed to be of a particular chosen form $|\tilde{\psi}(\alpha_1, \ldots, \alpha_M)\rangle$, where the variational parameters $\alpha_1, \ldots \alpha_M$ completely determine the state. For variational states depending on few parameters, the properties of the full system can be inferred without further approximation.

Naturally, the performance of a variational theory is limited by the validity of the approximation $|\psi\rangle \to |\tilde{\psi}\rangle$. While approximate forms which capture the essential ingredients of a physical system can usually be found in an equilibrium context, the difficulty of out-of-equilibrium physics again rears its ugly head. To infer the *dynamics* of a quantum system, the *time-dependent variational principle* restricts the evolution of a quantum state to the set of variational states by reducing the time evolution of $|\psi\rangle$ to the time evolution of the parameters $\alpha_1, \ldots \alpha_M$. However, the complex interplay of particles and their interactions may carry the system to quantum states for which no suitable variational approximation is available. In fact, it is often not a priori clear to *which* states the system will evolve, making even the error made in the variational calculation hard to estimate.

Fluctuations and quantum quenches

A central theme throughout this work will be the role of *quantum fluctuations* in the evolution of a many-body quantum system. A manifestation of the intrinsic uncertainty in quantum mechanics, fluctuations are the excitations of the quantum field representing the assembly of particles making up the system. Mathematically, they are described in terms of correlations between particles, which encode properties such as entanglement and superpositions. As they contain the full complexity of a many-body quantum system, fluctuations must be accounted for in an approximate way. This is done explicitly in the Gaussian variational theory, which neglects correlations between many particles by assuming that the statistics of fluctuations follow a Gaussian distribution. In this thesis, we make a small contribution to the vast research field of out-of-equilibrium dynamics by developing a new approach which drastically extends the validity of Gaussian variational quantum states. We do this by introducing a virtual environment which continuously measures the system, collapsing quantum superpositions at the expense of introducing classical noise to the evolution. This gives rise to a collection of *quantum trajectories*, each of which represent a possible evolution of the system.

In particular, we will focus on a selection of out-of-equilibrium phenomena belonging to the class of *quantum quenches*, where a quantum system prepared in the ground state $|\psi_0\rangle$ of its governing Hamiltonian $\hat{\mathcal{H}}$ is subject to a sudden change of a parameter through external manipulation. As this *quench* abruptly changes the Hamiltonian $\hat{\mathcal{H}} \to \hat{\mathcal{H}}'$, the initial state $|\psi_0\rangle$ no longer corresponds to the ground state of the modified system. Instead, the system is now in a *far-from-equilibrium* state, and will begin to evolve in an effort to find its new equilibrium. In general, the ensuing dynamics may cause the emergence of intricate correlations or *entanglement* between particles or regions of the system, while the collective many-body quantum state evolves into a complicated superposition of classical states. Such scenarios are notoriously difficult to tackle with variational theories, which are typically formulated on the assumption of limited entanglement and don't do well at representing superpositions of macroscopically different states.

Ultracold fluids and quantum simulation

In the remainder of this thesis, we narrow our focus from the somewhat vague notion of a quantum system to the specific case of *ultracold fluids*. When cooled below a certain critical temperature, these dilute atomic vapors undergo *Bose-Einstein condensation*, a phenomenon which brings quantum effects – typically manifested at atomic length scales – to the level of the entire fluid. As such, quantum fluids enable to study quantum mechanics in a controlled environment, where the geometry of the system and the nature of inter-particle interactions are tunable through laser beams and magnetic fields. Before delving into the details of these fluids, we address the obvious question, *What is it good for?*

After all, ultracold atomic fluids are largely artificial systems. They are man-made in a laboratory, but don't occur spontaneously in nature*. While there are as many opinions on this as there are physicists to express them, a prime motivation for the interest in quantum fluids is their role as analogues for naturally occurring systems. Ranging from liquid helium and superconducting materials to the interior of neutron stars and the structure of the early universe, the relation of these phenomena to the properties of ultracold fluids varies from actual physical resemblance to purely formal mathematical analogies – classifications which are often the subject of debate. A common factor among them, however, is the fact that they are either inaccessible to experimental observations, or defy theoretical description due to their complexity.

Well before the first realization of ultracold atomic fluids, the tunability and experimental accessibility of artificially engineered quantum systems have sparked interest in their application as *quantum simulators* for other quantum systems, as famously expressed by Richard Feynman in a speech delivered at the first conference on *Physics and Computation* in 1981 [1]:

> *"Nature isn't classical, dammit, and if you want to make a simulation of nature, you'd better make it quantum mechanical, and by golly it's a wonderful problem, because it doesn't look so easy."*

* For reference, the temperature of microwave background radiation in outer space is roughly 2.7 kelvin, a billion times higher than the nanokelvin scale at which atomic fluids undergo Bose-Einstein condensation.

Overview

Having set the scene of the research to come, we conclude this introductory chapter with an outline of the work.

In **Part I**, we lay out the general playing field of ultracold fluids and their approximate description. In **Chapter 2**, we introduce ultracold atomic fluids as a platform for studying many-body quantum dynamic, covering Bose-Einstein condensation and its experimental realization in weakly interacting atomic gases. We discuss how different trapping geometries allow experimentalists to realize lattice models and introduce the atomic hyperfine degree of freedom which gives rise to *multicomponent* spinor fluids and binary mixtures. In **Chapter 3**, we discuss approximate theoretical approaches to study the dynamics of these systems, introducing the Gross-Pitaevskii equation and the Bogoliubov theory of elementary excitations, to arrive at the Gaussian approximation of quantum states. We introduce the truncated Wigner approximation as its primary alternative, and discuss how these approaches change for open quantum systems.

Part II is dedicated to the development of the Gaussian trajectory approach (GTA), the main conceptual contribution presented in this work. In **Chapter 4**, we show how the dynamics of a Bose-Hubbard chain exhibit classical chaos and illustrate the failure of a Gaussian approximation to accurately keep track of the accompanying quantum fluctuations. Assuming that weak disturbances from the outside environment should not significantly affect the overall evolution of the system, we propose to improve the Gaussian approximation by introducing a *virtual environment*. Effectively measuring the system, the environment induces *decoherence* which continuously suppress fluctuations to a level captured by the Gaussian approximation. The price to pay for this improvement turns out to be the introduction of classical noise to the system, which requires to obtain its evolution as the average over many *quantum trajectories*. The feasibility of this approach is tested in **Chapter 5**, where we develop *artificial dissipation* into a virtual environment for the specific case of the chaotic Bose-Hubbard chain. We compare our method the the truncated Wigner approximation (TWA), and provide an outlook for systems where it is expected to outperform the latter.

In **Part III**, we apply the developed method to the spin mixing dynamics of a spin-1 condensate, a numerically tractable system in which recent experiments have uncovered the relaxation to a *fragmented condensate*. We introduce this system in **Chapter 6**, covering its exact and approximate descriptions as well as

the ground state phase diagram. Spin mixing dynamics are studied in **Chapter 7**, where we relate the growth of fluctuations in a Gaussian approximation to the emergence of particle entanglement in the fragmented steady state. Applying the Gaussian trajectory approach, we successfully replicate relaxation of the system in the interaction-dominated regime. Building on the crucial role of conservation laws in spin mixing dynamics, we turn our attention to a dissipative spin-1 condensate in **Chapter 8**. Within the TWA, we find that a weakly coupled environment results in the emergence of a steady state, followed by a breaking of integrability in the long-time limit. Observing that incoherent jumps induced by the environment ultimately stem from coherent interactions with a many-mode reservoir, we retrieve the same qualitative behaviour in the prethermalization of a spin-1 Bose-Hubbard chain. In the strongly dissipative regime, the Gaussian trajectory approach uncovers a dynamical phase transition in the dissipative steady state of spin mixing dynamics.

Finally, in **Part IV**, we continue our exploration of fluctuation-driven nonequilibrium dynamics in spinor condensates by studying their application as a platform for analog gravity. We introduce Hawking radiation of black holes in **Chapter 9** and show how it emerges as a general feature of quantum fields in a spacetime background flowing at a velocity higher than the propagation velocity of quantum fluctuations. **Chapter 10** is dedicated to the Hawking effect for spin waves in a binary mixture, where coherent coupling leads to an effectively massive field of excitations. Focussing on external stimulation of the otherwise notoriously weak spontaneous effect, we show how all of its spectral properties may be inferred from the scattering of wave packets. We study how the *Hawking temperature* of the emitted radiation depends on the spatial profile of the fluid, relating our observations to the surface gravity of the analog black hole.

I

Generalities

“Alles Gescheite ist schon gedacht worden, man muß nur versuchen, es noch einmal zu denken.”

– Johann Wolfgang von Goethe, *Wilhelm Meisters Wanderjahren*

2 | Quantum fluids

The quantum systems with which we will be concerned in this thesis are *ultracold atomic fluids*. Highly manipulable in experiments and well-suited to theoretical approximations, these systems are one of the prime test beds for many-body quantum theory. In this chapter, we cover the essential properties of ultracold bosonic gases and their distinctive feature of *Bose-Einstein condensation*. After briefly commenting on the experimental realization of atomic condensates and the construction of the *Bose-Hubbard* model using optical lattices, we introduce the hyperfine degree of freedom and the resulting extension to *spinor condensates* and *quantum mixtures*.

As an exhaustive review of these topics is far beyond the scope of this thesis, the interested reader may find refuge in a plethora of textbooks [2–7], lecture notes [8] and review articles [9–14].

2.1 A shortcut to Bose-Einstein condensation

The world is made up of a relatively small variety of particles, with the remarkably far-reaching property that all particles of a certain type are fundamentally *identical*. Any collection of particles can be expressed as a wave function $\psi(\mathbf{x}, t)$, where the vector $\mathbf{x} = (x_1, \ldots, x_n)$ denotes the positions of the particles evolving in time t. Reality – that is, observable properties of $\psi(\mathbf{x}, t)$ – is encoded in the probability distribution* $|\psi(\mathbf{x}, t)|^2$.

Considering a wave function of just two identical particles at positions x_1 and x_2,

* Hand-wavingly, this can be understood as a consequence of the wave nature of quantum mechanics, which requires the use of complex rather than real-valued wave functions to account for interference phenomena. Observable quantities are contained in strictly real-valued measurement outcomes, among which the absolute value $|\psi|$ of the wave function.

reality must remain unchanged upon swapping their positions:

$$|\psi(x_1, x_2)|^2 = |\psi(x_2, x_1)|^2. \tag{2.1}$$

On the level of the wave function, this *exchange symmetry* is satisfied by one of two choices with vastly different physical consequences,

$$\begin{aligned} \psi_B(x_1, x_2) &= +\psi_B(x_2, x_1) \qquad \text{(Bosons)}, \\ \psi_F(x_1, x_2) &= -\psi_F(x_2, x_1) \qquad \text{(Fermions)}, \end{aligned} \tag{2.2}$$

For fermions, setting $x_1 = x_2$ results in $\psi_F(x_1, x_1) = -\psi_F(x_1, x_1)$, inevitably implying that the quantum state cannot exist, i.e., $\psi_F = 0$. This is Pauli's *exclusion principle* [15], which states that no two fermions may occupy the same quantum state. For a many-body system such as the harmonic oscillator shown in Fig. 2.1(a), this results in a lowest energy state or *ground state* in which subsequent single-particle energy levels are filled up to an energy known as the Fermi level E_F.

The absence of such a restriction for bosons, on the other hand, leads to a ground state shown in Fig. 2.1(b). Striving to minimize the energy of the system, all particles are free to occupy the lowest energy state. This corresponds to the formation of a *Bose-Einstein condensate* (BEC), the occupation of *one* single-particle state by a macroscopic number of particles. This inherently quantum mechanical form of matter emerges in particular in a gas of N bosonic atoms cooled below some critical temperature T_c. With k_B the Boltzmann constant and μ the chemical potential, the distribution $\bar{n}(\varepsilon)$ of atoms among their single-particle energy states ε at thermal equilibrium is given by the Bose-Einstein distribution,

$$\bar{n}(\varepsilon) = \frac{1}{e^{(\varepsilon-\mu)/k_B T} - 1}, \tag{2.3}$$

derived by Satyendra Nath Bose in a 1924 paper which layed the foundations of quantum statistics [16]. In 1925, Einstein [17] noted that the finite number of atoms $N_{\text{th}} = \sum_{\varepsilon>0} \bar{n}(\varepsilon)$ leads to a *saturation* of the thermal distribution when $N_{\text{th}} < N$, a situation which occurs below some critical temperature T_c. Having nowhere to go but the $\varepsilon = 0$ state, the remaining atoms are forced by the condition $T < T_c$ to populate this lowest energy level, giving rise to a condensate.

2.1.1 A graphical picture

A more tangible view on Bose-Einstein condensation is offered by the wave-particle duality of atoms. In his 1924 doctoral thesis [19] – awarded the No-

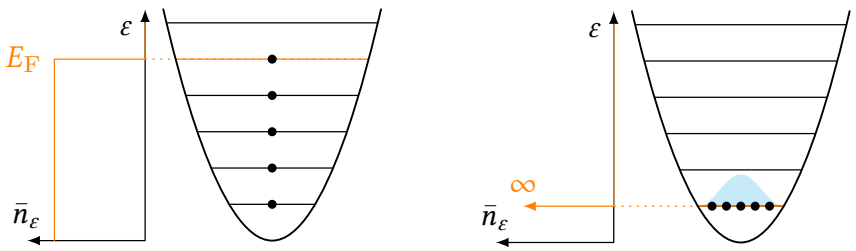

Figure 2.1 – Ground state of five fermions (a) and bosons (b) in a harmonic potential and the accompanying energy distribution $\overline{n}(\varepsilon)$. In (b), the formation of a condensate is represented by the blue wave function. Figure adapted from [18].

bel prize in physics in 1929 – Louis De Broglie postulated that, in analogy with Planck's law $E = \hbar\omega$ for the energy of photons, the energy content of any massive particle might be associated to a *matter wave* of frequency ω and a wavelength inversely proportional to its momentum,

$$\lambda_{\mathrm{dB}} = \frac{2\pi\hbar}{p}. \tag{2.4}$$

The proportionality factor $\hbar$ appearing here is the (reduced) *Planck constant*. Substituting p with the average momentum of a particle in a gas at temperature T, one arrives at the thermal wavelength

$$\lambda_{\mathrm{th}} = \sqrt{\frac{2\pi\hbar^2}{mk_{\mathrm{B}}T}}. \tag{2.5}$$

Interpreted as the spatial extent of the atom's matter wave, this implies that the uncertainty on the positions of atoms in the gas increases with decreasing temperature.

At high temperatures encountered in everyday life, the thermal wavelength of atoms is many orders of magnitude smaller than the average distance $d \sim n^{-1/3}$ between particles, with n the density of the gas. As shown in Fig. 2.2(a), the atoms therefore behave as point-like particles interacting through classical collisions. At lower temperatures, the spatial extent of the atoms' matter waves is no longer negligible, as shown in Fig. 2.2(b). The atoms in the gas now increasingly behave as waves, their interactions governed by interference rather than classical collisions. Finally, the formation of a Bose-Einstein condensate can be viewed as the situation in which the thermal wavelength is of the order of the

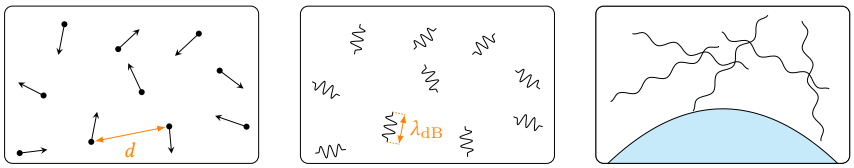

Figure 2.2 – Transition from classical to quantum behaviour in a gas of bosonic atoms. At high temperature (a), the interparticle spacing vastly outweighs the thermal wavelength and atoms are accurately represented as point particles. The wave nature of atoms becomes increasingly apparent with reduced temperature (b), ultimately leading to the formation of a condensate as the atoms' matter waves interfere significantly (c). Figure adapted from [18].

interparticle spacing, causing a significant overlap of the individual atoms' matter waves, shown in Fig. 2.2(c). The constructive interference of a macroscopic number of atomic matter waves gives rise to a single *many-body wavefunction* or *order parameter*, reducing the behaviour of a large collection of atoms to the coherent dynamics of a single collective matter wave.

Ultracold atomic gases typically contain 10^2 – 10^6 atoms. The formation of a condensate in such a gas thus magnifies the peculiarities of quantum mechanics – otherwise confined to the nanometer scale of individual atoms – to an object of experimentally observable size.

2.2 Ultracold atomic fluids

Unfortunately, the temperature at which atomic fluids undergo Bose-Einstein condensation as described above is low – nanokelvin low. While the kelvin regime was conquered when Heike Kamerlingh Onnes first liquified helium*† in 1908 [27], it was the development of the *magneto-optical trap* [28, 29] and *laser cooling* [29–31] in the 1980s which enabled exploration of the ultracold. This collection of techniques, based on capturing and slowing down atoms through their interaction with focussed light and magnetic fields, was rewarded with a Nobel prize shared

* Together with the first observation of superconductivity in 1911 [20], this achievement earned Onnes the 1913 Nobel prize in physics.

† Liquid helium became the first experimentally accessible quantum fluid when in 1938 Pyotr Kapitza discovered its superfluid properties [21], which were given a phenomenological description by Lev Landau in 1941 [22]. While its superfluid properties were proven to be the consequence of partial condensation [23, 24], liquid helium fundamentally differs from atomic condensates in the fact that even at $T = 0$, only $\sim 10\%$ of atoms are condensed into quantum degeneracy [25, 26].

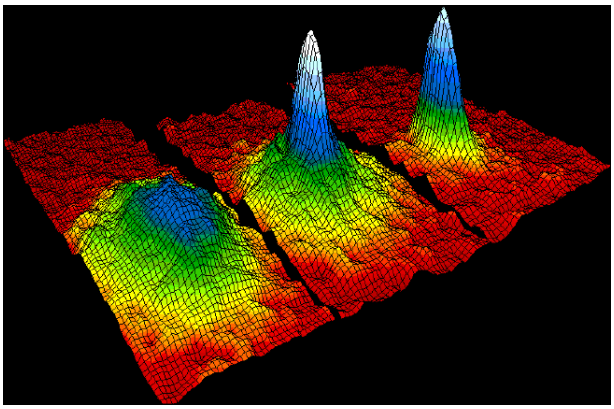

Figure 2.3 – Snapshots of the velocity distribution in a ^{87}Rb gas at approximately 400 nK (left), 200 nK (center) and 50 nK (right) [38] as measured by [35]. The sudden appearance of a zero-momentum spike in the center image signifies the formation of a Bose-Einstein condensate, which remains after further evaporation of the thermal cloud (right). Image credit NIST/JILA/CU-Boulder.

by Steven Chu, Claude Cohen-Tannoudji and William D. Philips in 1997 [32–34].

Building upon these developments, Bose-Einstein condensation in dilute atomic fluids of ^{87}Rb [35], ^{23}Na [36] and ^{7}Li [37] was finally realized in 1995 – 70 years after its theoretical prediction – following a close race between research teams at JILA (Boulder, CO), MIT (Boston, MA) and Rice University (Houston, TX) and culminating in the 2001 Nobel prize, jointly awarded to Eric Cornell, Carl Wieman and Wolfgang Ketterle [38, 39]. Figure 2.3 shows the velocity distribution of atoms in the first documented realization of a Bose-Einstein condensate by Anderson *et al.* [35]. Upon cooling of the atomic cloud, the thermal distribution of atoms acquires a sharply pronounced non-thermal peak* in its center, indicating the formation of a condensate in the zero-momentum state.

The quantum mechanical properties of atomic BECs were intensely studied following these early successes, resulting – among many others – in the observation of matter wave interference [40], frictionless flow [41], quantized vortices [42], quantum turbulence [43] and impurity polarons [44]. As an illustrative example, Fig. 2.4 shows a snapshot of the collision of two separate condensates (dark blobs) left to expand in close vicinity. The interference pattern (horizontal stripes) appear precisely due to the condensates' behaviour as collective matter waves.

* The non-thermal nature of this peak can be visually deduced from its lack of radial symmetry, indicating a preferential direction of the atoms' momentum.

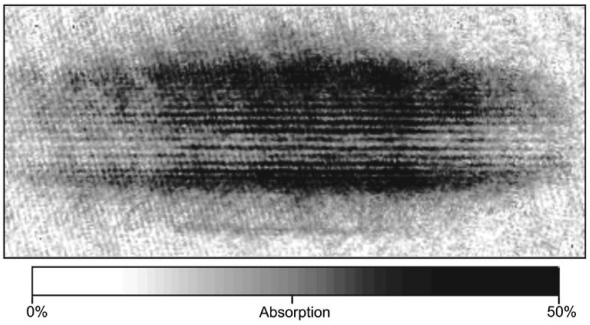

Figure 2.4 – Time-of-flight imaging of two expanding atomic condensates as measured by Andrews *et al.* [40], showing a fringe pattern typical of wave interference. Figure reproduced from [39].

2.2.1 The weakly interacting Bose gas

Having so far avoided mathematical notation, it is now time to introduce the weakly interacting Bose gas, governed by the Hamiltonian

$$\hat{\mathcal{H}} = \int \mathrm{d}\mathbf{r} \left[\hat{\psi}^\dagger(\mathbf{r}) \left(\frac{-\hbar^2 \nabla^2}{2m} + V_0(\mathbf{r}) \right) \hat{\psi}(\mathbf{r}) + \frac{g}{2} \hat{\psi}^\dagger(\mathbf{r}) \hat{\psi}^\dagger(\mathbf{r}) \hat{\psi}(\mathbf{r}) \hat{\psi}(\mathbf{r}) \right], \tag{2.6}$$

where $\hat{\psi}(\mathbf{r})$ is the bosonic field operator representing the fluid, m the mass of the constituting atoms and $V_0(\mathbf{r})$ the external (magneto-optical) potential. The restriction of interaction terms to binary collisions with a contact potential $V_i(\mathbf{r}-\mathbf{r}') = g\delta(\mathbf{r}-\mathbf{r}')$ derives from the weakly interacting nature of dilute atomic fluids. As the two-body wave function of two colliding atoms is at low temperatures dominated by its zero angular momentum contribution, interatomic interactions are assumed to occur through the corresponding s-wave scattering process. The resulting interaction constant g for long-wavelength interactions is obtained by applying the Born approximation to the Lippman-Schwinger equation governing the scattering process [3], yielding

$$g = \frac{4\pi\hbar^2 a_s}{m}, \tag{2.7}$$

with a_s the s-wave scattering length of the atomic species. The great tunability of ultracold atomic fluids partly derives from the fact that the s-wave scattering length may be manipulated by external magnetic fields tuned close to a *Feshbach resonance* [45].

The bosonic field operator describing the fluid obeys the standard bosonic commutation relations,

$$\left[\hat{\psi}^\dagger(\mathbf{r}), \hat{\psi}(\mathbf{r}')\right] = \delta(\mathbf{r} - \mathbf{r}'), \qquad \left[\hat{\psi}(\mathbf{r}), \hat{\psi}(\mathbf{r}')\right] = 0. \tag{2.8}$$

Its dynamics are governed by the *Heisenberg equation of motion*,

$$i\hbar\partial_t\hat{\psi}(\mathbf{r}, t) = \left[\hat{\psi}(\mathbf{r}, t), \hat{\mathcal{H}}\right], \tag{2.9}$$

which yields the equation formally governing the dynamics of the fluid,

$$i\hbar\partial_t\hat{\psi}(\mathbf{r}, t) = \left(\frac{-\hbar^2\nabla^2}{2m} + V_0(\mathbf{r}) + g\hat{\psi}^\dagger(\mathbf{r}, t)\hat{\psi}(\mathbf{r}, t)\right)\hat{\psi}(\mathbf{r}, t). \tag{2.10}$$

The *single-component* Bose gas presented here can be extended to fluids of multiple particle species. Before introducing the resulting *spinor condensates* and *quantum mixtures*, we briefly cover trapping geometries of ultracold fluids to arrive at the *Bose-Hubbard model*, which will serve as the platform on which we develop a new approach for the description of dynamics in Chapter 4.

2.3 Dimensional reduction and optical lattices

Increased experimental control over the trapping of atomic fluids has allowed for the creation of ever more complex geometries. On the one hand, the development of a *box-trap* permits to study Bose condensates of uniform density, bridging the gap between experimental reality and simplified theoretical descriptions [46]. On the other hand, anisotropic confinement of atomic clouds enables the creation of (quasi) one-dimensional *cigar* condensates [47, 48] and two-dimensional *pancake* condensates [49, 50], where a reduction of dimensionality affects both the appearance of long-range order and the dynamics of phase transitions [50–52]. Tight confinement in all three dimensions results in an effectively *zero-dimensional* condensate, where all excited modes of the harmonic potential ($\Delta\epsilon = \hbar\omega$) are inaccessible to the low-energy collisions of cold atoms, leaving the dynamics of the atoms' *internal* properties (i.e., *spin*) as the sole degree of freedom. From a pragmatic theorist's point of view, an additional advantage of such systems is the dramatic reduction of computational resources required to simulate them. As such, we will encounter atomic fluids of reduced dimensionality throughout this thesis, turning our attention to zero- and one-dimensional condensates in Parts III and IV, respectively.

Finally, the interference of several laser beams enables experimentalists to construct periodic trapping potentials. This results in an *optical lattice* in which multiple pancake, cigar, or zero-dimensional condensates are trapped in close vicinity, enabling atoms to *tunnel* or *hop* from one to the other, effectively realizing simplified theoretical models of discretized space [2, 7, 53]. Of particular interest is the paradigmatic Bose-Hubbard model [54–56] for cold atoms in an optical lattice.

2.3.1 The Bose-Hubbard model

Upon sufficient confinement of the condensates populating the individual sites of an optical lattice, the overlap of the site-localized *Wannier* wave functions may be neglected [7]. Additionally restricting the description to the lowest energy band of the periodic crystal's band structure, one can effectively describe an optical array of L tightly confined bosonic gases as a discretized quantum field $\hat{a}_j$, with the index $j \in [1, L]$ denoting the lattice sites [7, 57]. The atoms are free to move from one site to its nearest neighbours with hopping amplitude J, while the presence of more than one particle on a single site leads to interactions in the form of repulsive binary collisions with interaction energy* U. With $\hat{a}_j^{(\dagger)}$ the annihilation (creation) operator of a single atom on site j, these dynamics are enclosed in the Hamiltonian†

$$\hat{\mathcal{H}} = -J \sum_{\langle j,l \rangle} \left(\hat{a}_j^\dagger \hat{a}_l + \hat{a}_l^\dagger \hat{a}_j \right) + \frac{U}{2} \sum_{j=1}^{L} \hat{a}_j^\dagger \hat{a}_j^\dagger \hat{a}_j \hat{a}_j. \tag{2.11}$$

The summation $\langle j, l \rangle$ runs over all pairs of neighbouring sites, avoiding double-counting. Based on a perturbative treatment by Fisher *et al.* [54] and confirmed through exact diagonalization of the one-dimensional case‡ by Jaksch *et al.* [55], the phase diagram of the Bose-Hubbard model at integer filling was predicted to contain a phase transition from a superfluid to a Mott insulator with decreasing tunneling strength. In the following chapters, we will study the dynamics of this model in greater detail, restricting our discussion, however, to the superfluid regime $J \gg U$.

* The on-site interaction strength of bosons in an optical lattice is related to the contact potential (2.7) through $U = g \int \mathrm{d}\mathbf{r} w^4(\mathbf{r} - \mathbf{r}_j)$, with $w(\mathbf{r} - \mathbf{r}_j)$ the Wannier state at site j [7].

† In the grand-canonical ensemble, the chemical potential μ introduces an additional term $-\mu \sum_j \hat{a}_j^\dagger \hat{a}_j$ to the Hamiltonian. As we focus exclusively on number-conserving dynamics of isolated systems, its effect on the dynamics is limited to a constant precession $e^{i\mu t/\hbar}$ of the field amplitudes, and μ may thus be set to zero without loss of generality.

‡ The superfluid-Mott transition was shown to persist in higher dimensions via quantum Monte Carlo (QMC) calculations in 1D [58], 2D [59] and 3D [60].

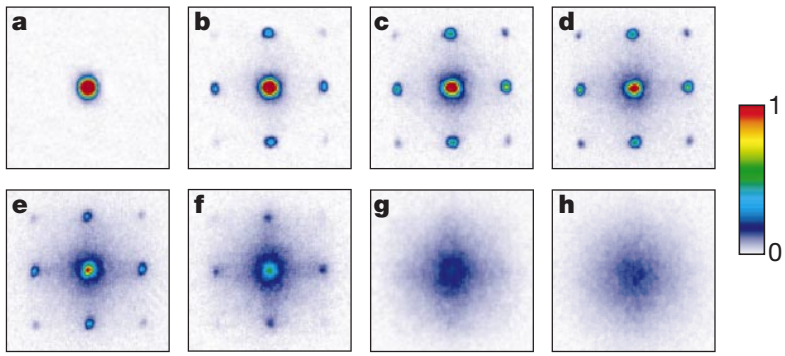

Figure 2.5 – Absorption images (in momentum space) of a three-dimensional atomic Bose-Hubbard system of increasing lattice depth, as observed by Greiner *et al.* [56]. In the superfluid regime (a-d), the atomic density is sharply peaked in momentum space, indicating a delocalization of all atoms across the entire lattice. Upon entering the Mott insulator phase (e-h), the coherent interference pattern is lost and replaced by an incoherent distribution, indicating the localization of atoms on individual lattice sites. Figure reproduced from [56].

After previous implementations in Josephson junction arrays [61–63], a 1D twelve-site atomic Bose-Hubbard system was first realized by Orzel *et al.* [64] in 2001. In 2002, Greiner *et al.* [56] realized a three-dimensional Bose-Hubbard array of ^{87}Rb atoms in a three-dimensional optical array of over 150.000 sites. Achieving on-site populations of $\sim 1-3$ atoms, they managed to observe the system's transition from a superfluid to a Mott insulator, as shown in Fig. 2.5. Besides multiple experiments based on ^{87}Rb [65–68], similar systems have since been realized using ^{171}Yb [69] and ^{7}Li atoms [70].

Finally, the Bose-Hubbard model has been studied in the presence of an external environment [57], both in *driven-dissipative* quantum optical setups [71–73] as well as in arrays of atomic condensates subject to local dissipation, where refilling dynamics result in a dissipative phase transition in the steady state population of the dissipated site [66, 67, 74, 75].

2.4 Spinor condensates

The weakly interacting Bose gas of a single atomic species, collectively described by the scalar matter field $\hat{\psi}(\mathbf{r}, t)$, can be generalized to fluids of several interacting fields $\hat{\psi}_m(\mathbf{r}, t)$, distinguished by an internal degree of freedom of the constituent atoms. For a three component fluid, this results in a description in terms of the

vectorial field

$$\hat{\Psi}(\mathbf{r},t) = \begin{pmatrix} \hat{\psi}_{+1}(\mathbf{r},t) \\ \hat{\psi}_{0}(\mathbf{r},t) \\ \hat{\psi}_{-1}(\mathbf{r},t) \end{pmatrix}. \tag{2.12}$$

As is the case for a scalar field, an assembly of atoms described by a vectorial field can undergo Bose-Einstein condensation, leading to the appearance of a macroscopic vectorial order parameter. What sets *spinor condensates* apart from *quantum mixtures* – discussed in the following section and also described by a multicomponent order parameter – is the fact that the dynamics of the vectorial order parameter are governed by spin operators. That is, the state vector Ψ rotates in a spin manifold, its components being merely the quantized levels of the projection along a preferential axis. In the projection basis, a rotation of the state vector then means that atoms transfer from one component to another. This property of *spin mixing* is characteristic to spinor fluids.

In the 25 years since their initial realization in 1998 [76], the intense study of spinor condensates has resulted in a vast body of literature. To restrict the present discussion to the essential ingredients, I happily refer the interested reader to the extensive review by Yuki Kawaguchi & Masahito Ueda [77] and a more concise overview by Dan Stamper-Kurn & Masahito Ueda [78]. A personal favourite and arguably the most accessible introduction to the subject is a series of lecture notes by Edward Marti and Dan Stamper-Kurn [79], presented by the latter at a 2015 Enrico Fermi summer school on ultracold quantum matter.

2.4.1 The hyperfine degree of freedom

In addition to their momentum, exchanged through pairwise collisions, the constituent atoms of a Bose gas carry additional *internal* degrees of freedom due to the structure of the nucleus and the electronic cloud. Such details of the atomic structure are largely irrelevant to the low-energy dynamics governing ultracold fluids, effectively restricting atoms to their nuclear and electronic ground state [78]. What remains accessible is the internal degree of freedom stemming from the interaction between the nucleus and the electronic cloud, giving rise to the so-called *hyperfine structure* [80, 81].

Following the addition rules for angular momentum, the combined state of a nucleus with spin I and an electron of spin $S = 1/2$ splits into two hyperfine manifolds of total angular momentum $F = I \pm S$. The alkali metals* ^{87}Rb, ^{23}Na,

* Like hydrogen, these elements have one valence electron, eliminating electron-electron inter-

^{7}Li and ^{41}K used for ultracold fluids all have nuclear spin $I = 3/2$, resulting in the appearance of $F = 1$ and $F = 2$ hyperfine levels. We will limit our discussion to atoms in the $F = 1$ manifold, such that the involved fields can be described in terms of the vectorial order parameter (2.12).

2.4.2 Single-particle energy

Each of the fields $\hat{\psi}_m(\mathbf{r}, t)$ independently carries a kinetic energy and an energy associated to the trapping potential $V_0(\mathbf{r})$, assumed to be equal for all components. In addition to these familiar contributions, the coupling to a weak external magnetic field* lifts the degeneracy of the hyperfine manifold. With m_F the projection of the internal angular momentum F along the z-axis, the perturbation by a magnetic field $\mathbf{B} = B\mathbf{e}_z$ shifts the energy levels of the $|F, m_F = -1, 0, +1\rangle$ substates as

$$\Delta E^{(1)}_{m_F} \propto \mu m_F B, \tag{2.13}$$

where $\mu > 0$ is the atomic magnetic moment. This is known as the linear hyperfine *Zeeman effect*†, illustrated in Fig. 2.6(a). Since interatomic interactions (see below) conserve $m_F^{(1)} + m_F^{(2)}$ of the colliding atoms, spin mixing processes are limited to $|0\rangle\,|0\rangle \leftrightarrow |+1\rangle\,|-1\rangle$, rendering the linear Zeeman energy a conserved quantity of the dynamics under the condition $\mu B \gg k_B T$, such that the Zeeman energy is inaccessible to thermal excitations [79].

In addition to the linear energy splitting, a *quadratic* Zeeman effect arises from second order interactions between the total angular momentum and the magnetic field, raising the energy levels of the $|m_F = \pm 1\rangle$ states equally with respect to $|m_F = 0\rangle$,

$$\Delta E^{(2)}_{m_F} \propto \mu m_F^2 B^2. \tag{2.14}$$

Specifically, this energy shift shown in Fig. 2.6(c) results from the energy repulsion between hyperfine states belonging to different F-manifolds, but may also be induced through a microwave dressing field tuned near resonance of the corres-

actions in a low energy description.

* The coupling to the magnetic field must be weaker than the interaction energy between the nuclear and electronic angular momenta to ensure that the total angular momentum F remains a good quantum number. The decoupling of nuclear and electronic angular momenta in the strong field case is known as the hyperfine *Paschen-Back effect* [82], shown in Fig. 2.6(b) as the mixing of spin manifolds.

† The Zeeman splitting of hyperfine levels should not be confused with a similar energy shift of the orbital electronic levels in the presence of an external magnetic field (the *normal* Zeeman effect), nor the shift experienced by the electron's spin states due to the magnetic field induced by its own orbital motion (the fine structure). Moreover, the predominant contribution to the hyperfine structure is in itself a Zeeman effect experienced by the nuclear magnetic moment in the magnetic field induced by the electronic angular momentum [81].

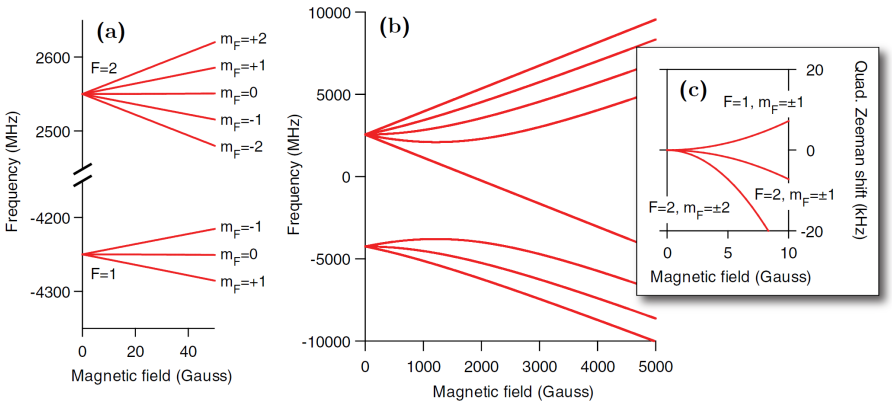

Figure 2.6 – Hyperfine structure for ^{87}Rb. (a) At weak magnetic field, the linear Zeeman effect induces a splitting of energy levels within each F-manifold. (b) In the strong field limit, F ceases to be a good quantum number as the Zeeman effect exceeds the splitting between hyperfine manifolds. (c) Quadratic correction to the Zeeman splitting after subtraction of the leading order linear term. Figure adapted from [78].

ponding transition [79]. Contrary to its linear counterpart, the quadratic Zeeman energy is no conserved quantity of spin mixing processes. The dynamics of the fluid are therefore sensitive to the resulting energy shift, making it the primary parameter for external manipulation in experiments. In total, the single-particle energy of the spin-1 fluid is given by

$$\hat{\mathcal{H}}_0 = \int \mathrm{d}\mathbf{r}\hat{\Psi}^\dagger(\mathbf{r})\left(\frac{-\hbar^2\nabla^2}{2m} + V_0(\mathbf{r}) + pf_z + qf_z^2\right)\hat{\Psi}(\mathbf{r}). \tag{2.15}$$

Here we introduced the vector of spin-1 matrices, $\mathbf{f} = (f_x,\, f_y,\, f_z)^T$, with

$$f^x = \frac{1}{\sqrt{2}}\begin{pmatrix} 0 & 1 & 0 \\ 1 & 0 & 1 \\ 0 & 1 & 0 \end{pmatrix}, \quad f^y = \frac{1}{\sqrt{2}}\begin{pmatrix} 0 & -i & 0 \\ i & 0 & -i \\ 0 & i & 0 \end{pmatrix}, \quad f^z = \begin{pmatrix} 1 & 0 & 0 \\ 0 & 0 & 0 \\ 0 & 0 & -1 \end{pmatrix}. \tag{2.16}$$

2.4.3 Interaction energy and Hamiltonian

As noted earlier, a defining feature of spinor condensates is the ability of atoms to transfer from one component of the field to another. In the absence of additional coupling between the spinor components by external electromagnetic fields, this occurs through collisions of atoms, where internal angular momentum is exchanged in the same way as linear momentum $\mathbf{k}$. The generalization of s-

wave scattering to the spin-1 gas is slightly more involved than the single-particle energy since interactions are required to obey the additional symmetries of the hyperfine spin manifold.

A binary collision of two atoms with internal states $|F, m_F^{(1)}\rangle$ and $|F, m_F^{(2)}\rangle$ can be described in terms of the two-body state $|\mathcal{F}, m_\mathcal{F}\rangle$, where $\mathcal{F}$ is the total angular momentum and $m_\mathcal{F} = m_F^{(1)} + m_F^{(2)}$ its projection along the z-axis. While individual atoms may change their internal state, the angular momentum of the two-particle state is conserved during the collision process. Interactions are therefore described in terms of the single-particle fields through the projection operators

$$\hat{P}_\mathcal{F} = \sum_{m_\mathcal{F}=-1}^{1} |\mathcal{F}, m_\mathcal{F}\rangle \langle \mathcal{F}, m_\mathcal{F}| \,. \tag{2.17}$$

In a scattering process of two spin-1 bosons, the total angular momentum takes a value $\mathcal{F} \in \{0, 1, 2\}$. However, since the exchange of two bosons of spin F changes the wave function by a factor of $(-1)^{2F} = 1$, the same should hold in the basis of total angular momentum, giving rise to two *interaction channels* of spin $\mathcal{F} = 0$ and $\mathcal{F} = 2$, respectively [79]. For dilute gases, scattering processes through both channels are approximated as contact interactions with interaction strength $g_\mathcal{F} = 4\pi\hbar^2 a_\mathcal{F}/m$, where $a_\mathcal{F}$ is the s-wave scattering length of the corresponding channel. The resulting interaction term is then similar to the scalar Bose gas,

$$\hat{\mathcal{H}}_i = \frac{1}{2} \int \mathrm{d}\mathbf{r} \int \mathrm{d}\mathbf{r}' \hat{\Psi}^\dagger(\mathbf{r}') \hat{\Psi}^\dagger(\mathbf{r}) \hat{V}_i(\mathbf{r} - \mathbf{r}') \hat{\Psi}(\mathbf{r}') \hat{\Psi}(\mathbf{r}), \tag{2.18}$$

with the contact interaction potential generalized to

$$\hat{V}_i(\mathbf{r} - \mathbf{r}') = \Big[g_0 \hat{P}_0 + g_2 \hat{P}_2 \Big] \delta(\mathbf{r} - \mathbf{r}'). \tag{2.19}$$

Finally, the projection operators $\hat{P}_\mathcal{F}$ can be eliminated by noting their completeness relation $\hat{P}_0 + \hat{P}_2 = \hat{1}$ and the identity $\hat{\mathbf{F}}^{(1)} \cdot \hat{\mathbf{F}}^{(2)} = \lambda_0 \hat{P}_0 + \lambda_2 \hat{P}_2$, where $\hat{\mathbf{F}}$ is the single-particle spin operator and $\lambda_\mathcal{F} = 1/2[\mathcal{F}(\mathcal{F}+1) - 2F(F+1)]$, resulting in [77]

$$\begin{cases} \hat{P}_0 + \hat{P}_2 = 1 \\ \hat{P}_2 - 2\hat{P}_0 = \hat{\mathbf{F}}^{(1)} \cdot \hat{\mathbf{F}}^{(2)} \end{cases} \Rightarrow \begin{cases} \hat{P}_0 = \dfrac{1 - \hat{\mathbf{F}}^{(1)} \cdot \hat{\mathbf{F}}^{(2)}}{3} \\ \hat{P}_2 = \dfrac{2 + \hat{\mathbf{F}}^{(1)} \cdot \hat{\mathbf{F}}^{(2)}}{3} \end{cases} . \tag{2.20}$$

The interaction potential is then rewritten as

$$\hat{V}_i(\mathbf{r} - \mathbf{r}') = \frac{1}{3} \Big[(g_0 + 2g_2) + \hat{\mathbf{F}}^{(1)} \cdot \hat{\mathbf{F}}^{(2)} (g_2 - g_0) \Big] \delta(\mathbf{r} - \mathbf{r}'), \tag{2.21}$$

containing spin-independent density interactions as well as a Heisenberg-like spin-dependent contribution, with respective interaction strengths

$$\begin{aligned} c_0 &= (g_0 + 2g_2)/3, \\ c_2 &= (g_2 - g_0)/3. \end{aligned} \tag{2.22}$$

Crucially, the sign of c_2 determines the ferromagnetic ($c_2 < 0$) or antiferromagnetic ($c_2 > 0$) nature of spin interactions. We will limit our discussion to the antiferromagnetic case. With $\hat{n}(\mathbf{r}) = \hat{\Psi}^\dagger(\mathbf{r})\hat{\Psi}(\mathbf{r})$ the density operator and $\hat{\mathbf{F}}(\mathbf{r}) = \hat{\Psi}^\dagger(\mathbf{r})\mathbf{f}\hat{\Psi}(\mathbf{r})$ the local spin-1 operator of the field, the interaction energy can then be written as

$$\hat{\mathcal{H}}_i = \int \mathrm{d}\mathbf{r} \left(\frac{c_0}{2} :\hat{n}^2: + \frac{c_2}{2} :\hat{\mathbf{F}}^2: \right). \tag{2.23}$$

The notation $:\hat{O}:$ represents *normal* ordering (or Wick ordering [83]), a convention in which all creation operators are placed to the left of all annihilation operators, i.e.,

$$:\hat{\psi}_i^\dagger \hat{\psi}_k \hat{\psi}_j^\dagger \hat{\psi}_l: = \hat{\psi}_i^\dagger \hat{\psi}_j^\dagger \hat{\psi}_k \hat{\psi}_l. \tag{2.24}$$

In their fully expanded form (and dropping the spatial dependence $\mathbf{r}$ for clarity), these interaction terms read

$$\begin{aligned} :\hat{n}^2: = {} & \hat{\psi}_{+1}^\dagger \hat{\psi}_{+1}^\dagger \hat{\psi}_{+1} \hat{\psi}_{+1} + \hat{\psi}_0^\dagger \hat{\psi}_0^\dagger \hat{\psi}_0 \hat{\psi}_0 + \hat{\psi}_{-1}^\dagger \hat{\psi}_{-1}^\dagger \hat{\psi}_{-1} \hat{\psi}_{-1} \\ & + 2\hat{\psi}_{+1}^\dagger \hat{\psi}_0^\dagger \hat{\psi}_{+1} \hat{\psi}_0 + 2\hat{\psi}_{+1}^\dagger \hat{\psi}_{-1}^\dagger \hat{\psi}_{+1} \hat{\psi}_{-1} + 2\hat{\psi}_0^\dagger \hat{\psi}_{-1}^\dagger \hat{\psi}_0 \hat{\psi}_{-1}, \end{aligned} \tag{2.25}$$

$$\begin{aligned} :\hat{\mathbf{F}}^2: = {} & \hat{\psi}_{+1}^\dagger \hat{\psi}_{+1}^\dagger \hat{\psi}_{+1} \hat{\psi}_{+1} + \hat{\psi}_{-1}^\dagger \hat{\psi}_{-1}^\dagger \hat{\psi}_{-1} \hat{\psi}_{-1} + 2\hat{\psi}_{+1}^\dagger \hat{\psi}_0^\dagger \hat{\psi}_{+1} \hat{\psi}_0 + 2\hat{\psi}_{-1}^\dagger \hat{\psi}_0^\dagger \hat{\psi}_{-1} \hat{\psi}_0 \\ & - 2\hat{\psi}_{+1}^\dagger \hat{\psi}_{-1}^\dagger \hat{\psi}_{+1} \hat{\psi}_{-1} + 2\hat{\psi}_0^\dagger \hat{\psi}_0^\dagger \hat{\psi}_{+1} \hat{\psi}_{-1} + 2\hat{\psi}_{+1}^\dagger \hat{\psi}_{-1}^\dagger \hat{\psi}_0 \hat{\psi}_0. \end{aligned} \tag{2.26}$$

Combining the single-particle energy (2.15) and interaction contribution (2.23), the Hamiltonian governing the spin-1 gas becomes [77–79]

$$\hat{\mathcal{H}} = \int \mathrm{d}\mathbf{r} \left[\hat{\Psi}^\dagger \left(\frac{-\hbar^2 \nabla^2}{2m} + V_0(\mathbf{r}) + q f_z^2 \right) \hat{\Psi} + \frac{c_0}{2} :\hat{n}^2: + \frac{c_2}{2} :\hat{\mathbf{F}}^2: \right]. \tag{2.27}$$

2.4.4 Experiments on spinor condensates

An atomic Bose-Einstein condensate with a spin-1 order parameter and antiferromagnetic interactions was first realized in the $F = 1$ hyperfine manifold of ^{23}Na

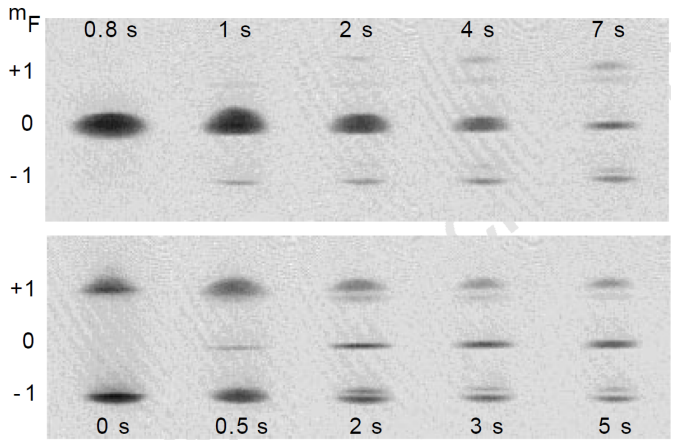

Figure 2.7 – First documented observation of spin dynamics in a ^{23}Na Bose gas by Stenger *et al.* [76]. Shown are time-of-flight absorption images of the atomic cloud after various evolution times, spin-separated by a Stern-Gerlach filter to show both spatial and hyperfine distributions. For two different initial conditions, the gas relaxes to the same spin-mixed equilibrium configuration. Additionally, the spatial structure of the clouds at late times indicates the spontaneous formation of magnetic domains, characteristic of antiferromagnetic interactions. Figure taken from [76].

[76] in 1998, a mere three years after the first reports of Bose-Einstein condensation in a scalar fluid*. Shown in Fig. 2.7, this experiment demonstrated the presence of spin mixing dynamics as well as the spontaneous formation of spin domains in the ground state.

Besides stimulating further studies on the formation of magnetic domains [86–88], the discovery of magnetic phases in the ground state allows one to study quantum phase transitions and their dynamics [89–91]. Much work in this context has been performed on ferromagnetic spinor condensates [86, 87, 92], which were produced in ^{87}Rb [93] and more recently ^{7}Li [88], and possess a richer phase diagram than their antiferromagnetic counterparts [77, 86]. Following a rapid quench of a ^{87}Rb condensate to a ferromagnetic state, Sadler *et al.* [86] observed the emergence of spatial spin textures due to spontaneous symmetry breaking, shown in Fig. 2.8(a), as well as the appearance of spin vortices, shown in Fig. 2.8(b). The latter are an example of topological defects which typically accompany the dynamics of symmetry breaking [94], and have been studied extensively in spinor condensates [95–98].

* Around the same time, concurrent Bose condensation in the $|F, m_F\rangle = |1, -1\rangle$ and $|2, 1\rangle$ hyperfine states of ^{87}Rb was realized [84, 85]. While such two-component fluids have been referred to as *pseudo spin*-1/2 [79], the lack of spin exchange interactions makes this system more aptly described as a *binary mixture*.

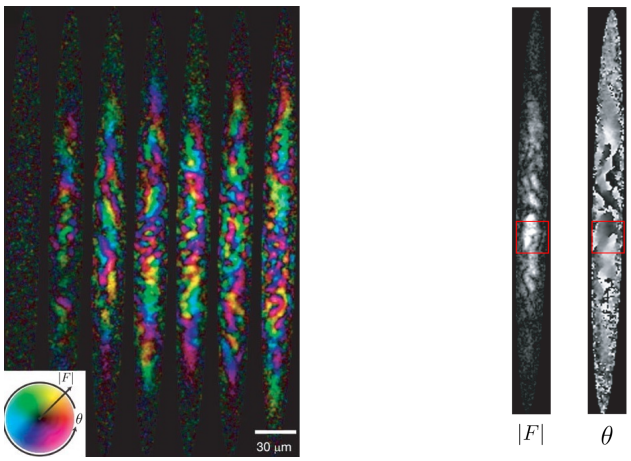

Figure 2.8 – Spontaneous emergence of spin textures as measured by Sadler *et al.* [86]. (a) In-situ images of the spin orientation $\theta = \arcsin[\langle \hat{F}_x \rangle / \langle \hat{F}_x + i\hat{F}_y \rangle]$ (color) and amplitude $|F| = \langle |\hat{F}|^2 \rangle^{1/2}$ (brightness) of the transverse magnetization density at several times following a quench to the ferromagnetic phase. (b) Spin vortex detected as a vanishing amplitude core and 2π phase jump. Figure adapted from [86].

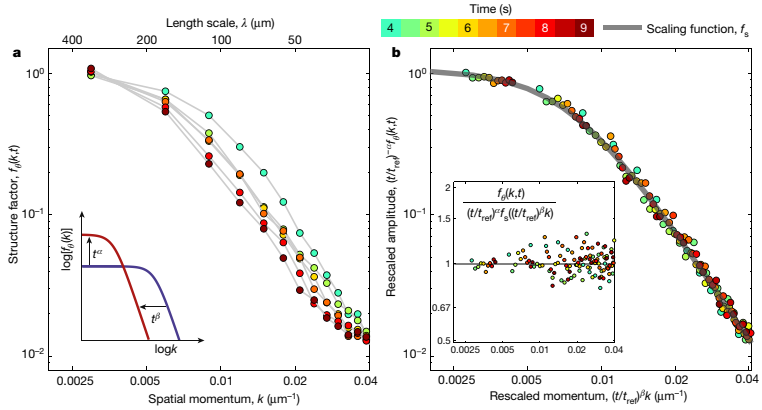

Figure 2.9 – Universal spin correlations in a non-thermal fixed point as quantified by the structure factor, the Fourier transform of the spatial two-point correlation function $\langle \theta(\mathbf{r}, t)\theta(\mathbf{r}', t) \rangle$. (a) The structure factor measured at various times after the initial preparation in a far-from-equilibrium state, evolving in time as shown in the inset. (b) The universal function onto which all structure factors collapse after a rescaling of momentum and time. Figure taken from [99].

Finally, the additional degree of freedom and associated time scale offered by spinor condensates makes them a practical platform for studying phenomena related to thermalization or the absence thereof [100]. In an antiferromagnetic sodium condensate prepared in a far-from-equilibrium state, Prüfer *et al.* [99] observed the evolution to a non-thermal fixed point, into which the system settles before eventual thermalization on a much longer time scale. As shown in Fig. 2.9, momentum-resolved two-point correlations $f_\theta(\mathbf{k}, t) = \mathcal{F}[\langle\theta(\mathbf{r}, t)\theta(\mathbf{r}', t)\rangle]$ of the spin orientation $\theta(\mathbf{r}, t) = \arcsin[\langle\hat{F}_x\rangle / \langle\hat{F}_x + i\hat{F}_y\rangle]$ in this long-lived nonequilibrium steady state were found to exhibit a spatio-temporal scaling of the form

$$f_\theta(\mathbf{k}, t) = t^\alpha f_s(t^\beta \mathbf{k}), \tag{2.28}$$

where the scaling function $f_s(\mathbf{k})$ and the exponents α and β are *universal* with respect to the parameters and initial conditions of the gas. In analogy with the establishment of universality classes in equilibrium statistical mechanics, ultracold fluids thus serve as a quantum simulator for nonequilibrium physics in, for example, cosmological or high-energy systems [101].

We will return to thermalization in more detail in Chapter 7 where we will employ the Gaussian trajectory method to study the dynamics of a spinor condensate evolving to a non-thermal fragmented state, and Chapter 8 where we will revisit non-thermal fixed points as a transient *prethermal* stage in the thermalization process. The analog simulation of cosmological physics in spinor gases, on the other hand, will be the focus of Part IV, where we will study analog Hawking radiation of spin excitations.

2.5 Coherently coupled binary mixtures

A system of intermediary complexity between the single-component Bose gas and its spin-1 extension is a *binary mixture*, described by a two-component vectorial field

$$\hat{\Psi}(\mathbf{r}, t) = \begin{pmatrix} \hat{\psi}_1(\mathbf{r}, t) \\ \hat{\psi}_2(\mathbf{r}, t) \end{pmatrix}. \tag{2.29}$$

Collisions among particles of the same species occur with equal intraspecies s-wave scattering lengths for both components $a_{11} = a_{22} = a$, while the interspecies scattering length $a_{12} \neq a$. With the respective interaction strength given by

$g_{ij} = 4\pi\hbar^2 a_{ij}/m$, the Hamiltonian of this system reads

$$\hat{\mathcal{H}} = \int \mathrm{d}\mathbf{r}\Big[\hat{\Psi}^\dagger\Big(\frac{-\hbar^2\nabla^2}{2m} + V_0(\mathbf{r})\Big)\hat{\Psi} + \frac{g}{2}\Big(\hat{\psi}_1^\dagger\hat{\psi}_1^\dagger\hat{\psi}_1\hat{\psi}_1 + \hat{\psi}_2^\dagger\hat{\psi}_2^\dagger\hat{\psi}_2\hat{\psi}_2\Big) + g_{12}\hat{\psi}_1^\dagger\hat{\psi}_2^\dagger\hat{\psi}_1\hat{\psi}_2 - \hbar\Omega\Big(\hat{\psi}_1^\dagger\hat{\psi}_2 + \hat{\psi}_2^\dagger\hat{\psi}_1\Big)\Big]. \quad (2.30)$$

The first line in this Hamiltonian describes two independent single-component fields as in Eq. (2.6), while the second line contains the coupling between the two components. In contrast to the full spin-1 manifold, interspecies interactions g_{12} conserve the number of atoms in each component. However, the resulting $U(1)\times U(1)$ symmetry is broken by the coupling term $\sim \Omega\hat{\psi}_1^\dagger\hat{\psi}_2$, which introduces coherent interspecies oscillations in the fluid. Physically, the coherent coupling stems from a radiofrequent field tuned to the hyperfine transition $\hbar\omega_{\mathrm{rf}}$ between the two components,

$$\Omega(t) = \Omega e^{i\omega_{\mathrm{rf}}t}, \quad (2.31)$$

where the amplitude, taken real and positive without loss of generality*, determines the coupling energy $\hbar\Omega$ [2]. Extending the case of the single-component Bose gas, the Heisenberg equations (2.9) governing the fields now yield

$$\begin{aligned} i\hbar\partial_t\hat{\psi}_1(\mathbf{r},t) &= \left(-\frac{\hbar^2\nabla^2}{2m} + V_0(\mathbf{r}) + g\hat{\psi}_1^\dagger\hat{\psi}_1 + g_{12}\hat{\psi}_2^\dagger\hat{\psi}_2\right)\hat{\psi}_1 - \hbar\Omega\hat{\psi}_2, \\ i\hbar\partial_t\hat{\psi}_2(\mathbf{r},t) &= \left(-\frac{\hbar^2\nabla^2}{2m} + V_0(\mathbf{r}) + g\hat{\psi}_2^\dagger\hat{\psi}_2 + g_{12}\hat{\psi}_1^\dagger\hat{\psi}_1\right)\hat{\psi}_2 - \hbar\Omega\hat{\psi}_1. \end{aligned} \quad (2.32)$$

Similarly to spin-1 fluids, the additional degree of freedom in the binary mixture gives rise to a rich variety of phenomena, including phase separation [85, 106–108], ferromagnetism [109] and topological excitations [110–113]. To limit the scope of this discussion, I refer to an elaborate overview of the system's properties provided by Abad and Recati [103], as well as a recent review of theoretical and experimental advances by Recati and Stringari [114].

The defining feature of binary mixtures which will be of interest in the final part of this thesis, is the fact that the interplay of two fluid components gives rise to two distinct types of *elementary excitations*, each with their own associated propagation velocity. In Chapter 10, we will use this fact to construct a *sonic horizon* for polarization sound waves, and study the analog Hawking effect it

* The amplitude and phase of the coupling term is a matter of convention. Some works use $\Omega/2$ instead of Ω [102], while others flip the sign convention for Ω [103–105], causing a phase difference π between the $\hat{\psi}_{1/2}$ fields in the ground state.

induces.

2.5.1 Experiments on binary mixtures

Being the most elementary extension of a single-component Bose gas, binary mixtures were proposed shortly after the first measurements of Bose-Einstein condensation [115], and soon after realized by concurrent condensation of atoms in the $|1,0\rangle, |2,0\rangle$ hyperfine states of ^{87}Rb [84, 85] and the $|F=1, m_F=\pm 1\rangle$ states of ^{23}Na [102, 113, 116–119]. Furthermore, two-component Bose condensates have been realized in heteronuclear ^{41}K-^{87}Rb mixtures, where the two components of the fluid consist of two different atomic species [120, 121]. Of these three systems, only the ^{23}Na mixture satisfies the equal masses and intracomponent scattering lengths for the two species assumed in the Hamiltonian (2.30). In practice, a $|F=1, m_F=\pm 1\rangle$ binary mixture is produced from a condensate of atoms in the $|F=1, m_F=0\rangle$ state through the application of a radiofrequent pulse which induces a Rabi oscillation in the spin-1 manifold, the duration of the pulse tuned to arrive at an equal population of the $|F=1, m_F=\pm 1\rangle$ states. To prevent the $m_F=0$ state from being repopulated through spin mixing processes, its energy level is raised through the addition of a negative quadratic Zeeman splitting, induced by a microwave dressing field on the $|1,0\rangle \leftrightarrow |2,0\rangle$ transition [116, 119, 122].

3 | Theoretical methods

Whether dealing with a three-dimensional fluid, a pancake or cigar condensate or even a single-mode zero-dimensional system, the exponential scaling of the Hilbert space dimension with system size ($\sim \exp\{N\}$) renders an exact description of the many-body wave function intractable for any sizable number of atoms N. As such, a wide range of perturbative and variational methods have been devised to obtain approximate solutions for the ground state and dynamic properties of these systems. In this chapter, we briefly cover the most commonly found items in the theoretical toolbox for weakly interacting quantum fluids.

3.1 Mean field theory: Gross-Pitaevskii equation

Setting the commutators (2.8) to zero, one may replace the quantum field $\hat{\psi}(\mathbf{r},t)$ by its classical expectation value $\psi(\mathbf{r},t) = \langle\hat{\psi}(\mathbf{r},t)\rangle$, reducing the Heisenberg equation of motion (2.10) for the weakly interacting Bose gas to the *Gross-Pitaevskii equation* (GPE) [2, 3],

$$i\hbar\partial_t\psi(\mathbf{r},t) = \left(\frac{-\hbar^2\nabla^2}{2m} + V_0(\mathbf{r}) + g|\psi(\mathbf{r},t)|^2\right)\psi(\mathbf{r},t). \tag{3.1}$$

This equation is equally obtained by replacing the Hamiltonian (2.6) with a classical energy functional $E = \langle\hat{\mathcal{H}}\rangle$ in which the classical fields $\psi(\mathbf{r},t) = \langle\hat{\psi}(\mathbf{r},t)\rangle$ and $\psi^*(\mathbf{r},t) = \langle\hat{\psi}^\dagger(\mathbf{r},t)\rangle$ take the role of canonically conjugate variables,

$$i\hbar\partial_t\psi(\mathbf{r},t) = \frac{\partial E}{\partial\psi^*(\mathbf{r},t)}. \tag{3.2}$$

This approach can be regarded as the lowest order of approximation in a formal expansion of the field $\hat{\psi}$ into its expectation value and quantum fluctuations,

$$\hat{\psi}(\mathbf{r},t) = \psi(\mathbf{r},t) + \delta\hat{\psi}(\mathbf{r},t). \tag{3.3}$$

As it neglects the effect of fluctuations altogether, the nonlinear Schrödinger equation (3.1) is commonly referred to as the *mean field* theory of the weakly interacting Bose gas. It replaces the entire fluid with the macroscopic order parameter describing the condensate. Originally introduced for the study of quantized vortices [123, 124], the Gross-Pitaevskii framework has become the main theoretical work horse of weakly interacting Bose fluids.

3.2 Bogoliubov theory of elementary excitations

Going beyond a mean field description, one may perturbatively include small quantum fluctuations in a weakly interacting fluid by explicitly performing the substitution (3.3) and expanding the Hamiltonian (2.6) to lowest non-vanishing order in the fluctuation operators $\delta\hat{\psi}$. This procedure, known as the *Bogoliubov approximation* [125], allows one to obtain an approximate quadratic Hamiltonian for the elementary excitations in a weakly interacting quantum system. However, its results may equally be derived from considering small amplitude oscillations on a stationary solution of the Gross-Pitaevskii equation (3.1) [2, 8, 124]. An additional advantage to this approach, which we will follow, is its emphasis on the fact that the properties of *quantum* fluctuations are to a large extent identical to those of *classical* excitations of a fluid. With $\psi_0(\mathbf{r})$ any solution of the time-independent Gross-Pitaevskii equation (GPE), one can expand the time-dependent GPE for the disturbed field,

$$\psi(\mathbf{r},t) = e^{-i\mu t/\hbar}[\psi_0(\mathbf{r}) + \delta\psi(\mathbf{r},t)], \tag{3.4}$$

up to first order in $\delta\psi(\mathbf{r},t)$, yielding

$$i\hbar\partial_t\delta\psi = \left(\frac{-\hbar^2\nabla^2}{2m} + V_0(\mathbf{r}) - \mu\right)\delta\psi + 2g|\psi_0|^2\delta\psi + g\psi_0^2\delta\psi^*. \tag{3.5}$$

As both $\delta\psi(\mathbf{r},t)$ and its complex conjugate occur, linearization requires both to be treated as independent variables, giving rise to the Bogoliubov equations,

$$i\hbar\partial_t\begin{pmatrix}\delta\psi\\ \delta\psi^*\end{pmatrix} = \begin{pmatrix}H_{GP} + g|\psi_0|^2 - \mu & g\psi_0^2\\ -g\psi_0^{*2} & -H_{GP} - g|\psi_0| + \mu\end{pmatrix}\begin{pmatrix}\delta\psi\\ \delta\psi^*\end{pmatrix}, \tag{3.6}$$

where the H_{GP} is the Gross-Pitaevskii operator given by the right hand side of Eq. (3.1). For a spatially uniform system ($V_0(\mathbf{r}) = 0$) at rest with stationary solution $\psi_0 = \sqrt{n}$ and chemical potential $\mu = gn$, the eigenmodes are plane

waves,

$$\begin{pmatrix} \delta\psi \\ \delta\psi^* \end{pmatrix} = \begin{pmatrix} U_{\mathbf{k}} \\ V_{\mathbf{k}} \end{pmatrix} e^{i(\mathbf{k}\cdot\mathbf{r}-\omega t)}, \tag{3.7}$$

reducing the above system to

$$\hbar\omega \begin{pmatrix} U_{\mathbf{k}} \\ V_{\mathbf{k}} \end{pmatrix} = \begin{pmatrix} \frac{\hbar^2 k^2}{2m} + gn & g\psi_0^2 \\ -g\psi_0^{*2} & -\frac{\hbar^2 k^2}{2m} - gn \end{pmatrix} \begin{pmatrix} U_{\mathbf{k}} \\ V_{\mathbf{k}} \end{pmatrix}. \tag{3.8}$$

This equation immediately yields the excitation spectrum

$$\hbar\omega_{\mathbf{k}} = \pm\sqrt{\frac{\hbar^2 k^2}{2m}\left(\frac{\hbar^2 k^2}{2m} + 2gn\right)}, \tag{3.9}$$

which allows for solutions of both positive and negative frequency. Quantization of the corresponding eigenmodes [126] allows one to arrive at an approximate quadratic Hamiltonian for the fluctuations [2],

$$\hat{\mathcal{H}} \approx \sum_{\mathbf{k}} \hbar\omega_{\mathbf{k}} \hat{b}_{\mathbf{k}}^\dagger \hat{b}_{\mathbf{k}}, \tag{3.10}$$

where the bosonic operators $\hat{b}_i$ and $\hat{b}_i^\dagger$ represent the annihilation and creation of elementary excitations. They are related to the momentum-space field operators in particle basis, $\hat{a}_{\mathbf{k}} = \int \delta\hat{\psi}(\mathbf{r},t) e^{i\mathbf{k}\cdot\mathbf{r}/\hbar} \mathrm{d}\mathbf{r}$, via the *Bogoliubov transformation*

$$\hat{b}_{\mathbf{k}} = U_{\mathbf{k}} \hat{a}_{\mathbf{k}} - V_{-\mathbf{k}}^* \hat{a}_{-\mathbf{k}}^\dagger, \tag{3.11}$$

and satisfy the correct bosonic commutation relation on the condition

$$|U_{\mathbf{k}}|^2 - |V_{-\mathbf{k}}|^2 = \pm 1. \tag{3.12}$$

The quantity $|U_{\mathbf{k}}|^2 - |V_{-\mathbf{k}}|^2$ is conserved during time evolution and is therefore referred to a s the *Bogoliubov norm** of a mode, its sign corresponding to the sign in Eq. (3.9). For positive-norm modes, the Bogoliubov coefficients are given by [2]

$$U_{\mathbf{k}}, V_{-\mathbf{k}} = \pm\left(\frac{\hbar^2 k^2 + gn}{2\hbar\omega_k} \pm \frac{1}{2}\right). \tag{3.13}$$

* Contrary to the classical definition of a norm, the Bogoliubov norm is not positive-definite as the Bogoliubov matrix $\mathcal{L}$ given in (3.8) is not Hermitian. Instead, the conserved Bogoliubov norm derives from its σ_z-pseudo-hermiticity, i.e., $\sigma_z \mathcal{L}^\dagger \sigma_z = \mathcal{L}$, with $\sigma_z = \mathrm{diag}(1,-1)$ the Pauli matrix.

We will return to the Bogoliubov problem in Part IV of this thesis, where we will study in more detail the consequences of negative frequency modes and the equivalence between quantum and classical excitations in the context of the *stimulated analog Hawking effect*. For now, we conclude that the Bogoliubov approximation reduces the dynamics of the Bose gas to *linear* dynamics of fluctuations on a *stationary* solution of the mean field, captured completely in the evolution of quadratic correlations $\langle \hat{b}_i \hat{b}_j \rangle$ and $\langle \hat{b}_i^\dagger \hat{b}_j \rangle$ – or equivalently $\langle \hat{\psi}_i \hat{\psi}_j \rangle$ and $\langle \hat{\psi}_i^\dagger \hat{\psi}_j \rangle$.

3.3 The Gaussian approximation

By neglecting the backreaction effect of fluctuation dynamics on the condensate itself (ψ_0), the Bogoliubov approximation is not number-conserving [8] and therefore generally unsuitable for the description of dynamics beyond early times. This limitation can be overcome by combining the Gross-Pitaevskii equations and a linearized account of fluctuations within a single self-consistent theory [127, 128]. This approach is referred to as the Gaussian variational approximation [129] as it results in a description in terms of the first and second moments of its fluctuation statistics – the expectation values $\psi = \langle \hat{\psi} \rangle$ and $\langle \hat{\psi}^{(\dagger)} \hat{\psi} \rangle$, respectively – in analogy to the mean μ and variance σ^2 of a Gaussian distribution.

Decomposing the field into its mean field mode and fluctuations of zero mean according to Eq. (3.3) and deriving the Heisenberg equations of motion (2.9) for these moments under the full Hamiltonian (2.6) gives rise to an infinite hierarchy of correlations, as the nonlinear dynamics of $\langle \delta\hat{\psi}^{(\dagger)} \delta\hat{\psi} \rangle$ introduce terms of order $\langle \delta\hat{\psi}^{(\dagger)} \delta\hat{\psi} \delta\hat{\psi} \rangle$, and so on. To close the hierarchy of correlations, the Gaussian approximation relies on the factorization of all even higher-order moments into products of quadratic correlations through a process of *Wick decomposition*[*],

$$\langle \hat{a}\hat{b}\hat{c}\hat{d} \rangle = \langle \hat{a}\hat{b} \rangle \langle \hat{c}\hat{d} \rangle + \langle \hat{a}\hat{c} \rangle \langle \hat{b}\hat{d} \rangle + \langle \hat{a}\hat{d} \rangle \langle \hat{b}\hat{c} \rangle , \tag{3.14}$$

while all odd-numbered moments are set to zero,

$$\langle \hat{a}\hat{b}\hat{c} \rangle = \langle \hat{a}\hat{b}\hat{c}\hat{d}\hat{e} \rangle = \cdots = 0. \tag{3.15}$$

This procedure amounts to neglecting all connected correlations or *cumulants*,

[*] Colloquially known as Wick's theorem after its first application to quantum operators by Gian Carlo Wick in 1950 [83], this convenient feature was first noted for classical Gaussian variables by Leon Isserlis in 1918 [130], predating Wick by 32 years. In classical probability, it is known as *Isserlis' theorem*. Confusingly, *Wick ordering* refers to the *normal ordering* of creation and annihilation operators, a procedure introduced in the same 1950 paper.

defined as

$$\begin{aligned}
\langle \hat{a}\hat{b}\hat{c}\rangle_{con} &= \langle \hat{a}\hat{b}\hat{c}\rangle\,, \\
\langle \hat{a}\hat{b}\hat{c}\hat{d}\rangle_{con} &= \langle \hat{a}\hat{b}\hat{c}\hat{d}\rangle - \langle \hat{a}\hat{b}\rangle\,\langle \hat{c}\hat{d}\rangle - \langle \hat{a}\hat{c}\rangle\,\langle \hat{b}\hat{d}\rangle - \langle \hat{a}\hat{d}\rangle\,\langle \hat{b}\hat{c}\rangle\,, \\
\langle \hat{a}\hat{b}\hat{c}\hat{d}\hat{e}\rangle_{con} &= \langle \hat{a}\hat{b}\hat{c}\hat{d}\hat{e}\rangle\,, \\
&\vdots
\end{aligned} \tag{3.16}$$

which at third and fourth order in fluctuations is equivalent to setting both the skewness and kurtosis of the distribution to zero, assuming fluctuations are symmetrically centered around their mean value and do not follow a heavy-tailed distribution. By retaining only terms up to second order in $\delta\hat{\psi}_m$, one thus arrives at a consistent, number-conserving description of the fields in terms of the first and second moments of their statistics.

3.3.1 Coherent and squeezed states

The set of Gaussian states encompasses the ground and thermal states of all Hamiltonians which are at most quadratic in the field operators $\hat{\psi}$ [129]. More specifically, these include the *vacuum* state, *coherent* states, *squeezed* states and mixtures thereof. To visualize these states for a single mode $\hat{\psi}$ in the complex plane, we introduce the *quadrature variables* commonly used in the field of quantum optics [129, 131],

$$\hat{X} = \frac{\hat{\psi} + \hat{\psi}^\dagger}{2}, \qquad \hat{P} = \frac{\hat{\psi} - \hat{\psi}^\dagger}{2i}. \tag{3.17}$$

Defined in analogy to the position and momentum operators of a harmonic oscillator, the quadrature variables in every quantum state must satisfy the Heisenberg uncertainty relation

$$\Delta\hat{X}\Delta\hat{P} \geq \frac{1}{4}, \tag{3.18}$$

where $\Delta\hat{O} = \sqrt{\langle\hat{O}^2\rangle - \langle\hat{O}\rangle^2}$ is the standard deviation of fluctuations in $\hat{O}$. The vacuum state, denoted $|0\rangle$, is defined as a state with vanishing mean field amplitude $\langle\hat{\psi}\rangle = 0$, or equivalently $\langle\hat{X}\rangle = \langle\hat{P}\rangle = 0$. Due to the Heisenberg relation, it is however characterized by nonzero fluctuations in the quadrature variables, $\Delta\hat{X} = \Delta\hat{P} = 1/2$, as pictured in Fig. 3.1(a). From the vacuum state, *canonical coherent states* (CCS) or simply *coherent states* [129, 132, 133], denoted $|\alpha\rangle_c$, are generated through the application of the displacement operator

$$\hat{D}(\alpha) = \exp\Big\{\alpha\hat{\psi}^\dagger - \alpha^*\hat{\psi}\Big\}, \tag{3.19}$$

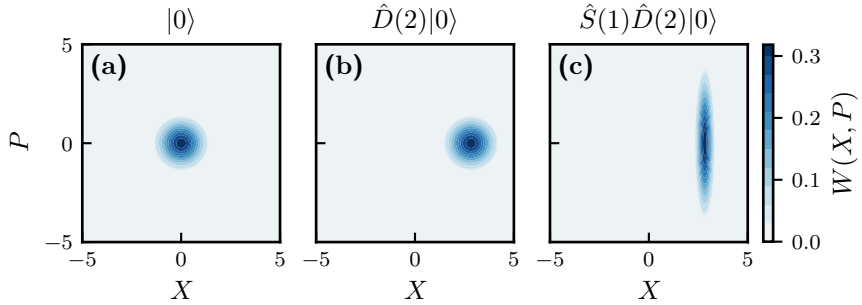

Figure 3.1 – Depiction of a single-mode quantum system in the complex plane spanned by the quadrature variables $\hat{X}$ and $\hat{P}$. Shown are a vacuum state (a), a coherent or displaced state (b) and a squeezed state (c). The heatmap of each state represents the respective Wigner distribution function, introduced in Sec. 3.4.

which displaces the vacuum to the mean field $\alpha = \langle\hat{\psi}\rangle$ while leaving its symmetric fluctuations unaltered, as shown in Fig. 3.1(b). As this operation is equivalent to the substitution underlying the mean field approximation of Sec. 3.1, coherent states may be regarded as the *most classical states*, and the mean field description can likewise be interpreted as a variational description in terms of coherent states. Finally, the archetypical Gaussian operation is the squeezing operator*

$$\hat{S}(\sigma) = \exp\left\{\frac{1}{2}\left[\sigma^*\hat{\psi}^2 - \sigma(\hat{\psi}^\dagger)^2\right]\right\}, \tag{3.21}$$

which (for $\sigma \in \mathbb{R}$) suppresses the variance of fluctuations by a factor $e^{-2\sigma}$ in $\hat{X}$ while increasing that in $\hat{P}$ by a factor $e^{2\sigma}$, maintaining the Heisenberg bound. Confining a quantum state beyond classical precision in one quadrature variable at the expense of a delocalization in the conjugate direction, the squeezing operation is highly non-classical and constitutes the main generalization of Gaussian states with respect to the largely classical physics captured by coherent states [134]. Depicted in Fig. 3.1(c) is a general Gaussian state, obtained from successive application of a squeezing and displacement operator on the vacuum state.

* Application of the squeezing operator to a generic quantum state corresponds to a Bogoliubov transformation of the field operators,

$$\hat{S}^\dagger(\sigma)\hat{\psi}\hat{S}^\dagger(\sigma) = \cosh(\sigma)\hat{\psi} - \sinh(\sigma)\hat{\psi}^\dagger, \tag{3.20}$$

with the coefficients indeed satisfying condition (3.12).

3.3.2 Gaussian states as a variational theory

Gaussian states, as described in this work, are ubiquitous in the field of continuous-variable quantum information [129, 133] and quantum optics [131, 135]. In the context of atomic gases, the Gaussian theory is commonly reffered to as the Hartree-Fock-Bogoliubov (HFB) approximation [127, 128, 136–138], since it comes down to a self-consistent inclusion of anomalous correlations of the form $\langle \delta\hat{\psi}_m \delta\hat{\psi}_n \rangle$, captured by Bogoliubov theory, into the Hartree-Fock approximation*, which forms the simplest description of a thermal gas by introducing excitations described by the statistically independent occupations $\langle \delta\hat{\psi}_m^\dagger \delta\hat{\psi}_m \rangle$ [2]. In the remainder of this work, we will use the terms *Gaussian approximation* and *HFB* interchangeably to denote this theory.

The Gaussian theory allows to infer the approximate dynamics of a generic quantum state as the evolution of the statistical moments $\langle \hat{\psi} \rangle$ and $\langle \delta\hat{\psi}^{(\dagger)} \delta\hat{\psi} \rangle$. As closing the dynamics at the Gaussian level restricts the evolution of a system initialized in a Gaussian state to the *variational* subspace of all such Gaussian states [129, 139], the dynamical Gaussian theory can be seen as a *time-dependent variational principle* (TDVP) [127, 140, 141]. While results from the Gaussian Ansatz become unpredictable when the actual state of the system develops significant non-Gaussianity, – i.e., the growth of higher order cumulants – its predictions inevitably correspond to physical states. Moreover, the self-consistency of Wick decomposition guarantees that Gaussian dynamics conserve the energy of the initial state. Linearized theories such as the Bogoliubov or Popov approximations, by contrast, are not number-conserving and therefore do not provide a variational description of a closed system.

Alternative approaches which retain higher-order correlations of fluctuations equally lack this variational quality, as the absence of an equivalent to Wick decomposition requires a manual truncation of the correlation hierarchy. Most notably, cumulant expansions up to third order in fluctuation operators have been shown to account for nonlinear Landau-Beliaev scattering responsible for equilibration in Bose gases [138, 142, 143], as well as the formation of three-body Efimov molecules in strongly interacting Bose gases [138, 144]. However, truncation of the correlation hierarchy at third order requires the ad hoc elimination of fourth- and fifth-order contributions to the equations of motion, resulting in a violation of

* By neglecting the nonlinear evolution of $\langle \delta\hat{\psi}^{(\dagger} \delta\hat{\psi} \rangle$ stemming from Wick factorization, the Hartree-Fock-Bogoliubov approach further reduces to the *Popov approximation*, which aims to include to lowest order the effect of quasiparticle pair creation (captured by the correlations $\langle \delta\hat{\psi} \delta\hat{\psi} \rangle$) in the finite temperature Hartree-Fock theory [3]. Equivalently, the Popov approximation thus serves as a finite-temperature extension to the Bogoliubov approach [128].

energy conservation. Besides precluding the study of long-time thermalization dynamics, the violation of energy conservation introduces an artefact in the dynamics which may lead the system to unphysical regions of its Hilbert space, such as states characterized by negative occupation numbers [138]. In contrast to a truncation at the Gaussian level, this limits the applicability of a third-order cumulant expansion to early time dynamics. As the time scale up to which reliable results are obtained is not known a priori, a third-order expansion is intrisically unstable. An energy-conserving theory is obtained by truncating the correlation hierarchy at the level of fourth-order correlations, but the computational cost of tracking their evolution makes this approach unfeasible to study long-time dynamics [138].

3.4 Phase space methods

Rather than considering the dynamics of wave functions in a Hilbert space, one can instead represent the quantum state in the *phase space* of the classical fields $\psi(\mathbf{r}), \psi^*(\mathbf{r})$, discretized as $\psi_j = \psi(\mathbf{r}_j)$ and $\psi_j^* = \psi^*(\mathbf{r}_j)$ on a finite-resolution grid to avoid divergences [145, 146]. Different from the mean field approximation, the quantum state is now represented by a distribution in phase space to account for quantum fluctuations. As the mapping from a quantum field $\hat{\psi}_j$ to a classical distribution loses the operator character and hence commutation relations, multiple phase space representations exist which correspond to different conventions for the ordering of operators. Among these, the most frequently used representations are the Glauber-Sudarshan P-representation (normal ordering), the Husimi Q-representation (anti-normal ordering) and the Wigner W-representation (symmetric ordering). While each of these approaches have their merits and limitations, we will limit our discussion to a brief introduction of the Wigner distribution and the truncation of its dynamics. A more elaborate treatment of phase space methods can be found in Ref. [147].

The Wigner distribution $W(\psi, \psi^*)$ of a single-mode quantum state, described by the density matrix $\hat{\rho}$, is constructed as the Fourier transform of its characteristic function $\chi(\lambda, \lambda^*)$ [145, 147],

$$W(\psi, \psi^*) = \frac{1}{\pi^2} \int e^{-\lambda\psi^* + \lambda^*\psi} \chi(\lambda, \lambda^*) \mathrm{d}^2\lambda, \tag{3.22}$$

where $\mathrm{d}^2\lambda = \mathrm{d}(\mathrm{Re}[\lambda])\, \mathrm{d}(\mathrm{Im}[\lambda])$ and the characteristic function is defined as

$$\chi(\lambda, \lambda^*) = \mathrm{Tr}\left[\hat{\rho} e^{\lambda\hat{\psi}^\dagger - \lambda^*\hat{\psi}}\right]. \tag{3.23}$$

Examples of Wigner distributions in the basis of quadrature variables were shown earlier in Fig. 3.1. The statistical moments of this *quasiprobability distribution** correspond to the expectation values of symmetrically ordered operators, i.e.,

$$\int (\psi^*)^s \psi^r W(\psi,\psi^*)\mathrm{d}^2\psi \equiv \langle (\psi^*)^s \psi^r \rangle_W = \langle (\hat{\psi}^\dagger)^s \hat{\psi}^r \rangle_{\mathrm{sym}}\,, \tag{3.24}$$

where the symmetrized expectation value $\langle (\hat{\psi}^\dagger)^s \hat{\psi}^r \rangle_{\mathrm{sym}}$ denotes the average of all possible permutations. Application of this symmetrization to the density operator $\hat{\psi}_j^\dagger \hat{\psi}_j$ of a multimode system yields

$$\langle \hat{\psi}_j^\dagger \hat{\psi}_j \rangle_{\mathrm{sym}} = \frac{1}{2}\langle \hat{\psi}_j^\dagger \hat{\psi}_j + \hat{\psi}_j \hat{\psi}_j^\dagger \rangle = \langle \hat{\psi}_j^\dagger \hat{\psi}_j \rangle + \frac{1}{2}, \tag{3.25}$$

implying that the Wigner expectation value $\langle \psi_j^* \psi_j \rangle_W$ adds an occupation of 1/2 particle to each mode of the system†.

Through a procedure of *operator correspondence*, the Heisenberg equations (2.9) for the discretized fields $\hat{\Psi} = \hat{\psi}_1, \ldots, \hat{\psi}_L$ can be mapped to a partial differential equation governing the Wigner function [146, 147],

$$\begin{aligned} i\hbar\partial_t W(\Psi,\Psi^*,t) = \sum_j \Bigg\{ &- \left(\frac{\partial}{\partial\psi_j}\mathcal{F}_j + \frac{\partial}{\partial\psi_j^*}\mathcal{F}_j^* \right) \\ &+ \frac{g}{4\Delta V^2}\frac{\partial^2}{\partial\psi_j\partial\psi_j^*}\left(\frac{\partial}{\partial\psi_j^*}\psi_j^* - \frac{\partial}{\partial\psi_j}\psi_j \right) \Bigg\} W(\Psi,\Psi^*,t), \end{aligned} \tag{3.26}$$

where ΔV is the grid discretization‡ and the force term $\mathcal{F}_j = \mathcal{F}(\mathbf{r} = \mathbf{r}_i)$ denotes the mean field (Gross-Pitaevskii) functional (3.1). In the mean field limit $g \to 0$ at finite interaction energy $g|\psi|^2$, the second line containing third-order derivatives may be neglected to arrive at the *truncated Wigner approximation* (TWA) [145],

$$i\hbar\partial_t W(\Psi,\Psi^*,t) \approx -\sum_j \left(\frac{\partial}{\partial\psi_j}\mathcal{F}_j + \frac{\partial}{\partial\psi_j^*}\mathcal{F}_j^* \right) W(\Psi,\Psi^*,t). \tag{3.27}$$

Within the TWA, the evolution of $W(\Psi,\Psi^*,t)$ can be mapped to a set of differ-

* While normalized over the entirety of phase space, the Wigner function is not strictly positive. As such, it cannot be interpreted as a probability distribution for the state of the system.

† It is precisely the representation of the quantum vacuum as a nonzero average occupation which allows the Wigner distribution to capture the effect of quantum fluctuations in a semiclassical theory. Equation (3.25) then illustrates the requirement of a finite number of modes to avoid an infinite amount of vacuum noise being added to the system.

‡ This factor is absent in intrinsically discrete systems such as the Bose-Hubbard model discussed in Chapter 4 and the single-mode spinor condensate of Chapters 7 and 8.

ential equations for the fields ψ_j,

$$i\hbar\partial_t\psi_j(t) = \mathcal{F}_j(t)\mathrm{d}t \tag{3.28}$$

which is identical to the time-dependent Gross-Pitaevskii equation (3.1). Now representing the evolution of the entire fluid instead of only the condensate, quantum fluctuations are included in the deterministic time evolution through the stochastic sampling of the initial conditions $\Psi(t=0)$ from the Wigner distribution of the initial state [145]. In accordance with the vacuum noise 1/2 added to each eigenmode of the system, the dynamics of an initially fully condensed fluid (i.e., a *coherent state*) with field amplitudes $\psi_j^{(0)}$ is retrieved by sampling the initial state as

$$\psi_j = \psi_j^{(0)} + \Delta Z_j, \tag{3.29}$$

where ΔZ_j is a complex Gaussian random variable with variance 1/2. Because of this sampling and the accompanying addition of 1/2 to the average occupation of each mode (3.25), a requirement for the validity of the truncated Wigner approximation is a mean mode occupation vastly outweighing this quantity [145]. With N the total number of particles and L the number of modes, this amounts to the condition

$$N \gg L/2. \tag{3.30}$$

In the presence of an external environment (see Sec. 3.6.4), the evolution of the Wigner distribution will acquire an additional diffusion term, resulting in a *Fokker-Planck* equation which is mapped to a stochastic differential equation instead of the fully deterministic Gross-Pitaevskii equation.

3.5 Other approaches

We have limited our discussion to the most fundamental approximate theories. However, a large variety of different perturbative and variational approaches are available for the study of many-body quantum systems, tailored to specific systems or physical regimes. Many variational approaches are based on a suitable factorization of the many-body wave function, among them Laughlin states [148], Dicke states [149, 150] and Gutzwiller states [151–153]. For weakly entangled many-mode systems, a computationally efficient representation is offered by *matrix product states* [141, 154–159] and their generalization to *tensor networks* [160–163]. Finally, recent years have seen the introduction of machine learning techniques in many areas of physics [164], among which the formulation of new variational approaches based on *neural network quantum states*

(NQS) [165–168].

3.6 Including the external environment

While atomic fluids trapped in a vacuum chamber are to a large extent isolated from their external environment, some leaking of atoms and energy out of the confinement potential remains unavoidable. This is true a fortiori for driven-dissipative optical systems, where the interplay between Hamiltonian dynamics and the loss and pumping of photons is crucial to the evolution of the system [169]. In these cases, the unitary evolution of the system of interest governed by its Hamiltonian $\hat{\mathcal{H}}_S$ must be extended to a description which includes the environment,

$$\hat{\mathcal{H}}_S \to \hat{\mathcal{H}}_S + \hat{\mathcal{H}}_E + \hat{\mathcal{H}}_C, \tag{3.31}$$

where $\hat{\mathcal{H}}_E$ denotes the Hamiltonian of the environment and $\hat{\mathcal{H}}_C$ contains the coupling between the environment and the system.

3.6.1 The Lindblad master equation

The combined system and its environment form a pure quantum state described by the density matrix $\hat{\rho} = |\psi\rangle\langle\psi|$. Containing much information irrelevant to observables pertaining to the system of interest, this density matrix is reduced to that of the system alone by taking the partial trace over the environment degrees of freedom,

$$\hat{\rho}_S = \mathrm{Tr}_E[\hat{\rho}]. \tag{3.32}$$

As the system and its environment are in general correlated, the reduced density matrix $\hat{\rho}_S$ represents a mixed state. An effective description of the system can therefore not be formulated on the level of a pure state $|\psi\rangle$, but must instead take the form of a master equation governing the density matrix $\hat{\rho}_S$.

In the *Born-Markov* approximation, the weakly coupled environment is assumed to be negligibly affected by its coupling to the system, and characterized by short correlation times with respect to the time scale on which the system relaxes due to its coupling to the environment [169]. The total density matrix may then be approximated as

$$\hat{\rho}(t) \approx \hat{\rho}_S(t) \otimes \hat{\rho}_E. \tag{3.33}$$

Neglecting memory effects arising from the interaction between the system and its environment, one arrives at the *Lindblad master equation* governing the density

matrix $\hat{\rho}_S$ of the system,

$$\frac{\mathrm{d}\hat{\rho}_S}{\mathrm{d}t} = -\frac{i}{\hbar}\left[\hat{\mathcal{H}}_S, \hat{\rho}_S\right] + \mathcal{D}(\hat{\rho}_S). \tag{3.34}$$

In addition to the unitary dynamics of the isolated system $\hat{\mathcal{H}}_S$, the coupling to the environment is then encoded in the *dissipator*

$$\mathcal{D}(\hat{\rho}) = \sum_j \left[\hat{\Gamma}_j \hat{\rho} \hat{\Gamma}_j^\dagger - \frac{1}{2}\left(\hat{\Gamma}_j^\dagger \hat{\Gamma}_j \hat{\rho} + \hat{\rho} \hat{\Gamma}_j^\dagger \hat{\Gamma}_j\right)\right], \tag{3.35}$$

where the *Lindblad operators* or *jump operators* $\hat{\Gamma}_j$ capture the decay processes to which the system is subject*. Depending on the details of the system, these may include, among others, single-particle or two-body losses, phase noise, three-body recombination, spin-flip processes and tunneling jumps [57]. In the remainder of this thesis, we will focus predominantly on single-particle losses due to the leaking of atoms out of the system at rate γ, represented by the Lindblad operator $\hat{\Gamma}_j = \sqrt{\gamma}\hat{\psi}_j$, where $\hat{\psi}_j$ is the annihilation operator for the mode (i.e., momentum state, lattice site or spin state) from which the atom is lost. Such single-atom losses originate from incoherent interactions with the environment imparting an atom with a kinetic energy which enables it to escape the trapping potential [169]. Alternatively, single-atom losses may be caused by deliberate external stimulation, such as an electron beam impinging on the system [66, 75], or may result from the spontaneous decay of particles to lower energy states in a state-selective trapping potential.

3.6.2 Quantum trajectories and measurement schemes

While the exact dynamics of a pure quantum state are already intractable beyond few-mode systems, the quadratic scaling of the density matrix $\hat{\rho}_S$ with the dimension of the Hilbert space renders an exact description of its evolution an even more hopeless endeavour. Besides the extension of matrix product states to mixed states in so-called *matrix product operators* (MPO) [155, 156, 170, 171] and related *renormalization* methods based a truncation of the Hilbert space to a physically motivated subspace [172], an efficient simulation of dynamics is achieved in the *quantum trajectory* or *wave function Monte Carlo* framework [169, 173–178]. In this method, the time evolution of the system is sampled through stochastic realizations of a pure quantum state $|\psi(t)\rangle$, known as *un-*

* In the combined Hilbert space $\mathscr{H}_S \otimes \mathscr{H}_E$ of the system and its environment, the coupling Hamiltonian is of the form $\hat{\mathcal{H}}_c = \sum_i (\hat{\Gamma}_i \otimes \hat{E}_i^\dagger + h.c.)$. The Lindblad operators thus capture the effect of these interaction terms on the system of interest [169].

ravelings of the underlying master equation [139, 169]. From the ensemble of stochastic realizations, one then infers the dynamics of the density matrix as the statistical average $\hat{\rho}_S(t) \approx \overline{|\psi(t)\rangle \langle\psi(t)|}$.

Physically, the stochastic evolution of a single trajectory derives from the incoherent coupling to the environment, which can be thought of as continuously measuring the system. The random outcomes of these measurements induce *jumps* in the system itself, resulting in stochastic trajectories. As such, the evolution of the sampled state $|\psi(t)\rangle$ depends on the chosen measurement scheme, all of which lead to the same ensemble average $\hat{\rho}_S(t)$. This can be understood from the fact that the decomposition of a density matrix into a mixture of pure states,

$$\hat{\rho}_S = \sum_j p_j \, |\psi_j\rangle \langle\psi_j| \,, \tag{3.36}$$

is not unique. Different measurement schemes unravel into different wave functions $|\psi_j\rangle$ with different weights p_j.

The simplest measurement scheme is *photon counting**, in which the unitary evolution of the system is interrupted by discrete *jumps* as a single particle dissipates from the system. In the remainder of this work we will instead focus on a more continuous measurement scheme called *quantum state diffusion* [177, 179], which explicitly maps the Lindblad equation (3.34) to a stochastic differential equation† for the quantum state $|\psi\rangle$,

$$\mathrm{d}\,|\psi\rangle = \left[-\frac{i}{\hbar}\hat{\mathcal{H}}_S \mathrm{d}t + \sum_j \left(\langle \hat{\Gamma}_j^\dagger \rangle \, \hat{\Gamma}_j - \frac{1}{2}\hat{\Gamma}_j^\dagger \hat{\Gamma}_j \right) \mathrm{d}t + \sum_j \hat{\Gamma}_j \mathrm{d}Z_j \right] |\psi\rangle \,. \tag{3.37}$$

The stochastic nature is captured by the appearance of uncorrelated complex Wiener processes satisfying

$$\begin{aligned} \langle \mathrm{d}Z_j^* \mathrm{d}Z_k \rangle &= \delta_{j,k} \mathrm{d}t \\ \langle \mathrm{d}Z_j \mathrm{d}Z_k \rangle &= 0. \end{aligned} \tag{3.38}$$

Upon the application of Itō's lemma,

$$\mathrm{d}(|\psi\rangle \langle\psi|) = |\psi\rangle \, (\mathrm{d}\,\langle\psi|) + (\mathrm{d}\,|\psi\rangle) \, \langle\psi| + (\mathrm{d}\,|\psi\rangle)(\mathrm{d}\,\langle\psi|), \tag{3.39}$$

* Like most terminology of open quantum systems, this term has its origin in optical implementations. For atomic fluids, *atom counting* would consist of detecting the number of atoms lost from the trapping potential.

† Throughout this thesis, we work in the Itō formalism for stochastic processes [180].

one readily finds that equation (3.37) is consistent with the Lindblad equation (3.34). This specific measurement scheme is called *heterodyne* unraveling due to its equivalence to the experimental heterodyne measurement protocol used in quantum optics. Its physical interpretation comes down the interference of atoms leaking from the system with a detuned reference beam, giving access to both the density and phase of the wave function.

3.6.3 Gaussian variational trajectories

While reducing the computational complexity from $\dim[\mathscr{H}_S]^2$ to $\dim[\mathscr{H}_S]$, the exact integration of the time evolution of a quantum trajectory $|\psi(t)\rangle$ remains unfeasible for large systems. This is true even more so than in the case of a closed quantum system, both because the coupling to the environment relaxes conservation laws within the system, and because of the large number of trajectories required to infer the evolution of $\hat{\rho}_S(t)$. The approximate methods outlined in Sec. 3 are thus still required to obtain tractable descriptions.

In variational theories such as the Gaussian approximation (see Sec. 3.3), the evolution of the variational state $|\psi(\alpha_1, \ldots, \alpha_M)\rangle$ is entirely captured in the evolution of the variational parameters $\alpha_1, \ldots, \alpha_M$, where $M \ll \dim[\mathscr{H}_S]$. To see how the Gaussian Ansatz can be straightforwardly implemented in the quantum trajectory framework, note that its variational parameters are simply the first and second moments of the fluctuations statistics of $\hat{\psi}$, i.e., the expectation values $\langle\hat{\psi}\rangle$ and $\langle\delta\hat{\psi}^{(\dagger)}\delta\hat{\psi}\rangle$. Within a single trajectory $|\psi(t)\rangle$, the evolution of the expectation value for a generic observable $\hat{O}$ is given by

$$\mathrm{d}\,\langle\psi|\hat{O}|\psi\rangle = \mathrm{d}(\langle\psi|)\,\hat{O}\,|\psi\rangle + \langle\psi|\,\hat{O}\,\mathrm{d}(|\psi\rangle) + \mathrm{d}(\langle\psi|)\,\hat{O}\,\mathrm{d}(|\psi\rangle)\,, \tag{3.40}$$

where $\mathrm{d}\,|\psi\rangle$ denotes the stochastic Schrödinger equation of the preceding section. For the heterodyne unraveling scheme (3.37), this results in

$$\mathrm{d}\,\langle\hat{O}\rangle = -\frac{i}{\hbar}\left\langle\left[\hat{O}, \hat{\mathcal{H}}_S\right]\right\rangle \mathrm{d}t - \frac{1}{2}\sum_j \left(\left\langle\left\{\hat{\Gamma}_j^\dagger\hat{\Gamma}_j, \hat{O}\right\}\right\rangle - 2\left\langle\hat{\Gamma}_j^\dagger\hat{O}\hat{\Gamma}_j\right\rangle\right)\mathrm{d}t + \sum_j \left(\left\langle\hat{\Gamma}_j^\dagger(\hat{O} - \langle\hat{O}\rangle)\right\rangle \mathrm{d}Z_j + c.c.\right), \tag{3.41}$$

where $\{\hat{a}, \hat{b}\} = \hat{a}\hat{b} + \hat{b}\hat{a}$. Applying Eq. (3.41) to the Gaussian expectation values, one computes the unraveling of the Lindblad master equation in a *Gaussian variational trajectory*. In Chapter 4, we will extend this framework to *isolated* systems, where the introduction of an artificial environment serves to improve the conventional Gaussian description of dynamics.

3.6.4 Mean field and phase space implementation

Conceptually distinct from the quantum trajectory method, but similarly resulting the simulation of wave functions rather than density matrices, is the extension of mean field and phase space methods (i.e., the truncated Wigner approximation) to systems interacting with an external environment. We will illustrate this for the case of single-atom losses $\hat{\Gamma}_j = \sqrt{\gamma}\hat{\psi}_j$. In the mean field approximation, such dissipation is included by the extension of the Gross-Pitaevskii equation (3.1) to account for the deterministic loss of atoms [146],

$$i\hbar\partial_t\psi(\mathbf{r},t) = \left(\frac{-\hbar^2\nabla^2}{2m} + V_0(\mathbf{r}) + g|\psi(\mathbf{r},t)|^2 - i\frac{\gamma}{2}\right)\psi(\mathbf{r},t). \tag{3.42}$$

In the Wigner representation of phase space, the evolution equation (3.26) of the Wigner function acquires an additional diffusion term of the form

$$\partial_t W(\Psi,\Psi^*,t) \sim \frac{\gamma}{2\Delta V}\sum_j \frac{\partial^2}{\partial\psi_j\partial\psi_j^*}W(\Psi,\Psi^*,t). \tag{3.43}$$

Upon truncation of the third-order derivatives, this generalizes its evolution to a *Fokker-Planck* equation which can be mapped to a stochastic differential equation of the form

$$i\hbar\partial_t\psi_j(t) = \mathcal{F}_j(t)\mathrm{d}t + \sqrt{\frac{\gamma}{4\Delta V}}\mathrm{d}Z_j, \tag{3.44}$$

with $\mathrm{d}Z_j$ uncorrelated complex Wiener noise as in (3.38). In addition to the stochastic sampling of the initial state $\psi(\mathbf{r}, t = 0)$ from its Wigner distribution, the truncated Wigner simulation of *open* quantum systems thus contains stochastic noise throughout its evolution.

II

Gaussian dynamics in a virtual environment

"The laws of statistics are valid only where large numbers or long periods are involved, and acts or events can statistically appear only as deviations or fluctuations. The justification of statistics is that deeds and events are rare occurrences in everyday life and in history. Yet the meaningfulness of everyday relationships is disclosed not in everyday life but in rare deeds, just as the significance of a historical period shows itself only in the few events that illuminate it. The application of the law of large numbers and long periods to politics or history signifies nothing less than the wilful obliteration of their very subject matter, and it is a hopeless enterprise to search for meaning in politics or significance in history when everything that is not everyday behavior or automatic trends has been ruled out as immaterial.

[...]

Statistical uniformity is by no means a harmless scientific ideal; it is the no longer secret political ideal of a society which, entirely submerged in the routine of everyday living, is at peace with the scientific outlook inherent in its very existence."

– Hannah Arendt, *The Human Condition*

4 | Gaussian trajectories for isolated systems

Having introduced the Bose-Hubbard model and approximate methods to capture its dynamics in Chapter 2, we will now use this model as a platform to develop the Gaussian trajectory approach (GTA) to many-body dynamics. The aim of this approach, the application of which forms a central contribution of this thesis, is to extend the time-dependent variational simulation of isolated systems to previously inaccessible regimes via the introduction of an artificial environment. Specifically focusing on the variational class of Gaussian states, we will show how its failure to adequately describe chaotic dynamics – and the associated growth of quantum fluctuations – can be overcome by the addition of suitably implemented artificial dissipation.

4.1 Gaussian theory of the Bose-Hubbard model

We again consider the Bose-Hubbard Hamiltonian (2.11) and develop the equations of motion within the Gaussian (or Hartree-Fock-Bogoliubov, HFB) variational Ansatz introduced in Sec. 3.3. To this end, the field operator is expanded as

$$\hat{a}_m = \alpha_m + \hat{\delta}_m, \tag{4.1}$$

such that, upon Wick factorization of higher moments, the dynamics are completely governed by coupled equations of motion for the mean field amplitudes $\langle \hat{a}_n \rangle$ on every site n and quadratic correlations of the corresponding fluctuations operators $\hat{\delta}_n$,

$$\begin{aligned} \alpha_n &\coloneqq \langle \hat{a}_n \rangle , \\ u_{nm} &\coloneqq \langle \hat{\delta}_n \hat{\delta}_m \rangle = \langle \hat{a}_n \hat{a}_m \rangle - \alpha_n \alpha_m, \\ v_{nm} &\coloneqq \langle \hat{\delta}_n^\dagger \hat{\delta}_m \rangle = \langle \hat{a}_n^\dagger \hat{a}_m \rangle - \alpha_n^* \alpha_m. \end{aligned} \tag{4.2}$$

These equations are derived by computing the Heisenberg equations (2.9) for the operators $\hat{a}_n$, $\hat{a}_n\hat{a}_m$ and $\hat{a}_n^\dagger\hat{a}_m$, respectively*. The former takes the form of a generalized Gross-Pitaevskii equation,

$$\mathrm{d}\alpha_n = \frac{i}{\hbar}\left[J\sum_{n'}\alpha_{n'} - U(|\alpha_n|^2\alpha_n + 2\alpha_n v_{nn} + \alpha_n^* u_{nn})\right]\mathrm{d}t, \tag{4.3}$$

while the latter read

$$\begin{aligned}\mathrm{d}u_{nm} = \frac{i}{\hbar}\Bigg[&J\left(\sum_{n'}u_{n'm} + \sum_{m'}u_{nm'}\right)\\ &- U\Big\{ + 2u_{nm}(|\alpha_n|^2 + |\alpha_m|^2 + v_{nn} + v_{mm}) + v_{nm}(\alpha_n^2 + u_{nn})\\ &\qquad + v_{mn}(\alpha_m^2 + u_{mm}) + \delta_{n,m}(\alpha_n\alpha_m + u_{nm})\Big\}\Bigg]\mathrm{d}t, \end{aligned}\tag{4.4}$$

$$\begin{aligned}\mathrm{d}v_{nm} = \frac{i}{\hbar}\Bigg[&- J\left(\sum_{n'}v_{n'm} - \sum_{m'}v_{nm'}\right)\\ &+ U\Big\{2v_{nm}(|\alpha_n|^2 - |\alpha_m|^2 + v_{nn} - v_{mm}) + u_{nm}(\alpha_n^{*2} + u_{nn}^*)\\ &\qquad - u_{nm}^*(\alpha_m^2 + u_{mm})\Big\}\Bigg]\mathrm{d}t. \end{aligned}\tag{4.5}$$

In the above equations, primed indices n' refer to summations over the nearest neighbours of site n without double counting.

4.1.1 Integrable and chaotic dynamics

To illustrate the limitations of the Gaussian variational theory and the improvements we will make to it in the sections to come, we will simulate the dynamics of a *classically chaotic* Bose-Hubbard chain.

In the superfluid regime, the Bose-Hubbard dynamics are said to be *integrable* for $L = 1$ and 2 lattice sites, as the number of degrees of freedom does not exceed

* To reduce the latter two to equations for u_{nm} and v_{nm}, one has to subtract the evolution of $\alpha_n^{(*)}\alpha_m$, derived from the equation for α_n. Alternatively, the Hamiltonian (2.11) can be explicitly expanded in orders of fluctuations $\hat{\delta}_n$. The equation of motion for α_n then arises from treating α_n and α_n^* as canonically conjugate variables as in Eq. (3.2), while the Heisenberg equations for u_{nm} and v_{nm} can be computed directly from the expanded Hamiltonian upon application of Wick decomposition.

the number of conserved quantities – in this case the total particle number and energy [181]. This translates to highly regular classical dynamics, governed by the Gross-Pitaevskii equation*

$$i\hbar\partial_t\alpha_n = -J\sum_{n'}\alpha_{n'} + U|\alpha_n|^2\alpha_n. \tag{4.6}$$

The regularity of the dynamics, experimentally verified for a bosonic fluid in a double-well potential [182], can be seen in the phase space trajectory† of a single on-site amplitude $\langle\hat{a}_1\rangle$ in the complex plane, shown for $L = 2$ as the light dashed line in Fig. 4.1(a). Besides a constant precession of its phase, the density $|\langle\hat{a}_1\rangle|^2$ exhibits small oscillations, causing the classical trajectory to explore only a small region of its phase space, as illustrated by the long-time evolution represented by the thin grey line. Beyond the trivial case $L = 2$, the system is no longer integrable and its classical trajectories may exhibit both regular and *chaotic* dynamics, depending on the energy and initial conditions of the trajectory‡ [183, 184]. The intermediary case for $L = 3$ is shown in Fig. 4.1(b), where the on-site amplitude explores a larger but finite region of its phase space. Finally, Fig. 4.1(c) shows the fully chaotic case for $L = 4$, where the long-time evolution has lost its periodicity and over time explores the entirety of its available phase space, limited only by conservation of energy. We will return to the property of integrability and its breaking in Part III, where we will study relaxation dynamics in a spinor condensate restricted by the conservation of magnetization.

As the Bose-Hubbard model is – of course – not classical, the classical field prediction provided by the Gross-Pitaevskii equation is valid only in the mean field limit $N/L \to \infty$ and $U \to 0$ (at a finite interaction energy UN/L). However, in the vicinity of this mean field limit, a reliable benchmark is provided by the truncated Wigner approximation (see Sec. 3.4). This approximation, shown in Fig. 4.1(a-c) as the dark blue line, will therefore serve as a benchmark for the development of the Gaussian trajectory approach throughout the remainder of this chapter as well as Chapter 5. In both integrable and chaotic cases, the Gross-Pitaevskii solution agrees with the truncated Wigner result only during a short period of coherent dynamics, before dephasing results in a convergence of the

* This equation is obtained from the Gaussian equation for α_n (4.3) upon setting $u_{nm} = v_{nm} = 0$, effectively reducing the Gaussian variational Ansatz to that of a coherent state.

† Note that this is not the full phase space of the system, in which the state occupies a quasi-probability distribution.

‡ Purely chaotic dynamics are retrieved in the limit $L \to \infty$, where the excitation spectrum approaches a continuum [183].

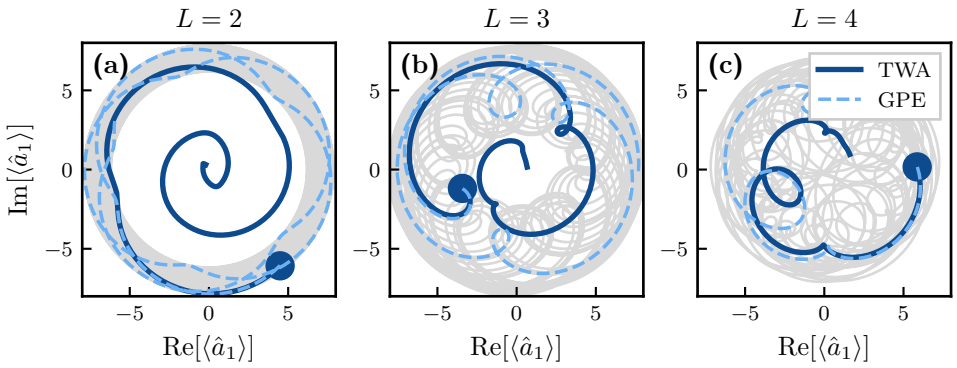

Figure 4.1 – Local phase space trajectories of $\langle \hat{a}_1 \rangle$ on a single site of a Bose-Hubbard chain with interaction strength $U/J = 0.1$, $N = 100$ particles and arbitrary initial condition (blue dot) on a lattice of $L = 2$, 3 and 4 sites. Dark full lines indicate the result of a truncated Wigner approximation (TWA) with 10^3 realizations, reducing the statistical error to below the width of the plotted line. Light dashed lines represent a single coherent trajectory as predicted by the Gross-Pitaevskii equation (GPE), both up to time $Jt/\hbar = 10$. Grey lines represent the region of phase space explored by the GPE trajectory for times up to $Jt/\hbar = 10^3$. As the size of the chain increases, classical dynamics evolve from regular to chaotic.

expectation value to $\langle \hat{a}_1 \rangle \to 0$. The accuracy of the mean field result improves with increasing number of particles per site, as illustrated in Fig. 4.2.

4.1.2 Gaussian dynamics

Figure 4.3 shows the Gaussian approximation result for on-site dynamics in a four-site system initialized in the arbitrary coherent state

$$(\alpha_1, \alpha_2, \alpha_3, \alpha_4) \sim (3, 1 + 2i, 4, 2i), \tag{4.7}$$

rescaled to a total particle number $N = 4000$ and represented by the grey dot. With an interaction strength $U/J = 0.01$ and mean interaction energy $UN/L = 10J$, the system is deep enough in the mean field regime to obtain a reliable benchmark from the truncated Wigner approximation (TWA). Shown as the thick grey line, the TWA again predicts a dephasing of the on-site amplitude in 4.3(a), accompanied by a relaxation of local populations (b) to their steady state value $N/L = 1000$ as a result of the ergodic dynamics. Both in the phase plot and evolution of local occupations, the Gaussian approximation (dashed blue line) accurately captures the early-time dynamics. At later times, however, it fails to capture dephasing of the amplitude and relaxation of population dynamics.

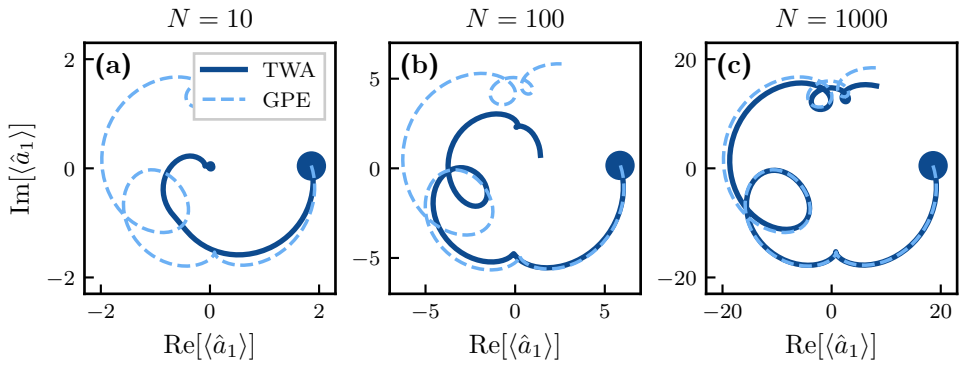

Figure 4.2 – Local phase space trajectories on a single site of the 4-site Bose-Hubbard in Fig. 4.1(c), rescaled to different total particle numbers at a fixed value $UN/J = 10$. The classical Gross-Pitaevskii approximation performs increasingly well deeper in the mean field limit $N \to \infty$.

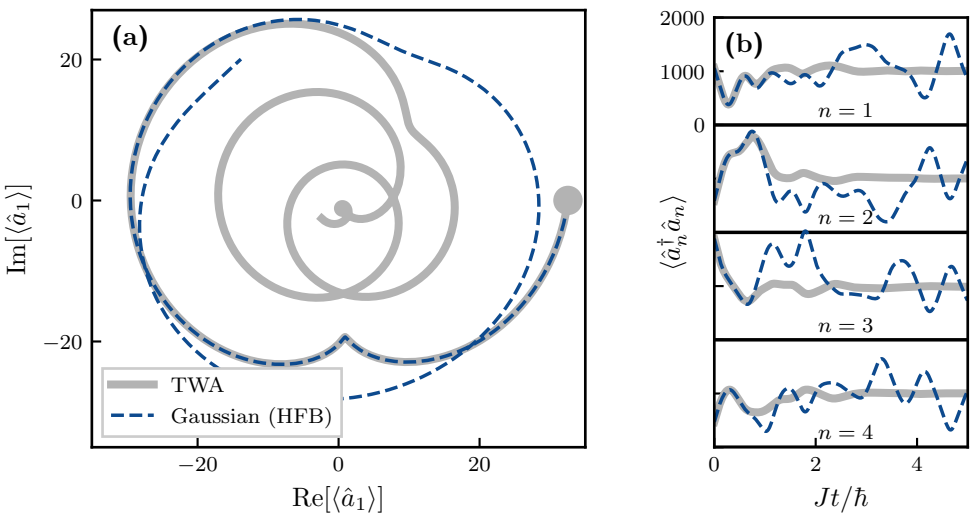

Figure 4.3 – (a) Dynamical trajectory of the on-site amplitude $\alpha_1 = \langle \hat{a}_1 \rangle$ in a four-site Bose-Hubbard chain with $N = 4000$ atoms and interaction strength $U/J = 0.01$. The initial coherent condition, Eq. (4.7), is represented by the grey dot. The thick grey line shows its time evolution up to $Jt/\hbar = 3$ as predicted by the truncated Wigner approximation (TWA), inferred from the average of 10^4 realizations. The result from a Gaussian variational Ansatz (HFB) is shown by the blue dashed line, truncated at $Jt/\hbar = 1.5$ to retain clarity. (b) Relaxation of the on-site occupations $\langle \hat{a}_n^\dagger \hat{a}_n \rangle$, not captured by the Gaussian prediction.

The inability of the Gaussian variational theory to reproduce the evolution of the Bose-Hubbard chain beyond early times results from the growth of fluctuations accompanying classically chaotic dynamics [185, 186]. We illustrate this in Fig. 4.4 for the dynamics of the local occupation $\langle \hat{a}_1^\dagger \hat{a}_1 \rangle$ (also shown in Fig. 4.3(b)), which equilibrates to its steady state value on a time scale $Jt \approx 3$ as predicted by the truncated Wigner approximation. Shown in Fig. 4.4(a), the Wigner result is obtained by averaging over classical trajectories sampled from the initial coherent state, which are seen to be extremely sensitive to slight variations of the initial condition (light and dark dashed lines). Figure 4.4(b) shows the manifestation of the same classical chaos in the dynamics of quantum fluctuations. Accompanying the exponential divergence of classical trajectories, fluctuations quantified by the variance

$$\langle \hat{\delta}_1^\dagger \hat{\delta}_1 \rangle = \langle \hat{a}_1^\dagger \hat{a}_1 \rangle - \alpha_1^* \alpha, \tag{4.8}$$

rise on the same time scale* to their maximal value allowed by conservation of particle number. Classical chaos causing the divergence of classical trajectories thus translates to the rapid rise of quantum fluctuations. On the other hand, by truncating the dynamics at second order in fluctuation operators, the Gaussian theory (HFB) places a strong assumption on the statistics of the quantum state and severely underestimates the growth of the variance (4.8), as shown by the evolution of the corresponding Gaussian fluctuation v_{11} (blue dashed line).

For chaotic dynamics of nonlinear systems, it is thus the growth of fluctuations which impedes a description in terms of Gaussian states. This observation is pictorially summarized in Fig. 4.5(a), which depicts the evolution of a single-mode quantum system from an initially coherent state (left) to an arbitrary state (right). Under the influence of chaotic dynamics, the phase space distribution retains its volume but deforms drastically due to the growth of fluctuations [134]. In a mean field approximation, the coherent state is represented by a single complex number α, evolving according to the classical Gross-Pitaevskii equation (GPE, dark blue arrow). To account for quantum fluctuations, the semiclassical truncated Wigner approximation (Sec. 3.4) infers the evolution of the entire Wigner distribution by sampling the initial conditions of the GPE from the coherent state (dashed lines). The Gaussian variational approximation of these dynamics is shown in Fig. 4.5(b). Since coherent states form a subset of the Gaussian variational manifold, the initial state is well represented by a coherent mode α and a single set of Gaussian fluctuations $\hat{\delta}$. However, as the system evolves in time, the Gaussian variational state develops significant squeezing (dark blue ellipse)

* The characteristic time of the exponential growth is given by the inverse of the finite-time Lyapunov coefficient [187] characterizing the exponential divergence of classical trajectories.

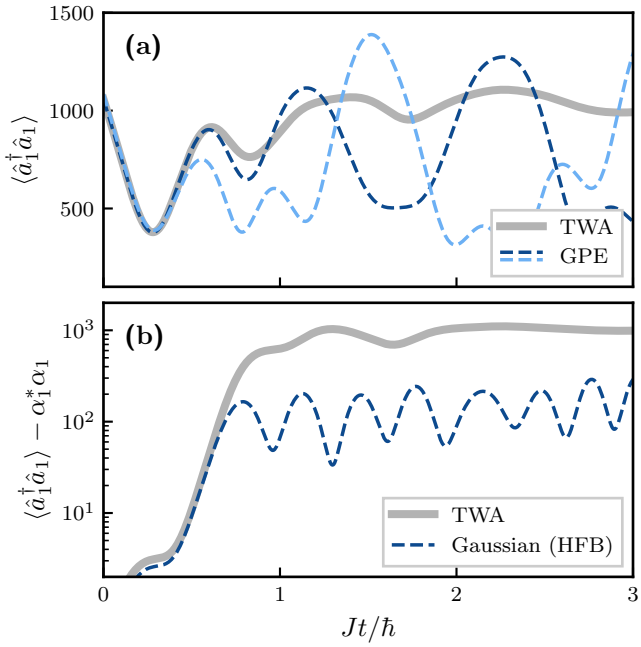

Figure 4.4 – Classical and quantum view of classically chaotic dynamics, witnessed in the on-site population statistics for the same dynamics as in Fig. 4.3. (a) Classical chaos in a quantum system appears as a rapid divergence of classical (GPE) trajectories with slightly different initial conditions, which are sampled to arrive at the truncated Wigner (TWA) prediction for the evolution of an expectation value. (b) Chaotic dynamics are accompanied by a rapid growth of fluctuations (4.8), underestimated by the Gaussian (HFB) theory.

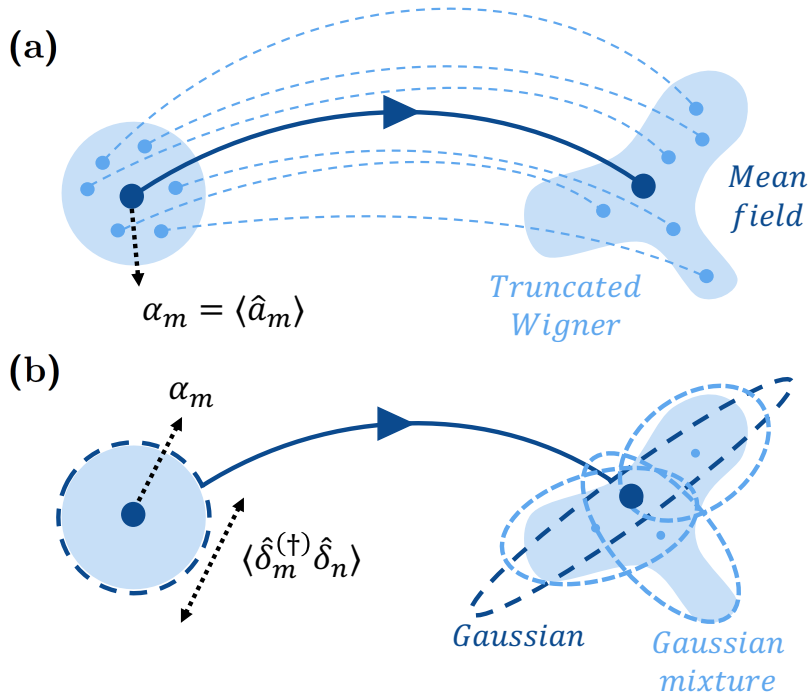

Figure 4.5 – Time evolution of an initially coherent quantum state depicted by its quasiprobability distribution in phase space and approximate methods to capture its dynamics. (a) The mean field Gross-Pitaevskii equation approximates the coherent state as a single complex number α_m, while the truncated Wigner approximation infers the evolution of the Wigner distribution by evolving mean field trajectories with initial conditions sampled from the coherent state. (b) Squeezing of a variational state consisting of a mean field mode α_m and Gaussian fluctuations $\hat{\delta}_m$ provides a crude approximation of the non-Gaussian final state, while a classical mixture of Gaussian states with smaller fluctuations produces a more accurate representation.

in an attempt to account for the nonlinear growth of fluctuations, eventually misrepresenting the actual state. The corrections required to reproduce the actual state of the system arise precisely from the terms of higher order in fluctuations appearing in the evolution (3.26) of the Wigner distribution, neglected by the Gaussian approximation. In the following sections, we will attempt to improve upon the Gaussian approximation by artificially introducing classical uncertainty in its dynamics.

4.2 The Gaussian trajectory approach

Figure 4.5(b) depicts the essence of the novel approach we will develop in the remainder of this chapter, and which was first proposed and applied to a small Bose-Hubbard chain in Ref. [188] following previous applications of Gaussian states in the context of driven-dissipative systems [139, 189, 190]. While a single squeezed state cannot account for the intricate correlations developing in the system, a more faithful representation of its actual state might be obtained by sampling the phase space distribution as a mixture of Gaussian states, each with small fluctuations. On the level of the Gaussian equations of motion, this translates to a suppression of the correlators u_{nm} and v_{nm} which, due to the application of Wick decomposition, only approximately capture fluctuations. The dynamics of the Gaussian state is then more predominantly determined by the evolution of α_n, which contains the nonlinearities leading to classical chaos without imposing additional approximations. The price to pay for this suppression of fluctuations is that we now require multiple Gaussian states to approximate the true state of the system. The result of this procedure, the feasibility of which we will justify more rigorously in Chapter 5, is that quantum fluctuations of the pure state are converted into classical uncertainty of a statistical mixture of variational states, all of which contain fluctuations small enough to validate the omission of their higher order correlations through the application of Wick decomposition.

To effect this transfer of fluctuations from quantum to classical and find an approximate representation of a pure state with large fluctuations as a classical mixture of states with small fluctuations, we will formulate an effective description of the unitary dynamics of the isolated system in terms of an *open* system coupled to an artificial environment. As the environment will be coupled only weakly to the system, its effect on the evolution of the system is well approximated by the Lindblad master equation (3.34), in which the unitary dynamics of the system are supplemented with dissipative processes modelled as jump operators $\hat{\Gamma}$. As explained in Sec. 3.6, this introduces incoherence and therefore classical uncertainty in the evolution of the system, which evolves from a pure state to a classical mixture. In the present case, however, classical uncertainty is no feature of the actual system, which is governed by purely unitary evolution. Instead, dissipation into an external environment is artificially added to the variational theory in order to introduce classical uncertainty and thus achieve a decomposition of a single Gaussian state into a mixture of states. Consequently, the coupling strength γ of the *artificial dissipation* will emerge as an additional parameter to be calibrated.

Working in the quantum trajectory framework introduced in Sec. 3.6.2, the dissipative evolution of the system's density matrix is sampled by the stochastic evolution of wave functions, with measurements taken in the form of heterodyne unraveling. In the Gaussian variational theory, the addition of jump processes then causes the unitary evolution of the moments α_n, u_{nm}, and v_{nm} to be supplemented with dissipative terms according to Eq. (3.41), its particular form depending on the chosen jump process [191]. In Chapter 5, we will motivate our choice of jump operator and its implementation in the dynamics to improve the variational description while minimally disturbing the unitary dynamics of the system. Before doing so, it is instructive to have a closer look at the implications of the proposed method, as well as related approaches found in the literature.

4.2.1 Dissipation, decoherence and Schrödinger cats

From the above discussion, it is clear that approximating the pure many-body state by an incoherent mixture of states with smaller fluctuations comes at the cost of neglecting coherences between states widely separated in phase space. As an example of coherence between macroscopically different configurations we show in Fig. 4.6(a) the Wigner distribution of the state $|\psi\rangle = |+2\rangle_c + |-2\rangle_c$, known as a *Schrödinger cat* state. In addition to the two Gaussian lobes corresponding to the individual coherent (i.e., classical) states, the superposition gives rise to interference fringes encoding their quantum coherence. For comparison, Fig. 4.6(b) shows the Wigner distribution of a statistical mixture of the same states. While both classical regions are still accurately recovered, any coherence between them has been lost.

Non-classical superpositions, of which the Schrödinger cat state is an extreme example, emerge in an isolated chaotic quantum system as a consequence of the rapid growth of fluctuations [134, 185], which we have illustrated in Sec. 4.1.2. More specifically, superpositions are encoded in higher order moments of the fluctuation statistics. They are therefore precisely those features not taken into account in a Gaussian approximation, where they have been decomposed through Wick factorization*. This explains why the Gaussian theory fails to reproduce the dynamics of a chaotic quantum system: it develops anomalously large squeezing in an attempt to account for coherent superpositions which are inherently beyond its reach.

* The fact that Gaussian states fail to capture superpositions of macroscopically distinct states can also be seen from their manifestation as regions of negative quasiprobability in the Wigner distribution of Fig. 4.6(a). As shown earlier in Fig. 3.1, Gaussian states have strictly positive Wigner distributions.

However, such coherences are extremely fragile to perturbations. In particular, it has been shown that even an infinitesimally weak coupling to an external environment – which always surrounds a physical system – results in the exponential decay of any cat-like superpositions on a timescale inversely proportional to their separation in phase space* [197]. As such, their role in the evolution of relevant observables in any macroscopic system is negligible. The irrelevance of such correlations then suggests that the ensemble dynamics of the mixture in Fig. 4.6(b) should still accurately capture the unitary evolution of the system.

In view of this intuition, we are led to assume that, also within the Gaussian approximation, the introduction of a weak decoherence mechanism should not be detrimental to the accuracy with which it captures the actual dynamics of the system. This is precisely what is effected by the introduction of a weakly coupled environment in the proposed trajectory approach. In fact, Fig. 4.6 illustrates why this approach should in fact *improve* the description of non-classical states in terms of a Gaussian variational Ansatz: through the introduction of classical uncertainty, the representation of the Schrödinger cat state in Fig. 4.6(a) is no longer a single highly squeezed state but a mixture like the one in Fig. 4.6(b), which arguably captures its physical features with much greater accuracy. The same reasoning applies to other variational states, but the explicit inclusion of squeezing – an intrinsically quantum mechanical property which *is* robust to weak perturbations [197] – makes the Gaussian theory a natural candidate for its implementation.

Interpreted as a constructed source of *decoherence*, the virtual environment and its associated artificial dissipation we propose acts on the unitary dynamics in the same way as the physical environment surrounding macroscopic objects (see Sec. 3.6) [198]. There, it is the continuous interaction of an object with its actual surroundings which causes the destruction of quantum coherence†, preventing the unbounded development of fluctuations predicted by its unitary evolution‡ [169].

---

* This is true even in mesoscopic systems of few atoms, where Schrödinger cat superpositions decay on a decoherence time scale of the order $10 - 100\mu$s [192–195]. In photonic systems, cat states have been created with lifetimes in the $10 - 100$ms regime [196].

† Whether or not a pure state is a superposition depends on the basis with respect to which it is expressed. More precisely than "destroying superpositions", the decoherence mechanism amounts to the emergence of correlations between the system and its environment which, upon tracing over the environment variables, result in the selection of a preferred set of classical states $|\psi_n\rangle$, whose overlap $\langle\psi_n|\psi_{m\neq n}\rangle$ decreases rapidly in time [169].

‡ As Wojciech Zurek points out [134], the Schrödinger equation in absence of environment-induced decoherence predicts even the solar system to be fundamentally non-classical, since chaotic features in planetary motion would cause fluctuations in their orbit to exceed the size of the solar system itself on a characteristic time scale shorter than its current lifetime, rendering the notion of classical orbits meaningless.

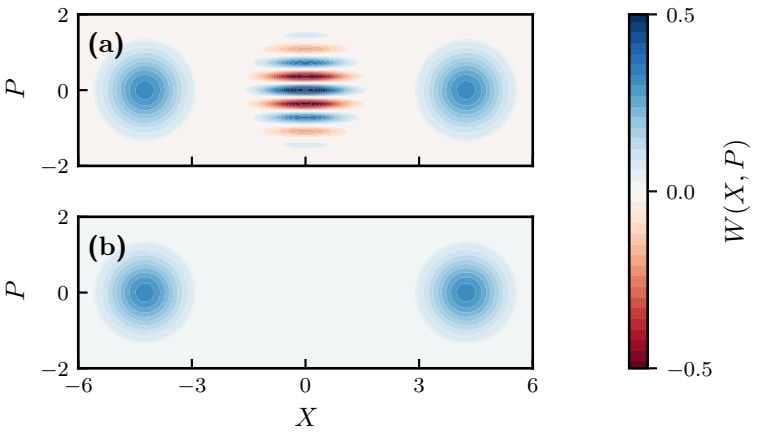

Figure 4.6 – Illustration of correlations lost in the approximation of a superposition of coherent states $|\alpha = \pm 2\rangle_c$ (a) by a statistical mixture of the same states (b). Interference fringes in the shown Wigner distributions are emblematic of non-classical coherence.

Just as physical decoherence allows for the notion of classical trajectories of macroscopic objects (i.e., the correspondence principle) by suppression of fluctuations around the classical trajectory [134, 199], the decoherence provided by artificial dissipation allows to describe the system in terms of a mixture of states with a well-defined mean field and small fluctuations.

The intricate connection between fluctuation growth, dissipation and decoherence was furthermore noted by Habib *et al.* [200], who argue that the flow of energy from the mean field to fluctuations not only imposes an arrow of time to the system, but can be interpreted as a dissipation from the system into the reservoir of its own fluctuations. The introduction of a classical environment then simply comes down to a change of the bath to which the system dissipates, eliminating the growth of quantum fluctuations in favor of classical uncertainty.

4.2.2 Relation to equilibrium statistical mechanics

The approximation of the dynamics of an entangled quantum state as a classical mixture of simpler variational states may also be viewed in analogy with equilibrium statistical mechanics. While the exact equilibrium state $|\psi_{\text{eq}}\rangle$ may deviate significantly from any variational state, the expectation value of any local operator $\hat{O}$ is equivalent to that of a thermal density matrix following a Gibbs distribution $\hat{\rho}_{\text{therm}} \propto e^{-\beta\hat{\mathcal{H}}}$ [201–203], well suited to an approximation in terms of a mixture of variational states $|\phi_j\rangle$ that are weakly entangled (Minimally entangled

typical thermal states, METTS) [157–159],

$$\langle\psi_{\mathrm{eq}}|\hat{O}|\psi_{\mathrm{eq}}\rangle \approx \mathrm{Tr}\Big[\hat{O}\hat{\rho}_{\mathrm{therm}}\Big] \approx \mathrm{Tr}\left[\hat{O}\sum_j p_j\,|\phi_j\rangle\,\langle\phi_j|\right]. \tag{4.9}$$

By virtue of the *eigenstate thermalization hypothesis* (ETH) [204–208], all non-integrable quantum systems are known to eventually thermalize,

$$\langle\psi(t)|\hat{O}|\psi(t)\rangle \approx \langle\psi_{\mathrm{eq}}|\hat{O}|\psi_{\mathrm{eq}}\rangle \quad (t\to\infty), \tag{4.10}$$

justifying the approximation (4.9) at late times. The Gaussian trajectory description developed in this chapter extends this approximation to intermediate times by similarly inferring expectation values of a pure state $|\psi(t)\rangle$ as those of a mixture of variational states $|\phi_j(t)\rangle$,

$$\langle\psi(t)|\hat{O}|\psi(t)\rangle \approx \mathrm{Tr}\left[\hat{O}\sum_j p_j\,|\phi_j(t)\rangle\,\langle\phi_j(t)|\right], \tag{4.11}$$

thus bridging the gap between early time dynamics, well described by a variational theory, and thermodynamic arguments valid in the long-time limit.

4.3 Related approaches

The effect of (real or virtual) measurements on the nature of quantum fluctuations and the potential of leveraging its properties to capture or alter the dynamics of many-body quantum systems has been explored in several lines of research. To conclude this chapter, we briefly comment on the most relevant related approaches found in contemporary literature.

4.3.1 Measurement-dependent scaling of entanglement

The growth of fluctuations during time evolution is closely related to the generation of entanglement entropy S_E, which – for one-dimensional systems – was shown to increase linearly in time [209]. Since the bond dimension of a matrix product state (MPS) scales exponentially with the entanglement entropy present in the system, this implies an exponential growth of computational complexity in simulating time evolution using MPS [210], a fact which has been coined the *entanglement barrier* [211]. In analogy to the extensive scaling of entanglement entropy with system size ($S_E \sim L^d$ with L and d the size and dimensionality of the system) [212], the relation $S_E \sim t$ is commonly referred to as the *volume law*

of entanglement scaling. However, it was shown that the interruption of unitary dynamics by local measurements at a sufficient rate reduces the growth of entanglement to $S_E \sim t^0$ (called the *area law* in analogy to $S_E \sim L^{d-1}$ [213]), separated from the volume law regime by a *measurement-induced phase transition** at which $S_E \sim \log(t)$ [216–218].

Like the quantum trajectory implementation of artificial dissipation proposed in this work, the resulting *unitary-projective* evolution thus reduces the generation of entanglement, avoiding the entanglement barrier and thereby extending the applicability of MPS variational states to the simulation of dynamics beyond short times. Crucially, however, frequent measurements in this case physically open the system to its environment, qualitatively altering its time evolution. By contrast, our current aim is to improve the performance of a variational description for isolated systems by similarly adding random measurements, but *without* significantly affecting the evolution of the ensemble.

4.3.2 Dissipation-assisted operator evolution

The use of an artificial environment to improve the description of *isolated* systems has recently been employed in the context of *operator spreading*, which relates entanglement generation in a system to the growth of the spatial support of an operator $\hat{O}(t)$ [219]. Inspired by the spreading of local operators during thermalization, Rakovsky *et al.* [220] developed a method of *dissipation-assisted operator evolution* (DAOE) to capture long-time diffusive transport of heat and spin correlations in Ising chains and XX ladders. To mitigate the growth of entanglement associated with operator spreading which hinders the validity of MPS algorithms, dissipation is introduced to specifically target non-local operators with a large spatial support, leaving physically relevant observables unaffected. In this way, entanglement is suppressed by eliminating backflow processes from complicated to simple operators, which in reality decay exponentially fast due to dephasing.

In the same vein as our approach, this method is thus based on the idea that a well-controlled omission of higher-order correlations – immaterial to the evolution of relevant observables – improves a description in terms of variational states which are primarily limited by the complexity of correlations they are able to capture. In contrast to our approach, however, DAOE is fully deterministic: the suppression of long-range correlations is not compensated by the introduction of

* As of 2023, the transition from extensive to sub-sextensive entanglement scaling as a function of the measurement rate has been observed in *noisy intermediate scale quantum* (NISQ) circuits of $\sim 10^1$ qubits at IBM Quantum [214] and Google Quantum AI [215].

any classical uncertainty, thus not conserving the total magnitude of fluctuations in the system.

4.3.3 Disordered systems

The explicit reformulation of unitary dynamics as stochastic dynamics in the presence of a virtual environment has been employed in the description of *disordered* systems [221–223]. There, dephasing between different realizations of the disorder ensemble lead to decoherence in the ensemble-averaged dynamics. As such, the ensemble dynamics can be recast in a master equation governing the density matrix $\hat{\rho}(t)$, with suitable Lindblad operators encoding the effect of decoherence [222]. This effectively dissipative evolution of the ensemble can subsequently be sampled in a quantum trajectory approach, resulting in a stochastic approximation of unitary dynamics in an isolated, disordered system. While this application differs from our approach in the fact that disorder naturally induces classical uncertainty, the equivalence of disorder to dissipative dynamics in conjunction with the fact that weak levels of disorder are unavoidable in any experiment, implies that any isolated system should be well approximated by a suitable dissipative description, supporting the intuition that generic many-body quantum dynamics are robust to the presence of a weakly coupled environment.

5 | Artificial dissipation in the Gaussian theory

The Gaussian trajectory approach (GTA) proposed in Chapter 4 consists of introducing a decoherence mechanism which suppresses fluctuations at the expense of introducing classical uncertainty, conserving to a good approximation the sum of quantum and classical fluctuations in the system. In practice, this requires the artificial addition of dissipation not present in the system's actual dynamics. Care must therefore be taken to achieve the desired transfer of fluctuations while simultaneously limiting disturbances to the system's ensemble evolution to a minimum. These considerations allow for a variety of approaches, which we will illustrate using the chaotic Bose-Hubbard model of four sites. As we lay out the details of artificial dissipation in the remainder of this chapter, we closely follow the path taken in Ref. [188], but provide a more in-depth discussion of the algorithm and the basis on which its parameters are determined. At the onset, we note that differences between the presented algorithms essentially amount to a fine-tuning procedure, the outcome of which is subject to the specific system as well as the initial conditions of its dynamics.

5.1 Single-particle losses reduce fluctuations

For the purpose of introducing artificial dissipation as a mathematical tool to improve the variational description of isolated systems, we have the freedom to choose a suitable jump operator. For simplicity, we will limit our discussion to the elemental process in which a single atom is lost from or added to the fluid. As discussed in Sec. 3.6.1, this process is modelled by the jump operator

$$\hat{\Gamma}_j^{(-)} = \sqrt{\gamma}\hat{a}_j, \tag{5.1}$$

which annihilates a single particle from site j. The associated dissipation strength γ is interpreted as the rate at which, on average, atoms are lost from the system. With measurements taken in the form of heterodyne unraveling (see Sec. 3.6.2), the expectation value of any local operator $\hat{O}$ evolves according to Eq. (3.41). For single-particle losses, this becomes

$$\mathrm{d}\langle\hat{O}\rangle = -\frac{i}{\hbar}\left\langle\left[\hat{O},\hat{\mathcal{H}}\right]\right\rangle\mathrm{d}t - \frac{\gamma}{2}\sum_j\Big(\Big\langle\Big\{\hat{a}_j^\dagger\hat{a}_j,\hat{O}\Big\}\Big\rangle - 2\left\langle\hat{a}_j^\dagger\hat{O}\hat{a}_j\right\rangle\Big)\mathrm{d}t \\ + \sqrt{\gamma}\sum_j\Big(\Big\langle\hat{a}_j^\dagger(\hat{O}-\langle\hat{O}\rangle)\Big\rangle\,\mathrm{d}Z_j + c.c.\Big). \quad (5.2)$$

Here, the Hamiltonian evolution is supplemented with a deterministic ($\propto \gamma\mathrm{d}t$) and stochastic ($\propto \sqrt{\gamma}\mathrm{d}Z_j$) dissipation term, with the latter containing uncorrelated complex Wiener processes $\mathrm{d}Z_j$. The evolution of the expectation value is inferred from the average over all stochastic quantum trajectories. Defining the dissipator $\mathcal{D}_-$ of single-particle losses as in the Lindblad equation (3.34), one finds for the first and second moments of the Gaussian state:

$$\mathcal{D}_-(\alpha_n) = -\frac{\gamma}{2}\alpha_n\mathrm{d}t + \sqrt{\gamma}\sum_j\Big(v_{jn}\mathrm{d}Z_j + u_{jn}\mathrm{d}Z_j^*\Big), \quad (5.3)$$

$$\mathcal{D}_-(u_{nm}) = -\gamma\left[u_{nm} + \sum_j(u_{mj}v_{jn} + u_{nj}v_{jm})\right]\mathrm{d}t, \quad (5.4)$$

$$\mathcal{D}_-(v_{nm}) = -\gamma\left[v_{nm} + \sum_j(v_{nj}v_{jm} + u_{nj}^*u_{jm})\right]\mathrm{d}t. \quad (5.5)$$

In contrast to the Hamiltonian equations (4.3), (4.4) and (4.5), summations in the above equations do *not* refer to nearest-neighbours but to the whole chain. The effect of single-particle losses on the evolution of the coherent wave function α_n consists primarily of a depletion at rate γ which is also present in the mean field Gross-Pitaevskii description of an open quantum system, given by Eq. (3.42). Specific to the Gaussian theory, however, are the additional terms $\sim \mathrm{d}Z_j$ which result in a stochastic growth of α_n. From the application of Itō's lemma,

$$\mathrm{d}\Big(\alpha_n^{(*)}\alpha_m\Big) = \alpha_n^{(*)}\mathrm{d}\alpha_m + \alpha_m\mathrm{d}\alpha_n^{(*)} + \mathrm{d}\alpha_n^{(*)}\mathrm{d}\alpha_m, \quad (5.6)$$

to Eq. (5.3), quadratic correlations between coherent modes are found to evolve under dissipation as

$$\mathcal{D}_-(\alpha_n^*\alpha_m) = -\gamma\left[\alpha_n^*\alpha_m \mathrm{d}t - \sum_j (v_{nj}v_{jm} + u_{nj}^* u_{jm})\right]\mathrm{d}t + \sqrt{\gamma}\sum_j \left[(\alpha_n^* v_{jm} + \alpha_m u_{jn}^*)\mathrm{d}Z_j + (\alpha_n^* u_{jm} + \alpha_m v_{nj})\mathrm{d}Z_j^*\right]. \quad (5.7)$$

Taking the statistical average over noise realizations by setting $\langle \mathrm{d}Z_j \rangle = 0$, we arrive at

$$\overline{\mathcal{D}_-(\alpha_n^*\alpha_m)} = -\gamma\left[\alpha_n^*\alpha_m \mathrm{d}t - \sum_j (v_{nj}v_{jm} + u_{nj}^* u_{jm})\right]\mathrm{d}t. \quad (5.8)$$

The total second moment of the Gaussian state, $\langle \hat{a}_n^\dagger \hat{a}_m \rangle = \alpha_n^*\alpha_m + v_{nm}$, then evolves on average as

$$\overline{\mathcal{D}_- \langle \hat{a}_n^\dagger \hat{a}_m \rangle} = -\gamma(\alpha_n^*\alpha_m + v_{nm})\mathrm{d}t = -\gamma \langle \hat{a}_n^\dagger \hat{a}_m \rangle \mathrm{d}t. \quad (5.9)$$

For the number of particles $n_j = \langle \hat{a}_j^\dagger \hat{a}_j \rangle$ present in a site, this reduces to $\mathcal{D}(n_j) = -\gamma n_j \mathrm{d}t$, the expected depletion of the system. Neglecting the terms resulting in this reduction of the total second moment – we will return to them later – we can compare Eq. (5.8) to (5.5) to arrive at the feature of dissipation most crucial to our approach: the stochastic growth of the coherent modes α_n is accompanied by a growth of the quadratic correlators $\alpha_n^*\alpha_m$ which is on average equal and opposite to the deterministic decrease of fluctuations v_{nm} in the presence of dissipation. This effect, captured in the terms $\sum_j (v_{nj}v_{jm} + u_{nj}^* u_{jm})$ in both equations, constitutes exactly the transfer of fluctuations from quantum to classical which we introduced conceptually in Sec. 4.2 (see in particular Fig. 4.5(b)), and which motivated the introduction of a virtual environment and its associated artificial dissipation. In the following Section, we will introduce an additional jump process to counteract the loss of particles from the system, and explicitly show how the resulting algorithm captures the dynamics of the isolated chaotic Bose-Hubbard chain of Chapter 4.

5.2 Pumping restores the isolated system

While single-particle jumps convert quantum fluctuations into classical uncertainty, the associated loss of particles and energy causes the system to deplete

over time. To serve as an approximate description of the original system, dissipation must therefore be supplemented with a way of restoring the dissipated state to the space of the isolated system, primarily determined by the conservation of particle number and energy. As we are free in our choice of jump operators, conservation of particle number can be restored by the addition of a second interaction process which counteracts the net particle losses in Eq. (5.9). Stochastic gains are introduced by the Lindblad operator

$$\hat{\Gamma}_j^{(+)} = \sqrt{\kappa}\hat{a}_j^\dagger, \tag{5.10}$$

which physically corresponds to an incoherent pump inserting atoms with random phases into the fluid [146]. The associated dissipator $\mathcal{D}_+$ is defined analogously to $\mathcal{D}_-$, affecting the dynamics of the Gaussian moments as

$$\mathcal{D}_+(\alpha_n) = +\frac{\kappa}{2}\alpha_n \mathrm{d}t + \sqrt{\kappa}\sum_j \left(u_{jn}\mathrm{d}\tilde{Z}_j + v_{jn}\mathrm{d}\tilde{Z}_j^*\right) + \sqrt{\kappa}\mathrm{d}\tilde{Z}_n^*, \tag{5.11}$$

$$\mathcal{D}_+(u_{nm}) = -\kappa\left[u_{nm} + \sum_j (u_{mj}v_{jn} + u_{nj}v_{jm})\right]\mathrm{d}t, \tag{5.12}$$

$$\mathcal{D}_+(v_{nm}) = -\kappa\left[v_{nm} + \sum_j (v_{nj}v_{jm} + u_{nj}^* u_{jm})\right]\mathrm{d}t, \tag{5.13}$$

in which the differentials $\mathrm{d}\tilde{Z}_j$ are independent from $\mathrm{d}Z_j$. As the presence of an incoherent pump serves as a continuous source of decoherence, the fluctuation correlators u_{nm} and v_{nm} acquire a suppression identical to that induced by particle losses, even though the number of particles increases. In comparison to Eq. (5.3), the dissipator (5.11) of the first moments α_n due to the incoherent pump contains an additional term $+\sqrt{\kappa}\mathrm{d}\tilde{Z}_n^*$, stemming from a commutator due to the ordering $\langle(\hat{a}_n - \alpha_n)\hat{a}_j^\dagger\rangle\,\mathrm{d}\tilde{Z}_j^*$ in $\mathcal{D}_+(\alpha_n)$. The total second moment $\langle\hat{a}_n^\dagger\hat{a}_m\rangle$ evolves due to $\mathcal{D}_+$ as

$$\overline{\mathcal{D}_+(\langle\hat{a}_n^\dagger\hat{a}_n\rangle)} = +\kappa\Big(\langle\hat{a}_n^\dagger\hat{a}_n\rangle + 1\Big)\mathrm{d}t. \tag{5.14}$$

Just as in the $\mathcal{D}_-$ jump channel, the overall second moment only dissipates trivially on average, while internally the mode $\alpha_n^*\alpha_n$ grows stochastically to compensate for the majority of losses occurring in v_{nm}.

Combining both particle losses and incoherent pumping in a single dissipator $\mathcal{D} = \mathcal{D}_- + \mathcal{D}_+$, one finds

$$\mathcal{D}(\alpha_n) = \frac{\kappa-\gamma}{2}\alpha_n \mathrm{d}t + \sqrt{\gamma}\sum_j \left(v_{jn}\mathrm{d}Z_j + u_{jn}\mathrm{d}Z_j^*\right) + \sqrt{\kappa}\sum_j \left(u_{jn}\mathrm{d}\tilde{Z}_j + v_{jn}\mathrm{d}\tilde{Z}_j^*\right) + \sqrt{\kappa}\mathrm{d}\tilde{Z}_n^*, \quad (5.15)$$

$$\mathcal{D}(u_{nm}) = -(\gamma+\kappa)\left[u_{nm} + \sum_j (u_{mj}v_{jn} + u_{nj}v_{jm})\right]\mathrm{d}t, \quad (5.16)$$

$$\mathcal{D}(v_{nm}) = -(\gamma+\kappa)\left[v_{nm} + \sum_j (v_{nj}v_{jm} + u_{nj}^* u_{jm})\right]\mathrm{d}t. \quad (5.17)$$

For the total second moment, this results in

$$\overline{\mathcal{D}(\langle \hat{a}_n^\dagger \hat{a}_n\rangle)} = \overline{\mathcal{D}_-(\langle \hat{a}_n^\dagger \hat{a}_n\rangle) + \mathcal{D}_+(\langle \hat{a}_n^\dagger \hat{a}_n\rangle)} = \left[(\kappa-\gamma)\langle \hat{a}_n^\dagger \hat{a}_n\rangle + \kappa\right]\mathrm{d}t. \quad (5.18)$$

Hence, the dynamics of a Bose-Hubbard chain with conserved number of particles can be described through quantum trajectories of Gaussian states, on the condition that the rates at which particles are lost (γ) and gained (κ) obey

$$\frac{\kappa}{\gamma} = \left(\frac{N/L}{N/L+1}\right), \quad (5.19)$$

such that single-particle losses are on average compensated by the stochastic insertion of atoms into the system, assuming that the number of particles per site in a homogeneous system satisfy for each site

$$\frac{1}{T}\int_0^T \langle \hat{a}_n^\dagger \hat{a}_n\rangle \,\mathrm{d}t \to N/L. \quad (5.20)$$

Note that the addition of the jump processes $\hat{\Gamma}_j^{\pm}$ changes the system from isolated to driven-dissipative. In general, one therefore expects both the dynamics and steady state of the system to be significantly altered [169]. However, on the basis of the arguments explained in Sec. 4.2.1, the dynamics are predicted to converge to those of the isolated system in the limit of weak dissipation, which, as we will show in the following section, suffices to drastically improve the Gaussian description.

5.2.1 Gaussian dynamics revisited

In Hilbert space as in the classical world, the proof of the pudding is in the eating. To test the performance of this approach, we therefore simulate in Fig. 5.1(a) the same trajectory of a single-site amplitude as in Fig. 4.3, now with the inclusion of artificial dissipation in the Gaussian description. Recall from Sec. 4.1.2 that the Gaussian variational theory, here represented by the grey dashed line, fails to account for dephasing of the on-site amplitude. As seen from the blue lines in this Figure, the Gaussian approximation improves drastically when supplemented with artificial dissipation γ, accompanied by an incoherent pumping κ tuned to preserve the total number of particles via (5.19). For an infinitesimally small $\gamma/J = 0.01$, corrections to the unitary Gaussian dynamics are too small to provide the decoherences necessary to account for dephasing, resulting in a limited improvement of the description. On the other hand, when the dissipation strength exceeds all other energy scales in the system ($\gamma/J = 10$), stochastic noise dominates the dynamics and results in an underestimation of the dephasing time scale. Within these bounds, however, a wide range of dissipation strengths ($10^{-2} \ll \gamma/J \ll 10^{1}$) accurately reproduces the dynamics of the on-site amplitude. In particular, the results for $\gamma/J = 0.1$ and $\gamma/J = 1$ are nearly indistinguishable. The relative insensitivity of the Gaussian trajectory approach to the value of γ is confirmed by Figure 5.1(b) which shows the evolution of the on-site occupation $n_1 = \langle \hat{a}_1^\dagger \hat{a}_1 \rangle$.

Note that, while the average of 10^4 Gaussian trajectories reproduces the relaxation dynamics as predicted by the truncated Wigner approximation – with a statistical error smaller than the thickness of the plotted lines –, individual trajectories do not contain this behaviour. Rather, they all exhibit dynamics qualitatively similar to the non-dissipative Gaussian result, but interrupted by stochastic jumps. We will revisit the nature of individual Gaussian trajectories when discussing a dissipative spinor condensate in Sec. 8.3.

5.2.2 Energy conservation

While the comparability of the dissipation strength to other energy scales in the system is a useful rule of thumb, a more precise criterion is required to eliminate the need for a benchmark provided by another approximate method (in this case TWA). Through the addition of incoherent pumping to our description, we have ensured the conservation of particle number, but so far neglected the conservation of energy in the system. Figure 5.1(c) shows the mean deviation ΔE from the initial energy E_0 of the coherent state for the same dissipation strengths as in

Fig. 5.1(a-b). At a large dissipation strength, the accompanying incoherent pump injects a large amount of energy into the system, resulting in the strong increase of energy seen for $\gamma/J = 10$. Conversely, at an infinitesimally low dissipation $\gamma/J = 0.01$, the conservation of particles on average – ensured by Eq. (5.19) – is outweighed by the stochastic term $\sim \sqrt{\kappa}\mathrm{d}\tilde{Z}_j$ of incoherent pumping, resulting in a noise-dominated violation of energy conservation.

Within these bounds, however, the range of dissipation strengths which accurately reproduce the dynamics of the first and second moments of the on-site quantum fields, corresponds precisely to the range of γ for which energy is approximately conserved during time evolution. The artificial dissipation strength optimal for capturing the dynamics of the isolated system may then be inferred as the one which conserves, on average, the energy in the system. For the dynamics shown in Fig. 5.1, this optimum is reached for $\gamma/J \approx 0.1$.

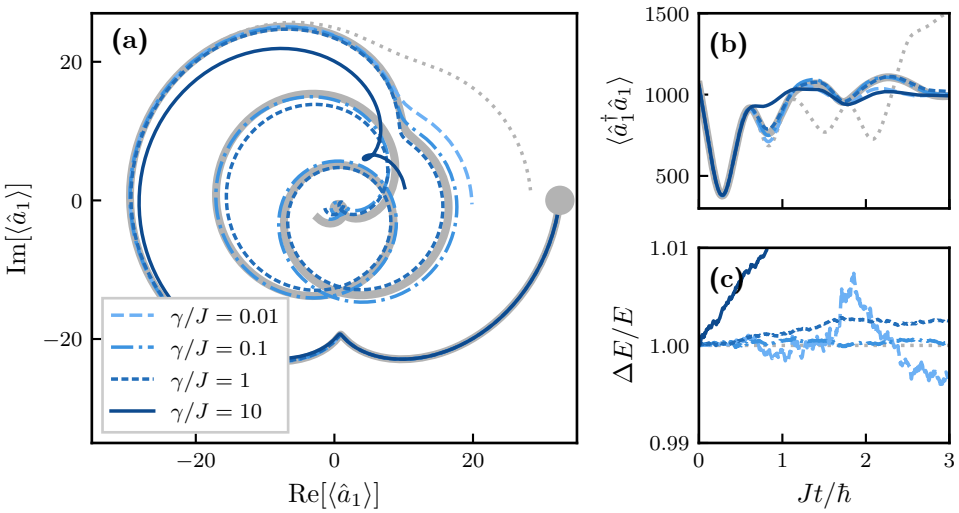

Figure 5.1 – Dynamics of a four-site Bose-Hubbard chain with initial coherent condition given by Eq. (4.7), $N = 4000$ atoms and interaction strength $U/J = 0.01$, evolving up to a time $Jt/\hbar = 3$. (a) Trajectory of the on-site amplitude $\alpha_1 = \langle \hat{a}_1 \rangle$, as previously shown in Fig. 4.3. The initial condition is represented by the grey dot, the thick grey line showing its time evolution as predicted by the truncated Wigner approximation. The non-dissipative Gaussian approximation ($\gamma = 0$) from Fig. 4.3 is shown by the grey dotted line, while blue lines represent the Gaussian trajectory result for various dissipation strength γ, accompanied by incoherent pumping κ preserving the total number of particles. Both truncated Wigner and Gaussian trajectory results represent the average of 10^4 realizations, such that the statistical error on the inferred result is smaller than the line thickness. Gaussian results for $\gamma/J = 0$, 0.01 and 10 were truncated to $Jt/\hbar = 1$ for clarity.

5.3 Projection of the dissipated state

The addition of incoherent pumping to compensate for particle losses ensures the number of particles to be conserved on average, but still allows for individual trajectories to deviate from this conservation law. In Chapter 7, we will study the dynamics of a spinor condensate evolving to a nonequilibrium steady state crucially determined by conservation of magnetization. There, we will find that a correct prediction of the long-time behaviour requires this restriction to the dynamics to be ensured within each individual trajectory.

To ensure that conservation laws remain satisfied within each trajectory of the artificially dissipative dynamics, we replace incoherent pumping at rate κ with continuous projections of the dissipated state onto the subspace of the isolated system*. Rather than maintaining the total number of particles only on average, this ensures its conservation at each time step of an individual trajectory. As illustrated in Fig. 5.2, a trajectory (red) which does not exactly obey a conservation law of the system, but instead relies on the balance between dissipation and pumping to remain in the vicinity of the corresponding subspace (blue surface), may adequately capture the true dynamics of the isolated system (black) at early times. However, deviations from the actual path may occur at late times in systems where conservation laws crucially determine the properties of the steady state, as we will encounter in Chapter 7. The omission of incoherent pumping initially results in a stronger violation of conservation laws by the dissipative dynamics, shown in dark blue. However, explicitly projecting the dissipated state back onto the subspace of the isolated system (light blue) following each time step, results in a trajectory which exactly obeys the imposed conservation laws, resulting in a more faithful description of the actual dynamics at late times. While the projected trajectories in general still deviate from the actual dynamics of the isolated system, they now do so only within the subspace determined by the system's conservation laws.

In practice, projecting a dissipated state onto a subspace determined by one or several conserved quantities is achieved by a rescaling of the mean field wave functions α_n. As opposed to an incoherent pump, such a rescaling physically corresponds to a *coherent* pump, where atoms are inserted with exactly the same phase as that of the condensate. In experimental terms, incoherent pumping requires knowledge only of the number of atoms dissipated whereas coherent pumping

* In principle, such projections can be implemented in conjunction with incoherent pumping. This is of little use, however, as the latter was initially introduced for the sole purpose of restoring on average the particle number of the isolated system.

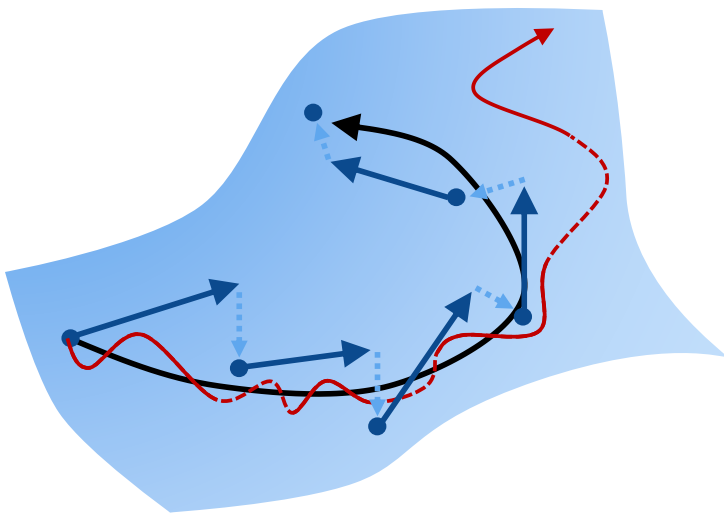

Figure 5.2 – Depiction of variational dynamics in a subspace determined by conservation laws of a quantum system. The exact dynamics (black) follow a path in the subspace (blue surface). A stochastic trajectory which fluctuates in the vicinity of the subspace (red) initially captures the path adequately, but may deviate at late times. By contrast, approximate dynamics which do not restrict the system to the conservation law subspace (dark blue) may provide a more accurate description when each time step is followed by a projection onto the subspace (light blue).

requires a feedback loop from the measured numbers *and* phases of atoms lost to the environment. In order to minimally affect the dissipated state, the projection is performed orthogonal to the desired manifold, i.e., along the gradient of the conserved quantities. For the total number of particles $\sum_j |\alpha_j|^2$ present in the mean field modes $\alpha_j = |\alpha_j| e^{i\theta}$, the gradient in the space of amplitudes $\boldsymbol{\alpha} = (\alpha_1, \ldots, \alpha_L)$ and phases $\boldsymbol{\theta} = (\theta_1, \ldots, \theta_L)$ is given by

$$\boldsymbol{\nabla} N(|\boldsymbol{\alpha}|, \boldsymbol{\theta}) = 2(|\boldsymbol{\alpha}|, 0). \tag{5.21}$$

The optimal projection to restore the total number of particles $N = \sum_j (|\alpha_j|^2 + v_{jj})$ to that of the isolated system (N_0) is then simply given by an equal rescaling of all amplitudes,

$$\alpha_n \to \sqrt{\frac{N_0 - \sum_j v_{jj}}{\sum_j |\alpha_j|^2}}\, \alpha_n, \tag{5.22}$$

where the subtraction of $\sum_j v_{jj}$ accounts for the present occupation of fluctuations*.

Analogously to the restoration of N to N_0, the dissipated state could be projected onto the manifold of E_0 to ensure energy conservation. To achieve this in conjunction with particle conservation, one can employ a generic *gradient descent* algorithm [224] to minimize a function of the form

$$F(\boldsymbol{\alpha}) = [E_0 - E(\boldsymbol{\alpha})]^2 + P[N_0 - N(\boldsymbol{\alpha})]^2, \tag{5.23}$$

with respect to the vector $\boldsymbol{\alpha}$, where E_0 and N_0 are the conserved quantities to be restored and $E(\boldsymbol{\alpha})$ and $N(\boldsymbol{\alpha})$ the energy and particle number functionals of the dissipated state, respectively. The proportionality factor P determines the relative weight given to both requirements, and can be set to $(E_0/N_0)^2$ to assign equal importance to both conservation laws. Fixing the conservation of energy exactly, however, eliminates small deviations from this conservation law as a criterion to select the optimal dissipation strength. In fact, we found that simultaneously enforcing particle number and energy conservation at the single-trajectory level reduces the average time evolution for different values of γ to a single result which severely underestimates dephasing. This indicates that enforcing all conservation laws of the system – in particular its energy – at the trajectory level poses too stringent a condition for the dynamics to benefit from the decoherence provided by artificial dissipation. In other words, the dynamics are overdetermined in the sense that the effect of artificial dissipation is nullified

* Note that we restrict this rescaling to the mean field modes α_n and not the fluctuations v_{nn} in order to retain the desired suppression of fluctuations.

entirely.

A second, more practical reason for replacing incoherent pumping with explicit projection of the dissipated state is the additional term $\sqrt{\kappa}\mathrm{d}\tilde{Z}_n$ in Eq. (5.11). When fluctuations are small, this term dominates over the stochastic growth of the mean field mode accompanying the reduction of fluctuations. Hence, the transfer of fluctuations from quantum to classical is in this case overshadowed by stochastic noise in the evolution of the coherent modes α_n. While the inclusion of incoherent pumping is arguably more elegant than the explicit restoration of conservation laws, it is for this reason less suitable when dealing with lowly occupied modes. As the dissipator for α_n stemming from single-particle losses (5.3) contains no such term, projection-supplemented dissipative dynamics do not suffer from this limitation.

Figure 5.3 shows the Gaussian trajectory dynamics of the same four-site Bose-Hubbard model as before, but now using continuous projection of the dissipated state in order to conserve the number of particles. While largely similar to the result of incoherent pumping shown in Fig. 5.1 for all $\gamma/J \leq 1$, a significant improvement to the description can be discerned in the regime of strong dissipation. In the case of $\gamma/J = 10$, dephasing of the first moment now occurs at the correct time scale due to the omission of stochastic noise caused by incoherent pumping. Note that this result for $\gamma/J = 10$ shown here is not simply the irrelevant case of an unsuitably large artificial dissipation strength, but more generally an example of a situation in which fluctuations are limited to a small value. Besides deliberate suppression by a large dissipation strength, such small fluctuations naturally occur in systems with lowly occupied modes. The improved performance of the Gaussian trajectory approach is confirmed by the local population dynamics in Fig. 5.3(b). Finally, deviations from the conserved energy in Fig. 5.3(c) indicate a reduction of energy violation in the strongly dissipative regime. As one of two decohering jump operators has been eliminated, the optimal strength of artificial dissipation has risen to $\gamma/J \approx 1$.

To summarize, replacing incoherent pumping as a way to balance the particles lost in dissipation with the explicit projection of the dissipated state onto a state with the correct particle number, results in a Gaussian trajectory approach which is more robust to the artificial dissipation strength and a regime of validity extended to systems with small fluctuations.

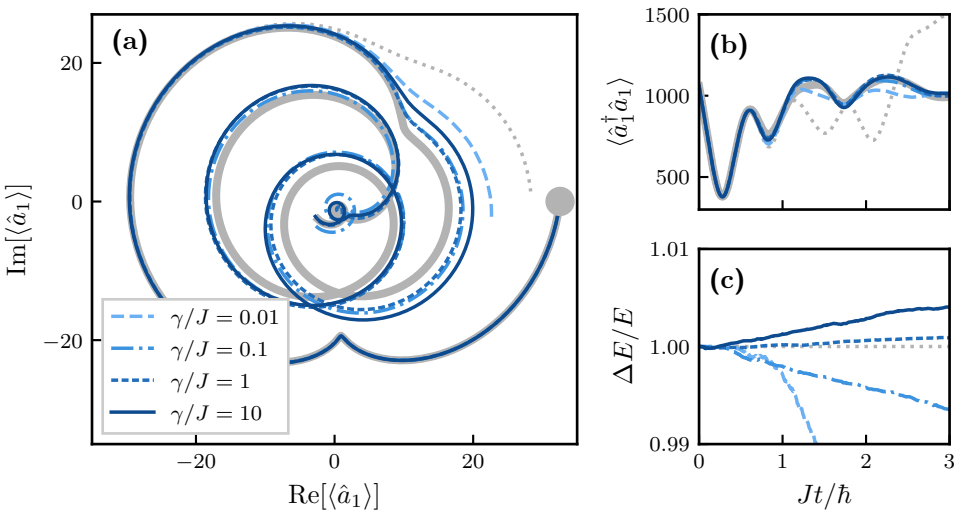

Figure 5.3 – Same dynamics as shown in Fig. 5.1, but with incoherent pumping at rate κ replaced by an explicit projection on the subspace of conserved particle number. In comparison to Fig. 5.1, this results in a lower sensitivity of the Gaussian trajectory approach to the artificial dissipation strength γ.

5.4 Two-step dissipation

A final refinement of the Gaussian trajectory approach with artificial dissipation can be obtained by reconsidering the position of dissipation in the time evolution of the system. So far, we have assumed the dissipator $\mathcal{D}$ to be an integral part of the dynamics, acting on the state at each time step according to Eq. (5.2) and thus reducing the dynamics to that of an open quantum system. This dissipation scheme results in a continuous suppression of fluctuations $\hat{\delta}_n$ to a magnitude determined by the interplay between the dissipation strength γ and the unitary growth of fluctuations.

However, as we are concerned with the dynamics of an isolated system, we may wish the time evolution of the operator to be driven by unitary dynamics and remain undisturbed by dissipation, as long as the magnitude of fluctuations within a trajectory remains limited. To keep the approximate dynamics more faithful to that of an isolated system, we follow an alternative approach which more explicitly separates artificial dissipation from unitary time evolution. This algorithm, to which we will refer as *two-step* dynamics, was first employed in Ref. [188] and consists in evolving the system according to its Hamiltonian alone. For an initially Gaussian variational state, this results in a growth of fluctuations, quantified by

the occupation of fluctuation modes*,

$$\Delta = \sum_n v_{nn} = \sum_n \langle \hat{\delta}_n^\dagger \hat{\delta}_n \rangle \,. \tag{5.24}$$

When the dynamics of the isolated system have caused fluctuations to exceed a critical value $\Delta > \Delta_\mathrm{c}$, time evolution is halted. At this instant t_0, the dissipator $\mathcal{D}\,\langle \hat{O} \rangle$ is applied until fluctuations have been suppressed below a lower critical value Δ_s which we will usually take $\Delta_s = \Delta_c/2$. During this dissipation step, Hamiltonian dynamics and hence time evolution are frozen. Similarly to real-time dissipation, the suppression of fluctuations is accompanied by a stochastic jump in the expectation value α_n. Following the dissipation step, the dissipated state is projected to restore relevant conservation laws and unitary dynamics resume. The result is a purely Hamiltonian time evolution interrupted by discrete, instantaneous dissipation steps.

While serving as a purely numerical refinement, this two-step procedure can be thought of as resembling the unitary-projective dynamics of quantum circuits which give rise to the measurement-dependent scaling of entanglement, as discussed in Sec. 4.3.1. As dissipation is reduced to an instantaneous process, the actual value of γ becomes irrelevant. Instead, the parameter of the Gaussian trajectory approach is now the maximal magnitude of fluctuations Δ_c allowed within each individual trajectory.

We illustrate the two-step dynamics in Fig. 5.4, repeating the dynamics previously shown in Figs. 5.1 and 5.3. With the constant dissipation at rate γ replaced by fluctuation-dependent dissipation steps, we find a similar performance and insensitivity to the parameter Δ_c.

5.4.1 Effective dissipation rate

Despite the apparent equivalence of real-time and two-step dissipation dynamics, the latter has a significant advantage in addition to eliminating continuous noise during unitary evolution. To see this, notice that an effective dissipation rate can be derived by relating the number $N_\mathcal{D}$ of instantaneous dissipation steps to the

* The quantification of fluctuations by their populations alone does not take into account all fluctuations included in the Gaussian approximation. In principle, one could construct similar criteria based on off-diagonal correlations $\langle \hat{\delta}_n^\dagger \hat{\delta}_{m\neq n} \rangle$ or the anomalous correlations $\langle \hat{\delta}_n \hat{\delta}_m \rangle$. However, we found the on-site fluctuations v_{nn} to be most practical as they are real-valued, strictly positive and carry the intuitive meaning of populations.

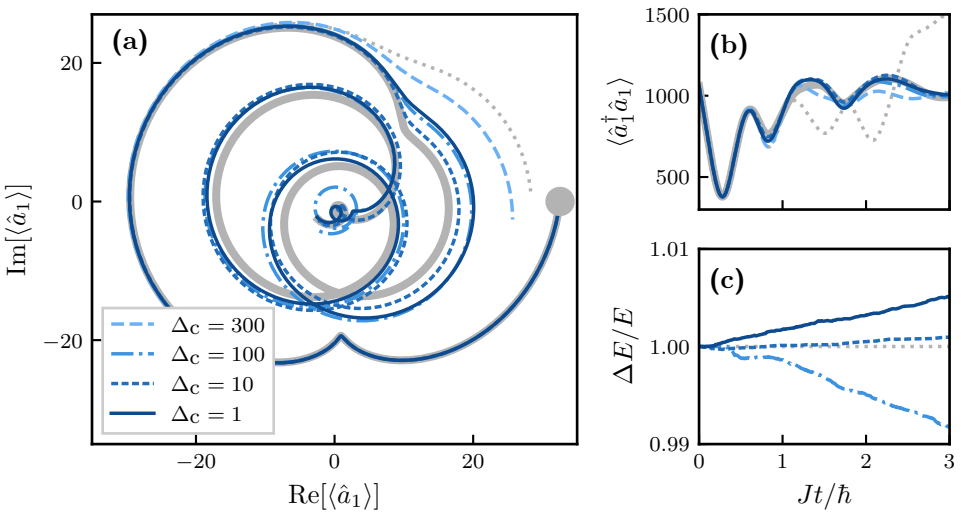

Figure 5.4 – Same dynamics as shown in Fig. 5.3, where continuous dissipation at rate γ is now replaced with the two-step prodecure outlined in Sec. 5.4. Fluctuations are subjected to instantaneous dissipation only when they reach Δ_c, resuming unitary evolution after a suppression to $\Delta_c/2$.

number $N_{\mathcal{H}}$ of unitary time steps preceding it,

$$\gamma_{\mathrm{eff}} = \frac{N_{\mathcal{D}}}{N_{\mathcal{H}}} \gamma_0, \tag{5.25}$$

where γ_0 is the (arbitrary) dissipation strength used in the algorithm and the numerical step size for dissipation and unitary evolution are presumed to be equal. This ratio not only varies between trajectories due to the stochastic nature of dissipation, but also throughout the time evolution of each trajectory. The resulting time dependence of γ_{eff} implies that the two-step algorithm, in addition to eliminating the artefact of continuous stochastic noise, has the benefit of being self-regulating. Indeed, as the two-step algorithm interrupts and resumes the unitary dynamics as often as needed to suppress fluctuations below a desired value, the effective dissipation rate is adaptive with respect to the generation of fluctuations. This property is particularly useful when the growth of fluctuations is non-uniform in time. We will encounter such a scenario in Chapter 7, where a sudden change in the ground state of a spinor condensate results in a short period of rapid fluctuation growth, followed by relaxation to a steady state. There, the two-step procedure will result in a strong suppression of fluctuations in the transient period, after which the effective dissipation rate settles on a low value, minimally disturbing the system after it has relaxed.

5.5 Gaussian trajectories as an alternative to the truncated Wigner approximation

In the preceding sections we have constructed a quantum trajectory method based on Gaussian variational states which reliably captures beyond mean field dynamics of a small Bose-Hubbard chain displaying chaotic dynamics. Doing so, the truncated Wigner approximation has served as a benchmark for the example system. We conclude our dicussion of the algorithm with a comparison of its computational performance and that of the truncated Wigner approximation, and anticipate the physical regimes in which it is expected to outperform the latter.

5.5.1 Number of trajectories

In order to obtain results of similar accuracy as the TWA, the number of Gaussian trajectories required to converge to the true solution should be comparable to the number of Wigner realizations. To illustrate that this is the case for our example system, we show in Fig. 5.5 the mean squared deviation of the true trajectory of an on-site first moment $\langle \hat{a}_1 \rangle$ from the prediction $\alpha_1^{(N_{\mathrm{traj}})}(t)$ resulting from a simulation of N_{traj} trajectories,

$$S^2_{\langle \hat{a}_1 \rangle}(N_{\mathrm{traj}}) = \frac{1}{T} \int_0^T \left| \alpha_1^{(N_{\mathrm{traj}})} - \langle \hat{a}_1 \rangle \right|^2 \mathrm{d}t. \tag{5.26}$$

For the example system studied here, the GTA and TWA require a near identical number of trajectories to obtain the same error. However, whereas each TWA realization requires the evolution of a vector of size L, Gaussian variational states consist of $L \times L$ correlation matrices, making the computational cost of evolving a single trajectory much larger*. For large systems in particular, the L^2 scaling of complexity makes it challenging to simulate long-time dynamics with the Gaussian trajectory approach.

5.5.2 Lowly occupied modes

As detailed in Sec. 3.4, the truncated Wigner approximation for dynamics of an initially coherent state adds an average of 1/2 to the occupation of each mode, limiting its validity to systems with an average mode occupation $N/L \gg$

* This is, of course, not the case for systems with quadratic Hamiltonians, whose displacement and squeezing dynamics are exactly captured by the Gaussian approximation (see Sec. 3.3.1). Likewise, dynamics of weakly non-Gaussian systems are expected to be adequately reproduced by fewer Gaussian trajectories than truncated Wigner realizations.

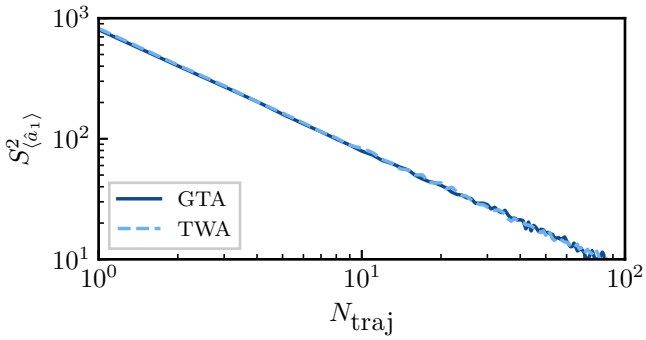

Figure 5.5 – The mean squared error to the predicted evolution of an on-site first moment $\langle \hat{a}_1 \rangle$, Eq. (5.26), as a function of the number of Gaussian or truncated Wigner trajectories sampled to obtain the result.

1/2. When this condition is not met, time evolution is predominantly driven by stochastic noise and the actual dynamics of the system are lost. Even in systems globally satisfying the above condition, the presence of lowly occupied modes may result in the prediction of unphysical negative mode occupations after subtraction of 1/2. This was found to be the case in the nonequilibrium steady state of a driven-dissipative Bose-Hubbard chain [142], where predominantly the truncated Wigner approximation overestimates the signature of spontaneous Beliaev decay from lowly-occupied high-momentum modes.

On the other hand, by encompassing the Bogoliubov theory of linearized fluctuations, the Gaussian variational theory provides a more faithful account of spontaneous excitations out of the quantum vacuum [145]. It is therefore expected to provide a more accurate description of lowly occupied modes.

5.5.3 Thermalization dynamics

A particular occurrence of lowly occupied modes arises during thermalization dynamics, in which the energy distribution of particles approaches the Bose-Einstein distribution (2.3), distinctly characterized by an exponential tail at high energy.

For a homogeneous Bose gas or uniform Bose-Hubbard chain, elementary excitations take the form of plane waves with momentum k. Thermalization then manifests itself as the emergence of a Bose-Einstein distribution for the occupation of momentum modes,

$$n_k = \langle \hat{a}_k^\dagger \hat{a}_k \rangle = \frac{1}{e^{\hbar\omega_k / k_B T} - 1}, \tag{5.27}$$

with ω_k the dispersion of elementary excitations. For the Bose-Hubbard model, this Bogoliubov spectrum is of the form

$$\omega_k = \sqrt{\epsilon_k(\epsilon_k + 2Un_0)}. \tag{5.28}$$

In this equation, the kinetic energy ϵ_k of modes in the first Brillouin zone is given by

$$\epsilon_k = 2J[1 - \cos(ka)], \tag{5.29}$$

with a the lattice spacing. By contrast, the truncated Wigner approximation replaces the quantum field with a classical field. It therefore predicts thermalization to a classical equilibrium state characterized by the equipartition distribution [145]

$$n_k^{(TWA)} = \frac{k_B T}{\hbar\omega_k} - \frac{1}{2}, \tag{5.30}$$

which can be seen as a low-frequency approximation to the Bose-Einstein distribution (5.27). Figure 5.6 shows the truncated Wigner prediction for the thermalized momentum distribution in a Bose-Hubbard chain with different numbers of particles, fitted to both a Bose-Einstein and classical equipartition distribution. At high particle number, the TWA result is indistinguishable from both a Bose-Einstein distribution and classical equipartition. As the number of particles and hence the occupation of momentum modes is decreased, the difference between the latter two becomes more apparent. In the regime $N \leq L$, the truncated Wigner approximation is clearly seen to thermalize to classical equipartition in favor of the (correct) Bose-Einstein distribution.

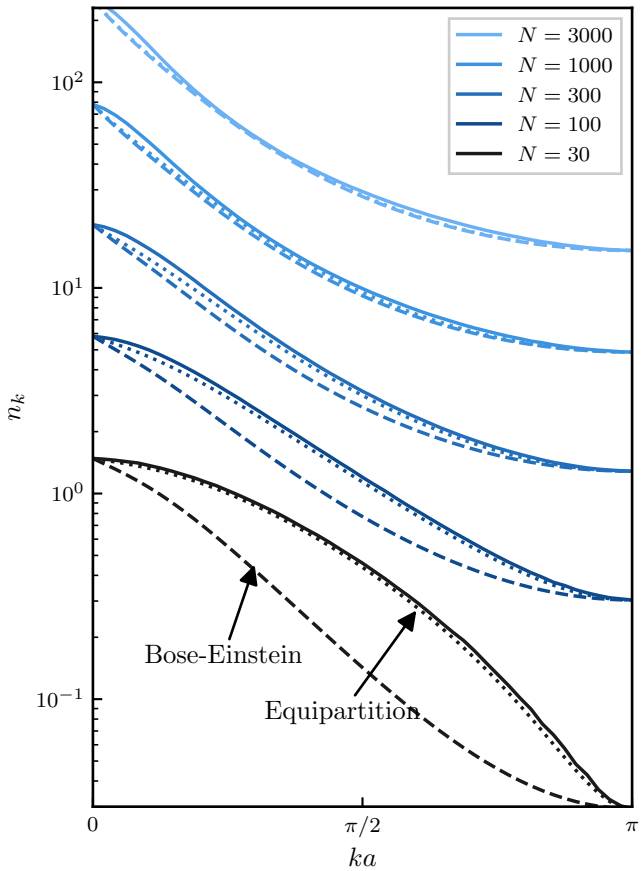

Figure 5.6 – High-temperature equilibrium momentum distribution of a 100-site Bose-Hubbard chain with different particle numbers, as predicted by the truncated Wigner approximation. As seen from the dashed and dotted lines, the TWA result corresponds to classical equipartition, which, in the limit of low mode occupation, deviates significantly from the Bose-Einstein distribution.

5.6 Outlook

In the following part of this thesis, we will employ the Gaussian trajectory approach as developed in this chapter to describe the relaxation dynamics of spin-1 condensate quenched to spin degeneracy. While sufficient for this application, multiple refinements to the proposed method can still be considered. To conclude this chapter, we comment briefly on the improvements we envision for future research, and provide an outlook on a recent approach which formalizes the heuristic approach of this work to the *classicization* of squeezed states.

5.6.1 Further refinements

To sophisticate the Gaussian trajectory approach in its current form, two directions are at present clear. First, one could consider interactions with the environment through stochastic processes different from single-particle loss and pumping considered in Secs. 5.1 and 5.2. These include, for example, tunneling jumps in which a particle hops to a neighbouring site, modelled by the jump operator

$$\hat{\Gamma}_j^{(tunnel)} = \sqrt{\tau}\hat{a}_j^\dagger \hat{a}_{j\pm1}. \tag{5.31}$$

The advantage of this jump operator would be its natural conservation of the total particle number. Likewise, one might try to minimally disturb the system by the annihilation of an elementary excitation rather than the loss of a particle. This process would be described by a Bogoliubov annihilation of the form

$$\hat{\Gamma}_k^{(Bog)} = \sqrt{\beta}\hat{b}_k = \sqrt{\beta}(U_k\hat{a}_k + V_k\hat{a}_{-k}^\dagger), \tag{5.32}$$

where U_k and V_k are the Bogoliubov coefficients (see Sec. 3.2) for the momentum eigenstates of the Bose-Hubbard chain. Which of such jump processes achieves a similar suppression of fluctuations might be the subject of future research.

Secondly, the two-step dynamics outlined in Sec. 5.4 essentially constitutes a crude on/off mechanism for dissipation. The resulting fluctuation-dependent dissipation may, however, be obtained in a more smooth way by including dissipation in the dynamics at a variable rate γ. One might, for example, linearly or nonlinearly interpolate γ from zero in the absence of fluctuations to a desired value at some given magnitude of fluctuations. Ultimately, a variable dissipation strength may be formally included in the dynamics by adding to the time evolution of the system an equation of the form

$$\frac{\mathrm{d}\gamma(t)}{\mathrm{d}t} = -\Delta \mathrm{d}t, \tag{5.33}$$

where Δ is a measure of fluctuations. Throughout this text, we have taken $\Delta = \sum_j v_{jj}$, but this definition is similarly open to further optimization.

5.6.2 Classicization of squeezed states

The artificial dissipation introduced in this chapter constitutes a continuous resampling of a Gaussian state with growing fluctuations. Recently, a more sophisticated strategy was proposed [225] which formalizes the stochastic resampling of a pure state into an approximate decomposition in coherent states $|\alpha\rangle$,

$$\hat{\rho} \to \int \mathrm{d}\alpha P(\alpha) \, |\alpha\rangle \, \langle\alpha| \, . \tag{5.34}$$

This is essentially the same decomposition as Eq. (4.11) upon replacement of the generic probabilities p_j with the Glauber-Sudarshan P-distribution, a quasiprobability distribution in terms of coherent states (see Sec. 3.4). Since such a superposition is possible only for *classical states* in which all fluctuations are consistent with classical correlations, resampling a squeezed state as a mixture of coherent states requires its volume in phase space to be extended by resetting fluctuations in squeezed directions to unity. As quantum coherences are captured by precisely such squeezed variances, this procedure of *classicization* results in an omission of physically irrelevant coherences equivalent to the effect of artificial dissipation, as explained in Sec. 4.2.1. However, explicit classicization comes down to the identification and subsequent targeted dissipation of those modes in which fluctuations exponentially increase*, rendering it intrinsically less invasive to the unitary evolution of the quantum state than the indifferent dissipation of all modes. The price to pay for the additional sophistication is that one needs to explicitly diagonalize the matrix of Gaussian fluctuations in order to determine the eigenvectors which dominate the growth of fluctuations. This has to be done continuously due to the time dependence of the Bogoliubov equations governing fluctuation dynamics, making this method computationally more intensive.

---

* Accompanied by squeezing in the canonically conjugate variable.

III

Spin mixing dynamics in spinor condensates

"Hello, CD listeners. We've come to the point in this album where those listening on cassette or record will have to stand up – or sit down – and turn over the record – or tape. In fairness to those listeners, we'll now take a few seconds before we begin side two.

Thank you. Here is side two."

– Tom Petty, *Full Moon Fever*

6 | The single-mode spin-1 condensate

With the Gaussian trajectory approach to dynamics of a weakly interacting quantum many-body system introduced and tested on a chaotic Bose-Hubbard chain in Part II, we now aim to apply the newly developed method to describe dynamics in multicomponent fluids. We will focus in particular on the dynamical appearance of a *fragmented condensate*. Involving a rapid growth of fluctuations inadequately captured by a Gaussian variational theory, this recently observed phenomenon is an ideal proving ground for the Gaussian trajectory approach.

Before moving on to a description of these dynamics, we dedicate this chapter to introducing the spin-1 fluid in the exactly solvable single-mode regime and outlining its ground state properties.

6.1 Single-mode approximation

The spatially extended spin-1 fluid of Sec. 2.4 is too large to obtain exact solutions for physically meaningful system sizes. We therefore further restrict our description to an interesting regime in which computational complexity reduces dramatically. As the scattering lengths a_0 and a_2 are typically of comparable magnitude [78, 226], the interaction strengths (2.22) satisfy $|c_2| \ll c_0$ and the dynamics are dominated by spin-independent interactions. Spin-dependent interactions can then be considered perturbations to a spatial wave function common to all three components of the vectorial order parameter [227–230]. Within this so-called *single-mode approximation* (SMA), the spatial wave function can be considered time-independent in the case of a tightly confined fluid, where excited states of the harmonic trapping potential are of much higher energy than the spin excitations, $\hbar\omega_{trap} \gg U$, with U the effective interaction constant defined

explicitly below. The field operators are factorized as

$$\hat{\psi}_m(\mathbf{r},t) = \chi(\mathbf{r})\hat{a}_m(t), \tag{6.1}$$

where $\hat{a}_m(t)$ creates a particle of spin m at time t. Both the spatial wave function and the spin populations are normalized through $\int \mathrm{d}\mathbf{r}|\chi(\mathbf{r})|^2 = 1$ and $\sum_m \langle \hat{a}_m^\dagger \hat{a}_m \rangle = N$. Decoupled from spatial dynamics, the low-energy dynamics of the three mode spin system is then governed by the Hamiltonian*

$$\hat{\mathcal{H}}_S = q\Big(\hat{a}_+^\dagger \hat{a}_+ + \hat{a}_-^\dagger \hat{a}_-\Big) + \frac{U}{2} :\hat{\mathbf{S}}^2:, \tag{6.2}$$

where the interaction constant $U = c_2 \int |\chi(\mathbf{r})|^4 \mathrm{d}\mathbf{r}$ depends on the spatial density profile [77]. Hence, the dynamics of the field operators, governed by their respective Heisenberg equations of motion,

$$i\hbar\partial_t \hat{a}_m = [\hat{a}_m, \hat{\mathcal{H}}_S]\,, \tag{6.3}$$

are determined solely by the ratios q/U and q/UN. While the SMA is unable to capture the formation of spatial spin structures [231], it remains a valid approximation for small condensates of low magnetization in tight confinement, where the formation of magnetic domains is suppressed [78, 228, 232–234]. As opposed to the spatially extended model, the reduction to a three mode spin system allows for a numerically exact solution of its ground state and dynamics, providing a minimal model to study spin mixing dynamics. Specifically, the last two contributions to the interaction term

$$\begin{aligned} :\hat{\mathbf{S}}^2:= \Big(&\hat{a}_+^\dagger \hat{a}_+^\dagger \hat{a}_+ \hat{a}_+ + \hat{a}_-^\dagger \hat{a}_-^\dagger \hat{a}_- \hat{a}_- - 2\hat{a}_+^\dagger \hat{a}_-^\dagger \hat{a}_+ \hat{a}_- \\ &+ 2\hat{a}_+^\dagger \hat{a}_0^\dagger \hat{a}_+ \hat{a}_0 + 2\hat{a}_-^\dagger \hat{a}_0^\dagger \hat{a}_- \hat{a}_0 \\ &+ 2\hat{a}_0^\dagger \hat{a}_0^\dagger \hat{a}_+ \hat{a}_- + 2\hat{a}_+^\dagger \hat{a}_-^\dagger \hat{a}_0 \hat{a}_0\Big) \end{aligned} \tag{6.4}$$

represent the creation and annihilation of $|+\rangle\,|-\rangle$ *spin pairs*, illustrated in Fig. 6.1 alongside the effective three-mode system. These scattering processes emblematic of the particles' spin nature enable the redistribution of particles among spin modes, conserving both the total particle number N and angular momentum $\langle \hat{S}_z \rangle = \langle \hat{a}_+^\dagger \hat{a}_+ - \hat{a}_-^\dagger \hat{a}_- \rangle$ along the z-axis.

* To avoid confusion, we will denote the spin operator in the single mode system (in terms of $\hat{a}_m$) as $\hat{\mathbf{S}}$, reserving $\hat{\mathbf{F}}$ for the spatially extended fields $\hat{\psi}_m$.

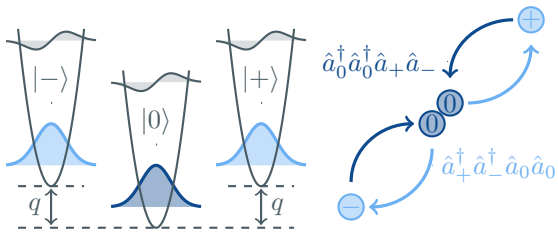

Figure 6.1 – The spin-1 Bose gas reduced to a three-mode spin system in its single-spatial-mode approximation (SMA). The illustrated scattering processes enable the creation and annihilation of spin pairs out of two spin zero particles.

6.2 Exact solution

As a primary benchmark, all obtained results will be compared to an exact solution of the many-body Schrödinger equation. As its name implies, this approach is based on no additional approximations and is therefore valid for all values of q/U. Restricting our discussion to initial configurations obeying $\langle \hat{S}_z \rangle = 0$, the $|+\rangle$ and $|-\rangle$ states are equally populated by a number of *spin pairs*, $N_p = \langle \hat{a}_\pm^\dagger \hat{a}_\pm \rangle$ [235]. The fractional pair number $n_p = N_p/N$ can thus take on values in the range $[0, 1/2]$ and will be the main observable of interest for the remainder of this chapter. For any such initial condition, the conservation of N and $\hat{S}_z$ restrict the evolution of the system to a subspace $\mathscr{H}_p$ of the full Hilbert space $\mathscr{H}$. This subspace is spanned by the basis of *pair number states* $|N_p\rangle = |N_p, N - 2N_p, N_p\rangle$, themselves a subset of the Fock states $|n_+, n_0, n_-\rangle$ characterized by a well-defined number of particles occupying each mode. The reduction to an effectively one-mode system described by the pair number states $|N_p\rangle$ can be understood from the spin exchange processes pictured in Fig. 6.1, which only allow for the creation and annihilation of spin pairs. As the number of spin pairs ranges from 0 to $N/2$, this subspace is $N/2+1$ dimensional, which, in contrast to the full Hilbert space of dimension N^2, allows for an exact integration of dynamics for relevant systems sizes up to $N \sim 10^3$ [227, 236].

Within the pair number subspace $\mathscr{H}_p$, the exact evolution of an arbitrary state $|\psi\rangle$ can be computed through the many-body Schrödinger equation

$$i\partial_t \langle n|\psi\rangle = \sum_{m=0}^{N/2} \langle n|\hat{\mathcal{H}}_S|m\rangle \langle m|\psi\rangle \,. \tag{6.5}$$

The matrix elements $H_{nm} = \langle n|\mathcal{H}_S|m\rangle$ were first given in [236] for the limiting

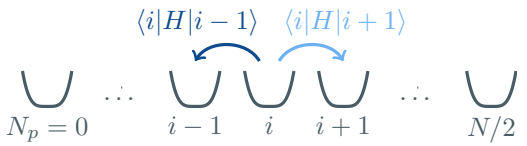

Figure 6.2 – Single-particle hopping Hamiltonian to which the exact solution of the single-mode spin-1 system is formally equivalent.

case $q = 0$, and are in general readily derived by applying the different interaction terms to the general Fock state $|n_+, n_0, n_-\rangle$ and making use of the ladder operator definitions

$$\hat{a}_i \,|\ldots, n_i, \ldots\rangle = \sqrt{n_i}\,|\ldots, n_i - 1, \ldots\rangle\,, \tag{6.6}$$

$$\hat{a}_i^\dagger \,|\ldots, n_i, \ldots\rangle = \sqrt{n_i + 1}\,|\ldots, n_i + 1, \ldots\rangle\,, \tag{6.7}$$

with $i = -1, 0, +1$. Orthonormality of Fock states $\langle n|m\rangle = \delta_{n,m}$ then leads to:

$$\begin{aligned} H_{nm} = m[2q + U(2(N-2m)-1)]\delta_{n,m} \\ + Um\sqrt{(N-2m+1)(N-2m+2)}\delta_{n,m-1} \\ + U(m+1)\sqrt{(N-2m)(N-2m-1)}\delta_{n,m+1}. \end{aligned} \tag{6.8}$$

Physically, the tridiagonal shape of the Hamiltonian is a consequence of the fact that maximum one spin pair at a time is created or annihilated by the scattering processes. The many-body system is therefore formally equivalent to a single particle on a chain with nearest-neighbour hopping amplitudes, as illustrated in Fig. 6.2.

6.2.1 Pair coherent states

Fock states – including the subset of pair number states – are highly non-classical, making them unsuitable as initial conditions for real-time dynamics if one wishes to compare the exact solution to any of the approximate approaches outlined in Chapter 3. More applicable in this respect are the *coherent states* $|\alpha\rangle_c$ introduced in Sec. 3.3.1. For a one-mode system, these eigenstates of the annihilation operator can be decomposed into a superposition of number states through

$$|\alpha\rangle_c = e^{-\frac{|\alpha|^2}{2}} \sum_{n=0}^{\infty} \frac{\alpha^n}{\sqrt{n!}}\,|n\rangle\,, \tag{6.9}$$

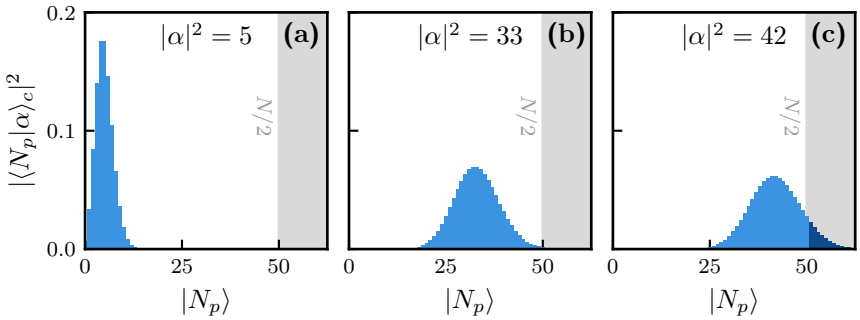

Figure 6.3 – Coherent states as a superposition of pair number states in a collection of $N = 100$ spin-1 atoms. The number of spin pairs follows a Poisson distribution with mean $\mathcal{N}_p = |\alpha|^2$. The grey shaded area denotes pair number states outside of the truncated subspace $\mathscr{H}_p$. Dark blue probabilities in this region are neglected in the numerically exact solution.

where the eigenvalue $\alpha = \sqrt{\tilde{n}}e^{i\theta}$ can be interpreted as a classical wave function of $\tilde{n}$ particles and phase θ. For the present case of a spin-1 system restricted to its pair number subspace, the above superposition becomes [236]

$$|\alpha\rangle_c = e^{-\frac{|\alpha|^2}{2}} \sum_{N_p=0}^{N/2} \frac{\alpha^{N_p}}{\sqrt{N_p!}} |N_p\rangle \,. \tag{6.10}$$

The amplitude and phase of the coherent wave function $\alpha = \sqrt{\mathcal{N}_p}e^{i\Delta}$ now determine the mean pair number $\mathcal{N}_p$ and the relative phase of the spin components $\Delta = \theta_+ + \theta_- - 2\theta_0$, taken to be $\Delta = 0$ throughout the remainder of this work. The global phase does not enter the dynamics due to the $U(1)$ symmetry of the system. As seen from this prescription, a coherent state is a superposition of pair number states in which the number of spin pairs follows a Poisson distribution with mean $|\alpha|^2 = \mathcal{N}_p$,

$$|\langle N_p|\alpha\rangle_c|^2 = \frac{|\alpha|^{2N_p}}{N_p!} e^{-|\alpha|^2}. \tag{6.11}$$

Figure 6.3 illustrates the probability distribution of N_p for coherent states of a few representative mean pair numbers $\mathcal{N}_p$. Note that the reduction of $\mathscr{H}$ to $\mathscr{H}_p$ for a given number of particles N places an upper bound $N/2$ on the allowed number of spin pairs. Comparing Eq. (6.10) to (6.9), this results in a truncation of the finite summation of Fock states. Therefore, the states $|\alpha\rangle_c$ are only approximately coherent within the prescribed subspace, and we will refer to them as *pair coherent states*. As seen from Fig. 6.3, the effect of this truncation is negligible for pair coherent states of $\mathcal{N}_p \lesssim N/3$, the regime to which we will limit our choice of initial conditions.

A special case is the vacuum of spin pairs, which is an eigenstate of both the annihilation operator and the number operator, and therefore corresponds to the pair coherent state with zero spin pairs,

$$|\alpha = 0\rangle_c = |N_p = 0\rangle \,. \tag{6.12}$$

Note that this is not the vacuum of the full Hilbert space $\mathscr{H}$, but rather the Fock state $|0, N, 0\rangle$. Also denoted $|0\rangle^{\otimes N}$, this state corresponds to a coherent superposition of all particles into a single $S_z = 0$ condensate, and will serve as the initial condition for much of Chapter 7.

6.2.2 Validity of the dimensional reduction

As the Hamiltonian conserves angular momentum $\hat{S}_z$, the dynamics may consistently be restricted to the manifold of all states obeying $\langle \hat{S}_z \rangle = 0$ for any initial state satisfying the same condition. However, the pair number subspace does not contain *all* such states, as the condition $\langle \hat{S}_z \rangle = 0$ is equally satisfied by superpositions of Fock states such as

$$|\psi\rangle = (|N, 0, 0\rangle + |0, 0, N\rangle)/\sqrt{2}, \tag{6.13}$$

which cannot be represented as a superposition of pair number states. This poses no restriction for the simulation of dynamics, as all initial conditions will be taken to be pair coherent states of the form (6.10). As the matrix elements H_{nm} connect these superpositions of pair number states only to other pair number states, the time evolution remains restricted to $\mathscr{H}_p$. However, this argument does not hold for obtaining properties of the ground state, found through imaginary time evolution of any initial condition which is not orthogonal to the ground state. By restricting the dynamics to the pair number subspace $\mathscr{H}_p$, the true ground state can only be inferred if it lies within $\mathscr{H}_p$. At $q/U = 0$, this is indeed the case, as the eigenstates of the Hamiltonian then reduce to eigenstates $|S, m_S\rangle$ of the angular momentum operator $\hat{\mathbf{S}}$. The ground state, $|S = 0, m_S = 0\rangle$, can be expressed as a superposition of pair number states [227] and thus lies within $\mathscr{H}_p$. At finite q/U, the eigenstates are no longer angular momentum states. In the high q/U regime, however, ground state predictions from the exact solution restricted to $\mathscr{H}_p$ agree with the Bogoliubov approximation detailed below and a continuum approximation of the many-body Schrödinger equation [230], both of which do not explicitly rely on the restriction to the pair number subspace $\mathscr{H}_p$.

6.3 Approximate approaches

In Chapter 7 we will employ the Gaussian trajectory approach (GTA) introduced in Part II to study the dynamics of fragmentation in the single-mode spin-1 gas. Before doing so, we briefly review the existing approximation schemes and the limitations to their validity.

6.3.1 Mean field and truncated Wigner approximation

In the thermodynamic limit $N \gg 1$, one can neglect the quantized nature of the system entirely, and replace the field operators with classical fields, $\phi_m = \langle \hat{a}_m \rangle$, yielding the mean field energy functional

$$E_S = \langle \hat{\mathcal{H}}_S \rangle = q(n_+ + n_-) + \frac{U}{2}\mathbf{S}^2, \tag{6.14}$$

with $n_m = |\phi_m|^2$. The classical equations of motion (3.2) then take the form of a set of three coupled Gross-Pitaevskii equations,

$$\begin{aligned} i\hbar\partial_t\phi_+ &= U\left[(n_0 + n_+ - n_-)\phi_+ + \phi_-^*\phi_0\phi_0\right] + q\phi_+, \\ i\hbar\partial_t\phi_0 &= U[(n_+ + n_-)\phi_0 + \phi_0^*\phi_+\phi_-], \\ i\hbar\partial_t\phi_- &= U\left[(n_0 + n_- - n_+)\phi_- + \phi_+^*\phi_0\phi_0\right] + q\phi_-. \end{aligned} \tag{6.15}$$

The ground state for the mean field energy functional is given by

$$(\phi_+ \quad \phi_0 \quad \phi_-) = \begin{cases} (0 \quad \sqrt{N} \quad 0) & q \geq 0, \\ (\sqrt{N/2} \quad 0 \quad \sqrt{N/2}) & q \leq 0, \end{cases} \tag{6.16}$$

which becomes degenerate for $q = 0$.

Following the truncated Wigner approximation developed in Sec. 3.4, leading order quantum corrections to the mean field description may be accounted for by sampling the initial conditions of the Gross-Pitaevskii equations (6.15) from the Wigner distribution of the initial coherent state, as in Eq. (3.29). Being a three-mode system with N of order $10^2 - 10^3$, the single-mode spin-1 fluid is well within the validity condition (3.30) of the truncated Wigner approximation, which is therefore expected to be accurate.

6.3.2 Bogoliubov expansion of spin excitations

For $n_p \ll 1$, the number of spin pairs created in the $|\pm\rangle$ states can be treated as a weak perturbation to a condensate of N particles in the $|0\rangle$ state, warranting

a linearized Bogoliubov approach as outlined in Sec. 3.2. Substituting the field operators accordingly as $(\hat{a}_+, \hat{a}_0, \hat{a}_-) \approx (\hat{\delta}_+, \sqrt{N}, \hat{\delta_-^\dagger})$, the Hamiltonian (6.2) can be expanded up to quadratic order in fluctuation operators $\hat{\delta}_\pm$, yielding

$$\hat{\mathcal{H}}_S \approx (q + UN)(\hat{\delta}_+^\dagger \hat{\delta}_+ + \hat{\delta}_-^\dagger \hat{\delta}_-) + UN(\hat{\delta}_+ \hat{\delta}_- + \hat{\delta}_+^\dagger \hat{\delta}_-^\dagger). \tag{6.17}$$

This quadratic Hamiltonian is diagonalized by a unitary transformation [2, 234]

$$\hat{\delta}_\pm = u\hat{b}_\pm + v\hat{b}_\mp^\dagger, \tag{6.18}$$

with Bogoliubov coefficients

$$u, v = \pm\sqrt{\frac{q + UN}{2\epsilon} \pm \frac{1}{2}}, \tag{6.19}$$

to arrive at a description in terms of non-interacting quasiparticles,

$$\hat{\mathcal{H}}_S \approx \epsilon(\hat{b}_+^\dagger \hat{b}_+ + \hat{b}_-^\dagger \hat{b}_-) + 2(v^2 + uv). \tag{6.20}$$

The last term in this expression denotes the ground state energy, while the quasiparticle spectrum is given by

$$\epsilon = \sqrt{q(q + 2UN)}. \tag{6.21}$$

Note that, similarly to the spectrum of the spatially extended Bose gas (3.9), the effect of interactions is quantified by the ratio q/UN. However, as the expansion is predicated on a perturbatively small number of spin pairs, its results are reliable only in the high-Zeeman regime $q/U \gg 1$. Hence, the range of magnetic field strengths for which Bogoliubov theory provides reliable predictions grows linearly with N.

6.3.3 Gaussian approximation

As the Bogoliubov approximation breaks down for any state with significant occupation of the $|\pm\rangle$ spin modes, a more general Gaussian Ansatz may be employed in which all three fields $\hat{a}_m$ are described by a classical wave function and small, linearized fluctuations. As detailed in Sec. 3.3, this comes down to the expansion $\hat{a}_m = \phi_m + \hat{\delta}_m$, decomposing the fields into a classical mode $\phi_m = \langle \hat{a}_m \rangle$ and fluctuations of zero mean. Factorizing higher order moments of statistics into products of quadratic correlations, one arrives at a self-consistent, number-conserving description of the fields in terms of the first and second moments of their statistics. The resulting system of equations, consisting of coupled Gross-

Pitaevskii equations for the fields ϕ_m and Heisenberg equations of motion for the quadratic correlators $\langle\hat{\delta}_m^{(\dagger)}\hat{\delta}_n\rangle$, is moved to Appendix A for compactness.

6.4 Spin pairs in the ground state

Before moving on to the dynamics of spin mixing in Chapter 7, we conclude our discussion of the single mode spin-1 gas with a brief description of its relevant ground state properties and their dependence on the parameters entering the Hamiltonian. Fig. 6.4(a) shows the number of spin pairs in the ground state of a gas consisting of $N = 400$ atoms. For each value of the dimensionless parameter q/U, the result was obtained through imaginary time evolution of the many-body Schrödinger equation (6.5) [237].

6.4.1 The Bogoliubov regime

At high Zeeman splitting*, the occupation of the $|\pm\rangle$ modes is energetically suppressed and the majority of particles condense in the $|0\rangle$ mode. The population of spin pairs is then well described by the Bogoliubov approach detailed in Sec 6.3.2. From the transformation (6.18), the number of Bogoliubov excitations $\langle\hat{b}_\pm^\dagger\hat{b}_\pm\rangle$ can be related to the number of spin pairs $\langle\hat{\delta}_\pm^\dagger\hat{\delta}_\pm\rangle$ in the atomic basis through

$$\langle\hat{\delta}_\pm^\dagger\hat{\delta}_\pm\rangle = v^2 + u^2\,\langle\hat{b}_\pm^\dagger\hat{b}_\pm\rangle + v^2\,\langle\hat{b}_\mp^\dagger\hat{b}_\mp\rangle + uv(\,\langle\hat{b}_+\hat{b}_-\rangle + \,\langle\hat{b}_+^\dagger\hat{b}_-^\dagger\rangle). \tag{6.22}$$

The ground state corresponds to the vacuum of elementary excitations $\langle\hat{b}_\pm^{(\dagger)}\hat{b}_\pm\rangle = 0$, and thus contains a finite average number of spin pairs,

$$\bar{n}_p^{eq} = \frac{v^2}{N} = \frac{q+UN}{2N\sqrt{q(q+2UN)}} - \frac{1}{2N}. \tag{6.23}$$

As indicated by the blue dashed line in Fig. 6.4(a), this prediction based on a linearization of lowly occupied spin pair excitations is indistinguishable from the exact result as long as $q/U \gg 1/N$. The decay of $\bar{n}_p^{eq}$ with increasing q is seen to scale according to a power law in two distinct regimes†, the exponents of which

* In the limit $q \to \infty$, the exact solution is limited by its finite resolution in n_p at numerically feasible system sizes N. For this reason, its result is cut off at $n_p \approx 1/N$.

† The point $q = UN$ at which the Zeeman splitting is equal to the interaction energy is conceptually equivalent to the *healing length* marking the crossover between collective and particle-like excitations in an extended Bose gas. We will return to this in Chapter 10.

follow directly from Eq. (6.23),

$$\bar{n}_p^{eq} \propto \begin{cases} (q/U)^{-1/2} & q/U \ll N, \\ (q/U)^{-2} & q/U \gg N. \end{cases} \tag{6.24}$$

The same scaling behaviour was found in a continuum approximation of the many-body Schrödinger equation [230] and through a mapping to the quantum rotor model [238]. Comparing Eq. (6.24) to (6.16), one sees how mean field theory fails to account for spontaneous depletion of the ϕ_0 mode at finite q/U caused by quantum fluctuations. In accordance with the validity of the Bogoliubov approach, the number of spin pairs in the high-q regime is expected to follow the Bose-Einstein distribution [234]

$$|\langle N_p|\psi_{eq}\rangle|^2 \sim \frac{1}{e^{n_p/\bar{n}_p^{eq}-\mu}-1} \sim \exp\Big\{-n_p/\bar{n}_p^{eq}\Big\}, \tag{6.25}$$

where the last equivalence results from the large negative chemical potential needed to account for the absence of a pair number condensate. Figure 6.4(d) shows the excellent agreement between this prediction and the pair number distribution at $q/U = 40/N$.

6.4.2 Spin degeneracy

As the quadratic Zeeman splitting decreases, the exactly calculated number of spin pairs deviates from the Bogoliubov prediction, as the significant occupation of the $|\pm\rangle$ modes violates the assumption $n_p \ll 1$. This is visible in the inset of 6.4(a), as well as in 6.4(c) which shows the pair number distribution in the crossover regime $q/U \sim 1/N$. For vanishing Zeeman splitting $q = 0$, the condensate is said to be *spin-degenerate* and the Hamiltonian (6.2) reduces to the total spin operator $\hat{\mathbf{S}}^2$ of the fluid. Its eigenstates are then the angular momentum eigenstates $|S, m_S\rangle$, where $S \in \{0, \ldots, N\}$ and $m_S \in \{-S, \ldots, S\}$. In the basis of angular momentum states, the expectation value for the number of spin pairs can be shown to be [230]

$$\langle S, m_S|\hat{n}_p|S, m_S\rangle = \frac{1}{2} - \frac{(S^2 - m_S^2)(N+S+1)}{2N(2S-1)(2S+1)} - \frac{(S^2+2S+1-m_S^2)(N-S)}{2N(2S+1)(2S+3)}. \tag{6.26}$$

From this matrix element, one readily derives that the number of spin pairs in the ground state $|S = 0, m_S = 0\rangle$ of a spin-degenerate condensate is $\bar{n}_p^{eq} = 1/3$,

in agreement with the value shown in the inset of Fig. 6.4(a). The distribution of spin pairs can be found by expressing the $|S = 0, m_S = 0\rangle$ ground state as a superposition of pair number states $|\psi_{eq}\rangle = \sum_{N_p=0}^{N/2} A_{N_p} |N_p\rangle$ with coefficients given by the recursion relation [227]

$$A_{N_p} = -\sqrt{\frac{N - 2N_p + 2}{N - 2N_p + 1}} A_{N_p - 1}. \tag{6.27}$$

As shown in Fig. 6.4(b), the distribution of the number of spin pairs in the regime $q/U < 1/N$ agrees well with this prediction.

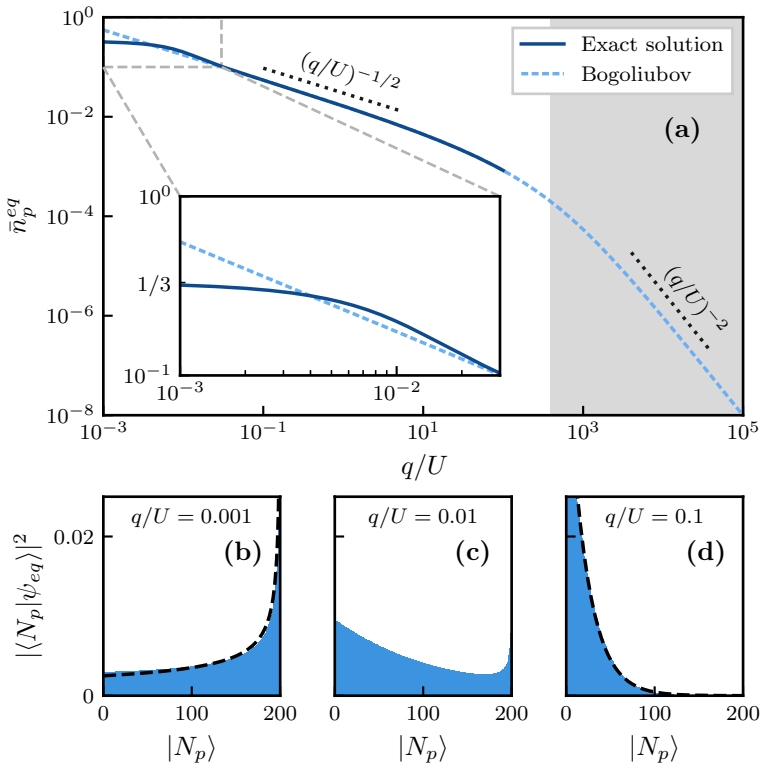

Figure 6.4 – Spin pair statistics in the ground state of an antiferromagnetic spin-1 gas of $N = 400$ and $\langle \hat{S}_z \rangle = 0$. (a) Expectation value of the pair number as a function of the Zeeman splitting q/U. The linearized Bogoliubov prediction (dashed line) is indistinguishable from the exact result of the many-body Schrödinger equation (full line) for $q/U \gg 1/N$ but diverges in the interaction-dominated regime, shown in the inset. The shaded region indicates the crossover between the two scaling regions of Eq. (6.24). (b-d) Distribution of the pair number in the interaction-dominated regime (b), crossover regime (c) and Bogoliubov regime (d). In (b) and (d), dashed lines correspond to $|S = 0, m_S = 0\rangle$ and a Bose-Einstein distribution, respectively.

7 | Fragmentation dynamics of a spin-1 condensate

The results presented in this chapter were published as [239]:

Gaussian trajectory description of fragmentation in an isolated spinor condensate
L. Fernandes, M. Wouters & J. Tempere
Physical Review A **105**, 013305 (2022).

7.1 Spin mixing dynamics

Having covered the ground state properties and main approximation methods for the antiferromagnetic single-mode spin-1 condensate in Chapter 6, we are now in a position to study its dynamics when driven out of equilibrium. In particular, we will consider the dynamics of a gas prepared in a collective state $|0\rangle^{\otimes N}$ (i.e., the Fock state $|0, N, 0\rangle$ which is the ground state for $q/U \to \infty$), following a sudden quench of the Zeeman splitting to a finite value of q/U, brought about by a sudden frequency modulation in the radiofrequent magnetic dressing field [234, 240]. As seen from the phase diagram in Fig. 6.4, this change in the Hamiltonian abruptly changes the ground state of the gas, effectively driving the system far-from-equilibrium. Studying the time evolution following this quench allows to probe the out-of-equilibrium dynamics as atoms scatter into the $|\pm\rangle$ orbitals.

7.1.1 Coherent oscillations and relaxation

Analogously to the ground state, the ensuing spin mixing dynamics can be categorized into two regimes, separated by a continuous crossover. When the system

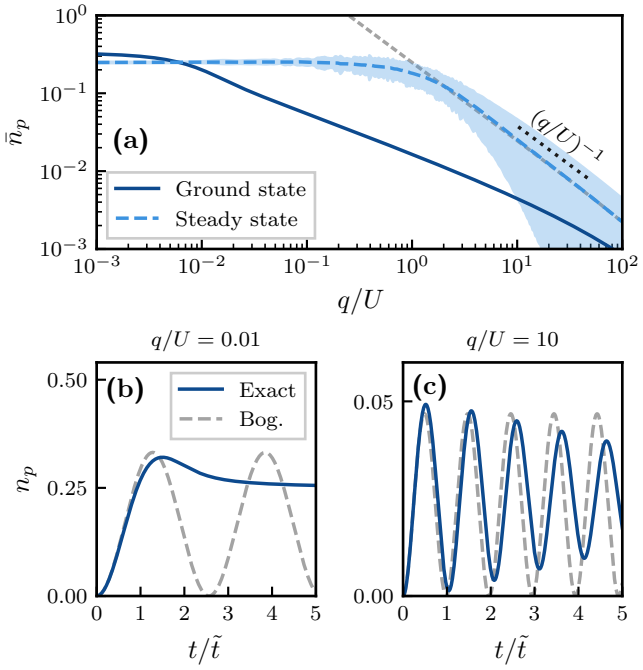

Figure 7.1 – Dynamical phase diagram for an antiferromagnetic spin-1 gas of $N = 400$ and $\langle \hat{S}_z \rangle = 0$. (a) The mean number of spin pairs in the nonequilibrium steady state reached through a quench from $q_i = \infty$ to $q_f = q$ (dashed line), calculated with the exact many-body Schrödinger equation. The shaded region represents the residual oscillation amplitude at late times. The ground state pair number of Fig. 6.4 is shown for comparison. The grey dashed line indicates the Bogoliubov prediction (7.4). (b-c) Typical dynamics of spin populations for quenches to values of q/U in two distinct regimes.

is quenched to $q/U \gg 1$, the dynamics are dominated by the quadratic Zeeman contribution to the Hamiltonian (6.2). The Heisenberg equations (6.3) for the fields $\hat{a}_m$ are therefore close to linear, and the number of spin pairs exhibits persistent coherent oscillations, as illustrated in Fig. 7.1(c). A drastically different situation arises, however, following a quench into the regime $q/U \ll 1$, where nonlinear interactions dominate the dynamics. Oscillations of the number of spin pairs are rapidly damped by the nonlinearity, causing the relaxation to a steady state, shown in Fig. 7.1(b). In both limits, the long time dynamics can be described as a steady state (either oscillatory or relaxed) with a well-defined mean number of spin pairs $\bar{n}_p$. Figure 7.1(a) shows this quantity as a function of q/U, with the shaded region around it indicating the amplitude of residual oscillations in the long time limit.

In the limit $\bar{n}_p \ll 1$, the mean number of spin pairs is seen to be inversely proportional to the quadratic Zeeman splitting q/U [88, 234, 240–243]. This scaling behaviour can again be derived from the Bogoliubov approximation outlined in Section 6.3.2. The oscillatory steady state is now no longer the vacuum of Bogoliubov excitations, but one can evaluate the number of spin pairs by considering that at $t = 0$ following the instantaneous quench, spin mixing dynamics have not yet led to the creation of spin pairs. The quadratic correlations are therefore

$$\langle \hat{\delta}_\pm^\dagger \hat{\delta}_\pm \rangle = \langle \hat{\delta}_+ \hat{\delta}_- \rangle = 0. \tag{7.1}$$

In the basis of Bogoliubov quasiparticles, this translates through (6.18) to

$$\langle \hat{b}_+^\dagger \hat{b}_+ \rangle = \langle \hat{b}_-^\dagger \hat{b}_- \rangle = |v|^2, \tag{7.2}$$

$$\langle \hat{b}_+ \hat{b}_- \rangle = -uv. \tag{7.3}$$

As the Bogoliubov transformation diagonalizes the Hamiltonian, the nonzero number of elementary excitations $\langle \hat{b}_\pm^\dagger \hat{b}_\pm \rangle$ is a constant of motion during the subsequent time evolution. On the other hand, the anomalous correlation $\langle \hat{b}_+ \hat{b}_- \rangle$ trivially rotates under time evolution. When taking time averages, one may therefore approximate $\langle \hat{b}_+ \hat{b}_- \rangle \approx 0$ [143]. Through Eq. (6.22), the number of atoms in the $|\pm\rangle$ modes at late times is therefore

$$n_p = (u^2 + v^2 + 1)\frac{v^2}{N} = \frac{(UN)^2}{2Nq(q + 2UN)}. \tag{7.4}$$

In the linear regime $q/U \gg 1$ this quantity indeed scales as $(q/U)^{-1}$.

In the limit $q/U \ll 1$, on the other hand, the scaling behaviour breaks down as the pair number converges to $\bar{n}_p = 1/4$, implying half of the atoms have settled in the $|\pm\rangle$ orbitals. In a continuum approximation of dynamics in the limit of a vanishing q/U, the time scale of relaxation was shown to be [227, 234]

$$\tilde{t} = \frac{\hbar}{U\sqrt{2N}}. \tag{7.5}$$

In terms of the fractional pair number n_p and the dimensionless time $t/\tilde{t}$, the dynamics of relaxation are universal with respect to the system size N and energy scale U [234]. Note that the relaxation time $\tilde{t}$ is not the same as the time scale determining the onset of spin mixing from an initial spin pair vacuum. The latter is instead set by the interaction energy appearing in the Bogoliubov

spectrum,

$$\tilde{t}_{Bog} = \frac{\hbar}{UN}. \tag{7.6}$$

We will return to this difference in time scales when discussing a strongly dissipative spinor condensate in Sec. 8.3.

7.1.2 The generalized Gibbs ensemble

While nonlinear interactions not included in Bogoliubov theory account for relaxation, it is important to note that the steady state does not correspond to thermal equilibrium, which for $q/U \to 0$ amounts to an equal population of all three orbitals, i.e., $\bar{n}_p^{eq} = 1/3$ (see Fig. 6.4). Instead, the relaxation of spin mixing is crucially affected by the conservation of the angular momentum $\hat{S}_z = \hat{a}_+^\dagger \hat{a}_+ - \hat{a}_-^\dagger \hat{a}_-$ along the z-axis. In view of the distinction between integrable and chaotic dynamics discussed in Sec. 4.1.1, the conservation of both $\hat{N}$ and $\hat{S}_z$ renders the three-mode system integrable, prohibiting it from ergodically exploring its phase space and therefore preventing thermalization. In the statistical ensemble of the relaxed system, this conservation of magnetization* appears as an additional constraint with a Lagrange multiplier given by the magnetic field along the z-direction, generalizing the Boltzmann distribution to a *generalized Gibbs ensemble* [100, 101, 203],

$$\hat{\rho}_{GGE} \sim \exp\left\{-\frac{\hat{H} - B_z \hat{S}_z}{k_B T}\right\}. \tag{7.7}$$

The resulting expectation value for $\bar{n}_p$ can be deduced in the limit $q = 0$, where the Hamiltonian (6.2) reduces to the total spin operator $\hat{\mathbf{S}}^2$ of the fluid. For eigenvalues $S \gg 1$, the expectation value of the pair number $\hat{n}_p$ (6.26) reduces to the approximate form [244]

$$\langle S, m_S | \hat{n}_p | S, m_S \rangle \approx \frac{1}{2} - \frac{S^2 - m_S^2}{4S^2}. \tag{7.8}$$

As the initial state $|0\rangle^{\otimes N}$ satisfies $\langle \hat{S}_z \rangle = m_S = 0$, conservation of magnetization reduces the relaxed ensemble to a mixture of the form

$$\hat{\rho}_{GGE} \sim \sum_S |S, 0\rangle \langle S, 0|, \tag{7.9}$$

* For this system we use the terms angular momentum and magnetization interchangeably, both understood to be $\hat{S}_z$.

where the appearing values of S are determined by the energy constraint in the ensemble (7.7) [234]. From the matrix element (7.8), one finds the pair number in each $|S,0\rangle$ state to be 1/4, such that $\bar{n}_p = \mathrm{Tr}[\hat{\rho}_{GGE}\hat{n}_p] = 1/4$. We will return to the role of this conservation law at the end of this chapter and throughout Chapter 8, where we will relate the breaking of integrability to the notion of *prethermalization*.

7.1.3 Gaussian dynamics

Even though the Bogoliubov approximation fails to reproduce relaxation in the limit of low q/U, Fig. 7.1(b) indicates that the early time growth of spin pairs is still accurately captured by the linearized approach. To incorporate nonlinear damping of the initial oscillation, the Bogoliubov approach is extended to the Gaussian variational Ansatz of Sec. 6.3.3. In contrast to the linearized dynamics of fluctuations $\hat{a}_\pm \to \hat{\delta}_\pm$, the decomposition $\hat{a}_m \to \phi_m + \hat{\delta}_m$ is suited to describe a macroscopic occupation of all three modes. However, as can be seen from the Gaussian equations of motion in Appendix A, the onset of spin mixing dynamics out of an initial state $|0\rangle^{\otimes N}$ results only in a growth of Gaussian fluctuations, leaving the ϕ_m modes themselves unoccupied. The Gaussian theory therefore coincides with the Bogoliubov predictions in Fig. 7.1(b-c).

Nonlinear dynamics can be achieved within the Gaussian approximation by considering coherently seeded dynamics [240], whereby a small number of atoms are prepared as $N_{seed} = n_p^{(0)} \times N$ spin pairs in the $\phi_\pm$ modes. Referring to the exact solution, the initial state then corresponds to a pair coherent state $|\sqrt{N_{\mathrm{seed}}}\rangle_c$, introduced in Sec. 6.2.1. As shown in Fig. 7.2 for an intermediary value of q/U, the activation of the $\phi_\pm$ modes in the Gaussian approximation adds a nonlinearity to the oscillations predicted by Bogoliubov theory (not shown), but still fails to reproduce relaxation to the steady state. For comparison, we also include a mean field approximation which considers only stimulated scattering encoded in the coupled Gross-Pitaevskii equations (6.15), thus requiring a seeded initial condition to produce spin mixing dynamics. Mean field theory captures the creation of spin pairs at early times, but, like Bogoliubov theory, is limited to coherent oscillations* [229, 245]. The fundamental limitation of the Gaussian theory remains the growth of fluctuations, which over time exceed the occupation of the mean field modes. This is illustrated by the blue shaded region in Fig. 7.2, which represents the population of spin pairs contained in linearized fluctuations $\hat{\delta}_m$ as

* Additionally, mean field theory predicts a divergence of the oscillation period at a finite value of q/U, which can be understood through a mapping to the separatrix of a simple pendulum [231]. Retrieved only in the thermodynamic limit of $N \to \infty$, this divergence is a mean field artefact for the small systems of $N \approx 100 - 400$ considered in the present work.

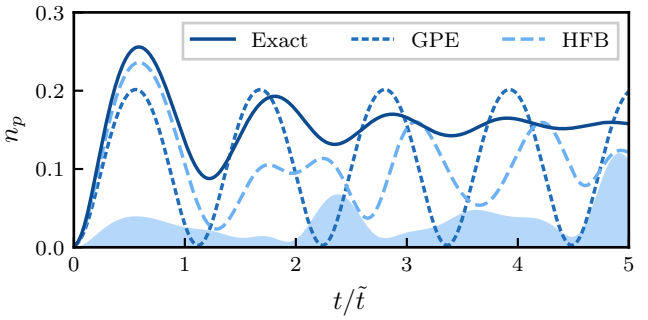

Figure 7.2 – Spin mixing dynamics at $q/U = 10$ for a gas of $N = 400$ atoms and seeded initial condition $N_{\text{seed}} = n_p^{(0)} \times N = 1$. The shaded region indicates the population of spin pairs captured in linearized fluctuations $\hat{\delta}_m$ as opposed to the coherent wave functions ϕ_m in the Gaussian (HFB) approximation. The exact solution and a purely mean field prediction (GPE) are shown for comparison.

opposed to the coherent wave functions ϕ_m subject to the nonlinearity. As the Gaussian approximation is predicated on a limited depletion $\langle \hat{\delta}_m^\dagger \hat{\delta}_m \rangle \ll |\phi_m|^2$, a Gaussian state dominated by fluctuations can no longer be expected to form an accurate representation of the actual dynamics of the system*.

7.2 From fluctuations to fragmentation

7.2.1 Pair number statistics

A better understanding of the role of fluctuations in the relaxation process is gained from a closer inspection of the exact solution of the many-body Schrödinger equation, and in particular the statistics of the pair number variable beyond its expectation value $n_p = \langle \hat{a}_\pm^\dagger \hat{a}_\pm \rangle$. As detailed in Sec. 6.2, the space available to spin mixing dynamics is spanned by the basis of pair number Fock states $|n_p\rangle$. Hence, the probability of observing n_p spin pairs in a given state $|\psi(t)\rangle$ is given by the projection

$$\mathcal{P}[n_p](t) = |\langle n_p | \psi(t) \rangle|^2. \tag{7.10}$$

Figure 7.3(a) shows the evolution of the probability density $\mathcal{P}[n_p](t)$ for the same dynamics as shown in Fig. 7.1(b). From this depiction, which may be seen as a time-dependent generalization of the histograms in Figs. 6.4(b-d), it is immediately clear that the growth of the mean number of spin pairs is accompanied by a rapid evolution into a nearly uniform superposition of all pair number states. The

* Excluding the case in which the system is in a coherent or squeezed state, exactly represented within the Gaussian theory.

initial rise and eventual relaxation of n_p thus conceal a complete delocalization of the pair number observable across its available range $[0, 1/2]$, highlighting the role of fluctuations in the relaxation process.

The regular patterns visible in $\mathcal{P}[n_p](t)$ are known as a *quantum carpet* [235, 246], and arise due to the interference of individual eigenmodes present in the initial state [247]. In this sense, mixing of the pair number states may be understood from the fact that the initial $|n_p = 0\rangle$ Fock state is no eigenstate of the quenched Hamiltonian. Orthogonality to the remaining pair number basis states is subsequently lost during time evolution, resulting in a superposition of all pair number states. Furthermore, the finite dimension of the Hilbert space requires all eigenstates comprising $|\psi(t)\rangle$ to constructively interfere on a finite timescale. This feature, shown as the sudden spike at $t/\tilde{t} \approx 45$ is an instance of a *quantum revival* [248, 249]. Due to the intricate interplay of many eigenmodes, quantum revivals are extremely sensitive to external noise, hindering their experimental observation in macroscopic systems*. For attainable system sizes of $N \sim 10^2 - 10^3$ atoms, quantum revival of the pair number lies well beyond the time scales accessible to current experiments [234]. In other ultracold setups, quantum revival of the many-body wave function has been predicted to occur [251, 252], and was observed in the interference pattern of Bose-Einstein condensates in an optical lattice [253].

It is relevant to note that rapid delocalization of n_p is not a universal feature of spin mixing dynamics. Figure 7.3(b-c) shows the time evolution of a gas with a seeded initial condition ($n_p^{(0)} = 0.05$). Whereas Fig. 7.3(b) is initialized in a pair number state, Fig. 7.3(c) is prepared in a pair coherent state, up to a rescaling of N equivalent to the one shown in Fig 6.3(a). Comparing their respective quantum carpets, it is clear that the probability distribution of the pair number remains peaked around its expectation value much longer for an initially coherent state than for the highly non-classical Fock state, testifying to the relatively classical nature of the former. Recall, however, that for $n_p = 0$, as in Fig. 7.3(a), the pair coherent state $|\alpha = 0\rangle_c$ coincides with the pair number state $|n_p = 0\rangle$ by virtue of the relation (6.10). Spin mixing dynamics from an unseeded initial condition $n_p^{(0)} = 0$ therefore necessarily involves a large growth of pair number fluctuations.

* A lower number of eigenstates shortens the time scale of quantum revival, reducing to integrable, non-relaxing dynamics in the few-body limit [236, 245]. As such, quantum revival can be viewed as an intermediary condition between integrable and chaotic quantum dynamics. The occurrence and time scale of quantum revivals is dependent on the initial state of the system; their presence in a quantum system has therefore been linked to *quantum scars*, rare states which break the ergodicity of an otherwise chaotic quantum system [250].

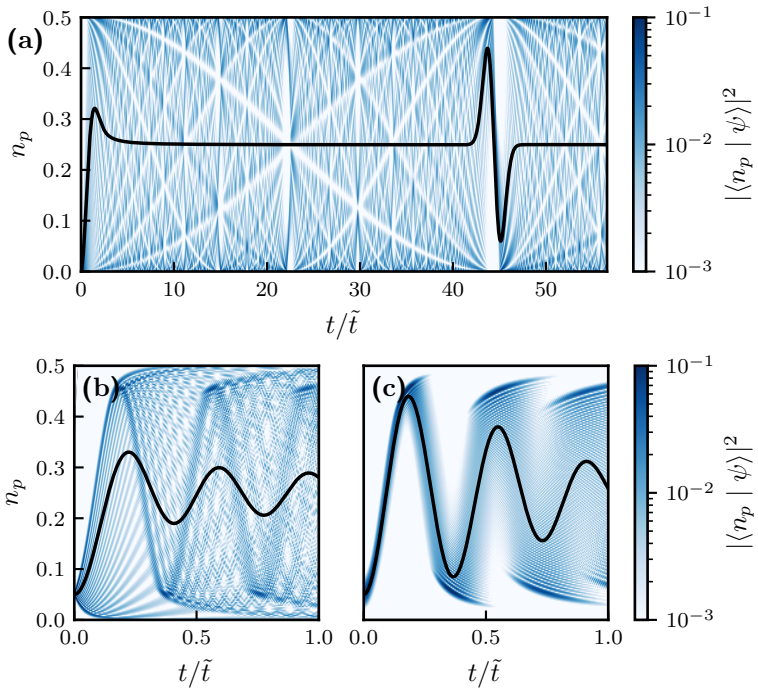

Figure 7.3 – Quantum carpet plots of the spin pair number in a gas of $N = 400$ atoms following a sudden quench to $q/U = 0$. (a) Long time evolution of an initial state $|0\rangle^{\otimes N}$ showing the delocalization of n_p over the subspace of the dynamics, interrupted by a quantum revival. The full line indicates the expectation value $\langle n_p \rangle$. (b-c) Comparison of the time evolution of an initial pair number state (b) and a pair coherent state (c), both containing an initial number of spin pairs $N_{\text{seed}}/N = 0.05$.

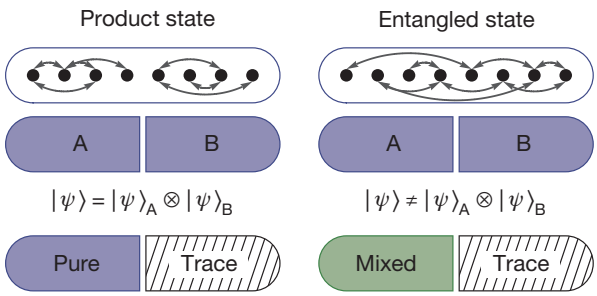

Figure 7.4 – Quantum states of a system are said to be separable if they can be written as a factorized product state. Tracing out one subsystem then leaves the other described by a pure state. Entangled states, on the other hand, are characterized by inseparability, leading to a mixed reduced density matrix of a constituent subsystem. Figure taken from [255].

7.2.2 Particle entanglement

Large fluctuations in the pair number statistics, witnessed in both the exact solution (Fig. 7.3) and the Gaussian approximation (Fig. 7.2), are related to the growth of *entanglement* [254], a distinctive feature of quantum systems. At its core, entanglement amounts to *inseparability*, intricate correlations within a quantum system which make it impossible to view the total state of the system as a factorized *product state* of its constituent subsystems [129]. As depicted in Fig. 7.4, inseparability of a pure quantum state implies that the reduced state of a constituent subsystem appears as a classical mixture upon tracing away the remainder of the system*. The entanglement discussed in the present context is *particle entanglement* [256, 257], related to correlations between the identical bosons in the fluid. In first quantization, it means that the many-body state $|\Psi\rangle$ cannot be factorized into wave functions pertaining to the N individual particles,

$$|\Psi\rangle \neq |\psi_1\rangle \otimes |\psi_2\rangle \otimes \cdots \otimes |\psi_N\rangle \,. \tag{7.11}$$

A similar but distinct form of entanglement is the more common *mode entanglement* [256]. In the second quantization picture, the spin-1 fluid consists of three modes $\hat{a}_+$, $\hat{a}_0$, $\hat{a}_-$. Mode inseparability of a many-body state then implies that it cannot be factorized as $|\phi_+\rangle \otimes |\phi_0\rangle \otimes |\phi_-\rangle$, with $|\phi_i\rangle$ a set of states pertaining to mode i.

* For example, recall from Sec. 3.6.1 that taking the trace over the environment degrees of freedom is what requires an open quantum system to be described by a density matrix, which is mixed precisely due to the entanglement between the system and its surroundings.

7.2.3 Single-particle density matrix

In the spin-1 fluid, particle entanglement manifests itself in the fact that the single-particle reduced density matrix, defined as

$$\rho_1^{(n,m)} = \langle \hat{a}_n^\dagger \hat{a}_m \rangle / N, \tag{7.12}$$

appears as a classical mixture, even as the fluid is in a pure many-body state*. The *mixedness* of the single-particle density matrix can be quantified by its *purity*, defined as $\mathrm{Tr}[\rho_1^2]$. As its name implies, the purity is maximized for a pure state, which by its definition $\hat{\rho}^2 = \hat{\rho}$ and normalization $\mathrm{Tr}[\hat{\rho}] = 1$ has a purity of 1. States with $\mathrm{Tr}[\hat{\rho}^2] < 1$ are said to be mixed, while the minimal purity attainable by a d-dimensional density matrix is $\mathrm{Tr}[\hat{\rho}^2] = 1/d$. For the single-particle density matrix ρ_1 of interest here, a purity $\mathrm{Tr}[\rho_1^2] < 1$ thus signals a correlation to the rest of the system which can be of both classical or quantum nature.

To evaluate the purity of $\hat{\rho}_1$, note that its form is readily deduced in the exact solution restricted to the pair number subspace $\mathscr{H}_p$. Indeed, for any state $|\psi\rangle \in \mathscr{H}_p$, the state $\hat{a}_n^\dagger \hat{a}_{m\neq n} |\psi\rangle$ is a superposition of strictly non pair number states, since the number of particles in the $|+\rangle$ and $|-\rangle$ orbitals are no longer equal. This renders the matrix element $\langle\psi|\hat{a}_n^\dagger \hat{a}_{m\neq n}|\psi\rangle = 0$ due to the orthogonality of Fock states, therefore simplifying the single-particle density matrix in the basis $(|+1\rangle, |0\rangle, |-1\rangle)^T$ to the diagonal form

$$\rho_1 = \begin{pmatrix} n_p & 0 & 0 \\ 0 & 1-2n_p & 0 \\ 0 & 0 & n_p \end{pmatrix}. \tag{7.13}$$

Like ρ_1 itself, the purity of any state in the pair number subspace is then fully determined by n_p,

$$\mathrm{Tr}\left[\rho_1^2\right] = 1 - n_p(4 - 6n_p). \tag{7.14}$$

Its dependence on n_p is shown in Fig. 7.5. The ground state configuration for $q/U = 0$ minimizes the purity and is correspondingly the maximally entangled state of the spin-1 fluid, while the steady state of a $|0\rangle^{\otimes N}$ state rapidly quenched to $q/U = 0$ lies slightly above this lower bound.

* Note that mixedness of the single-particle reduced density matrix does not *necessarily* originate from particle entanglement. Unequivocal observation of particle entanglement requires the use of many-body observables such as spin squeezing [256, 258, 259].

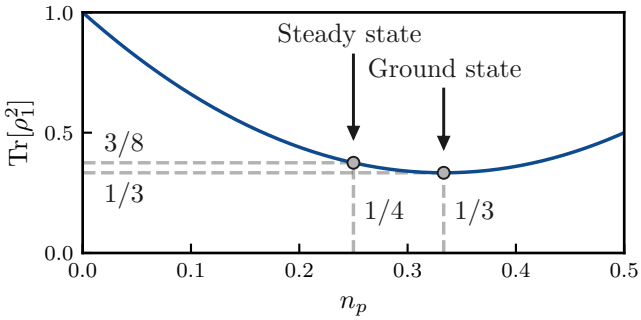

Figure 7.5 – Purity of the single-particle reduced density matrix ρ_1 as a function of the pair number $n_p = \langle \hat{a}_\pm^\dagger \hat{a}_\pm \rangle$ for any state in the subspace spanned by pair number states. Indicated are the ground state and steady state for $q/U = 0$.

7.2.4 Fragmented condensation

The diagonal nature of the single-particle reduced density matrix has a striking consequence for the nature of the condensate. Following the Penrose-Onsager criterion for Bose-Einstein condensation in interacting systems [25], a condensate is said to appear when a single eigenvalue of this density matrix becomes macroscopic, i.e., of the order of 1. As seen in Sec. 6.4, the ground state of the spin-1 gas for $q/U = 0$ contains $n_p = 1/3$ spin pairs. From the above prescription (7.13), however, this implies a density matrix of the form $\rho_1 = \mathrm{diag}(1/3, 1/3, 1/3)$, containing three equally macroscopic eigenvalues. A similar situation arises for the steady state following a quench to $q/U \to 0$, where the pair number $n_p = 1/4$ implies $\rho_1 = \mathrm{diag}(1/4, 1/2, 1/4)$. A many-body state in which multiple single-particle orbitals are macroscopically populated is an instance of *fragmented condensation* [260, 261]. First described by Nozières and Saint James in 1982 [262], this situation arises when the single-particle ground state is degenerate and symmetries of the Hamiltonian prohibit the formation of a single condensate in a superposition of these states [261, 263]. In the spin-1 gas, the former condition is met in the interaction-dominated regime $q/U \to 0$, while the latter results from the conservation of magnetization, as reflected in the necessarily diagonal nature of ρ_1. Recent experiments on a gas of antiferromagnetic ^{23}Na atoms in a single-mode confinement have confirmed the fragmented nature of the steady state following an adiabatic quench to spin degeneracy [263], reproduced in Fig. 7.6(a) alongside its eigenspectrum. By contrast, a comparable mean pair number n_p can be achieved by preparing the gas in a coherent superposition $(|-1\rangle + \sqrt{2}\,|0\rangle - |+1\rangle)^{\otimes N}$. Shown in Fig. 7.6(b), diagonalization of this density matrix results in a single macroscopic eigenvalue.

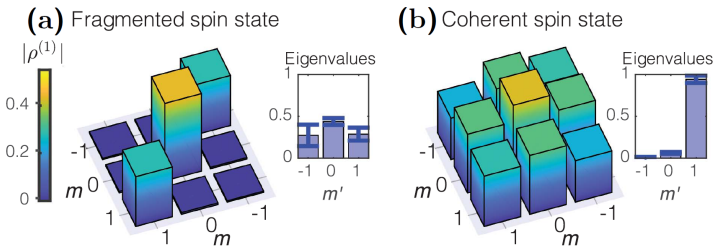

Figure 7.6 – Single-particle reduced density matrix of a single-mode spin-1 gas in a fragmented (a) and single condensate (b), as measured by Evrard *et al.* [263]. Figure adapted from [263].

7.3 A Gaussian trajectory approach

In Sec. 7.1 we have seen how the Gaussian approximation fails to capture relaxation of spin mixing dynamics in the interaction-dominated regime. A closer inspection of the exact dynamics in Sec. 7.2 has subsequently shown that large fluctuations hindering the Gaussian theory ultimately stem from the formation of a fragmented condensate. To mitigate these limitations, we will follow the reasoning developed in Chapters 4 and 5 and extend the Gaussian theory to a Gaussian trajectory approach (GTA), introducing dissipation into a virtual environment to suppress fluctuations. We will see how this adaptation allows to capture damped spin mixing dynamics and the evolution to a fragmented condensate.

Considering single-particle losses ($\hat{\Gamma}_m = \sqrt{\gamma}\hat{a}_m$) under heterodyne unraveling of the Lindblad master equation, the time evolution of an expectation value in a single trajectory is given by Eq. (5.2). As was the case for the Bose-Hubbard model in Chapter 5, the coupling to the external environment γ is an artificially introduced parameter and no physical property of the system. Referring to Appendix A for the full set of equations, the effect of single-particle losses on the time evolution of Gaussian moments can again be summarized in their effect on the average occupations $\langle|\phi_m|^2\rangle$ and $\langle\hat{\delta}_m^\dagger\hat{\delta}_m\rangle$ in the coherent wave functions and fluctuation modes,

$$\overline{\mathcal{D}_-(|\phi_m|^2)} = -\gamma\left[|\phi_m|^2 - \sum_n \left(|\langle\hat{\delta}_m\hat{\delta}_n\rangle|^2 + |\langle\hat{\delta}_m^\dagger\hat{\delta}_n\rangle|^2\right)\right]\mathrm{d}t, \tag{7.15}$$

$$\mathcal{D}_-(\langle\hat{\delta}_m^\dagger\hat{\delta}_m\rangle) = -\gamma\left[\langle\hat{\delta}_m^\dagger\hat{\delta}_m\rangle + \sum_n \left(|\langle\hat{\delta}_m\hat{\delta}_n\rangle|^2 + |\langle\hat{\delta}_m^\dagger\hat{\delta}_n\rangle|^2\right)\right]\mathrm{d}t. \tag{7.16}$$

While the first contribution to the above equations is the expected exponential decay of particles at a characteristic rate γ, additional terms arise from the stochastic contribution to the heterodyne equation (5.2). This latter contribution leads to additional decay of fluctuation modes, simultaneously compensated by a stochastic growth of the condensate wave functions. As motivated in Chapter 4, coupling the system to a virtual environment thus effectively converts quantum into classical fluctuations. The reduction of fluctuations at the expense of introducing a classical mixture allows one to form a composite Gaussian approximation of a single highly non-Gaussian many-body state.

Employing the two-step dynamics described in Sec. 5.4, we allow the isolated system to evolve undisturbed according to its Hamiltonian (6.2) until the total number of fluctuations $\Delta = \sum_m \langle \hat{\delta}_m^\dagger \hat{\delta}_m \rangle$ reaches an upper critical value Δ_c. The Hamiltonian evolution is then halted, after which the system is evolved at instantaneous time according to the dissipative part of the dynamics until fluctuations are suppressed below $\Delta_s = \Delta_\mathrm{c}/2$. The main advantage of this particular two-step procedure is that the dissipation rate evolves adaptively during the time evolution of the system, according to the growth of fluctuations at any given time. As seen from the first terms in (7.15) and (7.16), the added dissipation breaks the conservation of particle number and angular momentum $\langle \hat{S}_z \rangle$. In the dissipation scheme, this deviation is corrected by a rescaling of the amplitudes $|\phi_m|$ to enforce $|\phi_+| = |\phi_-|$ and $\sum_m (|\phi_m|^2 + \langle \hat{\delta}_m^\dagger \hat{\delta}_m \rangle) = N$ following each dissipation step, projecting the evolved state back onto the pair number space before Hamiltonian time evolution resumes.

7.4 Dynamics of fragmentation

7.4.1 Relaxation of the pair number

Fig. 7.7(a) shows the evolution of the number of spin pairs after an instantaneous quench of an initial $|0\rangle^{\otimes N}$ state into the interaction-dominated regime $q/U = 0$, where both the exact solution and experimental results [234] reveal a rapid relaxation to the fragmented state. While the Gaussian HFB approximation (black dashed line) accurately predicts the onset of spin mixing, it fails to reproduce the eventual relaxation, instead predicting perpetual oscillations of the pair number. For comparison, we show in grey the same HFB result for an inifinitesimal seeding $n_p^{(0)} = 5 \times 10^{-5}$, illustrating the sensitivity of the HFB result to the initial conditions of the gas. The Gaussian trajectory method eliminates this instability as the introduction of classical mixedness provides a natural ensemble average. Its results are shown in blue for different values of the critical fluctuation amp-

litude Δ_c. Both the early growth of spin pairs and the eventual final state appear robust with respect to the chosen value of Δ_c, its effect being most pronounced where the pair number reaches its maximum. In this intermediate regime, we find that a value of $\Delta_c \approx 15$ best replicates the exact result when fluctuations are suppressed to $\Delta_s = \Delta_c/2$ in each dissipation step. For this simulation, the exact result is indistinguishable from a truncated Wigner approximation (see Secs. 3.4 and 6.3.1).

The same quench scenario is shown in Fig. 7.7(b) for a coherently seeded initial state, where a fraction $n_p^{(0)} = 0.017$ of the atoms are prepared as spin pairs, activating the coupled mean field equations in the Gaussian theory. The seeded time evolution is marked by a longer persistence of oscillations, captured by the Gaussian approximation at early times. At intermediate times, the TWA prediction slightly underestimates the damping rate of oscillations. We find that the Gaussian trajectory result optimally replicates the relaxation dynamics for $\Delta_c \leq 1$. Below this value, the result is independent on Δ_c, while a larger Δ_c causes an overestimation of the oscillation amplitude. In the optimal regime, the Gaussian trajectory approach slightly outperforms the TWA prediction for intermediate times.

Finally, at high seeding $n_p^{(0)} = 0.075$, shown in Fig. 7.7(c), increasingly slow damping of spin pair oscillations indicates the crossover from dynamics driven by spontaneous scattering to highly coherent spin mixing, driven primarily by the stimulated dynamics of the condensate modes captured by the Gross-Pitaevskii equations (6.15). In this regime, limited growth of fluctuations hinders also their conversion into classical uncertainty in the Gaussian trajectory approach, as even a fluctuations tolerance $\Delta_c = 1$ of a single spin pair leads to an underestimation of the damping rate. In contrast to the qualitatively similar spin oscillations in the Zeeman-dominated regime of large q/U – well reproduced by Bogoliubov theory and thus by a Gaussian approximation – the interaction-dominated regime with large seeding thus constitutes a range in which neither the Gaussian approximation nor its trajectory extension provides an efficient description of spin mixing dynamics.

7.4.2 Entanglement growth

Our initial objective motivating the introduction of quantum trajectories was to obtain an approximate representation of a single, highly entangled state as a classical mixture of weakly entangled states. As the quenched fluid evolves to a fragmented steady state, entanglement and the associated growth of fluctuations

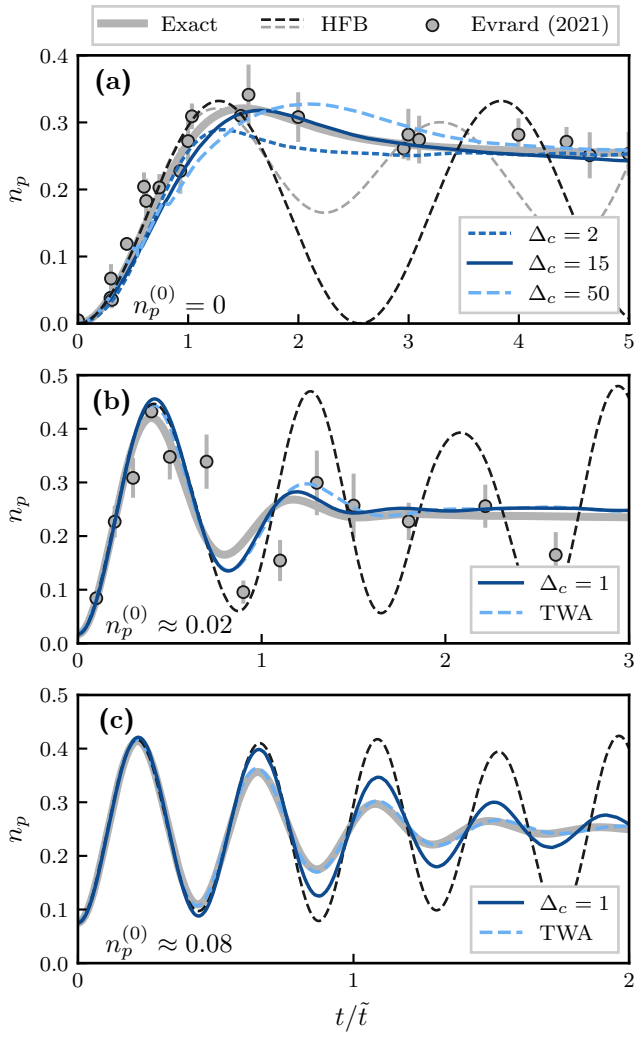

Figure 7.7 – Rapid relaxation of the pair number in the interaction-dominated regime ($q/U = 0$), showing the improvement of the variational description due to the added dissipation. Results are shown for a gas of $N = 200$ atoms initiated in the $|0\rangle^{\otimes N}$ state with initial spin pairs $n_p^{(0)} = 0$ (a), $n_p^{(0)} \approx 0.02$ (b) and $n_p^{(0)} \approx 0.08$ (c). The grey dashed line in (a) represents the Gaussian result for $n_p^{(0)} = 5 \times 10^{-5}$, illustrating its sensitivity to initial conditions. Both Gaussian trajectory and TWA results represent the average over 10^4 realizations, rendering the statistical error smaller than the width of plotted lines. Experimental data were provided by the authors of Refs. [234, 240].

is witnessed in a rapid decrease in purity of the single-particle reduced density matrix (see Sec. 7.2.3), shown in Fig. 7.8(a). The steady state value 3/8 reproduced by the trajectory average corresponds to the fragmented condensate with relative populations (1/4, 1/2, 1/4). By contrast, the frequent suppression of Gaussian fluctuations in the trajectory approach – shown as the sharp vertical jumps – enhances the purity within a single trajectory, evidencing the reduction of entanglement in each state comprising the classical mixture. For this Figure, the lower threshold of fluctuations Δ_s was set to $\Delta_c/10$ as opposed to $\Delta_c/2$ used in the rest of the work, to graphically emphasize the suppression of fluctuations at each dissipation step.

Note that the Gaussian trajectory *average* corresponds to an actual mixture of variational states. The mixedness of the reduced density matrix is affected by this classical uncertainty and is therefore no longer a direct measure of particle entanglement. However, the agreement between the purity in the trajectory average and exact solution testifies to the conservation of total (classical and quantum) fluctuations by the trajectory approach, as illustrated in Fig. 4.5.

The generation of entanglement during the formation of the fragmented condensate is also witnessed in the effective dissipation rate γ_{eff} of the employed two-step dynamics, as introduced in Sec. 5.4.1. Since the adaptive dissipation procedure described in Sec. 7.3 suppresses fluctuations below an upper critical value Δ_c, the effective dissipation strength may vary throughout a single trajectory, as the generation of fluctuations does not necessarily occur at a constant rate. To illustrate this, we show in Fig. 7.8(b) the average effective dissipation rate throughout the dynamics of Fig. 7.7(a), derived by relating the number of instantaneous dissipation steps to the duration of unitary evolution preceding it. At early times, fluctuations grow rapidly and a high dissipation rate is required to suppress the generated entanglement through frequent stochastic jumps. At late times the procedure evolves towards a lower dissipation rate as fluctuations saturate in the fragmented state. Due to the variable generation of entanglement, a constant continuous dissipation rate as initially described in Chapter 5 does not capture the fragmentation dynamics as well as the two-step method with explicitly constrained fluctuations.

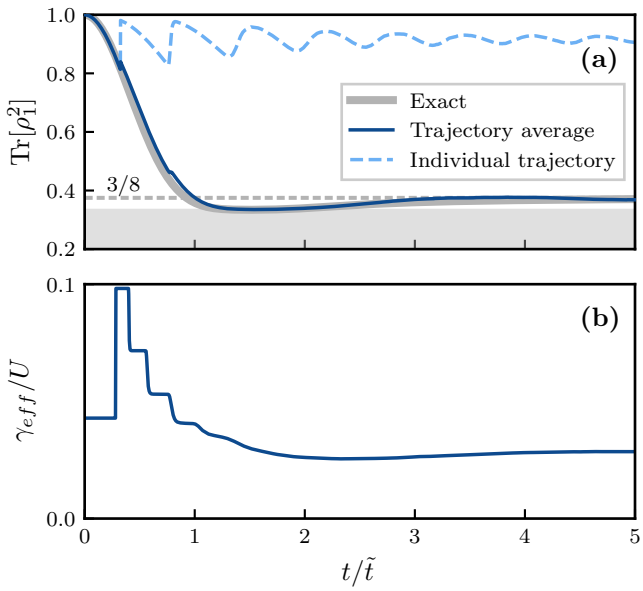

Figure 7.8 – Growth of entanglement during the dynamics of Fig. 7.7(a). (a) Evolution of the single-particle reduced density matrix's purity. The sudden jumps in the purity of individual trajectories correspond to instantaneous dissipation steps. To emphasize the suppression of fluctuations, the result is shown for $\Delta_s = \Delta_c/10$, leading to an optimal critical value of $\Delta_c = 20$. The grey shaded region indicates the minimal purity $\mathrm{Tr}\left[\rho_1^2\right] = 1/3$, corresponding to the ground state. The dashed line represents the steady state of relative populations $(n_+, n_0, n_-) = (1/4, 1/2, 1/4)$. (b) Effective dissipation rate γ_{eff} inferred from the Gaussian trajectory result. The discrete nature at early times is a consequence of relatively long Hamiltonian evolution followed by a single dissipation step, resulting in a finite resolution for $\gamma_{\mathrm{eff}}(t)$.

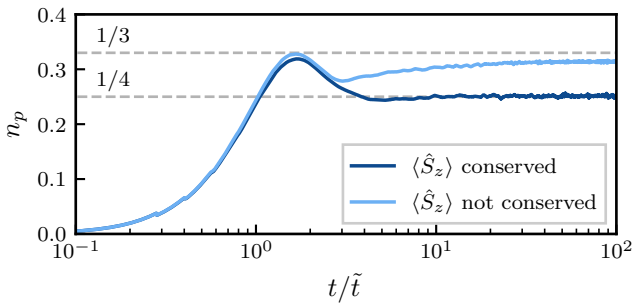

Figure 7.9 – Long time simulation of the relaxation pictured in Fig. 7.7(a), showing the effect of $\langle \hat{S}_z \rangle$ conservation within single trajectories.

7.4.3 Conservation of magnetization

As mentioned in Sec. 7.1.1, the steady state pair number $\overline{n}_p = 1/4$ in the fragmented condensate is a consequence of $\langle \hat{S}_z \rangle$ conservation which inhibits the system from reaching thermal equilibrium [234]. In the trajectory simulation of the isolated gas, this conservation law is fixed by restoring $|\phi_+| = |\phi_-|$ after each stochastic dissipation step. To study the role of $\langle \hat{S}_z \rangle$ conservation in more detail, we repeat the simulation of Fig. 7.7(a), this time loosening the conservation law on $\langle \hat{S}_z \rangle$ by omitting the above mentioned projection step. While $\langle \hat{S}_z \rangle = 0$ remains true on average, individual stochastic realizations may deviate to allow states with $\langle \hat{S}_z \rangle \neq 0$ to enter the ensemble. As shown in Fig. 7.9, the correct steady state value $\overline{n}_p = 1/4$ is recovered only when $\langle \hat{S}_z \rangle$ is conserved at the level of individual trajectories. The breaking of $\langle \hat{S}_z \rangle$ conservation within trajectories instead causes the pair number to converge towards the equilibrium value $\overline{n}_p = 1/3$. Concerning the dynamics of the isolated system, we thus conclude that the artificial dissipation in each individual Gaussian trajectory must reflect all symmetries of the Hamiltonian and preserve their associated conserved quantities. In Chapter 8 we will revisit this seemingly technical point in the context of a dissipative spinor condensate, where the breaking of $\langle \hat{S}_z \rangle$ conservation becomes a physical reality and causes the system thermalize.

7.5 Summary

In this chapter, we have studied spin mixing dynamics in a single-mode spin-1 fluid following a quench of the Zeeman splitting between hyperfine states. In the regime dominated by nonlinear interactions ($U \gg q$), we have seen how both a Bogoliubov approach of linearized spin fluctuations and a Gaussian approximation of the fields $\hat{a}_m$ are unable to capture relaxation of the number of spin pairs. While the latter is suited to represent states with a macroscopic number of spin pairs, the growth of linear fluctuations prevents the variational dynamics from relaxing to the correct steady state.

A closer inspection of the exact solution of the many-body Schrödinger equation has revealed the growth of fluctuations to be a consequence of entanglement growth as the system evolves to a fragmented condensate. Employing the Gaussian trajectory approach developed in Part II, we have extended the validity of the Gaussian variational Ansatz to the strongly interacting regime, and succeeded in describing relaxation of the quenched fluid to a state of fragmented condensation. From the two-step dynamics of unitary evolution interrupted by instantaneous dissipation steps, an effective artificial dissipation strength was inferred, and found to be directly proportional to the rate of entanglement growth at any point in the time evolution.

Finally, we studied the role of conservation laws in the spin mixing dynamics, and found that enforcing both conservation of particle number and magnetization at the level of individual trajectories is a crucial prerequisite for reproducing relaxation to the fragmented steady state. By contrast, when states of finite magnetization enter the classical mixture, the Gaussian trajectory approach incorrectly predicts the system to evolve to thermal equilibrium. In the following chapter, this observation will be the starting point for studying a dissipative spinor condensate, where the loss of particles to the environment causes a natural breaking of integrability.

8 | Equilibration of a dissipative spin-1 fluid

The results presented in this chapter are part of a manuscript under preparation*:

Integrability breaking in dissipative and multimode spinor condensates
L. Fernandes & M. Wouters

In Chapter 7 we have shown how the evolution of an isolated spin-1 fluid to a fragmented steady state can be captured with Gaussian variational states in a virtual environment, decomposing quantum fluctuations reflecting entanglement growth into classical uncertainty of a mixed ensemble. However, we have been concerned solely with developing an approximate representation of a system which is in reality isolated and governed by *integrable dynamics*. That is, its evolution was constrained by conservation of energy, particle number and magnetization, reducing the dimension of the Hilbert space to $N/2$. In Sec. 7.4.3, we have seen how a strict enforcement of both conservation laws at the trajectory level is required in order to find the correct steady state. In this final chapter on the spin-1 gas, we will investigate the implications of these findings for a dissipative condensate, where stochastic interactions with an actual environment naturally lead to a breaking of integrability.

* Working title.

8.1 Dissipation and integrability breaking

8.1.1 Aim of this chapter

The distribution of particles among spin states in the steady state of Chapter 7 hinged crucially on the symmetry of the isolated system. In particular, conservation of $\hat{S}_z$ – enforced by the pairwise creation of atoms in the $|\pm\rangle$ states – resulted in a relaxation to a generalized Gibbs ensemble with $\bar{n}_p = 1/4$ spin pairs rather than the equilibrium distribution with $\bar{n}_p^{eq} = 1/3$.

In the presence of an external environment, $\hat{S}_z$ conservation is naturally broken by incoherent dissipation processes. Indeed, as atoms from each spin state stochastically and independently leak from the fluid, the system is forced to leave the highly symmetrical pair number subspace $\mathscr{H}_p$ and instead explore a larger region of its full Hilbert space. Dissipation thus constitutes a source of *integrability breaking*, the loss of a constraint previously preventing the fluid from thermalizing [100]. Consequently, the system is free to evolve to its equilibrium spin distribution, raising the question whether – and in which way – the fragmentation dynamics of Chapter 7 are altered by the presence of an external environment.

While experimental results on the single-mode spin-1 fluid are well approximated by the assumption of perfect isolation, its dynamics have so far only been explored at early times [234, 240]. Besides the presumable destruction of quantum revivals due to their extreme sensitivity to decoherence (see Sec. 7.2.1), the role of environmental noise on the late time dynamics has not yet been explored. Note that all results presented in the remainder of this chapter rely on the explicit breaking of $\hat{S}_z$ conservation by single-atom losses. Incoherent processes obeying this conservation law (e.g., the stochastic creation or annihilation of spin pairs) are not expected to induce a similar breaking of integrability.

8.1.2 Dissipative equilibration

Integrability breaking and the ensuing equilibration of a many-body quantum system is a broadly studied topic, which has hence amassed a well-defined nomenclature. At the start of this chapter, it is therefore useful to clarify the type of equilibration which occurs in the late time dynamics of the dissipative system.

Integrability breaking is generally considered synonymous with *thermalization*, understood as the emergence of a Gibbs ensemble in an isolated quantum system

in the absence of additional conservation laws [100, 101]. In a dissipative system, by contrast, particles are continuously lost, rendering its final state inevitably and trivially fully depleted. Nevertheless, the internal spin degree of freedom allows us to consider at finite times the relaxation of the *relative* spin populations, regardless of the total number of atoms left in the fluid*. Rather than thermalization in its strict sense, we will therefore define *dissipative equilibration* more generally as the emergence of a distribution among spin states compatible with the equilibrium state of the spin-1 fluid.

In relation to thermalization, one could view this situation as the equilibration to a grand canonical ensemble given by a distribution over microscopic states of the form

$$P(E) \sim \exp\left\{-\frac{E-\mu(t)N}{k_{\mathrm{B}}T(t)}\right\}, \tag{8.1}$$

where the slowly time-varying chemical potential $\mu(t)$ and temeprature T account for depletion of the fluid. This approach has been adopted to study similar equilibration dynamics in a one-dimensional Bose gas described by the Lieb-Liniger model [264].

8.1.3 The dissipative spin-1 fluid

In principle, the exact solution outlined in Sec. 6.2 can be adapted to account for single-particle losses. However, as dissipation breaks both the conservation of particle number and magnetization, the accessible region of the Hilbert space quickly grows beyond computational feasibility. Conversely, the developed trajectory method is readily extended to a dissipative system without additional computational complexity by including the dissipator $\mathcal{D}_-$ in the time evolution of the Gaussian observables and omitting the projection steps which previously fixed the total particle number and angular momentum $\langle \hat{S}_z \rangle$. The resulting equations of motion (5.2) governing the Gaussian moments then describe a single-mode spin-1 fluid of N particles with quadratic Zeeman splitting q and interaction strength U, dissipating atoms into the environment at rate γ which are measured through heterodyne detection.

A similarly straightforward implementation can be performed in the truncated Wigner approximation. As explained in Sec. 3.6.4, its extension to a dissipative system in practice amounts to supplementing the coupled Gross-Pitaevskii

* Note that this does *not* correspond to a driven-dissipative system. There, the interplay between unitary dynamics, particle losses and (in)coherent pumping may result in the emergence of a nonequilibrium steady state fundamentally different from a thermalized closed system [146].

equations (6.15) governing the evolution of each stochastically sampled initial condition with

$$\frac{\mathrm{d}\phi_m}{\mathrm{d}t} \sim -\frac{\gamma}{2}\phi_m + \sqrt{\frac{\gamma}{2}}\mathrm{d}Z_m, \tag{8.2}$$

with $\mathrm{d}Z_m$ uncorrelated complex Gaussian noise satisfying $\langle \mathrm{d}Z_m^* \mathrm{d}Z_{m'} \rangle = \delta_{m,m'}\mathrm{d}t$.

8.1.4 Weak and strong dissipation regimes

With the exact solution no longer a viable option for benchmarking, more care must be taken in evaluating the validity regime of approximate approaches. To do so, we distinguish between a regime of weak coupling to the environment ($\gamma/U \ll 1$) and a strongly dissipative regime ($\gamma/U \gg 1$).

As we have seen in Sec. 7.1, results obtained using the Gaussian trajectory approach are unreliable in the limit $\gamma \to 0$. Indeed, it was precisely the addition of a non-negligible (artificial) dissipation which was needed for the Gaussian method to capture relaxation of the isolated fluid. This limitation could in principle be overcome by introducing two separate dissipation mechanisms; one coupling term γ_1 to an artificial environment, serving only to convert fluctuations into classical mixedness, and one term γ_2 describing the coupling to the true environment. While γ_1 is tuned to maximally approach the transient dynamics of the exact solution, arbitrarily small values of the true dissipation γ_2 can be studied. However, the absence of a reliable benchmark and the dependence of early time dynamics on the strength of artificial dissipation (see e.g. Fig. 7.7) makes it difficult to assess the accuracy of results. A more elegant solution is instead provided by the truncated Wigner approximation (TWA), the validity of which in the weakly dissipative regime is evidenced by its excellent reliability in the limit of vanishing γ (see again Fig. 7.7).

While the limit of weak dissipation can be accessed through the truncated Wigner approximation but not with Gaussian trajectories, the opposite is true in the strongly dissipative regime. There, rapid depletion of particles causes the system to stray further from the mean field limit during time evolution. Since the TWA takes fluctuations into account as stochastic noise to a mean field description, it becomes unreliable when the occupation of modes no longer dominates the vacuum noise, as quantified in the validity condition (3.30). By contrast, the validity of the Gaussian theory in the presence of strong dissipation is ensured by the fact that dynamics in this regime are dominated by linear contributions. Similarly to the isolated fluid in the high-Zeeman regime $q/U \gg 1$, its dissipative counterpart becomes approximately non-interacting in the limit $\gamma/U \gg 1$, rendering corrections to the Gaussian dynamics negligible.

8.2 Weak integrability breaking

We first turn our attention to the weakly dissipative regime. While the stochastic nature of any infinitesimal coupling to the external environment causes a breaking of $\hat{S}_z$ conservation, the experimental results plotted in Fig. 7.7 suggest that the system remains to good approximation described by the constrained dynamics of an isolated system. This raises the question as to how strong of a coupling is required to break the conservation of magnetization significantly enough to induce dissipative equilibration, or, conversely, how the dissipation rate is related to the time scale at which integrability breaking causes the system to depart from its nonequilibrium steady state.

8.2.1 Prethermalization

In an isolated quantum system, weak integrability breaking often results in *prethermalization* [265], whereby the system initially settles into a nonequilibrium steady state dictated by conservation of the unperturbed Hamiltonian, before evolving to equilibrium at a much longer time scale determined by the strength of the integrability-breaking perturbation [100, 266, 267].

We briefly encountered such a nonequilibrium steady state when discussing experimental progress on spinor condensates in Sec. 2.4.4. In Fig. 2.9, a quenched spinor fluid was found to reside for a long time in a *non-thermal fixed point* characterized by spatio-temporal scaling of spin correlations, before eventually departing to thermal equilibrium [99]. In a single-component Bose gas quenched to unitarity*, similar prethermalization was observed in the evolution of the momentum distribution to a nonequilibrium steady state on a universal timescale, before heating caused by three-body recombination breaks the condensate at late times [268]. In a weakly interacting Bose gas, more closely related to the present case, a quench of the interaction strength was predicted to result in a similar prethermalization of the momentum distribution [143]. After an initial relaxation driven by scattering of excited atoms with the condensate, weak integrability breaking due to Beliaev-Landau scattering between excited atoms was found to account for the eventual thermalization.

8.2.2 Equilibration of spin mixing

In the present setting, *pre-equilibration* is understood as the relaxation of the spin pair number to its $n_p = 1/4$ steady state, with the onset of true equilibration to

* In ultracold fluids, this is understood as the limit of infinite interaction strength, caused by a divergence of the s-wave scattering length [45].

$n_p = 1/3$ occuring at a later time scale. In Fig. 8.1(a) we show the long time evolution of the spin pair number in a dissipative fluid, initially prepared in the $|0\rangle^{\otimes N}$ state and quenched to spin degeneracy ($q/U = 0$) for several values of the dissipation strength γ. For coupling strengths up to $\gamma/U = 0.01$, significant deviation from the pre-equilibrated state is apparent only at time scales of the order $\sim 10^3\tilde{t}$, well beyond the reach of current experiments. The experimental data in Fig. 7.7 exhibit no sign of thermalization up to $5\tilde{t}$, suggesting that the system lies well into the weakly dissipative regime, $\gamma/U \ll 1$. As the dissipation rate increases, the lifetime of the steady state plateau decreases, showing a clear crossover to dissipative equilibration within numerically accessible times. As shown in Fig. 8.1(b), this crossover is accompanied by a maximal fragmentation of the fluid, as the purity of the single-particle density matrix converges to the lower bound $1/d$ set by the dimension $d = 3$ of the spin manifold, as previously argued in Sec. 7.2.3. Finally, for γ comparable to U, the steady state plateau is no longer discernible, as strong integrability breaking causes the fluid to evolve rapidly to its equilibrium state. Note that in this limit, fluctuations in the TWA result are amplified as the gas approaches depletion before spin mixing has relaxed. Breaking the validity condition (3.30), the TWA dynamics are reduced to predominantly stochastic noise, requiring a prohibitive number of samples to infer the long-time evolution. For this reason, results in Fig. 8.1 are truncated at the time scale where noise begins to dominate the TWA result. As anticipated in Sec. 8.1.4, the truncated Wigner approximation therefore does not provide access to the high-loss regime, where rapid depletion of the fluid occurs on the same time scale as pre-equilibration to the fragmented steady state.

Before employing the Gaussian trajectory approach to explore the high-loss regime, we determine the characteristic time scale of the crossover from the steady state plateau to equilibration of the dissipative fluid. Figure 8.2(a) shows the evolution of the pair number identically to Fig. 8.1 but rescaled to the time scale set by the dissipation strength. From this depiction it is clear that dissipative equilibration occurs on a time scale of the order $t_{\mathrm{therm}} = \hbar/\gamma$, irrespective of the time scale $\tilde{t} = \hbar/(U\sqrt{2N})$ at which interactions induce relaxation to the steady state plateau. Lastly, dissipative equilibration is shown in Fig. 8.2(b) for a range of particle numbers initially present in the system, showing that departure from the prethermal state occurs at a universal time scale independent of the system size*. This result does not come unexpected, as the Lindblad operator $\sqrt{\gamma}\hat{a}_m$ (in

* Note that the fraction of the initial number of atoms still present in the system at any time t is given by $\exp\{-\gamma t/\hbar\}$. As such, the fluid of initally $N = 40$ atoms contains on average fewer than a single atom beyond times $\gamma t/\hbar \approx 4$, limiting the relevance of these numerical results in the long-time limit.

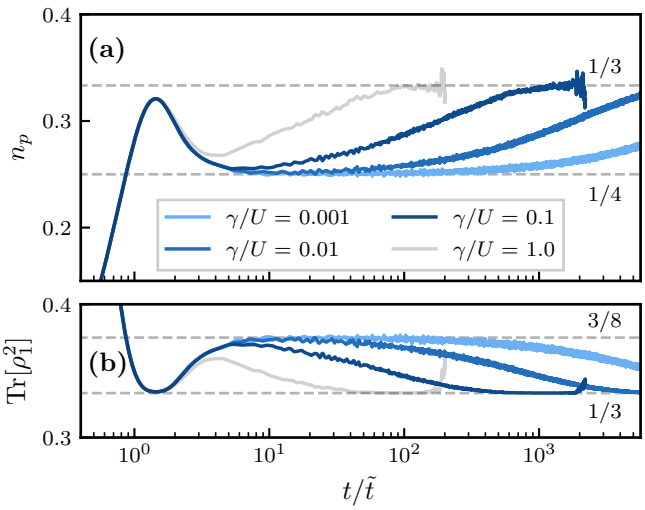

Figure 8.1 – Long time spin dynamics in a spin-1 fluid of $N = 400$ atoms dissipating into its environment with coupling strength γ. Results shown are the average of 3×10^4 TWA realizations. (a) Dissipation-induced integrability breaking causes the system to eventually leave its nonequilibrium steady state for any nonzero γ. (b) Single-particle purity growth during equilibration.

contrast to the interaction terms of the Hamiltonian) represents a single-particle process, the effect of which does not scale with the amplitude of the collective matter field. Relative to the relaxation time scale $\tilde{t}$, the lifetime of the steady state plateau thus scales as $U\sqrt{2N}/\gamma$, which is maximized in large systems weakly coupled to their surroundings.

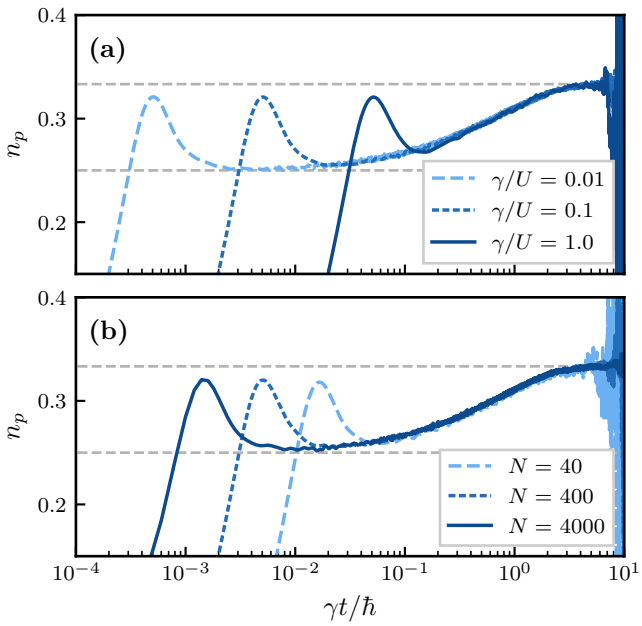

Figure 8.2 – Universal time scale of dissipative equilibration. Note the rescaling of the time axis to the characteristic time scale $\hbar/\gamma$ instead of the usual $\tilde{t} = \hbar/(U\sqrt{2N})$. Results shown are the average of 3×10^4 TWA realizations. (a) Long-time spin mixing dynamics at different dissipation strengths γ. (b) Independence of equilibration time on the particle number.

8.3 Gaussian trajectories in the high-loss regime

The truncated Wigner approximation is unable to access the high-loss regime, where rapid depletion of the fluid (containing only $10^2 - 10^3$ atoms) occurs on a time scale shorter than the relaxation time of spin mixing interactions. Dominated by linear contributions to the dynamics, this regime is well within the validity range of the Gaussian approximation*.

In Fig. 8.3(a) we simulate the time evolution of the spin pair number in the Gaussian trajectory approach for several values of the dissipation strength. In contrast to the TWA, the GTA description with finite constant dissipation does not converge to the correct dynamics of the isolated system in the limit $\gamma \to 0$, instead dramatically overestimating oscillations at early times. This limitation is expected, as it was precisely the invalidity of the unitary Gaussian theory which led us to introduce finite artificial dissipation in the description of the isolated fluid. Nevertheless, the late time evolution to the thermal state $\bar{n}_p = 1/3$ remains in agreement with the TWA result. In the strong coupling regime ($\gamma/U \gg 1$), where the GTA is expected to provide reliable results, strong integrability breaking eliminates the pre-equilibrated plateau from the dynamics, reducing the evolution to a monotonic increase towards the equilibrated state.

As seen from the Figure, the late time convergence to $\bar{n}_p^{\mathrm{eq}} = 1/3$ is insensitive to the dissipation rate (within the GTA's validity range) up to $\gamma/U \approx \sqrt{2N}$, as the internal dynamics are weakly affected by atom losses. For $\gamma/U \gtrsim \sqrt{2N}$, however, the number of spin pairs in the steady state decreases with γ. The steady state fraction of pairs $\bar{n}_p$ is shown in Fig. 8.3(b), indicating that the two cases outlined above are separated by a cusp at $\gamma/U \approx \sqrt{2N}$, bearing resemblance to a *phase transition*. Furthermore, the overlapping results for different system sizes indicate the universal behaviour of this transition.

The exact value of the phase transition corresponds to the point at which the time scale $\tilde{t}$ (7.5) of interaction-driven relaxation and dissipation-induced equilibration ($t_{\mathrm{therm}} = \hbar/\gamma$) are equal. Recall from Sec. 8.2 that this is the same dissipation strength at which the prethermal plateau vanishes. Unsurprisingly, the dissipation strength at which integrability breaking occurs on the same time scale as relaxation, is thus precisely the same γ at which the interaction processes are significantly disturbed the coupling to the external environment.

* In the Lindblad equation (3.34), this can be understood from the fact that some of the dissipative terms may be included as imaginary contributions $\hat{\Gamma}_j^\dagger \hat{\Gamma}_j$ to an *effective Hamiltonian*. Single-particle losses $\hat{\Gamma}_j = \sqrt{\gamma}\hat{a}_j$ then result in Hamiltonian terms quadratic in the field operators, and are therefore exactly captured by the Gaussian approximation.

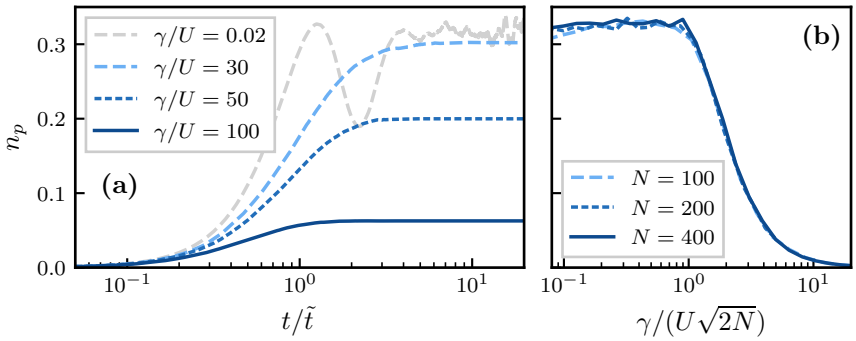

Figure 8.3 – Gaussian trajectory prediction of spin mixing dynamics in a dissipative spin-1 gas quenched to $q/U = 0$, for different values of the dissipation rate γ/U. (a) Relaxation of the pair number in a gas of initially $N = 400$ atoms. (b) Steady state pair fraction as a function of the ratio $\gamma/(U\sqrt{2N})$, coinciding for different system sizes.

However, recall from Eqs. (7.5) and (7.6) that this time scale is a factor $\sqrt{N/2}$ longer than that at which spin pairs are generated from the $|0\rangle^{\otimes N}$ initial state. As such, the sharp drop in the steady state spin distribution at a critical dissipation strength is no consequence of the early-time onset of spin mixing dynamics being inhibited by the depletion of the system. Rather, the suppression of spin mixing dynamics by losses can be understood as a manifestation of the *quantum Zeno effect* [269, 270], whereby the unitary evolution of a quantum state is inhibited by measurements occurring more frequently than the typical time scale of coherent processes. In the limit of strong dissipation, the fluid is therefore frozen in its initial spin pair vacuum. Similarly to this dissipative phase transition in a spin-1 condensate, the sharp onset of a quantum Zeno phase has been predicted in a quantum Ising chain subject to a continuous monitoring of its transverse magnetization [271].

8.3.1 Individual trajectories

Finally, we turn to the individual trajectories which, in the case of a dissipative system, correspond to experimental realizations of the dynamics. We have seen in previous chapters how dissipation decomposes the entangled pure state into a classical mixture of weakly entangled states. Following this reasoning, a single trajectory of a spin-1 fluid measured continuously through heterodyne detection should retain a high purity, in contrast to its ensemble average.

In order to track a single coherent trajectory, the dissipation strength should be weak enough to avoid significant depletion of the gas over experimentally relevant timescales (of the order $\tilde{t}$) or inhibit the onset of spin mixing as in Fig.

8.3. On the other hand, the dissipation strength should be sufficiently strong in order to suppress Gaussian fluctuations and recover a trajectory with a high condensate purity, as those comprising the mixture in Fig. 7.8. Fig. 8.4(a) illustrates this consideration by showing the average purity in a single trajectory for the same values of γ/U as in Fig. 8.3(a). While maintaining a high purity throughout the trajectory requires a sufficiently large dissipation strength, the decrease of the interaction energy at late times and consequent disappearance of the nonlinearity in the dynamics causes each trajectory to become pure in the long time limit.

We therefore quantify the purity of the trajectory as the minimal purity reached during its unraveling, shown in 8.4(b) as a function of the dissipation strength. Different from the steady state population in 8.3(b), the results for different system sizes coincide after a rescaling with $N\gamma/U \approx \sqrt{2N}$. This suggests that a compromise between low particle losses and high single-trajectory purity can be found within the range $1/\sqrt{2N} \ll \gamma/U < \sqrt{2N}$. In this window, which grows linearly with N, a trajectory of the spin-1 fluid may be observed which is on the one hand characterized by small Gaussian fluctuations and therefore to good approximation a coherent state, and on the other hand tractable until the time scale at which the system relaxes to equilibrium.

It is worth pointing out that these results, besides being situated in the high-loss regime, are not reproducable with the truncated Wigner approximation, since the evaluation of fluctuations within a single trajectory of a dissipative system is possible only in a quantum trajectory approach which explicitly includes quantum fluctuations. By contrast, the TWA only provides access to the combined inter- and intra-trajectory variance of observables by inferring the density matrix through an average of realizations [139].

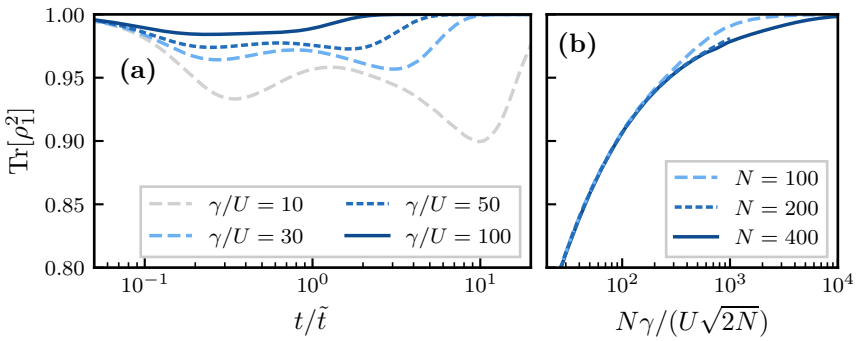

Figure 8.4 – (a) Average purity of a single heterodyne trajectory of a dissipative spin-1 gas ($N = 400$) quenched to $q/U = 0$, for different values of the dissipation rate γ/U. (b) Minimal purity reached during an average unraveling as a function of the ratio $N\gamma/(U\sqrt{2N})$, coinciding for different system sizes.

8.4 A multi-mode system

Recall from Sec. 3.6.1 that the Lindblad equation governing a system in a Markovian environment ultimately stems from taking the trace over a many-mode reservoir with which the system interacts in a coherent way. Following this reasoning in the opposite direction, we might wonder whether the integrability breaking of spin mixing dynamics, resulting from incoherent dissipation, similarly arises as a consequence of coherent interactions with a reservoir of additional modes. In view of the regular-to-chaotic crossover discussed in Sec. 4.1.1 for the Bose-Hubbard model, the extension of the three-mode spin-1 condensate to a number of modes exceeding the amount of conserved quantities – energy, particles and magnetization – is expected to break integrability and provide the system with the ergodicity required to explore a larger portion of its Hilbert space, eventually resulting in the thermalization of the fluid.

8.4.1 The spin-1 Bose-Hubbard model

To test this hypothesis, we concentrate on the dynamics of a *multi-mode* spin-1 fluid. Starting from an array of isolated single-mode spin-1 condensates, the multimode spin-1 fluid is constructed by introducing a hopping term of Bose-Hubbard form, allowing particles to tunnel to condensates sites while maintaining their internal spin state. As the number of particles in each site is no longer conserved in the presence of site-to-site hopping, density interactions omitted from the single-mode approximation re-emerge as on-site repulsive interactions. The resulting spin-1 Bose-Hubbard model, shown in Fig. 8.5 in comparison to a

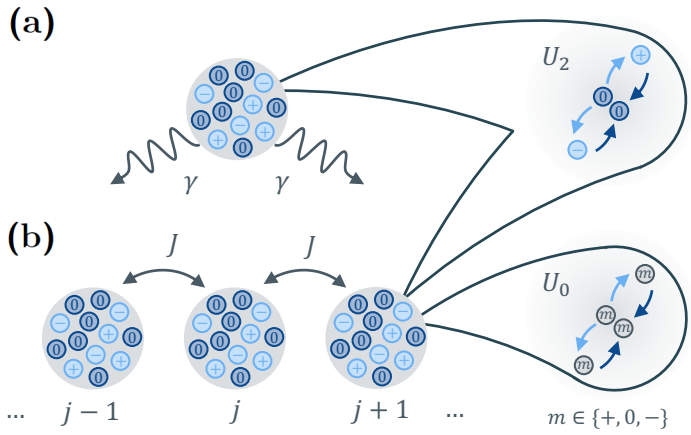

Figure 8.5 – (a) The single-mode spin-1 condensate subject to single-particle losses at rate γ. (b) A multimode spin-1 Bose-Hubbard chain with site-to-site hopping amplitude J. In the latter, spin-independent density interactions at strength U_0 occur in addition to spin exchange interactions at strength U_2.

dissipative single-mode condensate, is governed by the Hamiltonian

$$\hat{\mathcal{H}} = -J \sum_{m} \sum_{\langle j,l \rangle} \left(\hat{a}^{\dagger}_{j,m} \hat{a}_{l,m} + \hat{a}^{\dagger}_{l,m} \hat{a}_{j,m} \right) + \sum_{j} \left(\frac{U_0}{2} :\hat{n}_j^2: + \frac{U_2}{2} :\hat{\mathbf{S}}_j^2: \right), \tag{8.3}$$

where the operator $\hat{a}^{(\dagger)}_{j,m}$ annihilates (creates) a particle of spin m on site j, and the on-site density and spin interaction terms are straightforward generalizations of Eqs. (2.25) and (2.26), respectively.

This model, first studied by Imambekov *et al.* [272], exhibits ground state properties similar to the scalar Bose-Hubbard model of Sec. 2.3.1, but has a phase diagram enriched by the presence of magnetic phases [11]. While its ground state properties have been studied extensively [273–278], much less theoretical attention has been devoted to its dynamics [279–281]. To the best of my knowledge, no account has been given of its spin mixing dynamics as an extension of the single-mode case discussed in Chapter 7.

On the experimental side, Widera *et al.* [242] first studied on-site spin mixing dynamics of ^{87}Rb atoms in the Mott insulator phase at filling $N/L = 2$, observing coherent oscillations of the type shown in Fig. 7.1(c), with a damping suggested to originate from the tunneling between neighbouring sites*. In the superfluid

* Contrary to the superfluid phase at high filling $N/L \gg 1$ studied throughout this thesis, the

regime, similar coherent spin mixing and its damping were observed in a 2D triangular lattice by Becker *et al.* [279], while Zhao *et al.* [282] reported the relaxation of spin mixing to a steady state at long times. Crucially, the number of spin pairs at finite Zeeman splitting was found to decrease sigmoidally with increasing tunneling strength [282].

8.4.2 Equilibration of spin mixing

Setting the interaction strengths* $U_0 = U_2 \equiv U$ for simplicity, we simulate in Fig. 8.6(a) the spin mixing dynamics of a spin-1 Bose-Hubbard chain of $L = 10$ sites, initialized in a fully spin-0 collective state, i.e., $\langle \hat{a}_{j,m} \rangle = \sqrt{N/L}\delta_{m,0}$. The filling N/L of each site is set to 200, such that the system corresponds to a chain of single-mode condensates as considered earlier.

For an infinitesimal tunneling amplitude $J/U = 0.01$, site-to-site hopping is strongly suppressed and the system is well approximated by a collection of disconnected single-mode condensates. The relative number of spin pairs, now defined as

$$n_p = \frac{1}{N} \sum_j \langle \hat{a}^\dagger_{j,\pm1} \hat{a}_{j,\pm1} \rangle \,, \tag{8.4}$$

is therefore identical to the single-mode case at finite times. However, on the time scale set by the tunneling strength, the pair number deviates from its steady state value $\bar{n}_p = 1/4$, converging instead to the equilibrium distribution $n_p^{eq} = 1/3$. Identically to the steady state plateau of dissipative equilibration (see Fig. 8.1), the lifetime of this prethermal plateau inversely scales with the tunneling amplitude, disappearing completely when $J \approx U$.

Interestingly and different from the dissipative model, this trend is reversed upon entering the regime $J \gg U$. For $J/U = 10$, the single-mode dynamics are qualitatively recovered, with a characteristic time scale of relaxation now given by $\sqrt{L}\tilde{t}$. This can be understood from the scaling $\epsilon_k \sim J$ of the single-particle energy levels (5.29) in the Bose-Hubbard model. As J exceeds the energy of the initial condition, the system is frozen in its orbital ground state $k = 0$, forming an effective single-mode system in reciprocal space.

Figure 8.6(b) shows the convergence of the number of spin pairs in the long time limit as a function of J, indicating the regime $J \leq U$ where integrability break-

$N/L = 2$ Mott insulator regime reduces each lattice site to a two-particle system, for which spin mixing interactions alone are not expected to exhibit damping.

* Consistent with the Bose-Hubbard model and the single-mode spin-1 fluid, the interaction strengths are defined as $U_{0,2} = c_{0,2} \int \mathrm{d}\mathbf{r} w^4(\mathbf{r} - \mathbf{r}_j)$, with $c_{0,2}$ the spin-1 interaction strengths (2.22) and $w(\mathbf{r} - \mathbf{r}_j)$ the Wannier state at site j [7].

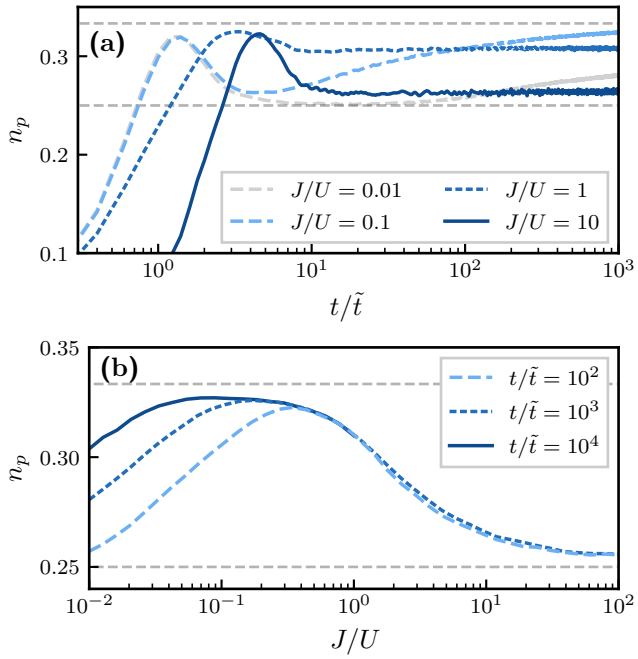

Figure 8.6 – Equilibration of spin mixing dynamics in a spin-1 Bose-Hubbard model of $L = 10$ sites at filling $N/L = 200$, inferred from 2×10^4 truncated Wigner samples. (a) Evolution of the number of spin pairs for different tunneling amplitude J. (b) Late time convergence of the pair number as a function of the tunneling amplitude.

ing causes a thermalization of the spin pair population to $n_p^{eq} = 1/3$. As seen from the time dependence, the lifetime of the prethermal plateau diverges in the limit $J \to 0$ in accordance with the tunneling time scale. Relating these results to the dissipative single-mode spin-1 fluid which raised our initial interest, we thus conclude that the breaking of integrability and ensuing equilibration of spin mixing in the weakly dissipative regime are phenomenologically similar to the non-integrable dynamics of a weakly-coupled multi-mode system. However, we stress that in the regime $\gamma/U \gg 1$ (resp. $J/U \gg 1$), the underlying dynamics of the two systems are fundamentally different. Whereas the Zeno effect induced by the competition between incoherent and coherent dynamics prevents the relaxation of spin mixing in a dissipative condensate, the reduction to single-mode dynamics in the spin-1 chain with a high tunneling amplitude results from a freezing of the system's spatial excitations.

8.5 Summary

In this chapter we have studied spin mixing dynamics in a quenched spin-1 fluid in the presence of an external environment, sparked by the crucial role of conservation laws in the isolated case. For weak coupling to an external environment, a breaking of integrability leads to an eventual departure from the nonequilbrium steady state, resulting in dissipative equilibration on a universal time scale set by the dissipation strength. In relation to interaction-driven relaxation of spin dynamics, the lifetime of the pre-equilibrated plateau scales as $\sim \sqrt{N}$. For dissipation strengths exceeding the interaction energy, rapid depletion of particles leads to a breakdown of the truncated Wigner approximation. Capturing relaxation in the high-loss regime, the Gaussian trajectory approach revealed a dissipative phase transition to a steady state with a suppressed number of spin pairs, interpreted as a quantum Zeno effect inhibiting the formation of spin pairs as incoherent jumps occur on a shorter time scale than the relaxation of spin mixing interactions. Inspired by the equivalence between incoherent dissipation and the coherent coupling to a many-mode reservoir, we showed how a weakly coupled multi-mode spin-1 fluid exhibits thermalization dynamics qualitatively similar to the weakly dissipative equilibration of a single-mode condensate. Deviating from the dissipative phase transition in the high-loss regime of the dissipative single-mode model, the extended chain was found to revert to single-mode dynamics in the limit of a high tunneling amplitude.

IV

Spinor fluids as a platform for analog gravity

"And how awkward is the human mind in divining the nature of things, when forsaken by the analogy of what we see and touch directly?"

– Ludwig Boltzmann, *Nature* **51** (1895) [283]

9 | The Analog Hawking effect in ultracold fluids

In the last part of this thesis, we leave behind us the development and application of the Gaussian trajectory approach, and instead consider a topic somewhat distinct from the relaxation dynamics considered in Parts II and III.

As mentioned in the introductory chapter, a prime motivation for the study of synthetic quantum fluids is the simulation of quantum mechanical properties of natural systems beyond the reach of experiment. Among the more peculiar research avenues of quantum simulation is the field of *analog gravity*, where one aims to formally replicate the consequences of spacetime curvature on quantum fields in a laboratory setting. While the underlying physics, governed by the theory of *general relativity*, differ greatly from ultracold atomic fluids, the analogies between their mathematical structures allows one to obtain meaningful insights on a range of cosmological phenomena.

Referring the interested reader to an extensive review by Barceló *et al.* [284], we narrow the scope of our discussion to black holes and the *Hawking radiation* they are theorized to emit. This phenomenon at the crossroads of quantum mechanics and general relativity is one of the focal points of analog gravity. After a brief introduction of black holes and the Hawking effect, we dedicate the remainder of this chapter to its analogue for sound waves in an ultracold atomic fluid. Motivated by recent experiments on binary mixtures (see Sec. 2.5), we will extend this framework in Chapter 10 to study the Hawking effect for spin waves in a two-component fluid.

9.1 Black holes and the Hawking effect

In the theory of general relativity, the Einstein field equations [285] governing the spacetime metric allow for divergent solutions. Such metrics, arising from configurations as simple as a single spherical mass in vacuum, contain elements which diverge to infinity at certain points in spacetime, commonly referred to as *spacetime singularities* [286]. For a spherical object to cause a spacetime singularity, its radius r must be smaller than the *Schwarzschild radius* determined by its mass M,

$$r_S = \frac{2GM}{c^2}, \tag{9.1}$$

with c the velocity of light and G the gravitational constant. In reality, spacetime singularities emerge from the gravitational collapse of massive stellar objects, leading to the formation of a *black hole*.

While diverging *at* the singularity, the spacetime metric is finite in its surroundings, reducing to flat (Minkowski) space at infinity. In what has been called the *river model* of black holes [287], spacetime curvature in the vicinity of a singularity may be viewed in analogy to accelerating flow [288]. To each point in spacetime one may assign a velocity, directed towards the singularity* and increasing proportionally to the curvature of spacetime. The gravitational acceleration of an object towards the singularity is then understood as its movement in the accelerating flow. From this arguably oversimplified analogy, it is clear that a surface must exist in the vicinity of a black hole at which the 'flow' of spacetime exceeds the finite velocity of light c. This surface is located at the Schwarzschild radius r_S and is referred to as the *event horizon*, as it marks the boundary beyond which light, matter or indeed any information is inevitably lost to the black hole [292]. As the horizon contains all extractable information of the black hole and defines its interactions with the exterior, it is considered the surface of the black hole, with the region $r < r_S$ understood as the inside of the black hole.

Following seminal work on the development of a thermodynamic theory for black holes [293–295], Stephen Hawking predicted in 1974 [296, 297] that black holes behave as *black bodies*, emitting thermal radiation at the *Hawking temperature*

$$T_H = \frac{\hbar c^3}{8\pi G M k_B}. \tag{9.2}$$

* Note that we limit our discussion to non-rotating and electrically neutral *Schwarzschild* black holes. The presence of electric charge or angular momentum complicates this description, giving rise to properties such as superradiance [289], black hole bombs [290] and black hole lasing [291].

The decrease in mass associated to this emission of energy eventually leads to the *evaporation* of a black hole* [296]. The emission originating from a black hole may be understood heuristically as a consequence of vacuum fluctuations at the event horizon. Upon the excitation of a particle-antiparticle pair at the horizon†, the antiparticle carrying negative energy may tunnel to the inside and remains trapped. Rather than recombining on a timescale set by the Heisenberg uncertainty relation $\Delta E \Delta t \leq \hbar/2$, the positive-energy excitation is now emitted to infinity [297, 300]. In view of our discussion of particle entanglement in Sec. 7.2.2, the thermal nature of the emitted radiation may be interpreted as a consequence from its entanglement to the negative energy flux inside the black hole [286].

Crucial for this process to take place is thus the presence of non-evanescent negative-energy modes on the inner side of the event horizon. In the following section, we will make this notion more concrete in the context of the condensed matter analogues to the Hawking process.

9.2 The analog Hawking effect

While disregarding the underlying intricacies of general relativity, the river model of black holes has far-reaching implications for the universality of their properties. Indeed, reversing the analogy one arrives at the striking conclusion that event horizons are a general property of flowing media. Imagining a fish swimming in a river which accelerates towards a waterfall [301, 302], there exists a similar *point-of-no-return* at which the flow velocity of the river exceeds the swimming velocity of the fish. Like information crossing the event horizon, the fish is doomed to accelerate towards the waterfall once it swims beyond this line. This is true not only for fish and other objects in the river, but also for *waves*, i.e., excitations of the fluid itself, which propagate at a finite and wavelength-dependent *group*

* To place these effects into perspective, we note for example that an object with a mass equal to that of the earth has a Schwarzschild radius of $r_S \approx 9$mm and emits radiation at a Hawking temperature $T_H \approx 0.02$K, obscured from observation by the cosmic microwave background at temperature $T \approx 2.72$K [298]. Its evaporation time is on the order of 10^{58}s, without taking into account the *lifetime problem* [299] posed by the effective accumulation rather than dissipation of energy in the presence of the microwave background. For comparison, the age of the universe is approximately 4×10^{17}s [286].

† Note that this picture in terms of particles is largely metaphorical, and should not be taken to be a literal description of physical processes occurring at the event horizon [297, 300]. Strictly speaking, the notion of a particle is well-defined only in flat spacetime, corresponding in this case to an observer located at infinite distance. In the vicinity of the black hole, *virtual particles* correspond simply to excitations of the quantum field under consideration [286, 297].

velocity $v_g(k)$ determined by the excitation spectrum $\omega(k)$,

$$v_g(k) = \frac{\partial \omega(k)}{\partial k}. \tag{9.3}$$

For linear excitation spectra (or in the $k \to 0$ linear regime of a general excitation spectrum), the group velocity is independent of wavelength and known as the sound velocity c. In an accelerating background flow, one thus defines a *sonic horizon* or *acoustic horizon* as the boundary dividing regions of subsonic flow $v < c$ and supersonic flow $v > c$. An important consequence of this analogy is that Hawking radiation is no phenomenon specific to black holes or spacetime curvature. Rather, it is a purely kinematic consequence of a horizon dividing regions of sub- and supersonic flow, and the presence of negative energy excitations in the latter [303]. As first noted by William Unruh in 1981 [288], this analogy paves the way for the realization of a *sonic black hole* or *dumb hole** [304], where one aims to observe the *analog Hawking effect* for sound waves in an accelerating flow.

The Hawking process on a black hole event horizon is intrinsically quantum, requiring the use of quantum fluids for the observation of its analogue. Alternatively, one may consider *stimulated* Hawking radiation in a classical fluid, which reproduces surprisingly much of the essential physics. We will return to the latter approach in Sec. 9.3.1 and throughout much of Chapter 10. In the following section, we will illustrate the basic characteristics of the analog Hawking effect in a weakly interacting Bose gas (see Sec. 2.2.1), deferring a more detailed discussion to Chapter 10, where we will focus on the extension to a binary mixture. Note that a similar reasoning applies to a variety of quantum and classical systems, which we will briefly cover in Sec. 9.3.1.

9.2.1 Bogoliubov theory in a moving fluid

In order to describe the Hawking effect for sound waves in an atomic fluid, we return to the Bogoliubov theory of elementary excitations on a stationary background†, detailed in Sec. 3.2. As anticipated in the excitation spectrum (3.9), the Bogoliubov equations allow for solutions of both positive and negative frequency‡

* A coinage referring to the property of not emitting sound, not to the intelligence of the object.

† Note that, like Hawking's original approach [297], the Bogoliubov treatment of excitations on a static uniform background does not take into account the *backreaction* effect of quantum fluctuations on the field modes (i.e., the spacetime metric itself). The consistent integration of quantum mechanical effects in the theory of general relativity is the main objective of *quantum gravity*, and is left as an exercise to the reader.

‡ Assuming an inifitely large system, we replace the discretized spectrum (3.9) with its continuum variant $\omega(\mathbf{k})$.

$\omega(\mathbf{k})$. More precisely, by taking the complex conjugate of the eigenmodes (3.7) it is clear that any solution $(U_{\mathbf{k}}, V_{\mathbf{k}})$ at frequency $\omega(\mathbf{k})$ implies the existence of another solution $(V^*_{\mathbf{k}}, U^*_{\mathbf{k}})$ at frequency $-\omega(\mathbf{k})$. This particle-antiparticle symmetry is a consequence of the linearization of $\hat{\psi}$ in terms of both $\delta\hat{\psi}$ and $\delta\hat{\psi}^\dagger$, which induces an effective doubling of the modes [8]. In order to account for this duality, one must either consider solely positive norm modes, or restrict the excitation spectrum to modes of positive frequency [305]. In the remainder of our discussion we will follow the latter approach, as it allows for a more natural description of scattering processes in Chapter 10. Describing the same physical mode, both solutions carry the same energy content, given by the product [2]

$$E = \hbar\omega(\mathbf{k})(|U_{\mathbf{k}}|^2 - |V_{-\mathbf{k}}|^2). \tag{9.4}$$

With the sign of the Bogoliubov norm (3.12) corresponding to the sign of $\omega(\mathbf{k})$, both positive-norm ($|U_{\mathbf{k}}|^2 - |V_{-\mathbf{k}}|^2 = 1$) and negative-norm ($|U_{\mathbf{k}}|^2 - |V_{-\mathbf{k}}|^2 = -1$) excitations describe an excitation with positive energy. The resulting spectrum of positive- and negative-norm modes is pictured in Fig. 9.1(a) where the energy and length scales are set by the chemical potential and the *healing length**

$$\mu = gn = \frac{\hbar^2}{2m\xi^2}, \qquad \xi = \frac{\hbar}{\sqrt{2m\mu}}. \tag{9.5}$$

In the long-wavelength limit of phononic excitations, the spectrum reduces to the linear form $\hbar\omega(\mathbf{k}) = \hbar c|\mathbf{k}|$, introducing the sound velocity defined as

$$c = \lim_{k\to 0} \frac{\omega(k)}{k} = \sqrt{\frac{\mu}{m}}. \tag{9.6}$$

The role of negative norm eigenmodes becomes apparent for a fluid which is not at rest but moving at a constant flow velocity v with respect to the laboratory reference frame. The excitation spectrum (3.9) then changes through a Galilean transform† to

$$\hbar\omega(\mathbf{k}) = \hbar v|\mathbf{k}| \pm \sqrt{\frac{\hbar^2k^2}{2m}\left(\frac{\hbar^2k^2}{2m} + 2gn\right)}, \tag{9.7}$$

shown in Fig. 9.1(b). When the flow velocity v exceeds the speed of sound c in the fluid, negative norm modes within a finite interval $[0, k_{\max}]$ acquire a positive

* This characteristic length scale determines the wavelength at which kinetic and interaction energies are equal, thus setting a crossover between collective and particle-like excitations in the Bogoliubov spectrum.

† The energy shift can also be interpreted as a Doppler shift of the frequency observed from a source moving at velocity v.

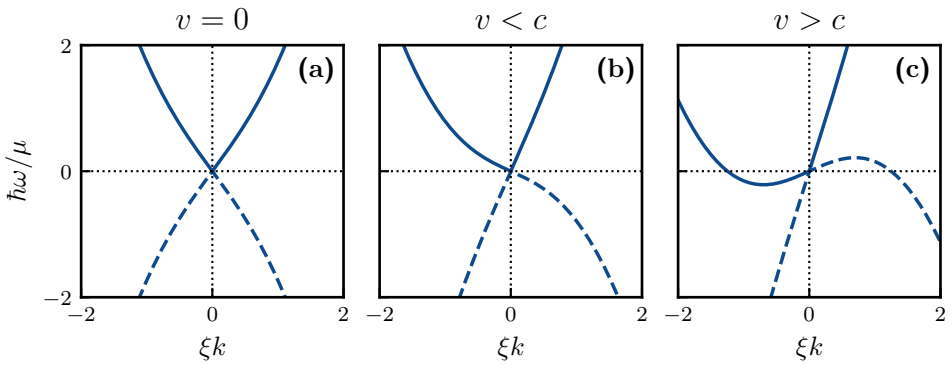

Figure 9.1 – Bogoliubov excitation spectrum in a co-moving (a), subsonically moving (b) and supersonically moving (c) reference frame. Full (dashed) lines represent positive (negative) norm solutions of the dispersion relation (3.9).

frequency and vice versa. This situation, illustrated in Fig. 9.1(c), has dramatic consequences for the qualitative behaviour of elementary excitations. As dictated by (9.4), the modes within this interval now carry a negative energy content*. With the presence of negative energy modes being the crucial prerequisite for the Hawking process, a sonic analogue to an event horizon may be created by spatial modulation of the sound velocity, as we will explain in the next section.

9.2.2 A sonic event horizon

In the river model of black holes, spacetime curvature corresponds to a spatially varying flow velocity. However, as mentioned in Sec. 2.2.1, the interaction strength and thus the velocity of sound propagation in a bosonic fluid can itself be spatially modulated. In the simplest scenario, we may consider an infinite one-dimensional condensate divided in two regions by a sharp spatial modulation of the chemical potential,

$$\mu(x) = \mu_u \Theta(-x) + \mu_d \Theta(x), \tag{9.8}$$

where $\Theta(x)$ is the Heaviside step function and $x = 0$ denotes the location of the horizon, resulting in the creation of an *upstream* and *downstream* region, a terminology deriving from the river analogy. Contrary to Fig. 9.1, it is thus the speed of sound which changes across the horizon, while the flow velocity v remains uniform throughout the fluid.

* The presence of negative energy modes consitutes an *energetic instability*, as the stationary background solution ψ_0 of the condensate no longer represented the energy minimum [2]

Figure 9.2(a) shows the velocity profile of the resulting *sonic horizon* dividing a *subsonic* upstream region ($c/v = 4/3$) from a *supersonic* downstream region ($c/v = 2/3$). Similarly to photons on the event horizon of a black hole, sound waves are unable to cross the dividing boundary from the downstream to the upstream region. The Bogoliubov excitation spectra on both sides of the horizon, shown in Fig. 9.2(c-d), indicate the modes present at some arbitrary $\omega > 0$. In the subsonic upstream region, all modes present at positive frequency are positive-norm modes (full lines) and thus carry positive energy content. Based on the propagation direction of a wave packet excited along the respective branch with respect to the horizon – set by the group velocity (9.3) –, we can distinguish modes which are either ingoing or outgoing. Respectively denoted u^{in} and u^{out}, these branches of the dispersion are indicated in Fig. 9.2(c) and their propagation direction illustrated in Fig. 9.2(b). The same picture holds in the supersonic downstream region above some frequency threshold $\omega_{\max}$, where the positive-norm modes, denoted d_1, can similarly be distinguished into d_1^{in} and d_1^{out} modes, as indicated in Fig. 9.2(d). Below the threshold $\omega_{\max}$, however, negative-norm modes (dashed lines) occur at positive frequencies. Analogously denoted d_2^{in} and d_2^{out}, these modes carry negative energy content and are precisely what enable the Hawking process to take place. At the horizon, vacuum fluctuations can lead to the excitation of a positive-energy u^{out} mode and a negative-energy d_2^{out} mode at the same frequency, conserving the total energy of the system. While the u^{out} *Hawking* particle propagates out of the sonic horizon, its antiparticle or *partner* particle d_2^{out} remains trapped inside the sonic black hole [306]. Analog Hawking radiation of sound waves emitted from the analog black hole then results from the continuous excitation of such correlated Hawking pairs at the sonic horizon.

Note that, contrary to the luminal dispersion $\omega = ck$ of light, the *superluminal* dispersion of excitations in a bosonic fluid provides a natural UV cutoff for modes participating in the Hawking effect. This property is particularly useful in the context of the *trans-Planckian problem* posed by the arbitrarily high-frequency modes involved in the astrophysical Hawking effect and the invalidity of the approximate quantum field theory at such high energies [284, 286]. A major achievement of analog gravity investigations in this respect has been the demonstration that the Hawking effect is primarily a low-frequency phenomenon robust to trans-Planckian artefacts [307–309].

The construction of a sonic event horizon for long-wavelength phonons in a Bose-Einstein condensate was first considered by Garay *et al.* [310] in 2000 and followed by a range of studies [284], among which the prediction of observable non-local density correlations across the horizon resulting from the creation of particle-

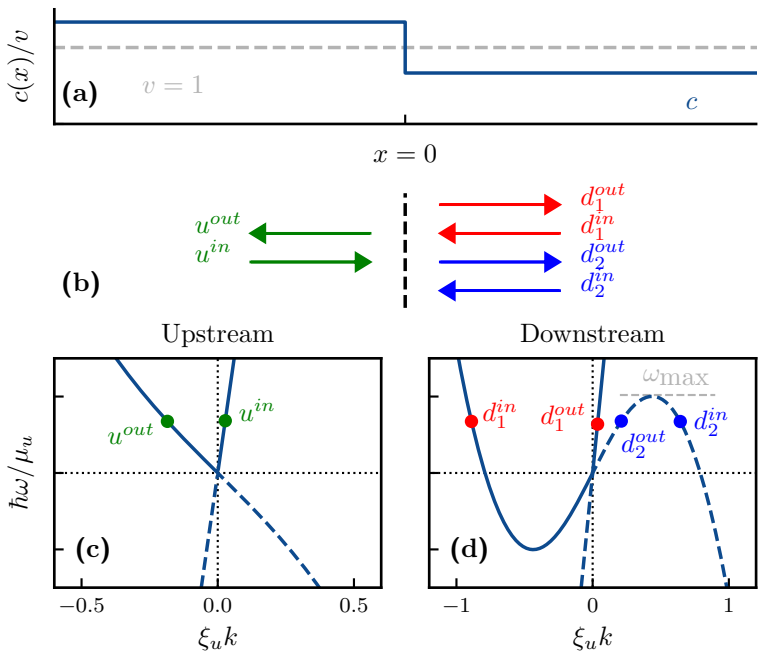

Figure 9.2 – An idealized sonic horizon. (a) Velocity profile obtained by sharp modulation (9.8) of the sound velocity c in a uniform background flow v. The velocity ratios are $c_u : v : c_d = 4/3 : 1 : 2/3$. (b) Ingoing and outgoing signals propagating in the upstream and downstream regions. (c-d) Upstream and downstream Bogoliubov spectra, indicating the branches of positive-frequency signals shown in (b).

antiparticle pairs [306]. This signature of the analog Hawking effect was observed by Carusotto *et al.* [311] in a truncated Wigner simulation of a one-dimensional fluid, and subsequently confirmed on the basis of a Bogoliubov theory approach by Recati *et al.* in 2009 [312].

We will study the spectral properties of the Hawking process in greater detail in Chapter 10, applied specifically to spin waves in a binary bosonic mixture. There, we will solidify the Bogoliubov description in terms of a *scattering matrix* solution, and explore the possibility of externally stimulating the Hawking process. To close this introductory chapter, we comment in the final section on recent progress on the experimental observation of the analog Hawking effect.

9.3 Experimental realization

The experimental observation of the analog Hawking effect in ultracold Bose fluids is challenging for serveral reasons. As an analog event horizon is formed through spatial modulation of the velocity profile, its construction requires either a spatially non-uniform interaction strength g, a non-uniform density or a non-uniform flow velocity. While the former approach would require precise spatial modulation of magnetic fields near a Feshbach resonance [45], the latter two options involve highly nonequilibrium configurations of the fluid, leading to the excitation of shock waves [313] and rapid heating of the atomic cloud [314] which is predicted to overshadow the faint signature of Hawking radiation.

A sonic horizon in a ^{87}Rb condensate was first realized by Lahav *et al.* [315] by accelerating a negative step potential formed by a half-blocked laser beam across the elongated fluid. Mimicking a waterfall, the condensate flows over the step and is accelerated in the downstream region. In the reference frame of the scanning potential, the fluid is accelerated to a velocity beyond that of sound propagation. Following additional experiments on black hole lasing [316], density correlations consistent with spontaneously created entangled Hawking pairs were observed in the same experimental setup by Jeff Steinhauer in 2016 [317], although the statistical significance of this observation has been questioned [318]. Since then, further refinements of the experimental setup have led to the observation of a thermal spectrum [319] and temporal stationarity of the analog Hawking signal [320]. In Fig. 9.3 we reproduce a measurement of density-density correlations,

$$g_2(x,x') = \frac{\langle \hat{n}(x)\hat{n}(x')\rangle - \langle \hat{n}(x)\rangle \langle \hat{n}(x')\rangle}{\langle \hat{n}(x)\rangle \langle \hat{n}(x')\rangle}, \tag{9.9}$$

from the latter reference and a corresponding theoretical prediction based on a

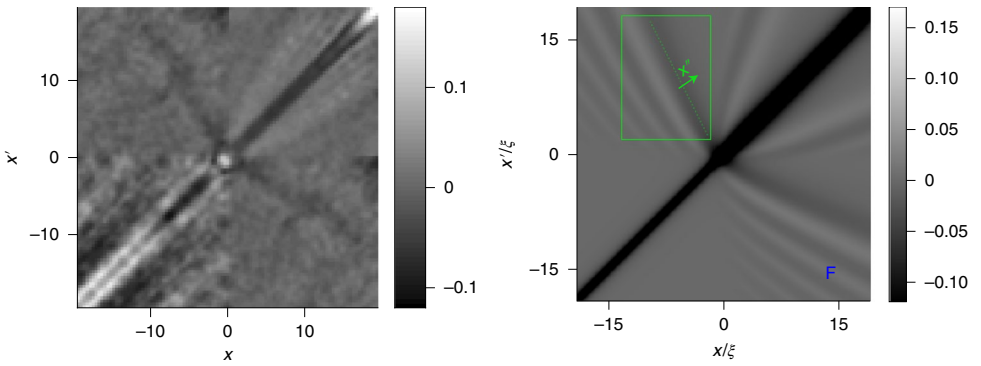

Figure 9.3 – Density-density correlations across a sonic horizon in a degenerate Bose gas, as measured by Kolobov *et al.* [320]. Experimental results (left) indicate an off-diagonal fringe resembling the signature of spontaneous pair creation at the horizon, as calculated in a Bogoliubov approximation by Isoard *et al.* [321] (right). Figure reproduced from [320].

Bogoliubov approach [321] as developed in Ref. [312]. In both the experimental and theoretical result, anti-diagonal lines can be seen emanating from the horizon location $x = x' = 0$. This *moustache* represents correlations between excitations on both sides of the horizon and forms the signature of spontaneous Hawking radiation. Its slope is given by the relative group velocities of the Hawking mode u^{out} and its antiparticle d_2^{out} [311, 312].

9.3.1 Alternative platforms

In addition to ultracold atomic fluids, the past decade has seen a surge in experimental efforts on Hawking radiation in a variety of platforms [322]. As the kinematics of wave propagation in supersonic flow are in itself a purely classical effect, analog event horizons have been realized for surface waves on water [323–326]. Lacking significant quantum fluctuations, the observation of the analog Hawking effect in this system requires the external stimulation of waves. Intrinsically quantum systems in which the analog Hawking effect has been studied include polariton fluids [327–329], photon fluid [330] and optical fibers [331, 332].

10 | Stimulated Hawking radiation in a binary mixture

The results presented in this chapter are part of a manuscript under preparation*:

Analog Hawking radiation in a coherently coupled spinor condensate
A. Berti, S. G. Butera, I. Carusotto, L. Fernandes & A. Recati

---

In the final chapter of this thesis, we extend the Bogoliubov approach to the analog Hawking effect, introduced in Chapter 9, to a coherently coupled two-component quantum fluid. Much like the spin-1 condensates studied in Part III, the interplay between both components introduces *spin* excitations, decoupled from the density degree of freedom and propagating at a distinct sound velocity. Combining both the semi-analytical Bogoliubov approach and scattering simulations of the classical Gross-Pitaevskii equation, we will show how this allows one to construct a spin-sonic horizon, and study the spectral properties of stimulated analog Hawking radiation of spin excitations.

10.1 Density sound and spin sound

In a binary mixture as described in Sec. 2.5, the interplay of two fluid components gives rise to two distinct types of *elementary excitations*. Following the Bogoliubov approach of Sec. 3.2, the excitation spectrum decouples into *density* fluctuations of the total density $\delta(n_1 + n_2)$ and *polarization* or *spin* fluctuations

* Working title with authors in alphabetical order.

of the density difference $\delta(n_1 - n_2)$. As the latter will be of most interest for the remainder of this chapter, we will for notational compactness denote quantities referring to the spin degree of freedom as simply ω, μ, c, and so on, while indicating the corresponding quantities of the density channel as ω_0, μ_0 and c_0. For a one-dimensional uniform fluid ($V_0(x) = 0$), density and spin excitations obey the dispersion relations [103]

$$\hbar\omega_0(k) = \hbar v k \pm \sqrt{\frac{\hbar^2 k^2}{2m}\left(\frac{\hbar^2 k^2}{2m} + \frac{2\mu_0}{\hbar}\right)}, \tag{10.1}$$

$$\hbar\omega(k) = \hbar v k \pm \sqrt{\left(\frac{\hbar^2 k^2}{2m} + 2\hbar\Omega\right)\left(\frac{\hbar^2 k^2}{2m} + \frac{2\mu}{\hbar} + 2\hbar\Omega\right)}. \tag{10.2}$$

where Ω is the coherent coupling between the components and the Doppler shift $\hbar v k$ appears as in Eq. (9.7) to account for a nonzero flow velocity v of the fluid with respect to the laboratory reference frame. The chemical potentials signify the interaction strength for the respective excitation branches. They are given in terms of the interaction constants and the uniform density $n = |\psi_1|^2 + |\psi_2|^2$ as

$$\mu_0 = (g + g_{12})n/2, \qquad \mu = (g - g_{12})n/2, \tag{10.3}$$

and in turn set the characteristic length scale as the healing lengths

$$\xi_0 = \frac{\hbar}{\sqrt{2m\mu_0}}, \qquad \xi = \frac{\hbar}{\sqrt{2m\mu}}. \tag{10.4}$$

In absence of coherent coupling, the dispersion relations for both density and spin excitations are phononic for $k \to 0$, reducing to the linear form

$$\omega_0(k) \approx (v + c_0)k, \qquad \omega(k) \approx (v + c)k \tag{10.5}$$

Characteristic of the binary mixture is thus the appearance of two distinct sound velocities for density and spin excitations, defined as

$$c_0 = \lim_{k\to 0} \frac{\omega_0(k)}{k}, \qquad c = \lim_{k\to 0} \frac{\omega(k)}{k}, \tag{10.6}$$

and related to the chemical potentials through

$$\mu_0 = mc_0^2, \qquad \mu = mc^2. \tag{10.7}$$

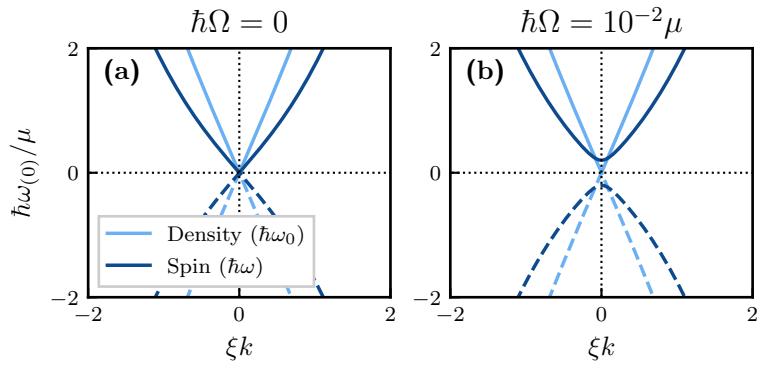

Figure 10.1 – Excitation spectra of a stationary two-component condensate with relative chemical potentials $\mu/\mu_0 = 1/4$. Full (dashed) lines represent positive (negative) norm solutions of the dispersion relations (10.1) and (10.2) in the absence of coherent coupling (a) and for a coherent coupling $\hbar\Omega = 10^{-2}\mu$ (b).

As both g and g_{12} are positive for the antiferromagnetic case to which we limit our discussion, Eq. (10.3) requires the sound velocity of spin excitations to be necessarily lower than that of density modes. Figure 10.1 shows the spin and density dispersions in of a two-component fluid in a co-moving reference frame ($v = 0$), both without and with coherent coupling Ω. In the uncoupled case (a), the linear behaviour for $k \to 0$ indicates the different sound velocities of the qualitatively similar spin and density spectra. The introduction of a coherent coupling term (b) leads to the opening of a spectral gap ω_p in the spectrum of spin excitations,

$$\omega_p = 2\sqrt{\Omega\left(\Omega + \frac{\mu}{\hbar^2}\right)}. \tag{10.8}$$

This *plasma frequency* represents the energy required to excite a $k = 0$ mode and serves as an effective mass for the spin quasiparticles. From a symmetry point of view, the opening of a spectral gap can be understood from the fact that the coherent transfer of atoms from $\hat{\psi}_1$ to $\hat{\psi}_2$ and back – enabled by the coupling term – breaks the conservation of particle number in each of the fields. From Goldstone's theorem, the effective mass then results from the explicitly broken $U(1)$ symmetry of the conjugated relative phase variable $\phi = \phi_1 - \phi_2$ [114]. In the presence of coherent coupling, the underlying physics of massive spin excitations is thus fundamentally different from the density modes, as will the spectral properties of the Hawking effect.

10.1.1 Experimental results

The intra- and intercomponent scattering lengths of ^{23}Na were measured by Knoop *et al.* [333] to be

$$a = 54.54(20)\, a_0, \qquad a_{12} = 50.78(40)\, a_0, \tag{10.9}$$

with a_0 the Bohr radius. Following Eqs. (10.3) and (10.7), the resulting ratio $g_{12}/g \approx 0.93$ between the respective interaction strengths implies that spin excitations indeed propagate at a velocity lower than density excitations, by a factor of approximately $c/c_0 \approx 0.189(11)$. In a pancake-shaped harmonic trap, the existence of these two sound modes in a $|1, \pm 1\rangle$ mixture of ^{23}Na atoms was observed by Kim *et al.* [119] through spin-separated imaging of the atomic cloud following a spin-dependent perturbation by a localized laser beam. Reproduced in Fig. 10.2, the relative velocity at which density and spin sound waves spread in the radial direction was inferred to be $c/c_0 = 0.193(22)$, in quantitative agreement with the results of Knoop *et al.* [333].

Introducing a coherent coupling Ω through the application of a radiofrequent field resonant with Rabi transitions between the $|1, \pm 1\rangle$ hyperfine states*, Cominotti *et al.* [102] studied the excitation spectra of a cigar-shaped ^{23}Na mixture through the imaging of Faraday patterns, plane waves emerging as a consequence of periodic modulation of the transverse trapping frequency. Relating the wave vector components of the spatial pattern to the external modulation frequency allows to reconstruct the entire dispersion relation, shown in Fig. 10.3. While the dispersion of density excitations in Fig. 10.3(a) is always phononic at low k, the spin dispersion was found to change from phononic (b) to gapped (c) with the introduction of coherent coupling, with both sound velocities and the spectral gap in quantitative agreement with the dispersion relations (10.1) and (10.2).

* This single-photon transition with negligible momentum transfer derives its name from the equivalence to the *Rabi* model of a two-level system interacting with light [334]. Alternatively, a coherent coupling can be achieved by the stimulation of two-photon *Raman* processes involving the exchange of momentum [114].

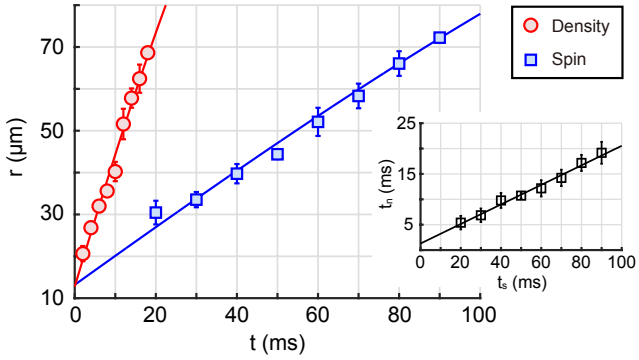

Figure 10.2 – Sound velocities for density and spin excitations in a ^{23}Na mixture, measured by Kim *et al.* through the radial propagation $r(t)$ of localized spin-dependent perturbations [119].

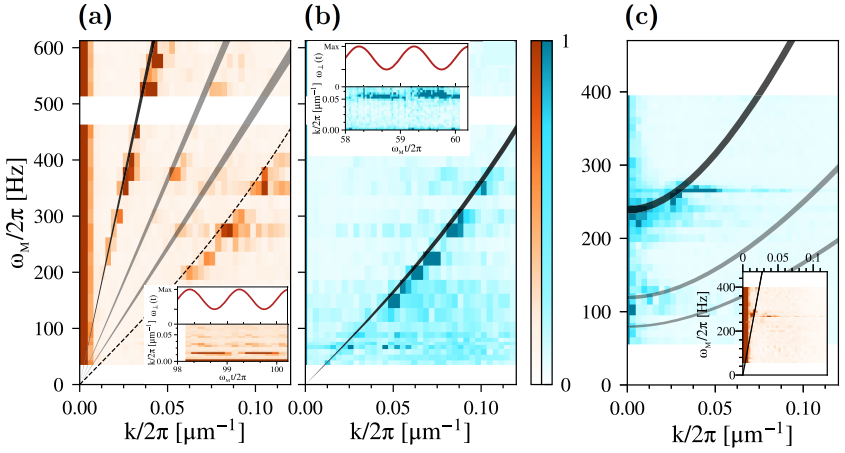

Figure 10.3 – Dispersion relations in a ^{23}Na binary mixture, as measured by Cominotti *et al.* [102]. The density dispersion (a) is linear at low k, while the linear character of the spin dispersion (b) is lost upon the introduction of coehrent coupling (c). Black and grey full lines represent the theoretical dispersions (10.1), (10.2) and their harmonics, respectively. The color scale indicates the spectral power density (a.u.) of the Faraday pattern measured at each modulation frequency ω_M. Figure adapted from [102].

10.2 The Hawking effect for spin excitations

The large difference between the sound velocity of density and spin excitations [119] requires a generalization of the sonic horizon introduced in Sec. 9.2, as three situations should now be considered. Whenever the flow velocity v is lower than either sound velocity, as shown in Fig. 10.4(a), density and spin excitations both retain positive energy content, as the signs of both $\omega_0(k)$ and $\omega(k)$ match that of the Bogoliubov norm of the mode. When v exceeds the sound velocity of spin modes but not that of density modes, as in Fig. 10.4(b), negative energy spin excitations appear, indicated by the presence of positive norm, negative frequency modes and vice versa. However, as the flow remains *density-subsonic*, no negative energy modes are present in the density excitations. Finally, when v exceeds both sound velocities as in 10.4(c), negative energy spin *and* density modes appear in the fluid.

In the presence of coherent coupling, one has to generalize the notion of sub- and supersonic flow. As the opening of a gap in the spin spectrum removes its phononic nature for $k \to 0$, a nonzero sound velocity can no longer be defined through Eq. (10.6). Instead, we define c as the Landau critical velocity for superfluidity in the spin channel,

$$c = \min_k \left(\frac{\omega(k)}{k} \right), \tag{10.10}$$

which reduces to (10.6) in the limit $\Omega \to 0$. With this criterion, supersonic flow is defined by the presence of negative energy spin modes.

10.2.1 Spin-supersonic flow

Of particular interest to our discussion is the configuration in which the flow velocity of the condensate is supersonic only with respect to the propagation of spin waves. In this intermediary regime, the decoupling of spin and density excitations* allows one to study the effects of energetic instabilities related to *spin-supersonic* flow in a *density-subsonic* fluid. Besides the additional physics provided by the coherent coupling, it is precisely this property which makes the two-component condensate a promising platform for the observation of the analog Hawking effect, as it largely eliminates the generation of density shock waves [313]

* As seen from the experimental measurement of the dispersion relations, reproduced in Fig. 10.3, imbalance in the spin populations in reality leads to weak crosstalk between spin and density excitations.

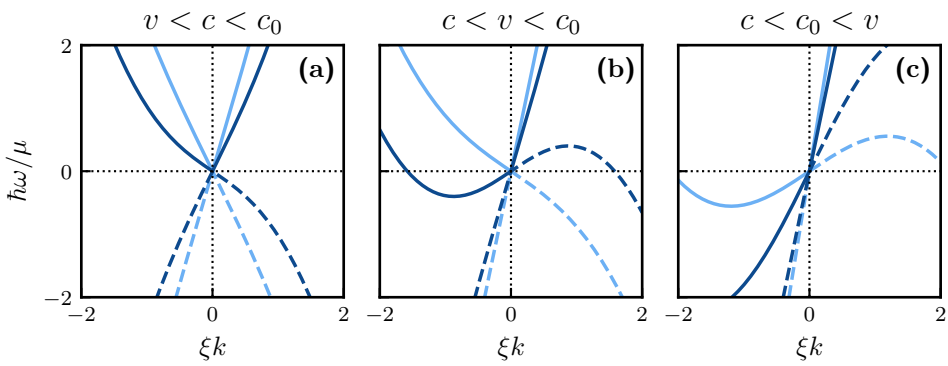

Figure 10.4 – Spin and density excitation spectra of an uncoupled two-component fluid with $\mu_0/\mu = 4$ for different flow velocities v. The occurrence of positive norm modes (full lines) at negative frequency and vice versa (dashed lines) indicates the appearance of negative energy excitations in the density (light blue) and spin (dark blue) degrees of freedom.

and phonons [314] resulting from the transition to supersonic flow*. Apart from being detrimental to superfluidity, these excitations outweigh the weak signature of spontaneous Hawking radiation [314].

10.2.2 An idealized spinsonic horizon

In Chapter 9 we have seen how the boundary between subsonic and supersonic flow acts as an analog event horizon for sound waves, which allows to observe Hawking emission resulting from the excitation of negative energy modes. In what follows, we will construct a sonic horizon between the two regimes in Figs. 10.4(a) and 10.4(b) and study the properties of the associated analog Hawking effect for spin excitations.

As in the single-component case, a sudden sonic horizon for spin excitations is constructed through a sharp spatial modulation of the spin chemical potential, this time leaving the density chemical potential homogeneous throughout the system,

$$\begin{aligned} \mu_0(x) &= \mu_0, \\ \mu(x) &= \mu_u \Theta(-x) + \mu_d \Theta(x), \end{aligned} \tag{10.11}$$

dividing the fluid into an *upstream* and *downstream* region. A schematic of the resulting velocity profile is shown in Fig. 10.5(a), in which the density sound velocity $c_0 > v$ exceeds that of the fluid's flow. Following the definition of the

* Strictly speaking, this only holds for one-dimensional fluids. In 2D and 3D, the excitation of topological defects breaks superfluidity at velocities well below c [313, 335].

chemical potentials (10.3) and considering for simplicity a fluid of uniform density* $n_1(x) = n_2(x) = n/2$, the configuration (10.11) is attained by fixing the sum $g + g_{12}$ to a constant value while independently modulating the difference $g - g_{12}$ across the horizon.

In the upstream region ($x < 0$), the flow is spin-subsonic and only spin modes of positive energy content are available. Restricting our view to positive frequencies†, we will refer to this branch of the dispersion relation as u^{in} and u^{out}, following the same definition as in Sec. 9.2.2. In the upstream region, ingoing (outgoing) modes have a positive (negative) group velocity, respectively. In the downstream region ($x > 0$), on the other hand, the flow velocity is spin-supersonic and both positive (d_1) and negative norm modes (d_2) are present at positive frequencies. Each containing both ingoing ($v_g < 0$) and outgoing ($v_g > 0$) excitations, these branches will be denoted as d_1^{in}, d_1^{out} and d_2^{in}, d_2^{out}, respectively. The spectra of spin excitations in the upstream and downstream regions of an uncoupled two-component condensate, shown in Fig. 10.5(c-d), are qualitatively identical to those of a single-component fluid in Fig. 9.2. Due to the superluminal nature of the dispersion, the Doppler shift $\hbar k v$ only changes the sign of the d_2 excitation branch within a finite range of wave vectors. In the downstream region, the negative-norm branch therefore reaches a maximum positive frequency $\omega_{\max}$ at finite momentum. As a consequence, negative energy modes are available only in the frequency range $\omega \leq \omega_{\max}$, indicated on Fig. 10.5(d).

Finally, Fig. 10.5(e-f) shows the same horizon configuration in the presence of coherent coupling, where the opening of a gap in the spin spectrum introduces a minimum frequency $\omega_{\min}$ below which no propagating modes are available in the upstream region. In the downstream region, Fig. 10.5(f), the specteal gap is equally present but does not lead to the unavailability of any excitation branches due to the pronounced Doppler shift of the dispersion relation.

---

* Note that this requires uniformity of the chemical potentials μ_1 and μ_2 of the two components, given by

$$\mu_{1/2}(x) = V(x) + \mu_0 - \Omega(x). \tag{10.12}$$

For a uniform coherent coupling, a constant density in the ground state is thus ensured by the uniformity of μ_0, without the need for external potentials. In case the coherent coupling strength is modulated across the horizon, one merely needs to set $V(x) = \Omega(x)$ to recover a uniform ground state.

† Recall that the doubling of modes in the Bogoliubov approximation permits one to either take into account only modes of positive frequency, or alternatively modes of positive norm.

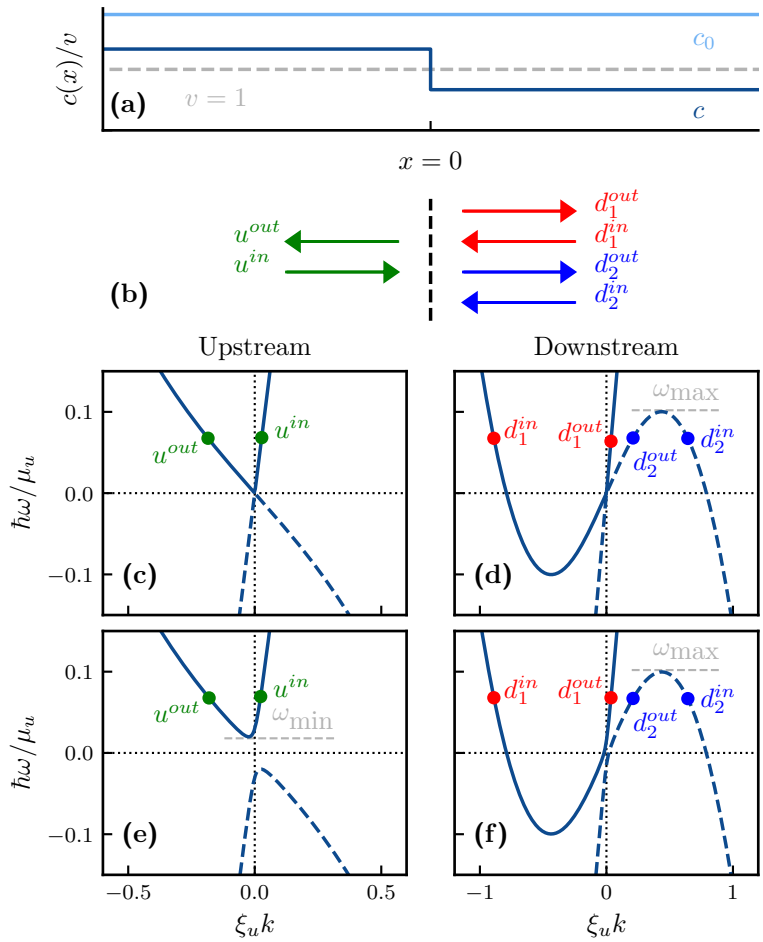

Figure 10.5 – An idealized sonic horizon for spin excitations in a two-component fluid. (a) Velocity profile obtained by modulation of the spin sound velocity c in a uniform background flow v. The velocity ratios are $c_u : v : c_d = 4/3 : 1 : 2/3$, while the density sound velocity is $c_0/v \approx 1.9$ throughout the fluid. (b) Ingoing and outgoing signals propagating in the upstream and downstream regions. (c-f) Upstream and downstream spin dispersion relations for coherent coupling $\hbar\Omega = 0$ (c-d) and $\hbar\Omega = 2\times10^{-4}\mu$ (e-f), indicating the branches of positive-frequency signals shown in (b) for the frequency of the scattering process depicted in Fig. 10.6(b).

10.2.3 Existing literature

In the past two decades, the versatility provided by a system with two experimentally manipulable sound modes and the possibility of additional coupling terms has sparked a variety of proposals regarding its application as a quantum simulator for analog cosmology, ranging from phenomenological quantum gravity [336] to models of early-universe inflation [337] and cosmological particle creation [338].

Within the context of the analog Hawking effect, Larré and Pavloff [339] were the first to study spontaneous analog Hawking radiation of polarization excitations in a two-component mixture, noting explicitly the decoupling from density excitations and suggesting implementations in both polarition condensates and the binary atomic mixture on which we focus. This seminal work, however, did not study the effect of coherent coupling, rendering the spin dispersion and the calculated correlation patterns equivalent to those of the single-component Bose gas studied in Refs. [311, 312]. In a coherently coupled two-component condensate, Butera *et al.* [105] studied black hole lasing, a phenomenon in which emitted Hawking radiation is self-amplified in an effective laser cavity formed by an inner and outer sonic horizon [291]. In a two-dimensional coherently coupled condensate, emission of phononic excitations resulting from the hydrodynamic instability of quantized vortices was studied by Berti *et al.* [340] as an analog model for superradiant emission from the ergoregion surrounding a rotating black hole.

Finally, during the course of our own investigation, two works by Syu *et al.* [341] and Syu and Lee [342] were published, studying in great detail the effect of the coherent coupling on the analog Hawking effect in both the spin and density modes of a two-component condensate. For spin excitations, the spectrum of Hawking radiation emitted out of the sonic black hole was shown to be thermal, with the presence of a finite spectral gap causing a suppression of emission below a threshold frequency [342]. Interestingly, the Hawking effect in the density degree of freedom was found to be affected by the coherent coupling as well, with the presence of gapped spin excitations being detrimental to the entanglement between excitations emitted out of the analog black hole and *partner* modes excited on the inside [341].

10.2.4 Current aims

In relation to these existing studies, the contribution of the present study is twofold. The primary aim of this chapter is to solidify the connection between the

Bogoliubov theory of an idealized sonic horizon [312] and classical simulations of wave packet scattering, i.e., stimulated excitation of the horizon. Going beyond illustrative examples of scattering processes to clarify different frequency regimes of spontaneous Hawking radiation [105, 312, 343], we establish our analysis on the interpretation of the sonic horizon as a scattering object for classical waves, governed by the Gross-Pitaevskii equations (10.13) and emerging from either inside or outside the analog black hole. This allows us to systematically reproduce all semi-analytical (Bogoliubov) predictions of the analog Hawking effect and its spectral properties. Secondly, in addition to deepening the correspondence between stimulated and spontaneous variants of the analog Hawking effect, such classical scattering simulations allow us to extend the semi-analytical results for an idealized horizon to more complicated geometries. In particular, we will explore the dependence of the Hawking process on the finite *width* of the sonic horizon. Besides its relevance to the accurate reproduction of experimental observations [315, 316, 319, 320, 344], this extension will be interpreted in terms of the *surface gravity* and hence Hawking temperature (9.2) of astrophysical black holes. In spite of their relevance to the experimental search for analog Hawking radiation, these two issues, to the best of my knowledge, have not yet been systematically studied in the literature.

10.3 Stimulated scattering of spin waves

With a sonic horizon for spin excitations constructed on the basis of their dispersion relation, we recall that this excitation spectrum equally arises for small amplitude oscillations on a steady state solution of the Gross-Pitaevskii equations (see Secs. 3.1 and 3.2),

$$\begin{aligned} i\hbar\partial_t\psi_1(x,t) &= \left(-\frac{\hbar^2\partial_x^2}{2m} + V_0(x) + g|\psi_1|^2 + g_{12}|\psi_2|^2\right)\psi_1 - \hbar\Omega\psi_2, \\ i\hbar\partial_t\psi_2(x,t) &= \left(-\frac{\hbar^2\partial_x^2}{2m} + V_0(x) + g|\psi_2|^2 + g_{12}|\psi_1|^2\right)\psi_2 - \hbar\Omega\psi_1. \end{aligned} \tag{10.13}$$

Within the mean field approximation, the time evolution of the fluid is inferred by solving the above equations for suitable inititial conditions using the split-operator method. Along with further specifics regarding the numerical implementation, the details of this procedure are moved to Appendix B.1 and B.2. Given the close connection between quantum and classical excitations – a correspondence which forms the basis for analog Hawking investigations in water waves mentioned in Sec. 9.3.1 –, the sonic horizon may be probed in a stimulated way

to observe a classical analogue of the Hawking effect in the scattering of plane waves. This allows one to numerically infer properties of the analog Hawking effect by simulating the time evolution of the Gross-Pitaevskii equations (10.13) without the need to take into account quantum fluctuations which give rise to the spontaneous Hawking effect.

From an experimental point of view, stimulated observation of the analog Hawking effect avoids the notorious weakness of the spontaneous signal in comparison to the thermal cloud of the condensate, three-body heating and shot noise encountered in measurements [314, 345]. While classically stimulated excitation of negative energy modes is not *equivalent* to the spontaneous Hawking effect, it can be considered a prerequisite for the occurrence of its spontaneous counterpart as the kinematic conditions for its observation are the same. In practice, excitations may be stimulated by a periodic modulation of the harmonic trap [102, 317], by means of Bragg spectroscopy [315, 346, 347], short Bragg pulses [348, 349] or through a local potential perturbation [119]. Through the application of a localized laser beam on a small region of an elongated condensate, a wave packet is generated which allows for explicit scattering experiments to be performed on the sonic horizon. Relating this process to the quench dynamics studied in Part III, one may consider the sudden optical perturbation as a temporary quench of the system's Hamiltonian. In a two-component superfluid, a localized spin wave is excited without disturbing the density degree of freedom by applying a spin-selective optical pulse [113, 119, 350] of the form

$$V(x,t) \sim \pm \exp\left(-\frac{t^2}{2\sigma_t^2} - \frac{x^2}{2\sigma_x^2}\right) \cos(kx - \omega t), \tag{10.14}$$

where σ_x^2 and σ_t^2 denote the spatial and temporal widths of the Gaussian pulse, and the sign $\pm$ refers to the potential experienced by the two components ψ_1 and ψ_2, respectively. If the wavelength $\hbar/k$ and frequency ω of the external pulse are tuned to resonance with a point on one of the spin dispersion branches, a propagating spin wave packet emerges in the fluid. Upon collision with the sonic horizon, the ingoing wave packet behaves as if scattering on a potential barrier, being partially reflected and transmitted into all outgoing modes available at the excited frequency ω on both the upstream and downstream side of the horizon.

For the coherently coupled case, Fig. 10.6 shows the outgoing spin waves following the scattering of an ingoing positive norm wave packet emerging from the downstream region – excited along the d_1^{in} branch of the dispersion – at three

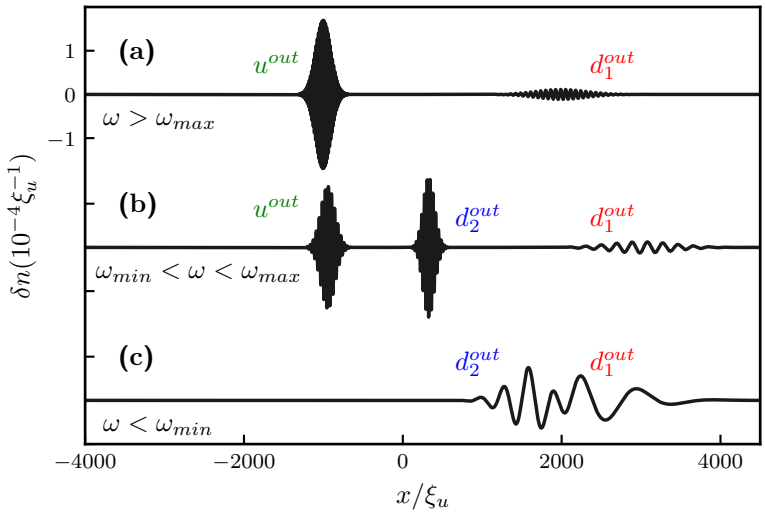

Figure 10.6 – Density profile of outgoing spin waves following the collision of a d_1^{in} wave packet ($\sigma_x = 200\xi$) with the sonic horizon located at $x = 0$. The grey shaded area represents the supersonic downstream region corresponding to the inside of the analog black hole. Depending on the frequency ω, the ingoing wave packet scatters into modes along the u^{out}, d_1^{out} and d_2^{out} dispersion branches. The velocity profile of the fluid is identical to that of Fig. 10.5.

different frequencies. For $\omega > \omega_{\max}$, Fig. 10.6(a), a single excitation is emitted on either side of the horizon, along the u^{out} and d_1^{out} branches of the dispersion, respectively. Below the frequency threshold $\omega \in [\omega_{\min}, \omega_{\max}]$, Fig. 10.6(b), an additional d_2^{out} signal is excited downstream. Recall that this mode, carrying negative energy content within the analog black hole, is characteristic of the Hawking effect. The frequency of this scattering process is indicated by the colored dots in Fig. 10.5(e-f). Finally, in Fig. 10.6(c), the sonic horizon acts as a perfect mirror for downstream ingoing modes of frequency $\omega < \omega_{\min}$, as no modes are available within the effective mass gap upstream. The same qualitative behaviour occurs for scattering of an ingoing d_2^{in} or u^{in} mode, with the restriction that no u^{in} exist at frequencies $\omega < \omega_{\min}$, such that the process of Fig. 10.6(c) cannot be reproduced with an upstream ingoing wave packet. Finally, we note that the difference in σ_x of the involved wave packets results from energy conservation and the different group velocities for each of the modes, a relation which is explained in more detail in Appendix B.3.

10.3.1 Scattering matrix solution

With the analog Hawking effect emerging in the scattering of classical waves on the sonic horizon, we may summarize its properties in terms of a square scattering matrix $\mathcal{S}(\omega)$, the dimension of which depends on the number of modes available at frequency ω. Within the range $\omega \in [\omega_{\min}, \omega_{\max}]$, the scattering matrix $\mathcal{S}(\omega)$ takes the form

$$\begin{pmatrix} \beta_u^{\text{out}} \\ \beta_{d_1}^{\text{out}} \\ \beta_{d_2}^{\text{out}} \end{pmatrix} = \mathcal{S}(\omega) \begin{pmatrix} \beta_u^{\text{in}} \\ \beta_{d_1}^{\text{in}} \\ \beta_{d_2}^{\text{in}} \end{pmatrix}, \tag{10.15}$$

relating the amplitude of spin waves scattering into the horizon to those of the outgoing excitations. For an ingoing signal consisting of an excitation of unit amplitude $\left|\beta^{in}\right|^2 = 1$ on a single branch of the upstream or downstream dispersion, the outgoing amplitudes $\left|\beta^{out}\right|^2$ are interpreted as reflection and transmission coefficients of the sonic horizon.

For the idealized scenario of a uniform condensate divided by an abrupt boundary, the elements of $\mathcal{S}(\omega)$ may be obtained in a semi-analytical way by considering small amplitude oscillations in the spin degree of freedom. As explained in Sec. 3.2, these solutions of the linearized Gross-Pitaevskii equations (10.13) have the same spectrum as the elementary Bogoliubov excitations involved in spontaneous Hawking radiation. In general, a spin perturbation of the fluid is represented by the spin wave function $\psi = \psi_1 - \psi_2$, in general of the form

$$\psi(x,t) = \mathcal{U}(x)e^{i\omega t} + \mathcal{V}(x)e^{-i\omega t}. \tag{10.16}$$

For the spatially uniform fluid under consideration, the Bogoliubov eigenfunctions $\mathcal{U}(x)$, $\mathcal{V}(x)$ are a superposition of plane waves,

$$\begin{pmatrix} \mathcal{U}(x) \\ \mathcal{V}(x) \end{pmatrix} = \sum_{k(\omega)} \frac{\beta_k}{\sqrt{4\pi|v_{g,k}|}} \begin{pmatrix} U_k \\ V_k \end{pmatrix} e^{ikx}, \tag{10.17}$$

with U_k and V_k given by Eq. (3.13) as solutions of the Bogoliubov equations (3.8). The sum runs over all modes (k, ω) present at the oscillation frequency ω, with a consistent solution requiring one to take into account not only the real-valued solutions represented by the available branches of the dispersion relation $\omega(k)$, but also complex-valued solutions representing evanescent waves [312, 321]. As in the textbook treatment of plane waves scattering on a potential step, physical solutions for $\mathcal{U}(x)$ and $\mathcal{V}(x)$ in both the upstream and downstream regions are

found by setting the amplitudes of the ingoing modes as initial conditions and requiring continuity of both functions and their derivative at the sonic horizon. In practice, this amounts to numerically solving four equations on $\mathcal{U}(x)$, $\mathcal{U}'(x)$, $\mathcal{V}(x)$ and $\mathcal{V}'(x)$ for the amplitudes β_k^{out} of the outgoing waves, allowing the scattering matrix to be inferred as

$$|\mathcal{S}_{ij}|^2 = \left|\frac{\beta_i^{out}}{\beta_j^{in}}\right|^2, \qquad i,j \in \{u, d_1, d_2\}. \tag{10.18}$$

10.3.2 Extracting scattering coefficients

In the above definition, the scattering matrix relates the amplitudes of *plane waves* in the *Bogoliubov* basis of eigenmodes. On the other hand, scattering simulations of the Gross-Pitaevskii equations (10.13) are performed in the *atomic* basis with finite-width *wave packets* in order to prevent the interference from boundary effects*. In order to relate the scattering matrix elements to the amplitudes of wave packets emerging from a scattering simulation, the latter are first transformed to the Bogoliubov basis according to

$$\beta_k = \int_{-\infty}^{+\infty} (U^*_{-k'}\psi_{k'} - V^*_{-k'}\psi^*_{-k'})\mathrm{d}k'. \tag{10.19}$$

where ψ_k is the Fourier transform of the spatial profile $\psi(x)$ of a single wave packet, and the integral is performed to account for the finite momentum resolution of a wave packet. Prescription (10.19) can be seen as the classical equivalent to the Bogoliubov transformation (3.11) for field operators. A more detailed account of the numerical procedure has been moved to Appendix B.4. By performing numerical scattering experiments of ingoing waves along the u^{in}, d_1^{in} and d_2^{in} branches of the dispersion and inferring the outgoing amplitudes of Bogoliubov modes, one can reconstruct the scattering matrix according to Eq. (10.18). As the presence and properties of Bogoliubov modes is frequency-dependent, the scattering matrix describing the Hawking process must be inferred separately for each frequency. Before studying the spectral properties of the scattering matrix in more detail in Sec. 10.5, we conclude this section with a distinctive illustration of the Hawking process.

* In particular, the creation of an analog black hole horizon in a system with periodic boundary conditions unavoidably leads to the formation of a *white hole horizon* at the opposite end.

10.3.3 Mode amplification

As noted in Sec. 3.2, the Bogoliubov norm is conserved during time evolution of the linearized Gross-Pitaevskii equations. This is equally true for the scattering dynamics of wave packets, where the definition of the norm* (3.12) is generalized in accordance with Eq. (10.16),

$$\|\psi(x,t)\|_B = \int \Big(|\mathcal{U}(x)|^2 - |\mathcal{V}(x)|^2\Big)\mathrm{d}x. \tag{10.20}$$

Let us consider an ingoing mode along the d_1^{in} branch, i.e., a positive-norm mode impinging on the horizon from inside the analog black hole. For $\omega \in [\omega_{\min}, \omega_{\max}]$, the ensuing scattering process is the one depicted in Fig. 10.6(b). To satisfy conservation of the Bogoliubov norm, we thus require

$$\|\psi_{d_1^{in}}\|_B = \|\psi_{u^{out}}\|_B + \|\psi_{d_1^{out}}\|_B + \|\psi_{d_2^{out}}\|_B. \tag{10.21}$$

Substitution of the Bogoliubov eigenfunction (10.17) in the definition of the norm (10.20) shows that the latter scales with the square of the amplitude $|\beta_k|^2$, such that Eq. (10.21) can be recast into

$$|\beta_{d_1^{in}}|^2 = |\beta_{u^{out}}|^2 + |\beta_{d_1^{out}}|^2 - |\beta_{d_2^{out}}|^2, \tag{10.22}$$

where the minus sign in the last term indicates the negative norm of the d_2^{out} mode. The excitation of a negative-norm d_2^{out} mode at non-vanishing amplitude therefore requires the amplitude of positive norm u^{out} and d_1^{out} modes to be amplified beyond the amplitude of the ingoing d_1^{in} mode. To illustrate this amplification, Fig. 10.7 shows the time evolution of the amplitudes involved in the scattering process. Before the scattering process – indicated by the shaded region – the spin perturbation consists solely of the d_1^{in} wave packet, the amplitude of which is normalized to 1. After collision with the spin-sonic horizon the ingoing spin wave scatters into all outgoing modes as pictured in Fig. 10.6(b). While the d_1^{out} excitation has a near-negligible amplitude, the appearance of a significant negative energy d_2^{out} mode causes the u^{out} wave to be amplified beyond the amplitude of the ingoing d_1^{in} excitation. Recall from Eq. (9.4) that the energy content of an excited mode is given by the product of its frequency and norm. As scattering occurs exclusively between modes of the same frequency as measured in the horizon frame of reference, the amplification of the norm thus implies that the positive energy leaving the analog black hole is larger than that of the

* Note that, in contrast to the quantized case, the Bogoliubov norm of a classical wave function need not be normalized to unity, but instead depends on the amplitude of the excited wave.

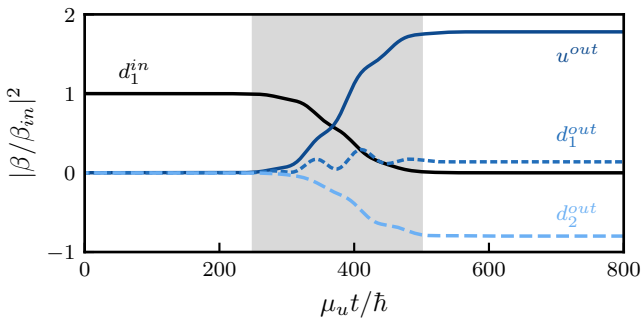

Figure 10.7 – Relative amplitudes of ingoing and outgoing signals in a scattering simulation of an ingoing d_1^{in} mode, illustrating the amplification of the outgoing u^{out} wave through the excitation of a negative energy d_2^{out} wave in the supersonic region. During the collision process (shaded area), small oscillations arise due to interference between the ingoing and outgoing wave packets. The velocity profile of the fluid is identical to that of Fig. 10.5.

initially excited mode on the inside. In what can be considered in analogy to the black hole evaporation discussed in Sec. 9.1, energy is lost from the analog black hole by the excitation of a negative-energy mode in the supersonic region inside.

Note that this process does *not* constitute the extraction of energy from the black hole through outside stimulation, which would require *superradiant* reflection [289] of u^{in} modes impinging from the outside of the analog black hole. As we will see in Sec. 10.5, this reflection is highly suppressed. Both in the astrophysical context [286, 290, 351] and in analog systems [340, 352], superradiant emission requires the black hole to possess either electric charge or angular momentum, extensions beyond the scope of this work.

10.4 Quantization and correlations

NOTE: *Results presented in this section were obtained by Anna Berti.*

Upon quantization of the modes, the scattering matrix solution presented above allows to study spontaneous emission of Hawking radiation resulting from quantum fluctuations at the sonic horizon [312, 339]. To this end, the classical field amplitudes β_j ($j \in \{u, d_1, d_2\}$) are replaced with field operators as in Sec. 3.2. Distinguishing between ingoing ($\hat{a}_j$) and outgoing ($\hat{b}_j$) modes, Eq. (10.15) then

generalizes to

$$\begin{pmatrix} \hat{b}_u(\omega) \\ \hat{b}_{d_1}(\omega) \\ \hat{b}^\dagger_{d_2}(\omega) \end{pmatrix} = \mathcal{S}(\omega) \begin{pmatrix} \hat{a}_u(\omega) \\ \hat{a}_{d_1}(\omega) \\ \hat{a}^\dagger_{d_2}(\omega) \end{pmatrix}. \tag{10.23}$$

The negative norm of d_2 modes is represented in their appearance as creation rather than annihilation operators. From a mathematical perspective, this fact is precisely at the origin of the spontaneous Hawking effect [312]. To see this, note that the number of excitations emitted into the upstream region – representing the outside of the analog black hole – is related to the number of excitations on the ingoing branches through

$$\langle \hat{b}^\dagger_u \hat{b}_u \rangle = |\mathcal{S}_{uu}|^2 \langle \hat{a}^\dagger_u \hat{a}_u \rangle + |\mathcal{S}_{ud1}|^2 \langle \hat{a}^\dagger_{d_1} \hat{a}_{d_1} \rangle + |\mathcal{S}_{ud2}|^2 \Big(\langle \hat{a}^\dagger_{d_2} \hat{a}_{d_2} \rangle + 1 \Big), \tag{10.24}$$

where we used the orthogonality of the ingoing modes, i.e., $\langle \hat{a}^\dagger_i \hat{a}_{j\neq i} \rangle = 0$. Immediately following the creation of the horizon in a system at zero temperature, the initial populations $\langle \hat{a}^\dagger_j \hat{a}_j \rangle$ of all excitation branches is zero. One then finds that a finite outgoing signal derives from the commutator in the last term of Eq. (10.24),

$$\langle \hat{b}^\dagger_u \hat{b}_u \rangle = |\mathcal{S}_{ud2}|^2, \tag{10.25}$$

which may be interpreted as the spontaneous creation of particle-antiparticle pairs at the horizon. As in the astrophysical context explained in Sec. 9.1, this process is enabled by the presence of negative energy modes in the downstream region. In contrast to the astrophysical case, however, the downstream region of a sonic horizon is accessible to optical measurements. As such, the creation of correlated excitations gives rise to non-local correlation patterns between both sides of the horizon, as previously shown in Fig. 9.3.

In a binary mixture, density-density correlations (9.9) are generalized to two-point correlation functions of the form

$$G_{aa}(x, x') = \frac{\langle :\hat{F}_a(x,t)\hat{F}_a(x',t): \rangle}{n^2}, \tag{10.26}$$

where $\hat{F}_a$ are the elements of the spin vector characterizing the two-component fluid,

$$\hat{\mathbf{F}} = \Big(2\,\mathrm{Re}\Big\{ \hat{\psi}^\dagger_1 \hat{\psi}_2 \Big\}, 2\,\mathrm{Im}\Big\{ \hat{\psi}^\dagger_1 \hat{\psi}_2 \Big\}, \hat{n}_1 - \hat{n}_2 \Big). \tag{10.27}$$

Upon expressing the elements of $\hat{\mathbf{F}}$ to first order in excitation operators, the correlations $G_{aa}(x, x')$ at zero temperature may be written in terms of the semi-

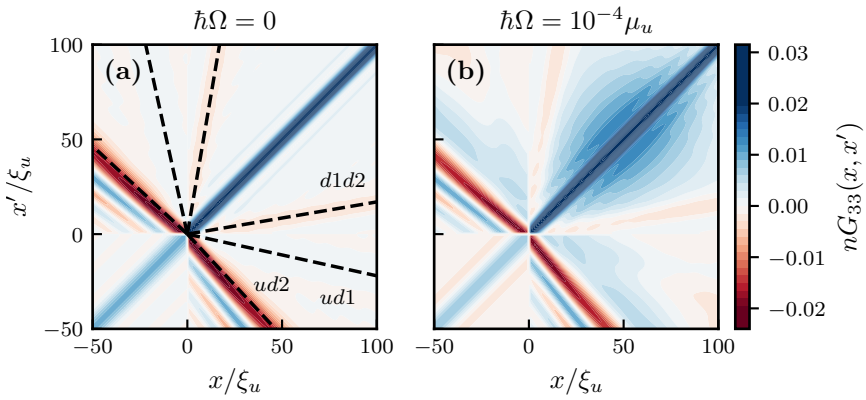

Figure 10.8 – Density correlations $G_{33}(x, x')$ across the spin-sonic horizon at $x = 0$ in an uncoupled binary mixture (a) and for coherent coupling $\hbar\Omega = 10^{-4}\mu_u$ (b). Dashed lines indicated in (a) represent the ratios of sound velocities ($xc_j = x'c_i$) for the indicated modes, and correspond to the expected location of correlation fringes.

analytically inferred scattering matrix elements $\mathcal{S}_{ij}$, generalizing the approach of Recati *et al.* [312] for a single-component Bose gas. Figure 10.8 shows the resulting density correlations $G_{33}(x, x')$ in the spin degree of freedom for both and an uncoupled and coherently coupled binary mixture across a sharp spinsonic horizon given by Eq. (10.11). Antidiagonal density correlations between both sides of the horizon are emblematic of the Hawking process. In particular, the main *moustache* corresponds to correlations between positive-energy u modes in the upstream region and negative-energy d_2 modes downstream, as evidenced by the agreement between its slope and the ratio of the respective sound velocities, ($xc_{d_2} = x'c_u$), shown by the $ud2$ dashed line.

Equation (10.25) represents a crucial insight underlying the present focus on the stimulated Hawking effect. Namely, the fact that the spectral properties of spontaneous Hawking radiation are wholly characterized by the properties of the sonic horizon as a scattering object for classical waves. We will build on this fact in the following section, where we study the frequency dependence of the analog Hawking effect for spin excitations via scattering simulations of wave packets.

10.5 Spectral properties of the Hawking effect

Having established the spin-sonic horizon and verified how it exhibits both the stimulated and spontaneous Hawking process for spin excitations described by

a single scattering matrix $\mathcal{S}(\omega)$, we proceed with a quantitative analysis of its spectral properties.

10.5.1 Reconstructing the dispersion

Before attempting to infer the frequency dependence of the scattering matrix elements through wave packet scattering, one must verify that this approach provides access to the entire dispersion of the fluid – in particular the appearance of the negative-norm d_2^{out} mode. To this end, we reconstruct the excitation spectrum of spin excitations on both sides of the horizon. This is achieved by numerical integration of the Gross-Pitaevskii equations (10.13) for scattering processes at different frequencies ω of the ingoing wave packet (10.14), and resolving the momentum spectrum $k(\omega)$ of the outgoing signals*. The result is shown in Fig. 10.9 for the case of ingoing d_1^{in} excitations both without (a, b) and with coherent coupling (c, d). Within the limits of the spectral resolution $\sigma_k^{out} \sim (\sigma_x^{in} v_g^{out}/v_g^{in})^{-1}$, the resulting heatmap of the inferred amplitudes (10.19) is in near perfect agreement with the predicted spectrum in both regions. In particular, the pronounced signal coinciding with the d_2^{out} branch of the downstream dispersion confirms the existence of negative energy excitations dinstinctive for the Hawking process at $\omega < \omega_{\mathrm{max}}$. Note that the high-$k$ part of the d_2 branch contains ingoing modes, which cannot be retrieved from any signal leaving the sonic horizon. In the upstream region, the absence of excitations at frequencies below the spectral gap ω_{min} illustrates the perfect reflection of downstream ingoing modes in this frequency regime.

10.5.2 Uncoupled mixture

Figure 10.10 shows the frequency dependence of scattering coefficients in an uncoupled mixture ($\Omega = 0$), inferred from scattering simulations of the Gross-Pitaevskii equations over a range of frequencies in the laboratory frame (thick, full lines). Panels (a), (b) and (c) show the elements of $\mathcal{S}(\omega)$ for ingoing u^{in}, d_1^{in} and d_2^{in} modes, respectively, while lines of different colors indicate the mode of the outgoing wave. Shown for comparison are the results of a semi-analytical calculation explained in Sec. 10.3.1 (dashed lines), exhibiting near-perfect agreement with the simulated result. As the spin spectrum of the uncoupled mixture is qualitatively the same as that of its density excitations (10.1) and thus the

* Alternatively, one may infer the entire spectrum immediately by simulating the fluid's response to an infinitesimally peaked perturbation $\delta(x - x_0)\delta(t - t_0)$ which excites the fluid at all frequencies and momenta. As off-resonant excitations are evanescent, a spatiotemporal Fourier transform $|\psi(k, \omega)|^2$ of the long-time evolution reveals the dispersion in both regions.

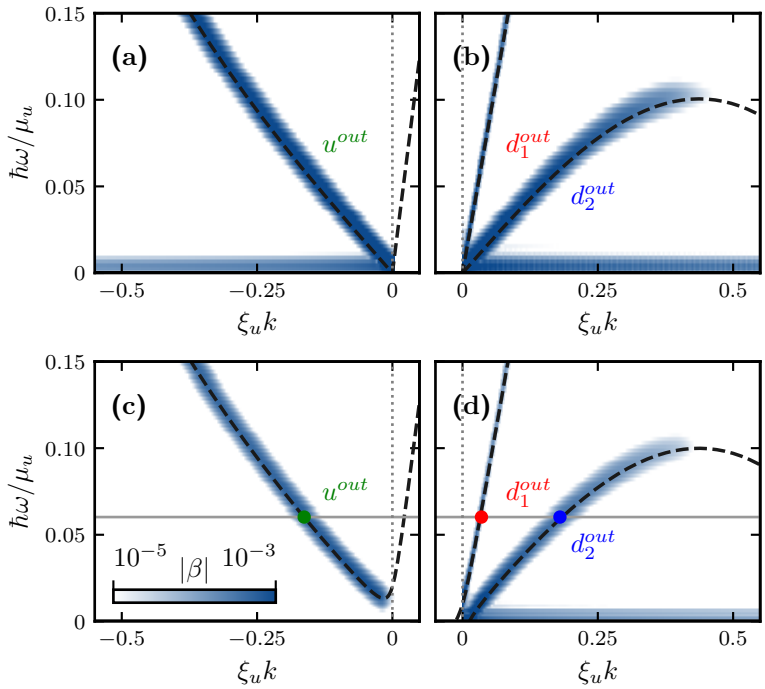

Figure 10.9 – Upstream (left) and downstream (right) spin dispersion probed through the scattering of d_1^{in} wave packets on the sonic horizon for $\hbar\Omega = 0$ (top) and $\hbar\Omega = 10^{-4}\mu_u$ (bottom). The velocity profile of the fluid is identical to that of Fig. 10.5. The horizontal line and markers in (c,d) indicate the frequency illustrated in Fig. 10.6(b). The horizontal width of the inferred signal is inversely proportional to the width of the ingoing wave packet, with relative differences between signals due to the difference in group velocity (see Appendix B.3).

dispersion a single-component Bose gas (3.9), this result is analogous to that in the study by Recati *et al.* [312].

Ingoing u^{in} modes, shown in Fig. 10.10(a), are predominantly transmitted to the d_1^{out} mode, with an additional transmission into the negative energy d_2^{out} mode appearing below the Hawking threshold $\omega < \omega_{\max}$. Note that, in contrast to the astrophysical case, the sonic horizon does not act as a perfect absorber, as its reflectivity $|\mathcal{S}_{uu}|^2$ vanishes only in the limit $\omega \to \infty$. No superradiant amplification of the ingoing mode is observed either, as $|\mathcal{S}_{uu}(\omega)|^2 < 1$ for all frequencies. As remarked earlier in Sec. 10.3.3, no energy can therefore be extracted from the analog black hole through outside stimulation.

More pronounced consequences of the analog Hawking effect can be witnessed in the scattering coefficients of ingoing d_1^{in} mode shown in Fig. 10.10(b), impinging on the horizon from the interior of the black hole. Above the Hawking threshold $\omega_{\max}$, the horizon again acts as a near-perfect transmitter into the u^{out} mode. This time, however, the negative energy d_2^{out} signal emerging for $\omega < \omega_{\max}$ does not saturate as in Fig. 10.10(a) as ω approaches zero. Rather, all the outgoing amplitudes are seen to diverge as $1/\omega$. This is a consequence of the $1/k$ divergence of the Bogoliubov coefficients (3.13) and is related to the presence of a Goldstone mode at $(k, \omega) = (0, 0)$. The absence of this feature in the scattering coefficients of a u^{in} ingoing mode is explained by the fact that the Bogoliubov amplitude of the ingoing mode in this case equally diverges. In analogy to the thermal spectrum of Hawking radiation (9.2), the $1/\omega$ divergence allows one to infer an analog Hawking temperature, as it corresponds to the low-frequency behaviour of the Bose-Einstein distribution [353],

$$\left|\frac{\beta}{\beta_{in}}\right|^2 = \frac{1}{\exp\left\{\frac{\hbar\omega}{k_B T_H}\right\} - 1} \approx \frac{k_B T_H}{\hbar\omega}, \quad (\hbar\omega \ll k_B T_H). \tag{10.28}$$

From the $|\mathcal{S}_{ud1}|$ and $|\mathcal{S}_{ud2}|$ signals in Fig. 10.10, we infer a finite analog Hawking temperature of about $k_B T_H \approx 10^{-1}\mu_u$, the interpretation of which we will comment on in Sec. 10.6. As previously observed in Fig. 10.7, the d_1^{out} signal is overshadowed by the amplitudes of d_2^{out} and u^{out} wave packets, which grow to equal magnitude in the limit $\omega \to 0$. Note that the divergence of $|\beta_{out}|^2$ does not imply that the energy emitted from the analog black hole diverges in the long wavelength limit, as the energy content of an excitation (9.4) is given by the product of its frequency and norm (which scales as $|\beta|^2$).

For ingoing modes excited along the negative energy d_2^{in} branch, Fig. 10.10(c), the qualitative behaviour is roughly the same, with the additional caveat that

scattering coefficients are defined only for $\omega < \omega_{\max}$, as no propagating d_2 modes are present at higher frequencies. Anticipating a quantized treatment of the scattering process – discussed in Sec. 10.4 –, it is relevant to remark that spontaneous Hawking radiation results from a finite vacuum occupation of d_2 modes and is thus captured precisely in the scattering properties of ingoing d_2^{in} waves.

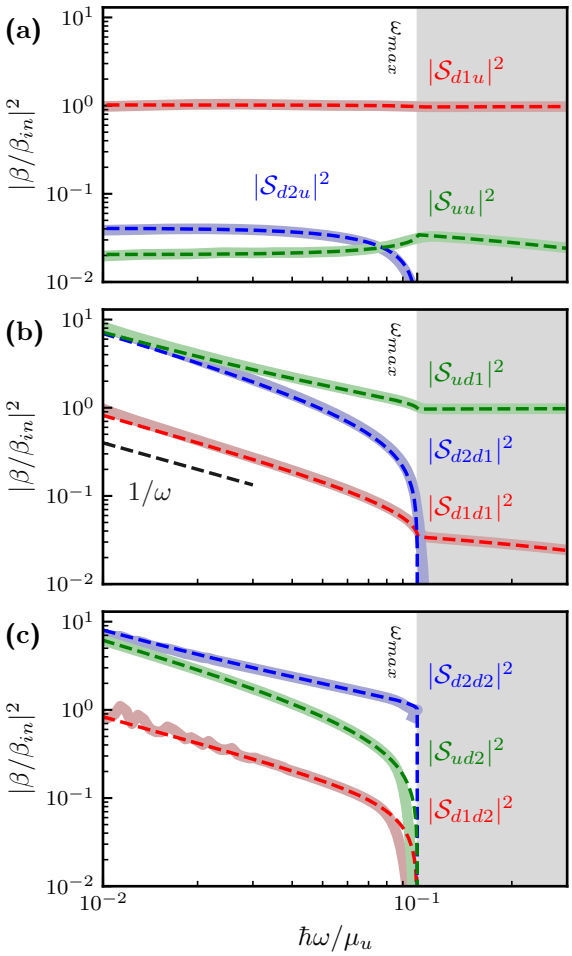

Figure 10.10 – Frequency dependence of the scattering matrix elements for $\hbar\Omega = 0$. Dashed lines indicate the Bogoliubov prediction, thick full lines represent the transmission and reflection coefficients inferred through wave packet scattering. The velocity profile of the fluid is identical to that of Fig. 10.5.

10.5.3 Coherent coupling

With the introduction of a coherent coupling Ω, the above result changes due to the opening of a spectral gap in the upstream region. Recall that this gap is present in the downstream region as well, but modes remain available at all frequencies due to the strong Doppler shift – see Fig. 10.5(f). The frequency dependence of the scattering matrix is shown in Fig. 10.11 for a weak homogeneous coupling $\hbar\Omega = 10^{-4}\mu_u$. While the results at high frequency remain the same as in Fig. 10.10, the low-frequency behaviour is strongly affected by effective mass of the spin field.

Let us first concentrate on the scattering properties of ingoing u^{in} modes impinging from the upstream region, shown in Fig. 10.11(a). For frequencies approaching the Doppler-shifted plasma frequency $\omega_{\min}$, the reflectivity $|\mathcal{S}_{uu}|^2$ shows a sharp increase, accompanied by a sudden drop in the transmission coefficients $|\mathcal{S}_{d1u}|^2$ and $|\mathcal{S}_{d2u}|^2$. While the sonic horizon thus becomes a perfect mirror for ingoing u^{in} excitations for $\omega \to \omega_{\min}$, the vanishing group velocity in this limit makes this rather trivial, as modes excited at this frequency don't propagate at all in the upstream region. For the same reason, increasingly long time evolution is required to perform scattering experiments with nearly stationary wave packets, resulting in relatively high levels of noise in the limit $\omega \to \omega_{\min}$.

For ingoing d_1^{in} and d_2^{in} modes emerging from the interior of the analog black hole, shown in Fig. 10.11(b, c), the upstream mass gap at $\omega_{\min}$ results in a perfect reflection, as the transmittivities $|\mathcal{S}_{ud_1}|^2$ and $|\mathcal{S}_{ud_2}|^2$ (green lines) decay to zero. Contrary to the sharp decrease predicted by Bogoliubov theory (dashed lines), the simulated result is smoothed due to the finite spectral resolution of wave packets. Importantly, the $1/\omega$ divergence of scattering coefficients into both the d_1^{out} (red) and d_2^{out} modes (blue) is regularized by the effective mass of spin excitations, converging to a finite value as $\omega \to 0$. Note that this implies, in view of Eq. (10.28), that no analog Hawking temperature can be assigned to the emitted radiation in the presence of coherent coupling. Whereas the effect of the coupling on scattering into the d_2^{out} mode (blue lines) is limited to this regularization, low-frequency scattering into d_1^{out} has increased significantly when compared to the uncoupled case in Fig. 10.10(b, c). Accompanying the disappearance of transmission into the u^{out} mode, this follows necessarily from the requirement that the total Bogoliubov norm remains conserved in the scattering process.

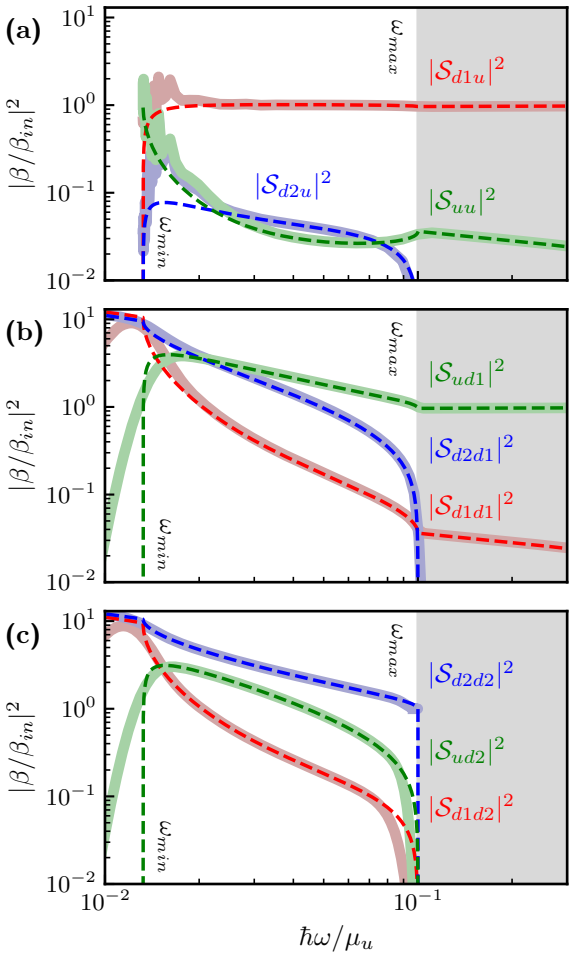

Figure 10.11 – Frequency dependence of the scattering matrix elements for $\hbar\Omega = 10^{-4}\mu_u$. Dashed lines indicate the Bogoliubov prediction, thick full lines represent the transmission and reflection coefficients inferred through wave packet scattering. The velocity profile of the fluid is identical to that of Fig. 10.5.

10.6 Analog Hawking temperature

We have so far considered an idealized sonic horizon formed by a sharp, step-like modulation of the interaction strength. While exhibiting the analog Hawking effect, this configuration constitutes an unphysical analogue to astrophysical black holes. In the final section of this chapter, we introduce the analog equivalent of a black hole's *surface gravity* and study how it affects the temperature of the analog Hawking radiation.

10.6.1 Surface gravity

In analogy to the surface gravity g of stellar objects, the surface gravity of a black hole may be defined as the acceleration of an object infinitesimally close to the event horizon*. For a Schwarzschild black hole, the surface gravity is given by [286, 293]

$$\kappa = \frac{c^4}{4GM}. \tag{10.29}$$

Through its dependence on the black hole mass, this quantity is linearly proportional to the Hawking temperature (9.2) of the emitted radiation spectrum,

$$k_B T_H = \frac{\hbar\kappa}{2\pi c}. \tag{10.30}$$

In the sonic analogue, an analog surface gravity may be defined as the local gradient of the flow velocity profile at the event horizon [288, 303, 308, 353, 354]. Considering as before a sonic horizon at $x = 0$ resulting from a spatially varying chemical potential in a uniform background flow velocity $v(x) = v$, we define

$$\kappa = -\left.\frac{\mathrm{d}c(x)}{\mathrm{d}x}\right|_{x=0} = -\left.\frac{1}{2m}\frac{\mathrm{d}\mu(x)}{\mathrm{d}x}\right|_{x=0}, \tag{10.31}$$

where the sign choice ensures a positive surface gravity, while the last equality stems from Eq. (10.6) and the fact that $c = v$ at the horizon. In the step-like modulation of the sound velocity studied thus far, the local gradient of μ diverges at the sonic horizon, corresponding therefore to a black hole of infinite surface gravity with an associated emission spectrum at $T_H \to \infty$.

However, we have seen in Fig. 10.10 that this is not the case, as the $1/\omega$ divergence of the amplitude implied a finite Hawking temperature through Eq. (10.28). As

* Note that since the acceleration experienced by an object at the event horizon with respect to its proper time diverges, the acceleration is defined in the reference frame of a distant observer, such that a diverging time dilation between this frame and the event horizon results in a well-defined, finite surface gravity [286].

anticipated in Sec. 9.2.2, this can be understood from the natural UV cutoff of the analog Hawking effect in a superluminal dispersion [307, 308]. Indeed, Fig. 10.5 shows that negative-energy modes are present up to a finite maximum momentum, introducing a minimal length scale set by the healing length (9.5). On shorter length scales, the hydrodynamic approximation is violated by the nonlinear dispersion, and no negative-energy modes are present to participate in the Hawking process [303, 306, 310]. This limits the length scale of features (including the spatial velocity profile) affecting the Hawking effect, and therefore places an upper bound on the effective surface gravity of the sonic horizon and the temperature of analog Hawking radiation. To study the finite temperature of the analog Hawking effect in more detail, we extend in this final section the step-like velocity profile across the sonic horizon to a smooth spatial profile.

Besides the astrophysical analogue, the predicted changes to the Hawking radiation emerging from a smooth horizon are also relevant from an experimental point of view. Indeed, recall from Sec. 9.3 that a sonic horizon in reality results from a modulation of the fluid's density and velocity by an external potential. The maximal steepness of the density modulation of the fluid is bound by the healing length ξ, but is in reality often of the order of several healing lengths [315, 317, 319]. In order to predict the intensity of the analog Hawking signal in experimentally realistic settings, a clear understanding of its dependence on the spatial profile of the spinsonic horizon is therefore required.

10.6.2 Smooth interaction step

To generalize the step-like horizon (10.11) to one of finite surface gravity, we consider a spin chemical potential with a smoothly varying spatial profile of the form

$$\mu(x) = \frac{\mu_u + \mu_d}{2} + \left(\frac{\mu_d - \mu_u}{2}\right) \tanh\left(\frac{x}{\sigma_x}\right), \tag{10.32}$$

where σ_x denotes the width of the sigmoid function, shown in Fig. 10.12(a). As anticipated in Sec. 10.2.4, we note that this extension is not possible within the Bogoliubov approach of Sec. 10.3.1 [312], which relies on the matching of wave functions on both sides of a sharp, discrete sonic horizon.

The slope of $\mu(x)$ is locally linear at the sonic horizon, resulting in a finite surface gravity inversely proportional to the horizon width,

$$\kappa = \frac{c_u^2 - c_d^2}{4\sigma_x}. \tag{10.33}$$

The upper bound to this quantity is set by the shortest length scale to which

the fluid is sensitive*, $\sigma_x^{(\min)} \approx \xi/2$, which in turn sets a approximate maximal analog Hawking temperature through Eq. (10.30),

$$k_B T_H^{(\max)} \approx \frac{\hbar(c_u^2 - c_d^2)}{4\pi c\xi}. \tag{10.34}$$

Figure 10.12(b) shows the frequency dependence of the scattering matrix elements inferred from the transmission and reflection of ingoing d_1^{in} wave packets on a sonic horizon for different values of σ_x, shown in the inset of Fig. 10.12(a). Dashed lines indicate the semi-analytical result for a sharp horizon as shown in Fig. 10.10. The Hawking effect, most predominantly witnessed in the amplification of the u^{out} and d_2^{out} modes in Figs. 10.12(a) and (c), is seen to diminish with increasing width of the horizon.

In each scattering experiment, the relative smoothness of the horizon depends on the ratio of its length scale and the wavelength of the impinging packet, i.e., $\sigma_x k_{d_1^{in}}(\omega)$. As a result, changes to the scattering properties are apparent first in the high-k regime, whereas long-wavelength excitations are more robust to the width of the horizon. In the limit $\sigma_x \to \infty$, the scattering process reduces to perfect transmission into the u^{out} mode, consistent with the fact that no reflection takes place on a locally constant potential.

Shown in Fig. 10.12(c), the analog Hawking temperature is found to scale as σ^{-1} in the regime $\sigma_x \geq \xi_u$, consistent with Eqs. (10.30) and (10.33). For sharper modulations $\sigma_x < \xi_u$, the Hawking temperature saturates nearly perfectly to the estimated maximum (10.34), consistent with the fact that excitations in the spin degree of freedom are insensitive to spatial features of length scales shorter than ξ. Small deviations from the $1/\sigma_x$ trend in the regime $\sigma_x \gg \xi_u$ are a consequence of a departure from the approximate thermal spectrum $|\mathcal{S}_{ud2}| \sim 1/\omega$ at the frequencies for which it is inferred, as visible in Fig. 10.12(b).

As noted earlier, no Hawking temperature can be assigned to the radiation spectrum in a coherently coupled fluid, where the opening of a gap in the upstream dispersion introduces an infrared cutoff which regularizes the $1/\omega$ divergence of the scattering coefficients. Nevertheless, the dependence of the emitted radiation on the width of the horizon is qualitatively similar to that of the uncoupled mixture, as shown in Fig. 10.13. While the limit of a sharp horizon retains the

* Here we introduced the geometrical mean $\xi = \sqrt{\xi_u \xi_d}$ of the upstream and downstream spin healing lengths as the relevant length scale [317, 319, 321], as both are at play at the spinsonic horizon. The factor 1/2 accounts for the fact that the width of the velocity profile (10.32) is given by $2\sigma_x$.

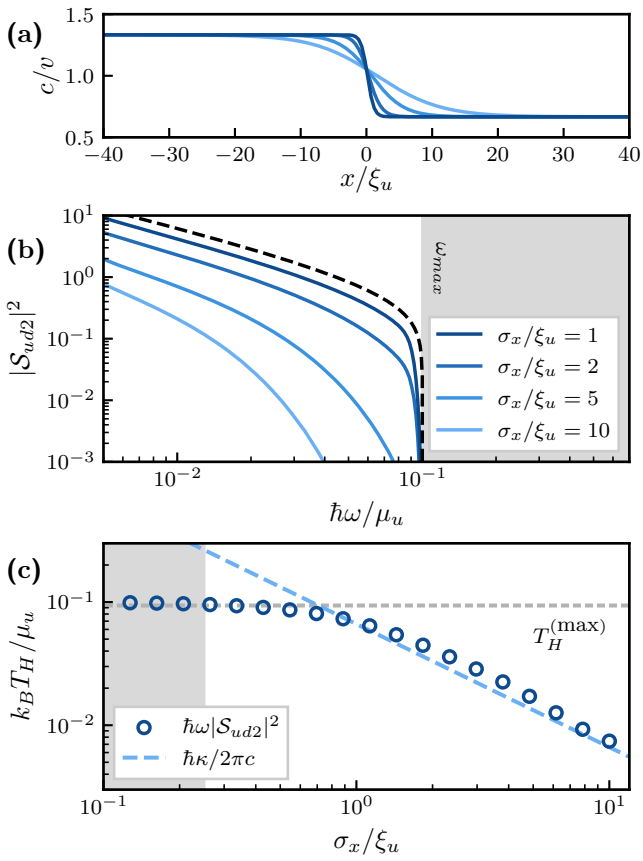

Figure 10.12 – Hawking signal emitted from a finite-width spinsonic horizon in an uncoupled mixture ($\Omega = 0$). (a) Velocity profile resulting from a spatial modulated chemical potential (10.32) of different widths σ_x. (b) Scattering coefficients $\mathcal{S}_{ud2}$ corresponding to spontaneously emitted Hawking radiation from the horizons shown in (a). The dashed line indicates the Bogoliubov prediction for a sharp horizon, previously shown in Fig. 10.10(c). (c) Hawking temperature of the emitted signal, inferred according to Eq. (10.28) from the low-frequency solution ($10^{-3} < \hbar\omega/\mu_u < 2\times10^{-2}$) of the scattering matrix elements in (b). The grey region indicates the grid discretization $\Delta_x = \xi_u/4$.

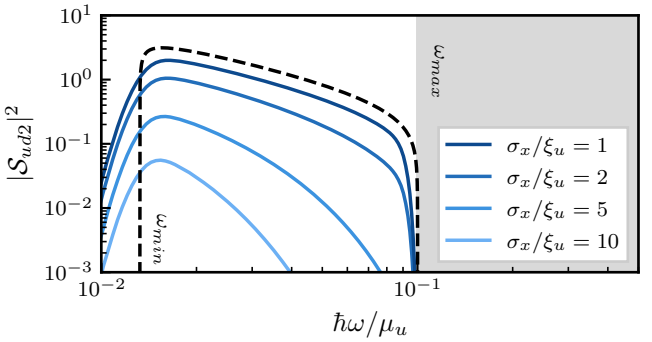

Figure 10.13 – Scattering coefficients $\mathcal{S}_{ud2}$ corresponding to the Hawking signal emitted from a finite-width spinsonic horizon in the presence of a coherent coupling term $\hbar\Omega = 10^{-4}\mu_u$. Velocity profiles are the same as in Fig. 10.12(a). The dashed line indicates the Bogoliubov prediction for a sharp horizon, previously shown in Fig. 10.11(c).

approximately thermal $1/\omega$ scaling for $\omega_{\text{min}} \ll \omega \ll \omega_{\text{max}}$, the emission spectrum of a smooth horizon ($\sigma_x \gg \xi_u$) contains no such regime.

Contrary to the uncoupled case, the absence of an infrared regime in which the emission coefficient remains of the order ~ 1 in the limit of a smooth horizon, implying that spontaneous Hawking radiation of gapped excitations may be extremely difficult to observe for any spinsonic horizon of finite width $\sigma_x \geq \xi_u$. However, both in the absence and presence of coherent coupling, the insensitivity of the Hawking spectrum to the width of the horizon up to the order $\sigma_x \approx \xi$ suggests that the limit of a sharp horizon may be easier to realize for spin excitations in a binary mixture than for density sound modes of a single-component fluid. Indeed, the spatial modulation of a density profile is limited only by the density healing length defined in Eq. (10.4), which for a binary mixture of ^{23}Na atoms is $\xi_0 \approx \xi/5$ [119, 333]. This implies that spin excitations are insensitive to spatial features of the sonic horizon up to widths of $5\xi_0$. As such, spin excitations and their analog Hawking signal are insensitive to spatial features of the sonic horizon up to widths of the order $\sigma_x \approx 5\xi_0$, a length scale below which they should be in agreement with the semi-analytical prediction of a sharp horizon.

10.7 Summary

In this chapter, we have studied the application of a two-component spinor fluid as a platform for the observation of analog Hawking radiation. We have shown how the additional degree of freedom gives rise to spin excitations with a propagation velocity distinct from density sound waves, and allows for the study of massive modes upon the introduction of a coherent coupling. Constructing a spinsonic horizon in a density-subsonic fluid, the analog Hawking effect for spin excitations was studied through scattering simulations of classical wave packets. Finding near perfect agreement of the inferred magnitude of emitted radiation with a semi-analytical Bogoliubov prediction, we have found that the spectral properties of the Hawking effect may be inferred both in absence and presence of coherent coupling. To guide future experiments, we have studied the effect of the horizon's steepness on the Hawking temperature of the emitted radiation. The rise of the Hawking temperature with increasing surface gravity was found to saturate at a length scale set by the spin healing length, suggesting that the construction of an effectively sharp spinsonic horizon through density modulation may be within reach of current experiments. For spinsonic horizons which are smooth on a longer scale than the healing length, the infrared cutoff introduced by the mass gap of a coherently coupled fluid was shown to limit the expected amplitude of spontaneous Hawking emission.

– *"So, Kramer, what are you going to do?"*

– *"Do? Do?!*
Hey, I'm doing what I do.
You know, I've always done what I do.
I'm doing what I do, the way I've always done it.
And the way I'll always do it."

– *"Kramer, what the hell are you talking about?"*

– *Seinfeld*, S4E02

11 | Conclusions and outlook

In this thesis, we have explored three interconnected topics regarding the role of fluctuations in many-body quantum systems, specifically applied to the dynamics of ultracold bosonic fluids.

In **Part II**, we have developed the Gaussian trajectory approach to extend the regime of applicability of Gaussian variational states. Taking inspiration from the paradigm of open quantum systems, this was done by introducing a virtual environment which provides decoherence of quantum superpositions inadequately captured by Gaussian states. We have argued how a suitable implementation of the resulting artificial dissipation may provide an accurate description of the isolated quantum system, and demonstrated its feasibility in a small Bose-Hubbard chain. Chaotic dynamics in this system were shown to cause a rapid growth of fluctuations, resulting in large squeezing of a Gaussian variational state in an attempt to capture non-classical correlations. Adding a weakly coupled virtual environment, we have observed a drastic improvement in the performance of the Gaussian theory. Within a range of the chosen dissipation strength spanning over an order of magnitude, the developed approach robustly reproduces transient dynamics of the chain. As regards the fine-tuning of free parameters, we have found that the conservation of energy emerges as a natural criterion. The approach was further refined with a projection protocol for dissipated states to exactly satisfy conservation laws. In addition, we have introduced a two-step procedure which effectively results in an adaptive dissipation strength, regulating the growth of quantum fluctuations to a chosen tolerance.

In **Part III**, we have turned our attention to spin mixing dynamics in a spin-1 fluid, where a sudden quench to degeneracy of the hyperfine states causes the relaxation to a fragmented condensate. Similarly manifesting as an intractable

growth of fluctuations, the evolution to this highly entangled many-body state is beyond the Gaussian variational approximation. Applying the trajectory approach developed in Part II, we have succeeded in describing the fragmentation process within the Gaussian variational theory. While exhibiting a similar robustness with respect to the dissipation strength in the transient regime, the evolution to the generalized Gibbs (GGE) steady state in the long-time limit was found to be insensitive to the free parameter within over an order of magnitude.

Motivated by the crucial role of conservation laws and their enforcement in the dynamics, we have studied the dynamics of a dissipative spin-1 condensate. Within the truncated Wigner approximation, a weakly coupled environment was found to cause a breaking of integrability, causing the system to relax from a generalized Gibbs ensemble to an internal distribution of spin populations in agreement with thermal equilibrium. Occurring on a universal time scale set by the dissipation strength, this process results in the appearance of a long-lived plateau for single-body observables, bearing analogy to prethermalization in an isolated system. To solidify the equivalence between decoherence from the environment and coherent interactions leading to thermalization in a larger, isolated quantum system, we studied the long-time dynamics of an extended spin-1 Bose-Hubbard model, finding a similar prethermal plateau with a lifetime set by the site-to-site tunneling amplitude. In the regime dominated by tunneling dynamics, an effective single-mode system was recovered in the lowest single-particle orbital of the chain. Finally, we related this observation to the high-loss regime of a dissipative single-mode fluid, where rapid depletion of the condensate invalidates the truncated Wigner approximation. Reducing to approximately linear dynamics, this regime is well within reach of the Gaussian trajectory approach, which uncovered evidence for the existence of a dissipative phase transition in the fractional steady state spin population, interpreted in terms of the quantum Zeno effect. As a function of the dissipation rate, we characterized the purity of individual trajectories and found that highly coherent instances of the fluid may be measured within a window of the dissipation strength which grows linearly with the number of atoms in the system.

Finally, in **Part IV**, we shifted our focus to the application of spinor condensates as a platform for analog gravity. Inspired by recent experiments which revealed the appearance of a distinct spin sound velocity in a two-component mixture and the possibility of constructing an effectively massive field of spin excitations, we studied the analog Hawking radiation of spin waves emerging from a spinsonic event horizon in a density-subsonic fluid. By performing semiclassical simulations of wave packet scattering on a sharp horizon dividing the fluid in regions of sub-

sonic and supersonic flow, we have focused on the observation of analog Hawking signatures through external stimulation by means of Bragg spectroscopy. Doing so, we have shown how the appearance of negative energy modes in the supersonic region enables the amplification of modes in the subsonic region, effectively representing the evaporation of energy from the analog black hole. Going beyond qualitative signatures of the Hawking effect, we inferred the spectral properties of the spinsonic horizon, finding near perfect agreement with a semi-analytical solution based on the Bogoliubov theory of elementary excitations, both in the absence and presence of coherent coupling between the components of the superfluid.

Extending to geometries beyond the reach of the Bogoliubov prediction, we studied the spectrum of Hawking radiation emitted from a spinsonic horizon formed by a smooth velocity profile. For the uncoupled mixture, we found the analog Hawking temperature to be inversely proportional to the width of the horizon, finding quantitative agreement with an analytical prediction based on an analogy to the surface gravity of an astrophysical black hole. For a coherently coupled mixture, we related the decay of the Hawking signal with decreasing surface gravity to the maximal intensity of the emitted radiation, predicting the observation of Hawking radiation of massive excitations to be more severely hampered by spatial artefacts in the velocity profile of the sonic horizon. Finally, we found the Hawking effect of both massless and massive excitations to be unaffected by spatial features on length scales shorter than the spin healing length. In currently realized ^{23}Na mixtures, this length scale is 5 times larger than the density healing length limiting the modulation of the sound velocity, suggesting that the idealized case of a sharp sonic horizon may be within experimental reach for spin waves.

Outlook

The work presented in this thesis naturally leaves many questions unanswered, and has sparked an abundance of ideas for additional investigations. To conclude, we suggest some possible directions for future research.

For the Gaussian trajectory approach developed and benchmarked in this thesis, a natural next challenge lies in the extension to larger systems. In spite of general criteria such as the eigenstate thermalization hypothesis (ETH), a general understanding of the dynamics of thermalization remains an open question. As anticipated in Sec. 5.5, the consistency of the Gaussian variational theory with the Bose-Einstein distribution suggests that the Gaussian trajectory approach

may capture thermalization of systems far outside the mean field limit, where classical field theories such as the truncated Wigner approximation are limited by their convergence to classical equipartition. This is the subject of our current efforts.

In spinor fluids, we have limited our investigation of spatially extended systems to a concise comparison with a dissipative single-mode model. However, lattice models such as the spin-1 Bose-Hubbard chain allow to study in more detail the interplay between spatial dynamics and spin mixing. Among these, we envision further investigations into the connection between particle entanglement in the spin degree of freedom and mode entanglement throughout the chain, presumably generated during the thermalization process. Here again, the Gaussian trajectory approach may be a suitable option to capture thermalization in extended spinor systems. Related to the interplay between spin and spatial dynamics is the growth of long-range spin correlations. Further investigation of this could be interesting in the context of magnetic domain formation, where domain walls are predicted to spontaneously form as topological defects, driven by the Kibble-Zurek mechanism.

Research into the application of spinor fluids as an analog gravity platform is still in its early stages, leaving many avenues for future work. Among these, we envision the extension to non-uniform coupling between the fluid components. Preliminary work in this direction suggests that the signature of the Hawking signal emitted out of the analog black hole may be drastically amplified upon the introduction of a spectral gap in the interior region, suggesting a new method of overcoming the notorious weakness of the Hawking signal. Furthermore, long-time dynamics of correlations may be affected by the back-reaction of Hawking excitations on the condensate background – a topic which has received increasing attention over the last years. This phenomenon could be taken into account by extending the Bogoliubov approach to the Gaussian (Hartree-Fock-Bogoliubov) variational theory. Given the tendency of this approximation to become invalid when confronted with a unbounded growth of fluctuations, the Gaussian trajectory approach developed and employed in Parts II and III of this thesis may be a promising candidate to study the long-time evolution of analog Hawking radiation in weakly interacting Bose fluids.

Appendix

A | Additional details for the spin-1 fluid

A.1 Gaussian equations of motion

Employing a Gaussian Ansatz for the field operators $\hat{a}_m \equiv \phi_m + \hat{\delta}_m$ $(m = -, 0, +)$, the many-body dynamics contained in the Hamiltonian (6.2) are reduced to a closed system governing the evolution of the first moments $\phi_m = \langle \hat{a}_m \rangle$ and all quadratic correlations of the fluctuations operators $\hat{\delta}_m$, satisfying $\langle \hat{\delta}_m \rangle = 0$. We denote these second central moments as

$$\begin{aligned}
n_+ &= \langle \hat{\delta}_+^\dagger \hat{\delta}_+ \rangle\,, & c_+ &= \langle \hat{\delta}_+ \hat{\delta}_+ \rangle\,, & b_+ &= \langle \hat{\delta}_0 \hat{\delta}_+ \rangle\,, & d_+ &= \langle \hat{\delta}_0^\dagger \hat{\delta}_+ \rangle\,, \\
n_0 &= \langle \hat{\delta}_0^\dagger \hat{\delta}_0 \rangle\,, & c_0 &= \langle \hat{\delta}_0 \hat{\delta}_0 \rangle\,, & b_1 &= \langle \hat{\delta}_+ \hat{\delta}_- \rangle\,, & d_1 &= \langle \hat{\delta}_+^\dagger \hat{\delta}_- \rangle\,, \\
n_- &= \langle \hat{\delta}_-^\dagger \hat{\delta}_- \rangle\,, & c_- &= \langle \hat{\delta}_- \hat{\delta}_- \rangle\,, & b_- &= \langle \hat{\delta}_0 \hat{\delta}_- \rangle\,, & d_- &= \langle \hat{\delta}_0^\dagger \hat{\delta}_- \rangle\,.
\end{aligned} \tag{A.1}$$

The Gaussian nature of fluctuations is reflected in the application of Wick's theorem to all higher order moments,

$$\langle \hat{a}\hat{b}\hat{c}\hat{d} \rangle = \langle \hat{a}\hat{b} \rangle \langle \hat{c}\hat{d} \rangle + \langle \hat{a}\hat{c} \rangle \langle \hat{b}\hat{d} \rangle + \langle \hat{a}\hat{d} \rangle \langle \hat{b}\hat{c} \rangle\,, \tag{A.2}$$

$$\langle \hat{a}\hat{b}\hat{c} \rangle = \langle \hat{a}\hat{b}\hat{c}\hat{d}\hat{e} \rangle = \cdots = 0, \tag{A.3}$$

closing the dynamics at the Gaussian level. To make the calculations tractable, the Hamiltonian is expanded in orders of fluctuation operators $\hat{\delta}_m$. Contributions of first and third order can be omitted as their effect vanishes under the Gaussian Ansatz, leading to

$$\hat{\mathcal{H}}_S \approx E_0 + \hat{H}_2 + \hat{H}_4, \tag{A.4}$$

where

$$\begin{aligned}
E_0 = q\big(|\phi_+|^2 + |\phi_-|^2\big) + \frac{U}{2}\Big(&|\phi_+|^4 + |\phi_-|^4 - 2|\phi_+|^2|\phi_-|^2 \\
&+ 2|\phi_+|^2|\phi_0|^2 + 2|\phi_-|^2|\phi_0|^2 + 2\phi_+^*\phi_-^*\phi_0\phi_0 + 2\phi_0^*\phi_0^*\phi_+\phi_-\Big),
\end{aligned} \tag{A.5}$$

$$
\begin{aligned}
\hat{H}_2 =& q\big(\hat{\delta}_+^\dagger\hat{\delta}_+ + \hat{\delta}_-^\dagger\hat{\delta}_-\big)\\
&+\frac{U}{2}\Big(\phi_+^*\phi_+^*\hat{\delta}_+\hat{\delta}_+ + \phi_+\phi_+\hat{\delta}_+^\dagger\hat{\delta}_+^\dagger + 4|\phi_+|^2\hat{\delta}_+^\dagger\hat{\delta}_+\Big)\\
&+\frac{U}{2}\Big(\phi_-^*\phi_-^*\hat{\delta}_-\hat{\delta}_- + \phi_-\phi_-\hat{\delta}_-^\dagger\hat{\delta}_-^\dagger + 4|\phi_-|^2\hat{\delta}_-^\dagger\hat{\delta}_-\Big)\\
&-U\Big(|\phi_+|^2\hat{\delta}_-^\dagger\hat{\delta}_- + |\phi_-|^2\hat{\delta}_+^\dagger\hat{\delta}_+ + \phi_+^*\phi_-^*\hat{\delta}_+\hat{\delta}_- + \phi_+\phi_-\hat{\delta}_+^\dagger\hat{\delta}_-^\dagger + \phi_+^*\phi_-\hat{\delta}_-^\dagger\hat{\delta}_+ + \phi_-^*\phi_+\hat{\delta}_+^\dagger\hat{\delta}_-\Big)\\
&+U\Big(|\phi_+|^2\hat{\delta}_0^\dagger\hat{\delta}_0 + |\phi_0|^2\hat{\delta}_+^\dagger\hat{\delta}_+ + \phi_+^*\phi_0^*\hat{\delta}_+\hat{\delta}_0 + \hat{\delta}_+^\dagger\hat{\delta}_0^\dagger\phi_+\phi_0 + \phi_+^*\phi_0\hat{\delta}_0^\dagger\hat{\delta}_+ + \phi_0^*\phi_+\hat{\delta}_+^\dagger\hat{\delta}_0\Big)\\
&+U\Big(|\phi_-|^2\hat{\delta}_0^\dagger\hat{\delta}_0 + |\phi_0|^2\hat{\delta}_-^\dagger\hat{\delta}_- + \phi_-^*\phi_0^*\hat{\delta}_-\hat{\delta}_0 + \hat{\delta}_-^\dagger\hat{\delta}_0^\dagger\phi_-\phi_0 + \phi_-^*\phi_0\hat{\delta}_0^\dagger\hat{\delta}_- + \phi_0^*\phi_-\hat{\delta}_-^\dagger\hat{\delta}_0\Big)\\
&+U\Big(\phi_0^*\phi_0^*\hat{\delta}_+\hat{\delta}_- + \hat{\delta}_0^\dagger\hat{\delta}_0^\dagger\phi_+\phi_- + 2\phi_0^*\phi_+\hat{\delta}_0^\dagger\hat{\delta}_- + 2\phi_0^*\phi_-\hat{\delta}_0^\dagger\hat{\delta}_+\Big)\\
&+U\Big(\phi_+^*\phi_-^*\hat{\delta}_0\hat{\delta}_0 + \phi_0\phi_0\hat{\delta}_+^\dagger\hat{\delta}_-^\dagger + 2\phi_+^*\phi_0\hat{\delta}_-^\dagger\hat{\delta}_0 + 2\phi_-^*\phi_0\hat{\delta}_+^\dagger\hat{\delta}_0\Big),
\end{aligned}
\tag{A.6}
$$

$$
\begin{aligned}
\hat{H}_4 = \frac{U}{2}\Big(&\hat{\delta}_+^\dagger\hat{\delta}_+^\dagger\hat{\delta}_+\hat{\delta}_+ + \hat{\delta}_-^\dagger\hat{\delta}_-^\dagger\hat{\delta}_-\hat{\delta}_- - 2\hat{\delta}_+^\dagger\hat{\delta}_-^\dagger\hat{\delta}_+\hat{\delta}_- + 2\hat{\delta}_+^\dagger\hat{\delta}_0^\dagger\hat{\delta}_+\hat{\delta}_0\\
&+ 2\hat{\delta}_-^\dagger\hat{\delta}_0^\dagger\hat{\delta}_-\hat{\delta}_0 + 2\hat{\delta}_0^\dagger\hat{\delta}_0^\dagger\hat{\delta}_+\hat{\delta}_- + 2\hat{\delta}_+^\dagger\hat{\delta}_-^\dagger\hat{\delta}_0\hat{\delta}_0\Big).
\end{aligned}
\tag{A.7}
$$

The evolution of an observable under heterodyne unraveling (5.2) can be rewritten as

$$
\mathrm{d}\,\langle\hat{O}\rangle = -\frac{i}{\hbar}\,\big\langle\big[\hat{O},\hat{\mathcal{H}}_S\big]\big\rangle\,\mathrm{d}t + \mathcal{D}(\,\langle\hat{O}\rangle), \tag{A.8}
$$

where the dissipator $\mathcal{D}$ contains all effects of dissipation. As the first moments ϕ_m of the operators $\hat{a}_m$ were explicitly substituted in the expanded Hamiltonian, the above commutator can no longer be used to find their time evolution. Instead, the time evolution of these classical wave functions is equivalently found by treating ϕ_m and ϕ_m^* as canonical variables of a classical Hamiltonian [138], resulting in

$$
\mathrm{d}\phi_m = -\frac{i}{\hbar}\left\langle\frac{\partial(E_0+\hat{H}_2)}{\partial\phi_m^*}\right\rangle\mathrm{d}t + \mathcal{D}(\phi_m). \tag{A.9}
$$

For the second moments, Eq. (A.8) reduces to

$$
\mathrm{d}\,\langle\hat{\delta}_m^{(\dagger)}\hat{\delta}_n\rangle = -\frac{i}{\hbar}\,\big\langle\big[\hat{\delta}_m^{(\dagger)}\hat{\delta}_n,(\hat{H}_2+\hat{H}_4)\big]\big\rangle\,\mathrm{d}t + \mathcal{D}(\,\langle\hat{\delta}_m^{(\dagger)}\hat{\delta}_n\rangle), \tag{A.10}
$$

A.1.1 Hamiltonian evolution

For the mean field modes $\phi_m = \langle\hat{a}_m\rangle$, one finds the Hamiltonian part of (A.9) as

$$
\begin{aligned}
\left\langle\frac{\partial(E_0+\hat{H}_2)}{\partial\phi_+^*}\right\rangle &= q\phi_+ + U\big[(|\phi_0|^2+|\phi_+|^2-|\phi_-|^2)\phi_+ + \phi_-^*\phi_0\phi_0\big]\\
&+U[(n_0+2n_+-n_-)\phi_+ + \phi_0^*b_+ + \phi_0d_+ + \phi_-^*c_0 + 2\phi_0d_-^* + \phi_+^*c_+ - \phi_-^*b_1 - \phi_-d_1^*],
\end{aligned}
\tag{A.11}
$$

$$
\begin{aligned}
\left\langle\frac{\partial(E_0+\hat{H}_2)}{\partial\phi_0^*}\right\rangle &= U\big[(|\phi_+|^2+|\phi_-|^2)\phi_0 + 2\phi_0^*\phi_+\phi_-\big]\\
&+U[(n_++n_-)\phi_0 + \phi_+^*b_+ + \phi_-^*b_- + \phi_+d_+^* + \phi_-d_-^* + 2\phi_0^*b_1 + 2\phi_+d_- + 2\phi_-d_+],
\end{aligned}
\tag{A.12}
$$

$$\left\langle \frac{\partial(E_0+\hat{H}_2)}{\partial\phi_-^*} \right\rangle = q\phi_- + U\big[(|\phi_0|^2+|\phi_-|^2-|\phi_+|^2)\phi_- + \phi_+^*\phi_0\phi_0\big]$$
$$+ U[(n_0+2n_--n_+)\phi_- + \phi_0^*b_- + \phi_0 d_- + \phi_+^* c_0 + 2\phi_0 d_+^* + \phi_-^* c_- - \phi_+^* b_1 - \phi_+ d_1], \quad \text{(A.13)}$$

where the first and second lines denote the contributions of E_0 and $\hat{H}_2$, respectively.

The evolution of the quadratic moments (A.1) under $\hat{H}_2$ is given by:

$$\big\langle \big[\hat{n}_+, \hat{H}_2\big] \big\rangle = 2Ui\,\mathrm{Im}\Big\{(\phi_0^*\phi_+ + 2\phi_-^*\phi_0)d_+^* - \phi_-^*\phi_+ d_1$$
$$+ \phi_+\phi_0 b_+^* + \phi_+\phi_+ c_+^* + (\phi_0\phi_0 - \phi_+\phi_-)b_1^*\Big\}, \quad \text{(A.14)}$$

$$\big\langle \big[\hat{n}_0, \hat{H}_2\big] \big\rangle = 2Ui\,\mathrm{Im}\Big\{(\phi_0\phi_+^* + 2\phi_0^*\phi_-)d_+ + (\phi_0\phi_-^* + 2\phi_0^*\phi_+)d_-$$
$$+ 2\phi_+\phi_- c_0^* + \phi_0\phi_+ b_+^* + \phi_0\phi_- b_-^*\Big\}, \quad \text{(A.15)}$$

$$\big\langle \big[\hat{n}_-, \hat{H}_2\big] \big\rangle = 2Ui\,\mathrm{Im}\Big\{(\phi_0^*\phi_- + 2\phi_+^*\phi_0)d_-^* - \phi_+^*\phi_- d_1^*$$
$$+ \phi_-\phi_0 b_-^* + \phi_-\phi_- c_-^* + (\phi_0\phi_0 - \phi_-\phi_+)b_1^*\Big\}, \quad \text{(A.16)}$$

$$\big\langle \big[\hat{c}_+, \hat{H}_2\big] \big\rangle = 2\big[q + U(|\phi_0|^2 + 2|\phi_+|^2 - |\phi_-|^2)\big]c_+$$
$$+ 2U\Big[(\phi_0^*\phi_+ + 2\phi_-^*\phi_0)b_+ - \phi_-^*\phi_+ b_1 + \phi_+\phi_0 d_+$$
$$+ \phi_+\phi_+(n_+ + 1/2) + (\phi_0\phi_0 - \phi_+\phi_-)d_1^*\Big] \quad \text{(A.17)}$$

$$\big\langle \big[\hat{c}_0, \hat{H}_2\big] \big\rangle = 2U\big[|\phi_+|^2 + |\phi_-|^2\big]c_0$$
$$+ 2U\Big[(\phi_0\phi_+^* + \phi_0^*\phi_-)b_+ + (\phi_0\phi_-^* + 2\phi_0^*\phi_+)b_-$$
$$+ 2\phi_+\phi_-(2n_0+1) + \phi_0\phi_+ d_+^* + \phi_0\phi_- d_-^*\Big] \quad \text{(A.18)}$$

$$\big\langle \big[\hat{c}_-, \hat{H}_2\big] \big\rangle = 2\big[q + U(|\phi_0|^2 + 2|\phi_-|^2 - |\phi_+|^2)\big]c_-$$
$$+ 2U\Big[(\phi_0^*\phi_- + 2\phi_+^*\phi_0)b_- - \phi_+^*\phi_- b_1 + \phi_-\phi_0 d_-$$
$$+ \phi_-\phi_-(n_- + 1/2) + (\phi_0\phi_0 - \phi_+\phi_-)d_1\Big] \quad \text{(A.19)}$$

$$\big\langle \big[\hat{b}_+, \hat{H}_2\big] \big\rangle = \big[q + U(|\phi_0|^2 + 3|\phi_+|^2)\big]b_+$$
$$+ U\Big[(\phi_0\phi_+^* + 2\phi_0^*\phi_-)c_+ + (\phi_0\phi_-^* + 2\phi_0^*\phi_+)b_1 + 2\phi_+\phi_- d_+$$
$$+ \phi_0\phi_- d_1^* + (\phi_0^*\phi_+ + 2\phi_-^*\phi_0)c_0 - \phi_-^*\phi_+ b_-$$
$$+ \phi_+\phi_0(n_0 + n_+ + 1) + \phi_+\phi_+ d_+^* + (\phi_0\phi_0 - \phi_+\phi_-)d_-^*\Big] \quad \text{(A.20)}$$

$$\begin{aligned}\left\langle\left[\hat{b}_1,\hat{H}_2\right]\right\rangle = &\left[2q+U(2|\phi_0|^2+|\phi_+|^2+|\phi_-|^2)\right]b_1\\ &+U\Big[(\phi_0^*\phi_+ + 2\phi_-^*\phi_0)b_- + (\phi_0^*\phi_- + 2\phi_+^*\phi_0)b_+ - \phi_+^*\phi_- c_+\\ &\quad - \phi_-^*\phi_+ c_- + \phi_0\phi_+ d_- + \phi_0\phi_- d_+ + \phi_+\phi_+ d_1\\ &\quad + \phi_-\phi_- d_1^* + (\phi_0\phi_0 - \phi_+\phi_-)(n_+ + n_- + 1)\Big]\end{aligned} \tag{A.21}$$

$$\begin{aligned}\left\langle\left[\hat{b}_-,\hat{H}_2\right]\right\rangle = &\left[q+U(|\phi_0|^2+3|\phi_-|^2)\right]b_-\\ &+U\Big[(\phi_0\phi_-^* + 2\phi_0^*\phi_+)c_- + (\phi_0\phi_+^* + 2\phi_0^*\phi_-)b_1 + 2\phi_+\phi_- d_-\\ &\quad + \phi_0\phi_+ d_1 + (\phi_0^*\phi_- + 2\phi_+^*\phi_0)c_0 - \phi_+^*\phi_- b_+\\ &\quad + \phi_-\phi_0(n_0 + n_- + 1) + \phi_-\phi_- d_-^* + (\phi_0\phi_0 - \phi_+\phi_-)d_+^*\Big]\end{aligned} \tag{A.22}$$

$$\begin{aligned}\left\langle\left[\hat{d}_+,\hat{H}_2\right]\right\rangle = &\left[q+U(|\phi_0|^2+|\phi_+|^2-2|\phi_-|^2)\right]d_+\\ &+U\Big[(\phi_0^*\phi_+ + 2\phi_-^*\phi_0)n_0 - \phi_-^*\phi_+ d_- + \phi_+\phi_0 c_0^* + \phi_+\phi_+ b_+^*\\ &\quad + (\phi_0\phi_0 - \phi_+\phi_-)b_-^* - (\phi_0^*\phi_+ + 2\phi_0\phi_-^*)n_+\\ &\quad - (\phi_0^*\phi_- + 2\phi_0\phi_+^*)d_1^* - 2\phi_+^*\phi_-^* b_+ - \phi_0^*\phi_+^* c_+ - \phi_0^*\phi_-^* b_1\Big]\end{aligned} \tag{A.23}$$

$$\begin{aligned}\left\langle\left[\hat{d}_1,\hat{H}_2\right]\right\rangle = U\Big[&3(|\phi_-|^2 - |\phi_+|^2)d_1 + (\phi_0^*\phi_- + 2\phi_+^*\phi_0)d_+^* + \phi_+^*\phi_-(n_- - n_+)\\ &+ \phi_-\phi_0 b_+^* + \phi_-\phi_- b_1^* + (\phi_0\phi_0 - \phi_+\phi_-)c_+^* - \phi_+^*\phi_0^* b_-\\ &- (\phi_0\phi_+^* + 2\phi_-\phi_0^*)d_- - \phi_+^*\phi_+^* b_1 - (\phi_0^*\phi_0^* - \phi_+^*\phi_-^*)c_-\Big]\end{aligned} \tag{A.24}$$

$$\begin{aligned}\left\langle\left[\hat{d}_-,\hat{H}_2\right]\right\rangle = &\left[q+U(|\phi_0|^2+|\phi_-|^2-2|\phi_+|^2)\right]d_-\\ &+U\Big[(\phi_0^*\phi_- + 2\phi_+^*\phi_0)n_0 - \phi_+^*\phi_- d_+ + \phi_-\phi_0 c_0^* + \phi_-\phi_- b_-^*\\ &\quad + (\phi_0\phi_0 - \phi_+\phi_-)b_+^* - (\phi_0^*\phi_- + 2\phi_0\phi_+^*)n_-\\ &\quad - (\phi_0^*\phi_+ + 2\phi_0\phi_-^*)d_1 - 2\phi_+^*\phi_-^* b_- - \phi_0^*\phi_-^* c_- - \phi_0^*\phi_+^* b_1\Big]\end{aligned} \tag{A.25}$$

The Wick-contracted correction to their time evolution coming from $\hat{H}_4$ is given by:

$$\left\langle\left[\hat{n}_+,\hat{H}_4\right]\right\rangle = 2Ui\,\mathrm{Im}\,\{b_1^* c_0 + 2d_+^* d_-^*\}, \tag{A.26}$$

$$\left\langle\left[\hat{n}_0,\hat{H}_4\right]\right\rangle = 2Ui\,\mathrm{Im}\,\{2c_0^* b_1 + 4d_+ d_-\}, \tag{A.27}$$

$$\left\langle\left[\hat{n}_-,\hat{H}_4\right]\right\rangle = 2Ui\,\mathrm{Im}\,\{b_1^* c_0 + 2d_-^* d_+^*\}, \tag{A.28}$$

$$\left\langle\left[\hat{c}_+,\hat{H}_4\right]\right\rangle = Uc_+ + 2U\Big[3n_+c_+ - 2d_1^*b_1 - n_-c_+ + n_0c_+ + 2d_+b_+ + d_1^*c_0 + 2d_-^*b_+\Big], \quad \text{(A.29)}$$

$$\left\langle\left[\hat{c}_0,\hat{H}_4\right]\right\rangle = 2U\Big[n_+c_0 + 2d_+^*b_+ + n_-c_0 + 2d_-^*b_- + 2n_0b_1 + 2d_+b_- + 2d_-b_+ + b_1\Big] \quad \text{(A.30)}$$

$$\left\langle\left[\hat{c}_-,\hat{H}_4\right]\right\rangle = Uc_- + 2U\Big[3n_-c_- - 2d_1b_1 - n_+c_- + n_0c_- + 2d_-b_- + d_1c_0 + 2d_+^*b_-\Big], \quad \text{(A.31)}$$

$$\left\langle\left[\hat{b}_+,\hat{H}_4\right]\right\rangle = U\Big[4n_+b_+ + 2d_+^*c_+ + 4d_+b_1 + 2d_-c_+ + 2n_0b_+ + d_+c_0 + 3d_-^*c_0 + b_+\Big], \quad \text{(A.32)}$$

$$\left\langle\left[\hat{b}_1,\hat{H}_4\right]\right\rangle = U\Big[-b_1 + c_0 + 2n_0b_1 + 2d_+b_- + 2d_-b_+ + n_-c_0 + 2d_-^*b_- + n_+c_0 + 2d_+^*b_+\Big], \quad \text{(A.33)}$$

$$\left\langle\left[\hat{b}_-,\hat{H}_4\right]\right\rangle = U\Big[4n_-b_- + 2d_-^*c_- + 4d_-b_1 + 2d_+c_- + 2n_0b_- + d_-c_0 + 3d_+^*c_0 + b_-\Big], \quad \text{(A.34)}$$

$$\left\langle\left[\hat{d}_+,\hat{H}_4\right]\right\rangle = U\Big[2n_0d_+ + c_0^*b_+ + 2n_0d_-^* + b_-^*c_0 - 2b_-^*b_1 - 2d_+n_- - 2d_-d_1^* - 2b_1^*b_+ - 2d_+^*d_1^* - 2n_+d_-^*\Big], \quad \text{(A.35)}$$

$$\left\langle\left[\hat{d}_1,\hat{H}_4\right]\right\rangle = U\Big[2b_1^*c_- + 4n_-d_1 - 2c_+^*b_1 - 4n_+d_1 + c_+^*c_0 + 2d_+^*d_+^* - c_0^*c_- - 2d_-d_-\Big], \quad \text{(A.36)}$$

$$\left\langle\left[\hat{d}_-,\hat{H}_4\right]\right\rangle = U\Big[2n_0d_- + c_0^*b_- + 2n_0d_+^* + b_+^*c_0 - 2b_+^*b_1 - 2d_-n_+ - 2d_+d_1 - 2b_1^*b_- - 2d_-^*d_1 - 2n_-d_+^*\Big]. \quad \text{(A.37)}$$

Being of fourth order in fluctuation operators, this contribution of $\hat{H}_4$ to the dynamics is negligible in the trajectory description, as fluctuations are suppressed by construction. However, their effect is significant in the unaltered HFB theory, where fluctuations eventually dominate the dynamics.

A.1.2 Dissipation

Referring to Eq. (5.2) in the main text, the dissipator is given by

$$\mathcal{D}(\langle\hat{O}\rangle) = -\frac{\gamma}{2}\sum_m\Big(\Big\langle\Big\{\hat{a}_m^\dagger\hat{a}_m,\hat{O}\Big\}\Big\rangle - 2\left\langle\hat{a}_m^\dagger\hat{O}\hat{a}_m\right\rangle\Big)\mathrm{d}t + \sqrt{\gamma}\sum_m\Big(\left\langle\hat{a}_m^\dagger(\hat{O}-\langle\hat{O}\rangle)\right\rangle\mathrm{d}Z_m + c.c.\Big). \quad \text{(A.38)}$$

For the first moments $\phi_m = \langle \hat{a}_m \rangle$, one finds

$$\mathcal{D}(\phi_+) = -\frac{\gamma}{2}\phi_+ \mathrm{d}t + \sqrt{\gamma}(n_+ \mathrm{d}Z_+ + c_+ \mathrm{d}Z_+^* + d_+ \mathrm{d}Z_0 + b_+ \mathrm{d}Z_0^* + d_1^* \mathrm{d}Z_- + b_1 \mathrm{d}Z_-^*), \tag{A.39}$$

$$\mathcal{D}(\phi_0) = -\frac{\gamma}{2}\phi_0 \mathrm{d}t + \sqrt{\gamma}(d_+^* \mathrm{d}Z_+ + b_+ \mathrm{d}Z_+^* + n_0 \mathrm{d}Z_0 + c_0 \mathrm{d}Z_0^* + d_-^* \mathrm{d}Z_- + b_- \mathrm{d}Z_-^*), \tag{A.40}$$

$$\mathcal{D}(\phi_-) = -\frac{\gamma}{2}\phi_- \mathrm{d}t + \sqrt{\gamma}(d_1 \mathrm{d}Z_+ + b_1 \mathrm{d}Z_+^* + d_- \mathrm{d}Z_0 + b_- \mathrm{d}Z_0^* + n_- \mathrm{d}Z_- + c_- \mathrm{d}Z_-^*). \tag{A.41}$$

The dissipator of the second moments $\langle \hat{\delta}_m^{(\dagger)} \hat{\delta}_n \rangle = \langle \hat{a}_m^{(\dagger)} \hat{a}_n \rangle - \phi_m^{(*)} \phi_n$ is found by first calculating $\mathcal{D}(\phi_m^{(*)} \phi_n)$ using Itō's lemma

$$\mathrm{d}\big(\phi_m^{(*)} \phi_n\big) = \phi_m^{(*)} \mathrm{d}\phi_n + \phi_n \mathrm{d}\phi_m^{(*)} + \mathrm{d}\phi_m^{(*)} \mathrm{d}\phi_n, \tag{A.42}$$

and subtracting it from $\mathcal{D}(\langle \hat{a}_m^{(\dagger)} \hat{a}_n \rangle)$. The stochastic part is found to vanish, leaving only a deterministic dissipation:

$$\mathcal{D}(n_+) = -\gamma\big[n_+(n_+ + 1) + |c_+|^2 + |d_+|^2 + |b_+|^2 + |d_1|^2 + |b_1|^2\big]\mathrm{d}t, \tag{A.43}$$

$$\mathcal{D}(n_0) = -\gamma\big[n_0(n_0 + 1) + |c_0|^2 + |d_+|^2 + |b_+|^2 + |d_-|^2 + |b_-|^2\big]\mathrm{d}t, \tag{A.44}$$

$$\mathcal{D}(n_-) = -\gamma\big[n_-(n_- + 1) + |c_-|^2 + |d_-|^2 + |b_-|^2 + |d_1|^2 + |b_1|^2\big]\mathrm{d}t, \tag{A.45}$$

$$\mathcal{D}(c_+) = -\gamma[c_+(2n_+ + 1) + 2d_+ b_+ + 2b_1 d_1^*]\mathrm{d}t, \tag{A.46}$$

$$\mathcal{D}(c_0) = -\gamma[c_0(2n_0 + 1) + 2d_+^* b_+ + 2d_-^* b_-]\mathrm{d}t, \tag{A.47}$$

$$\mathcal{D}(c_-) = -\gamma[c_-(2n_- + 1) + 2d_- b_- + 2b_1 d_1]\mathrm{d}t, \tag{A.48}$$

$$\mathcal{D}(b_+) = -\gamma[b_+(n_+ + n_0 + 1) + d_+^* c_+ + c_0 d_+ + d_-^* b_1 + b_- d_1^*]\mathrm{d}t, \tag{A.49}$$

$$\mathcal{D}(b_1) = -\gamma[b_1(n_+ + n_- + 1) + c_+ d_1 + c_- d_1^* + d_+ b_- + b_+ d_-]\mathrm{d}t, \tag{A.50}$$

$$\mathcal{D}(b_-) = -\gamma[b_-(n_- + n_0 + 1) + d_-^* c_- + c_0 d_- + d_+^* b_1 + b_+ d_1]\mathrm{d}t, \tag{A.51}$$

$$\mathcal{D}(d_+) = -\gamma[d_+(n_+ + n_0 + 1) + b_+^* c_+ + c_0^* b_+ + d_- d_1^* + b_-^* b_1]\mathrm{d}t, \tag{A.52}$$

$$\mathcal{D}(d_1) = -\gamma[d_1(n_+ + n_- + 1) + c_+^* b_1 + c_- b_1^* + d_+^* d_- + b_+^* b_-]\mathrm{d}t, \tag{A.53}$$

$$\mathcal{D}(d_-) = -\gamma[d_-(n_- + n_0 + 1) + b_-^* c_- + c_0^* b_- + d_+ d_1 + b_+^* b_1]\mathrm{d}t. \tag{A.54}$$

B | Additional details for the Hawking effect

B.1 The dimensionless Hamiltonian

To numerically implement the dynamics of a spatially extended Bose gas, one must take care to consistently choose a practical set of units. In principle, this is trivial. In reality, it is the place where π's and $\sqrt{2}$'s get lost, never to be found again. I include this procedure of *non-dimensionalization* here for the coherently coupled mixture, in hopes of helping another confused student like me.

With the average density of a single component defined as $\tilde{n} = L^{-1}\int_0^L |\psi_\pm|^2$, let us introduce the single-component chemical potential* $\tilde{\mu}$ and the associated healing length $\tilde{\xi}$ as the characteristic energy and length scales:

$$\tilde{\mu} = \tilde{g}\tilde{n} = \frac{\hbar^2}{2m\tilde{\xi}^2}, \qquad \tilde{\xi} = \frac{\hbar}{\sqrt{2m\tilde{g}\tilde{n}}}. \tag{B.1}$$

Defining dimensionless space through $\tau = x/\tilde{\xi}$ and rescaling the fields as $\phi = \sqrt{\xi}\psi$ to maintain normalization, the Hamiltonian (2.30) in units of $\tilde{\mu}$ becomes

$$H/\tilde{\mu} = \int_0^{L/\tilde{\xi}} \mathrm{d}\tau \Bigg\{ \phi_1^\dagger\big(-\partial_\tau^2 + V/\tilde{\mu}\big)\phi_1 + \phi_2^\dagger\big(-\partial_\tau^2 + V/\tilde{\mu}\big)\phi_2 + \frac{g}{2\tilde{\xi}\tilde{g}\tilde{n}}\big(\phi_1^\dagger\phi_1^\dagger\phi_1\phi_1 + \phi_2^\dagger\phi_2^\dagger\phi_2\phi_2\big) + \frac{g_{12}}{\tilde{\xi}\tilde{g}\tilde{n}}\phi_1^\dagger\phi_2^\dagger\phi_1\phi_2 - \frac{\Omega}{\tilde{\mu}}\big(\phi_1^\dagger\phi_- 1\phi_2^\dagger\phi_1\big)\Bigg\}. \tag{B.2}$$

The dimensionless system is now obtained by consistently setting a set of dimensional parameters to unity. Setting $\tilde{\mu} = \tilde{\xi} = 1$ sets the length and energy scale. With $\hbar = 1$, this requires through Eq. (B.1) that $m = 1/2$ in order to obtain a consistent set of units. Lastly, we set the interaction strength $\tilde{g} = 1$, which for consistency with the chosen energy scale also implies the density $\tilde{n} = 1$.

* Note that this quantity only corresponds to the chemical potential $(g + g_{12})n_0$ for density interactions on the condition that $g_{12} = 0$, i.e. in absence of interspecies interactions.

Omitting these units we get the numerically implemented Hamiltonian

$$\mathtt{H} = \int_0^{\mathtt{L}} \mathrm{d}\mathtt{x} \Bigg\{ \phi_1^\dagger \big(-\partial_{\mathtt{x}}^2 + \mathtt{V}\big)\phi_1 + \phi_2^\dagger \big(-\partial_{\mathtt{x}}^2 + \mathtt{V}\big)\phi_2 + \frac{\mathtt{g}}{2}\big(\phi_1^\dagger\phi_1^\dagger\phi_1\phi_1 + \phi_2^\dagger\phi_2^\dagger\phi_2\phi_2\big) + \mathtt{g}_{12}\phi_1^\dagger\phi_2^\dagger\phi_1\phi_2 + \mathbf{\Omega}\big(\phi_1^\dagger\phi_2 + \phi_2^\dagger\phi_1\big) \Bigg\}, \quad \text{(B.3)}$$

where the numerical units are related to physical dimensions through

$$\mathtt{H} = H/\tilde{\mu}, \quad \mathtt{t} = \tilde{\mu}t, \quad \mathtt{x} = \tau = x/\tilde{\xi}, \quad \mathtt{L} = L/\tilde{\xi}, \quad \text{(B.4)}$$

$$\mathbf{\Omega} = \Omega/\tilde{\mu}, \quad \mathtt{V} = V/\tilde{\mu}, \quad \mathtt{g} = g/\tilde{g}, \quad \mathtt{g}_{12} = g_{12}/\tilde{g} \quad \text{(B.5)}$$

The coupled Gross-Pitaevskii equations governing the dynamics of the rescaled fields $\phi_{1/2}$ then reduce to:

$$\begin{aligned} i\partial_{\mathtt{t}}\phi_1 &= \big(-\partial_{\mathtt{x}}^2 + \mathtt{V} + \mathtt{g}|\phi_1|^2 + \mathtt{g}_{12}|\phi_2|^2\big)\phi_1 - \mathbf{\Omega}\phi_2, \\ i\partial_{\mathtt{t}}\phi_2 &= \big(-\partial_{\mathtt{x}}^2 + \mathtt{V} + \mathtt{g}|\phi_2|^2 + \mathtt{g}_{12}|\phi_1|^2\big)\phi_2 - \mathbf{\Omega}\phi_1, \end{aligned} \quad \text{(B.6)}$$

For the idealized sonic horizon obtained through spatial modulation of the spin interaction strengths, the units are defined as those in one of the two regions, e.g. $\tilde{g} = g^{(down)}$. As the density interaction strength $g + g_{12}$ is kept constant throughout space, the density is uniformly $n = 1$.

B.2 Split-operator method

Vectorially, the system of dimensionless GPE's is of the form

$$i\hbar\partial_t\mathbf{\Phi} = \tilde{H}\mathbf{\Phi} = (T + V + I + R)\mathbf{\Phi}, \quad \text{(B.7)}$$

where $\mathbf{\Phi} = (\phi_1 \quad \phi_2)^T$ and the GPE operator $\tilde{H}$ is split into the kinetic, trapping, interaction and coherent coupling terms. This system is integrated in time through the split operator method, which is based on a factorization of the unitary evolution operator,

$$\mathbf{\Phi}(x, t + \Delta t) = e^{-i\tilde{H}\Delta t/\hbar}\mathbf{\Phi}(x, t) \approx e^{-iT\Delta t/\hbar}e^{-i(V+I)\Delta t/\hbar}e^{-iR\Delta t/\hbar}\mathbf{\Phi}(x, t), \quad \text{(B.8)}$$

with Δt the numerical time step. This factorization, known as the Lie product formula or Trotter product formula, introduces an error as the different terms in the Hamiltonian do not commute. Its exact validity is recovered in the limit $\Delta t \to 0$ [355].

The approximate factorization is required as different terms in the Hamiltonian do not share the same eigenbasis. In particular, circumventing the derivative in the kinetic energy requires a Fourier transform to reciprocal space, whereas the trapping, interaction and coupling terms V, I and R can be exponentiated in real space. An intermediate Fourier transform is therefore used:

$$\mathbf{\Phi}(x, t + \Delta t) \approx \mathcal{F}^{-1}\big[e^{-iT\Delta t/\hbar}\mathcal{F}\big[e^{-i(V+I)\Delta t/\hbar}e^{-iR\Delta t/\hbar}\mathbf{\Phi}(x, t)\big]\big] \quad \text{(B.9)}$$

Contrary to T, V and I, the coherent coupling term R is not diagonal in the spin vector $\mathbf{\Phi}$.

Instead, its eigenvalues and -vectors are given by

$$\lambda_1 = +\Omega_R \qquad \chi_1 = (\phi_1 - \phi_2)/\sqrt{2} \tag{B.10}$$

$$\lambda_2 = -\Omega_R \qquad \chi_2 = (\phi_1 + \phi_2)/\sqrt{2}. \tag{B.11}$$

With the unitary transformation denoted $\mathbf{X} = U_\Omega \mathbf{\Phi}$, the exponential of the coupling term is calculated as $\mathbf{X}(x, t + \Delta t) = U_\Omega^{-1} e^{-i R \Delta t/\hbar} U_\Omega \mathbf{X}(x, t)$. In the original basis, this results in [104]

$$\partial_t \begin{pmatrix} \phi_1 \\ \phi_2 \end{pmatrix} \sim \begin{pmatrix} \cos\left(\frac{\Omega_R \Delta t}{\hbar}\right) & i \sin\left(\frac{\Omega_R \Delta t}{\hbar}\right) \\ i \sin\left(\frac{\Omega_R \Delta t}{\hbar}\right) & \cos\left(\frac{\Omega_R \Delta t}{\hbar}\right) \end{pmatrix} \begin{pmatrix} \phi_1 \\ \phi_2 \end{pmatrix}. \tag{B.12}$$

B.3 A note on wave packets

While elementary excitations in the uniform fluid are a superposition of plane waves, the focused beam (10.14) generates a localized wave packet. Upon collision with the sonic horizon, the outgoing excitations are similarly localized waves, which spatially separate due to their different group velocities. From a numerical point of view, this spatial separation facilitates the analysis of the different signals (see Appendix B.4) and avoids noise originating from the periodic boundaries of the system. Comparing the different signals in Fig. 10.6(b) shows vast differences in both the amplitude and width of the outgoing wave packets. While a more rigorous study of the amplitudes and their frequency dependence is included in Sec. 10.5 of the main text, it is instructive to understand the spreading and narrowing of the outgoing signals – absent in a textbook treatment of plane wave scattering – from the general properties of wave packets and simple arguments of energy conservation.

Let us assume the incoming excitation is a Gaussian wave packet of width σ_x, its momentum and frequency centered around a point (k_0^{in}, ω_0) along the dispersion in the comoving frame. Observed in the laboratory, frequencies of the propagating wave acquires a Doppler shift $\omega = \omega' + kv$, with v the flow velocity of the fluid and ω' the frequency as measured in a reference frame co-moving with the fluid. Assuming $\sigma_x \gg \xi$, the wave packet is sharply peaked in reciprocal space and we may linearize the dispersion relation around k_0^{in} to approximate

$$\omega(k) \approx \omega_0 + (k - k_0^{in}) v_g^{in}, \tag{B.13}$$

where the group velocity $v_g^{in} = \partial\omega/\partial k|_{k_0^{in}}$ of the main wave vector dictates the speed of nondispersive propagation. The approaching excitation is then of the form

$$\psi^{in}(x, t) = A \exp\left\{ \frac{-(x - v_g^{in} t)^2}{2\sigma_x^2} \right\} e^{i(k_0^{in} x - \omega_0 t)}, \tag{B.14}$$

Omitting the plane wave for compactness, the Gaussian prefactor in reciprocal space becomes

$$\psi^{in}(k, t) \sim \sqrt{\sigma_x^2} \exp\left\{ -(k - k_0^{in})^2 \frac{\sigma_x^2}{2} \right\}, \tag{B.15}$$

$$\sim \sqrt{\sigma_x^2} \exp\left\{ -(\omega' - \omega_0)^2 \frac{\sigma_x^2}{2 {v_g^{in}}^2} \right\}, \tag{B.16}$$

where the latter step is due to the approximation (B.13). As energy is conserved in the laboratory

frame, the outgoing packets are peaked around the same ω_0', and we may similarly approximate the wave packets emerging after the scattering process as

$$\omega(k) \approx \omega_0 + (k - k_0^{out}) v_g^{out}, \tag{B.17}$$

The outgoing packet then acquires a prefactor

$$\psi^{out}(k,t) \sim \sqrt{\sigma_x^2} \exp\left\{ -(k-k_0^{out})^2 \frac{\sigma_x^2}{2} \frac{v_g^{out\,2}}{v_g^{in\,2}} \right\}, \tag{B.18}$$

and upon inverse Fourier transform,

$$\psi^{out}(x,t) \sim \frac{v_g^{in}}{v_g^{out}} \exp\left\{ \frac{-(x - v_g^{out} t)^2}{2\sigma_x^2} \frac{v_g^{in\,2}}{v_g^{out\,2}} \right\}. \tag{B.19}$$

Hence, the width and amplitude of the outgoing packet changes with respect to the incoming signal as through the ratio of their respective group velicities,

$$\sigma_x \to \frac{v_g^{out}}{v_g^{in}} \sigma_x, \qquad A \to \frac{v_g^{in}}{v_g^{out}} A. \tag{B.20}$$

In case multiple outgoing waves emerge from the scattering of a single incoming wave packet, as in Fig. 10.6, their relative amplitudes and widths may be deduced from the same argument. Comparing Fig. 10.6(b) to the corresponding dispersion relations in Fig. 10.5(e, f) thus explains the comparably lower amplitude and larger width of the d_1^{out} wave as a consequence of its higher group velocity with respect to the u^{out} and d_2^{out} modes.

B.4 Extracting Bogoliubov amplitudes

The elements of the scattering matrix defined in Eq. (10.15) are inferred from the amplitudes of the ingoing and outgoing Bogoliubov excitations in a scattering simulation. In this appendix we outline the numerical procedure to do so, illustrated for the ingoing d_1^{in} wave packet shown in Fig. 10.7.

1. Each simulation consists of evolving the dimensionless Gross-Pitaevskii equations (B.6) according to the split-operator scheme described in Appendix B.2. In order to achieve sufficiently separated wave packets (explained in more detail below) and avoid boundary effects, typical system sizes are of the order $\mathtt{L} = 10^4$ with a grid discretization $\Delta\mathtt{x} = 1/4$ and periodic boundary conditions. The fields are initialized in the state $\phi_{1/2} = \sqrt{n} e^{i\S(x)}$, with the phase set to account for the flow velocity $v = 1$ according to $v = (\hbar/m)\nabla S(x)$.
2. A scattering process is set in motion by the application of a potential perturbation of the form in Eq. (10.14). Its spread in space (σ_x) and time (σ_t) are maximized to increase the spectral resolution, and limited by the computational cost of integrating large systems over long times. This trade-off results in typical pulses of $\sigma_t \sim 10\mu_u^{-1}$ and $\sigma_x \sim 10^2 \xi_u$. Crucially, its amplitude should be low enough to result in a *linear* response in both the density and phase of each fluid component $\phi_{1/2}$.
3. The time-dependent wave functions $\phi_1(x,t)$ and $\phi_2(x,t)$ are transformed to the reference frame co-moving with the fluid flow by multiplying them with the phase gradient associated to the uniform flow $e^{-iS(x)}$.

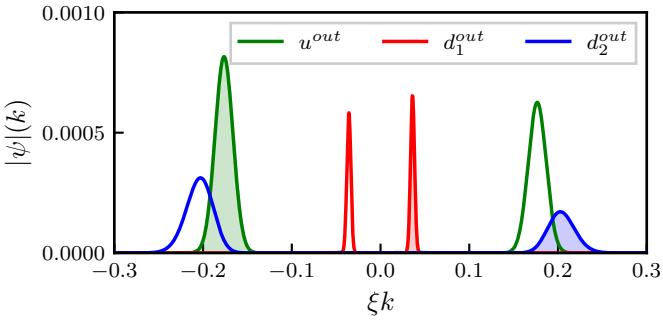

Figure B.1 – Momentum spectrum of the outgoing excitations in Figure 10.7. Positive-norm parts of each excitation (the C_k constribution in Eq. (B.21)) are shown as shaded peaks, negative-norm (D_k) parts are unshaded.

4. A t_{in} and t_{out} time is chosen at which the ingoing and outgoing wave packets are clearly visible and maximally separated in space, resulting in a signal as shown in Fig. 10.6.

5. The phase of the uniform background condensate oscillates at a frequency given by the chemical potential. Since the Bogoliubov coefficients can be chosen as real-valued only for a strictly real background condensate, the wave function snapshots at times t_{in} and t_{out} are multiplied by a phase factor to set the background phase zero. Since the background of spin excitations is zero in the initial state, its phase is ill-defined. Removing the constant phase is therefore performed for the individual components $\phi_{1/2}$, whose time evolution is identical in regions far away from polarization excitations.

6. The spatial profile of the polarization wave function $\phi = \phi_1 - \phi_2$ at t_{out} is separated into 3 regions isolating the u^{out}, d_1^{out} and d_2^{out} wave packets.

7. The spin wave function is Fourier transformed to momentum space. The resulting spectral distributions $|\phi(k)|$, shown in Fig. B.1, contain contributions peaked at k and $-k$, as can be understood from the doubling of modes in Bogoliubov theory. More specifically, the excitation in each mode is of the form

$$\delta\psi(x,t) = \int_k C_k e^{i(k_i x - \omega t)} + D_{-k} e^{-i(k_i x - \omega t)} \mathrm{d}k, \tag{B.21}$$

which contains contributions corresponding to both the positive and negative norm branches of the Bogoliubov dispersion, as explained in Sec. 9.2.1. The negative-norm character of the d_2^{out} signal can be inferred from the fact that $\int D_k \mathrm{d}k > \int C_k \mathrm{d}k$. In accordance with the result of Appendix B.3, the spectral widths of the u^{out} and d_2^{out} contributions are comparable, while the d_1^{out} Hawking signal is significantly more localized in k-space.

8. The amplitudes of the corresponding Bogoliubov modes are determined by performing the transformation

$$\beta_k = u^*_{-k}\delta\psi_k - v^*_{-k}\delta\psi^*_{-k}. \tag{B.22}$$

Since the otherwise uniform fluid's mode amplitudes at k and $-k$ are respectively given by C_k and D_k, the amplitude of the Bogoliubov mode is simply found as

$$\beta_k = u^*_{-k}C_k - v^*_{-k}D^*_{-k}. \tag{B.23}$$

As the transformation assumes a single $+k$ and $-k$ contribution of positive and negative norm, respectively, the numerical transformation is restricted to the correct side of k for each packet. E.g., for the u^{out}-branch the positive norm part is right-moving ($k < 0$), yielding:

$$\beta_k = u_k C_k - v^*_{-k} D^*_{-k} \rightarrow \beta_k = u_{k<0}\psi_{k<0} - v^*_{-k>0}\psi^*_{-k>0} \tag{B.24}$$

In the above expressions, ψ^*_{-k} refers to a negative-k component of the complex conjugate of $\psi(x)$, i.e. $\psi^*_{-k} = (\mathrm{FFT}[\psi(x)])^*(-k)$.

9. The Bogoliubov transformation above results in a Gaussian profile $\beta_j(k)$ for each excitation, centered around the value k_0 of the mode in the positive-frequency dispersion branch. The Bogoliubov amplitudes β_j used in the main text are retrieved by integrating $\beta_j(k)$ for each excitation. Their absolute value depends on the amplitude of the Bragg pulse and is therefore irrelevant. The elements of the scattering matrix are inferred as

$$\mathcal{S}_{ij} = \frac{\left|\beta_i^{out}\right|^2}{\left|\beta_j^{in}\right|^2}. \tag{B.25}$$

Bibliography

[1] R. P. Feynman. Simulating physics with computers. *Int. J. Theor. Phys.* **21**(6-7):467–488, (1982).

[2] L. P. Pitaevskiĭ & S. Stringari. *Bose-Einstein Condensation and Superfluidity*. Number 164 in International Series of Monographs on Physics. Oxford University Press, Oxford, United Kingdom, first edition edition, (2016). ISBN 978-0-19-875888-4.

[3] C. Pethick & H. Smith. *Bose-Einstein Condensation in Dilute Gases*. Cambridge University Press, Cambridge ; New York, (2002). ISBN 978-0-521-66194-2.

[4] J. F. Annett. *Superconductivity, Superfluids, and Condensates*. Number 5 in Oxford Master Series in Physics Condensed Matter Physics. Oxford Univ. Press, Oxford, repr edition, (2011). ISBN 978-0-19-850756-7.

[5] C. Gardiner & P. Zoller. *The Quantum World of Ultra-Cold Atoms and Light Book III: Ultra-Cold Atoms*, volume 05 of *Cold Atoms*. World Scientific (Europe), (2017). ISBN 978-1-78634-417-5.

[6] A. Griffin, D. W. Snoke, & S. Stringari, editors. *Bose-Einstein Condensation*. Cambridge University Press, 1 edition, (1995). ISBN 978-0-521-46473-4.

[7] M. Lewenstein, A. Sanpera, & V. Ahufinger. *Ultracold Atoms in Optical Lattices: Simulating Quantum Many-Body Systems*. Oxford University Press, Oxford, U.K, 1st ed edition, (2012). ISBN 978-0-19-957312-7.

[8] Y. Castin. Bose-Einstein condensates in atomic gases: Simple theoretical results, arXiv:cond-mat/0105058, (2001).

[9] F. Dalfovo, S. Giorgini, L. P. Pitaevskii, & S. Stringari. Theory of Bose-Einstein condensation in trapped gases. *Rev. Mod. Phys.* **71**(3):463–512, (1999).

[10] A. J. Leggett. Bose-Einstein condensation in the alkali gases: Some fundamental concepts. *Rev. Mod. Phys.* **73**(2):307–356, (2001).

[11] M. Lewenstein, A. Sanpera, V. Ahufinger, B. Damski, A. Sen(De), & U. Sen. Ultracold atomic gases in optical lattices: Mimicking condensed matter physics and beyond. *Advances in Physics*. **56**(2):243–379, (2007).

[12] I. Bloch. Ultracold quantum gases in optical lattices. *Nat. Phys.* **1**(1):23–30, (2005).

[13] I. Bloch, J. Dalibard, & W. Zwerger. Many-body physics with ultracold gases. *Rev. Mod. Phys.* **80**(3):885–964, (2008).

[14] I. Bloch, J. Dalibard, & S. Nascimbène. Quantum simulations with ultracold quantum gases. *Nat. Phys.* **8**(4):267–276, (2012).

[15] W. Pauli. Über den Zusammenhang des Abschlusses der Elektronengruppen im Atom mit der Komplexstruktur der Spektren. *Z. Physik.* **31**(1):765–783, (1925).

[16] Bose. Plancks Gesetz und Lichtquantenhypothese. *Z. Physik.* **26**(1):178–181, (1924).

[17] A. Einstein. Quantentheorie des einatomigen idealen Gases. Zweite Abhandlung. In D. Simon, editor, *Albert Einstein: Akademie-Vorträge*, pages 245–257. Wiley, 1 edition, (2005). ISBN 978-3-527-40609-8.

[18] N. Verhelst. *Over vortices en vortexstructuren in ultrakoude kwantumgassen.* Ph.D. thesis, UAntwerpen, (2019).

[19] L. De Broglie. Recherches sur la théorie des Quanta. *Ann. Phys.* **10**(3):22–128, (1925).

[20] H. K. Onnes. Further experiments with Liquid Helium. D. On the change of Electrical Resistance of Pure Metals at very low Temperatures, etc. V. The Disappearance of the resistance of mercury. In *Proc. KNAW*, volume 14, pages 113–115, (1911).

[21] P. Kapitza. Viscosity of Liquid Helium below the λ-Point. *Nature.* **141**(3558):74–74, (1938).

[22] L. Landau. Theory of the Superfluidity of Helium II. *Phys. Rev.* **60**(4):356–358, (1941).

[23] F. London. The λ-Phenomenon of Liquid Helium and the Bose-Einstein Degeneracy. *Nature.* **141**(3571):643–644, (1938).

[24] A. F. G. Wyatt. Evidence for a Bose–Einstein condensate in liquid 4He from quantum evaporation. *Nature.* **391**(6662):56–59, (1998).

[25] O. Penrose & L. Onsager. Bose-Einstein Condensation and Liquid Helium. *Phys. Rev.* **104**(3):576–584, (1956).

[26] V. F. Sears, E. C. Svensson, P. Martel, & A. D. B. Woods. Neutron-Scattering Determination of the Momentum Distribution and the Condensate Fraction in Liquid He 4. *Phys. Rev. Lett.* **49**(4):279–282, (1982).

[27] H. K. Onnes. The liquefaction of helium. In *Proc. KNAW*, volume 11, pages 168–185, (1909).

[28] E. L. Raab, M. Prentiss, A. Cable, S. Chu, & D. E. Pritchard. Trapping of Neutral Sodium Atoms with Radiation Pressure. *Phys. Rev. Lett.* **59**(23):2631–2634, (1987).

[29] S. Chu, L. Hollberg, J. E. Bjorkholm, A. Cable, & A. Ashkin. Three-dimensional viscous confinement and cooling of atoms by resonance radiation pressure. *Phys. Rev. Lett.* **55**(1):48–51, (1985).

[30] W. D. Phillips & H. Metcalf. Laser Deceleration of an Atomic Beam. *Phys. Rev. Lett.* **48**(9):596–599, (1982).

[31] A. Aspect, E. Arimondo, R. Kaiser, N. Vansteenkiste, & C. Cohen-Tannoudji. Laser Cooling below the One-Photon Recoil Energy by Velocity-Selective Coherent Population Trapping. *Phys. Rev. Lett.* **61**(7):826–829, (1988).

[32] S. Chu. Nobel Lecture: The manipulation of neutral particles. *Rev. Mod. Phys.* **70**(3):685–706, (1998).

[33] C. N. Cohen-Tannoudji. Nobel Lecture: Manipulating atoms with photons. *Rev. Mod. Phys.* **70**(3):707–719, (1998).

[34] W. D. Phillips. Nobel Lecture: Laser cooling and trapping of neutral atoms. *Rev. Mod. Phys.* **70**(3):721–741, (1998).

[35] M. H. Anderson, J. R. Ensher, M. R. Matthews, C. E. Wieman, & E. A. Cornell. Observation of Bose-Einstein Condensation in a Dilute Atomic Vapor. *Science.* **269**(5221): 198–201, (1995).

[36] K. B. Davis, M. O. Mewes, M. R. Andrews, N. J. Van Druten, D. S. Durfee, D. M. Kurn, & W. Ketterle. Bose-Einstein Condensation in a Gas of Sodium Atoms. *Phys. Rev. Lett.* **75**(22):3969–3973, (1995).

[37] C. C. Bradley, C. A. Sackett, J. J. Tollett, & R. G. Hulet. Evidence of Bose-Einstein Condensation in an Atomic Gas with Attractive Interactions. *Phys. Rev. Lett.* **75**(9): 1687–1690, (1995).

[38] E. A. Cornell & C. E. Wieman. Nobel Lecture: Bose-Einstein condensation in a dilute gas, the first 70 years and some recent experiments. *Rev. Mod. Phys.* **74**(3):875–893, (2002).

[39] W. Ketterle. Nobel lecture: When atoms behave as waves: Bose-Einstein condensation and the atom laser. *Rev. Mod. Phys.* **74**(4):1131–1151, (2002).

[40] M. R. Andrews, C. G. Townsend, H. J. Miesner, D. S. Durfee, D. M. Kurn, & W. Ketterle. Observation of Interference Between Two Bose Condensates. *Science.* **275**(5300):637–641, (1997).

[41] O. M. Maragò, S. A. Hopkins, J. Arlt, E. Hodby, G. Hechenblaikner, & C. J. Foot. Observation of the Scissors Mode and Evidence for Superfluidity of a Trapped Bose-Einstein Condensed Gas. *Phys. Rev. Lett.* **84**(10):2056–2059, (2000).

[42] A. L. Fetter. Rotating trapped Bose-Einstein condensates. *Rev. Mod. Phys.* **81**(2):647–691, (2009).

[43] M. C. Tsatsos, P. E. Tavares, A. Cidrim, A. R. Fritsch, M. A. Caracanhas, F. E. A. Dos Santos, C. F. Barenghi, & V. S. Bagnato. Quantum turbulence in trapped atomic Bose–Einstein condensates. *Physics Reports.* **622**:1–52, (2016).

[44] N. B. Jørgensen, L. Wacker, K. T. Skalmstang, M. M. Parish, J. Levinsen, R. S. Christensen, G. M. Bruun, & J. J. Arlt. Observation of Attractive and Repulsive Polarons in a Bose-Einstein Condensate. *Phys. Rev. Lett.* **117**(5):055302, (2016).

[45] C. Chin, R. Grimm, P. Julienne, & E. Tiesinga. Feshbach resonances in ultracold gases. *Rev. Mod. Phys.* **82**(2):1225–1286, (2010).

[46] A. L. Gaunt, T. F. Schmidutz, I. Gotlibovych, R. P. Smith, & Z. Hadzibabic. Bose-Einstein Condensation of Atoms in a Uniform Potential. *Phys. Rev. Lett.* **110**(20):200406, (2013).

[47] M. Olshanii. Atomic Scattering in the Presence of an External Confinement and a Gas of Impenetrable Bosons. *Phys. Rev. Lett.* **81**(5):938–941, (1998).

[48] T. P. Meyrath, F. Schreck, J. L. Hanssen, C. S. Chuu, & M. G. Raizen. Bose-Einstein condensate in a box. *Phys. Rev. A.* **71**(4):041604, (2005).

[49] D. Rychtarik, B. Engeser, H. C. Nägerl, & R. Grimm. Two-Dimensional Bose-Einstein Condensate in an Optical Surface Trap. *Phys. Rev. Lett.* **92**(17):173003, (2004).

[50] Z. Hadzibabic, P. Krüger, M. Cheneau, B. Battelier, & J. Dalibard. Berezinskii–Kosterlitz–Thouless crossover in a trapped atomic gas. *Nature.* **441**(7097):1118–1121, (2006).

[51] N. D. Mermin & H. Wagner. Absence of Ferromagnetism or Antiferromagnetism in One- or Two-Dimensional Isotropic Heisenberg Models. *Phys. Rev. Lett.* **17**(22):1133–1136, (1966).

[52] V. Bagnato & D. Kleppner. Bose-Einstein condensation in low-dimensional traps. *Phys. Rev. A.* **44**(11):7439–7441, (1991).

[53] O. Morsch & M. Oberthaler. Dynamics of Bose-Einstein condensates in optical lattices. *Rev. Mod. Phys.* **78**(1):179–215, (2006).

[54] M. P. A. Fisher, P. B. Weichman, G. Grinstein, & D. S. Fisher. Boson localization and the superfluid-insulator transition. *Phys. Rev. B.* **40**(1):546–570, (1989).

[55] D. Jaksch, C. Bruder, J. I. Cirac, C. W. Gardiner, & P. Zoller. Cold Bosonic Atoms in Optical Lattices. *Phys. Rev. Lett.* **81**(15):3108–3111, (1998).

[56] M. Greiner, O. Mandel, T. Esslinger, T. W. Hänsch, & I. Bloch. Quantum phase transition from a superfluid to a Mott insulator in a gas of ultracold atoms. *Nature.* **415**(6867):39–44, (2002).

[57] G. Kordas, D. Witthaut, P. Buonsante, A. Vezzani, R. Burioni, A. I. Karanikas, & S. Wimberger. The dissipative Bose-Hubbard model: Methods and examples. *Eur. Phys. J. Spec. Top.* **224**(11):2127–2171, (2015).

[58] R. T. Scalettar, G. G. Batrouni, & G. T. Zimanyi. Localization in interacting, disordered, Bose systems. *Phys. Rev. Lett.* **66**(24):3144–3147, (1991).

[59] W. Krauth & N. Trivedi. Mott and Superfluid Transitions in a Strongly Interacting Lattice Boson System. *Europhys. Lett.* **14**(7):627–632, (1991).

[60] B. Capogrosso-Sansone, N. V. Prokof'ev, & B. V. Svistunov. Phase diagram and thermodynamics of the three-dimensional Bose-Hubbard model. *Phys. Rev. B.* **75**(13):134302, (2007).

[61] R. M. Bradley & S. Doniach. Quantum fluctuations in chains of Josephson junctions. *Phys. Rev. B.* **30**(3):1138–1147, (1984).

[62] H. S. J. Van Der Zant, F. C. Fritschy, W. J. Elion, L. J. Geerligs, & J. E. Mooij. Field-induced superconductor-to-insulator transitions in Josephson-junction arrays. *Phys. Rev. Lett.* **69**(20):2971–2974, (1992).

[63] A. Van Oudenaarden & J. E. Mooij. One-Dimensional Mott Insulator Formed by Quantum Vortices in Josephson Junction Arrays. *Phys. Rev. Lett.* **76**(26):4947–4950, (1996).

[64] C. Orzel, A. K. Tuchman, M. L. Fenselau, M. Yasuda, & M. A. Kasevich. Squeezed States in a Bose-Einstein Condensate. *Science.* **291**(5512):2386–2389, (2001).

[65] A. M. Kaufman, M. E. Tai, A. Lukin, M. Rispoli, R. Schittko, P. M. Preiss, & M. Greiner. Quantum thermalization through entanglement in an isolated many-body system. *Science.* **353**(6301):794–800, (2016).

[66] R. Labouvie, B. Santra, S. Heun, & H. Ott. Bistability in a Driven-Dissipative Superfluid. *Phys. Rev. Lett.* **116**(23):235302, (2016).

[67] J. Benary, C. Baals, E. Bernhart, J. Jiang, M. Röhrle, & H. Ott. Experimental observation of a dissipative phase transition in a multi-mode many-body quantum system. *New J. Phys.* **24**(10):103034, (2022).

[68] B. Yang, H. Sun, R. Ott, H. Y. Wang, T. V. Zache, J. C. Halimeh, Z. S. Yuan, P. Hauke, & J. W. Pan. Observation of gauge invariance in a 71-site Bose–Hubbard quantum simulator. *Nature.* **587**(7834):392–396, (2020).

[69] M. Miranda, R. Inoue, Y. Okuyama, A. Nakamoto, & M. Kozuma. Site-resolved imaging of ytterbium atoms in a two-dimensional optical lattice. *Phys. Rev. A.* **91**(6):063414, (2015).

[70] K. Kwon, K. Kim, J. Hur, S. Huh, & J. y. Choi. Site-resolved imaging of a bosonic Mott insulator of Li 7 atoms. *Phys. Rev. A.* **105**(3):033323, (2022).

[71] B. Cao, K. W. Mahmud, & M. Hafezi. Two coupled nonlinear cavities in a driven-dissipative environment. *Phys. Rev. A.* **94**(6):063805, (2016).

[72] C. Noh & D. G. Angelakis. Quantum simulations and many-body physics with light. *Rep. Prog. Phys.* **80**(1):016401, (2017).

[73] M. Mamaev, L. C. G. Govia, & A. A. Clerk. Dissipative stabilization of entangled cat states using a driven Bose-Hubbard dimer. *Quantum.* **2**:58, (2018).

[74] C. Mink, A. Pelster, J. Benary, H. Ott, & M. Fleischhauer. Variational truncated Wigner approximation for weakly interacting Bose fields: Dynamics of coupled condensates. *SciPost Phys.* **12**(2):051, (2022).

[75] R. Ceulemans & M. Wouters. Nonequilibrium steady states and critical slowing down in the dissipative Bose-Hubbard model. *Phys. Rev. A.* **108**(1):013314, (2023).

[76] J. Stenger, S. Inouye, D. M. Stamper-Kurn, H. J. Miesner, A. P. Chikkatur, & W. Ketterle. Spin domains in ground-state Bose–Einstein condensates. *Nature.* **396**(6709):345–348, (1998).

[77] Y. Kawaguchi & M. Ueda. Spinor Bose-Einstein condensates. *Physics Reports.* **520**(5): 253–381, (2012).

[78] D. M. Stamper-Kurn & M. Ueda. Spinor Bose gases: Symmetries, magnetism, and quantum dynamics. *Rev. Mod. Phys.* **85**(3):1191–1244, (2013).

[79] G. E. Marti & D. M. Stamper-Kurn. Spinor Bose-Einstein gases, arXiv:1511.01575, (2015).

[80] E. Fermi. Uber die magnetischen Momente der Atomkerne. *Z. Physik.* **60**(5-6):320–333, (1930).

[81] W. Demtröder. *Atoms, Molecules, and Photons: An Introduction to Atomic-, Molecular-, and Quantum-Physics.* Springer, Berlin ; New York, (2006). ISBN 978-3-540-20631-6.

[82] S. Goudsmit & R. F. Bacher. The Paschen-Back Effect of Hyperfine Structure. *Phys. Rev.* **34**(11):1499–1500, (1929).

[83] G. C. Wick. The Evaluation of the Collision Matrix. *Phys. Rev.* **80**(2):268–272, (1950).

[84] C. J. Myatt, E. A. Burt, R. W. Ghrist, E. A. Cornell, & C. E. Wieman. Production of Two Overlapping Bose-Einstein Condensates by Sympathetic Cooling. *Phys. Rev. Lett.* **78**(4):586–589, (1997).

[85] D. S. Hall, M. R. Matthews, J. R. Ensher, C. E. Wieman, & E. A. Cornell. Dynamics

of Component Separation in a Binary Mixture of Bose-Einstein Condensates. *Phys. Rev. Lett.* **81**(8):1539–1542, (1998).

[86] L. E. Sadler, J. M. Higbie, S. R. Leslie, M. Vengalattore, & D. M. Stamper-Kurn. Spontaneous symmetry breaking in a quenched ferromagnetic spinor Bose–Einstein condensate. *Nature.* **443**(7109):312–315, (2006).

[87] J. Guzman, G. B. Jo, A. N. Wenz, K. W. Murch, C. K. Thomas, & D. M. Stamper-Kurn. Long-time-scale dynamics of spin textures in a degenerate F = 1 87 Rb spinor Bose gas. *Phys. Rev. A.* **84**(6):063625, (2011).

[88] S. Huh, K. Kim, K. Kwon, & J. y. Choi. Observation of a strongly ferromagnetic spinor Bose-Einstein condensate. *Phys. Rev. Research.* **2**(3):033471, (2020).

[89] K. Jiménez-García, A. Invernizzi, B. Evrard, C. Frapolli, J. Dalibard, & F. Gerbier. Spontaneous formation and relaxation of spin domains in antiferromagnetic spin-1 condensates. *Nat. Commun.* **10**(1):1422, (2019).

[90] L. Y. Qiu, H. Y. Liang, Y. B. Yang, H. X. Yang, T. Tian, Y. Xu, & L. M. Duan. Observation of generalized Kibble-Zurek mechanism across a first-order quantum phase transition in a spinor condensate. *Sci. Adv.* **6**(21):eaba7292, (2020).

[91] H. Liang, L. Qiu, Y. Yang, H. Yang, T. Tian, Y. Xu, & L. Duan. Observation of heat scaling across a first-order quantum phase transition in a spinor condensate. *New J. Phys.* **23**(3):033038, (2021).

[92] R. Barnett, A. Polkovnikov, & M. Vengalattore. Prethermalization in quenched spinor condensates. *Phys. Rev. A.* **84**(2):023606, (2011).

[93] M. D. Barrett, J. A. Sauer, & M. S. Chapman. All-Optical Formation of an Atomic Bose-Einstein Condensate. *Phys. Rev. Lett.* **87**(1):010404, (2001).

[94] A. Del Campo & W. H. Zurek. Universality of phase transition dynamics: Topological defects from symmetry breaking. *Int. J. Mod. Phys. A.* **29**(08):1430018, (2014).

[95] H. Saito, Y. Kawaguchi, & M. Ueda. Kibble-Zurek mechanism in a quenched ferromagnetic Bose-Einstein condensate. *Phys. Rev. A.* **76**(4):043613, (2007).

[96] M. Ueda. Topological aspects in spinor Bose–Einstein condensates. *Rep. Prog. Phys.* **77**(12):122401, (2014).

[97] L. A. Williamson & P. B. Blakie. Universal coarsening dynamics of a quenched ferromagnetic spin-1 condensate. *Phys. Rev. Lett.* **116**(2):025301, (2016).

[98] S. Lannig, C. M. Schmied, M. Prüfer, P. Kunkel, R. Strohmaier, H. Strobel, T. Gasenzer, P. G. Kevrekidis, & M. K. Oberthaler. Collisions of three-component vector solitons in Bose-Einstein condensates. *Phys. Rev. Lett.* **125**(17):170401, (2020).

[99] M. Prüfer, P. Kunkel, H. Strobel, S. Lannig, D. Linnemann, C. M. Schmied, J. Berges, T. Gasenzer, & M. K. Oberthaler. Observation of universal dynamics in a spinor Bose gas far from equilibrium. *Nature.* **563**(7730):217–220, (2018).

[100] M. Ueda. Quantum equilibration, thermalization and prethermalization in ultracold atoms. *Nat Rev Phys.* **2**(12):669–681, (2020).

[101] A. Polkovnikov, K. Sengupta, A. Silva, & M. Vengalattore. Colloquium: Nonequilibrium dynamics of closed interacting quantum systems. *Rev. Mod. Phys.* **83**(3):863–883, (2011).

[102] R. Cominotti, A. Berti, A. Farolfi, A. Zenesini, G. Lamporesi, I. Carusotto, A. Recati, & G. Ferrari. Observation of Massless and Massive Collective Excitations with Faraday Patterns in a Two-Component Superfluid. *Phys. Rev. Lett.* **128**(21):210401, (2022).

[103] M. Abad & A. Recati. A study of coherently coupled two-component Bose-Einstein condensates. *Eur. Phys. J. D.* **67**(7):148, (2013).

[104] Sartori, Alberto. *Dynamical Properties of Bose-Bose Mixtures*. Ph.D. thesis, Universita degli studi di Trento, (2016).

[105] S. Butera, P. Öhberg, & I. Carusotto. Black-hole lasing in coherently coupled two-component atomic condensates. *Phys. Rev. A.* **96**(1):013611, (2017).

[106] S. B. Papp, J. M. Pino, & C. E. Wieman. Tunable Miscibility in a Dual-Species Bose-Einstein Condensate. *Phys. Rev. Lett.* **101**(4):040402, (2008).

[107] K. L. Lee, N. B. Jørgensen, I. K. Liu, L. Wacker, J. J. Arlt, & N. P. Proukakis. Phase separation and dynamics of two-component Bose-Einstein condensates. *Phys. Rev. A.* **94** (1):013602, (2016).

[108] E. Nicklas, M. Karl, M. Höfer, A. Johnson, W. Muessel, H. Strobel, J. Tomkovič, T. Gasenzer, & M. K. Oberthaler. Observation of Scaling in the Dynamics of a Strongly Quenched Quantum Gas. *Phys. Rev. Lett.* **115**(24):245301, (2015).

[109] R. Cominotti, A. Berti, C. Dulin, C. Rogora, G. Lamporesi, I. Carusotto, A. Recati, A. Zenesini, & G. Ferrari. Ferromagnetism in an Extended Coherently Coupled Atomic Superfluid. *Phys. Rev. X.* **13**(2):021037, (2023).

[110] M. R. Matthews, B. P. Anderson, P. C. Haljan, D. S. Hall, C. E. Wieman, & E. A. Cornell. Vortices in a Bose-Einstein Condensate. *Phys. Rev. Lett.* **83**(13):2498–2501, (1999).

[111] E. J. Mueller & T. L. Ho. Two-Component Bose-Einstein Condensates with a Large Number of Vortices. *Phys. Rev. Lett.* **88**(18):180403, (2002).

[112] R. A. Battye, N. R. Cooper, & P. M. Sutcliffe. Stable Skyrmions in Two-Component Bose-Einstein Condensates. *Phys. Rev. Lett.* **88**(8):080401, (2002).

[113] A. Farolfi, D. Trypogeorgos, C. Mordini, G. Lamporesi, & G. Ferrari. Observation of Magnetic Solitons in Two-Component Bose-Einstein Condensates. *Phys. Rev. Lett.* **125** (3):030401, (2020).

[114] A. Recati & S. Stringari. Coherently Coupled Mixtures of Bose-Einstein Condensed Gases. *Annu. Rev. Condens. Matter Phys.* **13**(1):407–432, (2022).

[115] T. L. Ho & V. B. Shenoy. Binary Mixtures of Bose Condensates of Alkali Atoms. *Phys. Rev. Lett.* **77**(16):3276–3279, (1996).

[116] T. Bienaimé, E. Fava, G. Colzi, C. Mordini, S. Serafini, C. Qu, S. Stringari, G. Lamporesi, & G. Ferrari. Spin-dipole oscillation and polarizability of a binary Bose-Einstein condensate near the miscible-immiscible phase transition. *Phys. Rev. A.* **94**(6):063652, (2016).

[117] E. Fava, T. Bienaimé, C. Mordini, G. Colzi, C. Qu, S. Stringari, G. Lamporesi, & G. Ferrari. Observation of Spin Superfluidity in a Bose Gas Mixture. *Phys. Rev. Lett.* **120** (17):170401, (2018).

[118] A. Farolfi, A. Zenesini, D. Trypogeorgos, C. Mordini, A. Gallemí, A. Roy, A. Recati, G.

Lamporesi, & G. Ferrari. Quantum-torque-induced breaking of magnetic interfaces in ultracold gases. *Nat. Phys.* **17**(12):1359–1363, (2021).

[119] J. H. Kim, D. Hong, & Y. Shin. Observation of two sound modes in a binary superfluid gas. *Phys. Rev. A.* **101**(6):061601, (2020).

[120] G. Modugno, M. Modugno, F. Riboli, G. Roati, & M. Inguscio. Two Atomic Species Superfluid. *Phys. Rev. Lett.* **89**(19):190404, (2002).

[121] G. Thalhammer, G. Barontini, L. De Sarlo, J. Catani, F. Minardi, & M. Inguscio. Double Species Bose-Einstein Condensate with Tunable Interspecies Interactions. *Phys. Rev. Lett.* **100**(21):210402, (2008).

[122] L. Zhao, J. Jiang, T. Tang, M. Webb, & Y. Liu. Dynamics in spinor condensates tuned by a microwave dressing field. *Phys. Rev. A.* **89**(2):023608, (2014).

[123] E. P. Gross. Structure of a quantized vortex in boson systems. *Nuovo Cim.* **20**(3):454–477, (1961).

[124] L. P. Pitaevskii. Vortex lines in an imperfect Bose gas. *Sov. Phys. JETP.* **13**(2):451–454, (1961).

[125] N. Bogoliubov. On the theory of superfluidity. *J. Phys.* **11**(1):23, (1947).

[126] A. L. Fetter. Nonuniform states of an imperfect bose gas. *Annals of Physics.* **70**(1):67–101, (1972).

[127] J. P. Blaizot & G. Ripka. *Quantum Theory of Finite Systems.* MIT Press, Cambridge, Mass, (1986). ISBN 978-0-262-02214-9.

[128] A. Griffin. Conserving and gapless approximations for an inhomogeneous Bose gas at finite temperatures. *Phys. Rev. B.* **53**(14):9341–9347, (1996).

[129] A. Serafini. *Quantum Continuous Variables: A Primer of Theoretical Methods.* CRC Press, Taylor & Francis Group, CRC Press is an imprint of the Taylor & Francis Group, an informa business, Boca Raton, (2017). ISBN 978-1-4822-4634-6.

[130] L. Isserlis. On a Formula for the Product-Moment Coefficient of any Order of a Normal Frequency Distribution in any Number of Variables. *Biometrika.* **12**(1/2):134, (1918).

[131] M. O. Scully & M. S. Zubairy. *Quantum Optics.* Cambridge University Press, Cambridge ; New York, (1997). ISBN 978-0-521-43458-4.

[132] R. J. Glauber. Coherent and Incoherent States of the Radiation Field. *Phys. Rev.* **131** (6):2766–2788, (1963).

[133] C. Weedbrook, S. Pirandola, R. Garcia-Patron, N. J. Cerf, T. C. Ralph, J. H. Shapiro, & S. Lloyd. Gaussian Quantum Information. *Rev. Mod. Phys.* **84**(2):621–669, (2012).

[134] W. H. Zurek. Decoherence, Chaos, Quantum-Classical Correspondence, andthe Algorithmic Arrow of Time. *Physica Scripta.* **T76**(1):186, (1998).

[135] R. Schnabel. Squeezed states of light and their applications in laser interferometers. *Physics Reports.* **684**:1–51, (2017).

[136] A. Boudjemâa & M. Benarous. Variational self-consistent theory for trapped Bose gases at finite temperature. *Eur. Phys. J. D.* **59**(3):427–434, (2010).

[137] T. Guaita, L. Hackl, T. Shi, C. Hubig, E. Demler, & J. I. Cirac. Gaussian time dependent

variational principle for the Bose-Hubbard model. *Phys. Rev. B.* **100**(9):094529, (2019).

[138] V. E. Colussi, H. Kurkjian, M. Van Regemortel, S. Musolino, J. van de Kraats, M. Wouters, & S. J. J. M. F. Kokkelmans. Cumulant theory of the unitary Bose gas: Prethermal and Efimovian dynamics. *Phys. Rev. A.* **102**(6):063314, (2020).

[139] W. Verstraelen & M. Wouters. Gaussian Quantum Trajectories for the Variational Simulation of Open Quantum-Optical Systems. *Applied Sciences.* **8**(9):1427, (2018).

[140] P. Kramer & M. Saraceno. *Geometry of the Time-Dependent Variational Principle in Quantum Mechanics.* Number 140 in Lecture Notes in Physics. Springer, Berlin, (1981). ISBN 978-3-540-10579-4 978-0-387-10579-6.

[141] J. Haegeman, J. I. Cirac, T. J. Osborne, I. Pižorn, H. Verschelde, & F. Verstraete. Time-Dependent Variational Principle for Quantum Lattices. *Phys. Rev. Lett.* **107**(7):070601, (2011).

[142] M. Van Regemortel, W. Casteels, I. Carusotto, & M. Wouters. Spontaneous Beliaev-Landau scattering out of equilibrium. *Phys. Rev. A.* **96**(5):053854, (2017).

[143] M. Van Regemortel, H. Kurkjian, M. Wouters, & I. Carusotto. Prethermalization to thermalization crossover in a dilute Bose gas following an interaction ramp. *Phys. Rev. A.* **98**(5):053612, (2018).

[144] S. Musolino, H. Kurkjian, M. Van Regemortel, M. Wouters, S. J. J. M. F. Kokkelmans, & V. E. Colussi. Bose-Einstein Condensation of Efimovian Triples in the Unitary Bose Gas. *Phys. Rev. Lett.* **128**(2):020401, (2022).

[145] A. Sinatra, C. Lobo, & Y. Castin. The truncated Wigner method for Bose-condensed gases: Limits of validity and applications. *J. Phys. B: At. Mol. Opt. Phys.* **35**(17):3599–3631, (2002).

[146] I. Carusotto & C. Ciuti. Quantum fluids of light. *Rev. Mod. Phys.* **85**(1):299–366, (2013).

[147] C. W. Gardiner & P. Zoller. *Quantum Noise: A Handbook of Markovian and Non-Markovian Quantum Stochastic Methods with Applications to Quantum Optics.* Springer Series in Synergetics. Springer, Berlin ; New York, 3rd ed edition, (2004). ISBN 978-3-540-22301-6.

[148] R. B. Laughlin. Anomalous Quantum Hall Effect: An Incompressible Quantum Fluid with Fractionally Charged Excitations. *Phys. Rev. Lett.* **50**(18):1395–1398, (1983).

[149] R. H. Dicke. Coherence in Spontaneous Radiation Processes. *Phys. Rev.* **93**(1):99–110, (1954).

[150] J. K. Stockton, R. Van Handel, & H. Mabuchi. Deterministic Dicke-state preparation with continuous measurement and control. *Phys. Rev. A.* **70**(2):022106, (2004).

[151] M. C. Gutzwiller. Effect of Correlation on the Ferromagnetism of Transition Metals. *Phys. Rev. Lett.* **10**(5):159–162, (1963).

[152] D. Huybrechts & M. Wouters. Cluster methods for the description of a driven-dissipative spin model. *Phys. Rev. A.* **99**(4):043841, (2019).

[153] V. E. Colussi, F. Caleffi, C. Menotti, & A. Recati. Quantum Gutzwiller approach for the two-component Bose-Hubbard model. *SciPost Phys.* **12**(3):111, (2022).

[154] D. Perez-Garcia, F. Verstraete, M. M. Wolf, & J. I. Cirac. Matrix product state repres-

entations. *Quantum Info. Comput.* **7**(5):401–430, (2007).

[155] F. Verstraete, J. J. García-Ripoll, & J. I. Cirac. Matrix Product Density Operators: Simulation of Finite-Temperature and Dissipative Systems. *Phys. Rev. Lett.* **93**(20):207204, (2004).

[156] F. Verstraete, V. Murg, & J. Cirac. Matrix product states, projected entangled pair states, and variational renormalization group methods for quantum spin systems. *Advances in Physics.* **57**(2):143–224, (2008).

[157] S. R. White. Minimally Entangled Typical Quantum States at Finite Temperature. *Phys. Rev. Lett.* **102**(19):190601, (2009).

[158] E. M. Stoudenmire & S. R. White. Minimally entangled typical thermal state algorithms. *New J. Phys.* **12**(5):055026, (2010).

[159] M. Berta, F. G. S. L. Brandão, J. Haegeman, V. B. Scholz, & F. Verstraete. Thermal states as convex combinations of matrix product states. *Phys. Rev. B.* **98**(23):235154, (2018).

[160] R. Orús. Tensor networks for complex quantum systems. *Nat Rev Phys.* **1**(9):538–550, (2019).

[161] R. Orús. A practical introduction to tensor networks: Matrix product states and projected entangled pair states. *Annals of Physics.* **349**:117–158, (2014).

[162] S. Montangero. *Introduction to Tensor Network Methods: Numerical Simulations of Low-Dimensional Many-Body Quantum Systems.* Springer International Publishing, Cham, (2018). ISBN 978-3-030-01408-7.

[163] F. Verstraete & J. I. Cirac. Renormalization algorithms for Quantum-Many Body Systems in two and higher dimensions, cond-mat/0407066, (2004).

[164] G. Carleo, I. Cirac, K. Cranmer, L. Daudet, M. Schuld, N. Tishby, L. Vogt-Maranto, & L. Zdeborová. Machine learning and the physical sciences. *Rev. Mod. Phys.* **91**(4):045002, (2019).

[165] G. Carleo & M. Troyer. Solving the quantum many-body problem with artificial neural networks. *Science.* **355**(6325):602–606, (2017).

[166] R. G. Melko, G. Carleo, J. Carrasquilla, & J. I. Cirac. Restricted Boltzmann machines in quantum physics. *Nat. Phys.* **15**(9):887–892, (2019).

[167] M. J. Hartmann & G. Carleo. Neural-Network Approach to Dissipative Quantum Many-Body Dynamics. *Phys. Rev. Lett.* **122**(25):250502, (2019).

[168] G. Torlai & R. G. Melko. Machine-Learning Quantum States in the NISQ Era. *Annu. Rev. Condens. Matter Phys.* **11**(1):325–344, (2020).

[169] H. P. Breuer & F. Petruccione. *The Theory of Open Quantum Systems.* Oxford University Press, Oxford ; New York, (2002). ISBN 978-0-19-852063-4.

[170] U. Schollwöck. The density-matrix renormalization group. *Rev. Mod. Phys.* **77**(1):259–315, (2005).

[171] J. Cui, J. I. Cirac, & M. C. Bañuls. Variational Matrix Product Operators for the Steady State of Dissipative Quantum Systems. *Phys. Rev. Lett.* **114**(22):220601, (2015).

[172] S. Finazzi, A. Le Boité, F. Storme, A. Baksic, & C. Ciuti. Corner-Space Renormalization

Method for Driven-Dissipative Two-Dimensional Correlated Systems. *Phys. Rev. Lett.* **115** (8):080604, (2015).

[173] J. Dalibard, Y. Castin, & K. Mølmer. Wave-function approach to dissipative processes in quantum optics. *Phys. Rev. Lett.* **68**(5):580–583, (1992).

[174] R. Dum, P. Zoller, & H. Ritsch. Monte Carlo simulation of the atomic master equation for spontaneous emission. *Phys. Rev. A.* **45**(7):4879–4887, (1992).

[175] H. Carmichael. *An Open Systems Approach to Quantum Optics: Lectures Presented at the Université Libre de Bruxelles October 28 to November 4, 1991*, volume 18 of *Lecture Notes in Physics Monographs*. Springer Berlin Heidelberg, Berlin, Heidelberg, (1993). ISBN 978-3-540-56634-2.

[176] A. Barchielli & V. P. Belavkin. Measurements continuous in time and a posteriori states in quantum mechanics. *J. Phys. A: Math. Gen.* **24**(7):1495–1514, (1991).

[177] M. B. Plenio & P. L. Knight. The quantum-jump approach to dissipative dynamics in quantum optics. *Rev. Mod. Phys.* **70**(1):101–144, (1998).

[178] A. J. Daley. Quantum trajectories and open many-body quantum systems. *Advances in Physics.* **63**(2):77–149, (2014).

[179] N. Gisin & I. C. Percival. The quantum-state diffusion model applied to open systems. *J. Phys. A: Math. Gen.* **25**(21):5677–5691, (1992).

[180] C. W. Gardiner & C. W. Gardiner. *Stochastic Methods: A Handbook for the Natural and Social Sciences*. Springer Series in Synergetics. Springer, Berlin, 4th ed edition, (2009). ISBN 978-3-540-70712-7.

[181] A. J. Lichtenberg, M. A. Lieberman, & A. J. Lichtenberg. *Regular and Chaotic Dynamics*. Number v. 38 in Applied Mathematical Sciences. Springer-Verlag, New York, 2nd ed edition, (1992). ISBN 978-0-387-97745-4.

[182] M. Albiez, R. Gati, J. Fölling, S. Hunsmann, M. Cristiani, & M. K. Oberthaler. Direct Observation of Tunneling and Nonlinear Self-Trapping in a Single Bosonic Josephson Junction. *Phys. Rev. Lett.* **95**(1):010402, (2005).

[183] A. R. Kolovsky. Bose–Hubbard Hamiltonian: Quantum chaos approach. *Int. J. Mod. Phys. B.* **30**(10):1630009, (2016).

[184] A. A. Bychek, P. S. Muraev, D. N. Maksimov, E. N. Bulgakov, & A. R. Kolovsky. Chaotic and regular dynamics in the three-site Bose-Hubbard model. In *AIP Conf. Proc.*, volume 2241, page 020007, Moscow, Russia, (2020).

[185] W. H. Zurek. Decoherence, einselection, and the quantum origins of the classical. *Rev. Mod. Phys.* **75**(3):715–775, (2003).

[186] E. Bianchi, L. Hackl, & N. Yokomizo. Linear growth of the entanglement entropy and the Kolmogorov-Sinai rate. *J. High Energ. Phys.* **2018**(3):25, (2018).

[187] R. Ding & J. Li. Nonlinear finite-time Lyapunov exponent and predictability. *Physics Letters A.* **364**(5):396–400, (2007).

[188] M. Wouters. Quantum trajectories for the variational description of closed systems: A case study with Gaussian states. *Phys. Rev. E.* **102**(4):043314, (2020).

[189] W. Verstraelen & M. Wouters. Classical critical dynamics in quadratically driven Kerr

resonators. *Phys. Rev. A.* **101**(4):043826, (2020).

[190] W. Verstraelen, R. Rota, V. Savona, & M. Wouters. Gaussian trajectory approach to dissipative phase transitions: The case of quadratically driven photonic lattices. *Phys. Rev. Research.* **2**(2):022037, (2020).

[191] W. Verstraelen. *Gaussian Quantum Trajectories for the Variational Simulation of Open Quantum Systems, with Photonic Applications.* Ph.D. thesis, UAntwerpen, (2020).

[192] C. Monroe, D. M. Meekhof, B. E. King, & D. J. Wineland. A "Schrödinger Cat" Superposition State of an Atom. *Science.* **272**(5265):1131–1136, (1996).

[193] M. Brune, E. Hagley, J. Dreyer, X. Maître, A. Maali, C. Wunderlich, J. M. Raimond, & S. Haroche. Observing the Progressive Decoherence of the "Meter" in a Quantum Measurement. *Phys. Rev. Lett.* **77**(24):4887–4890, (1996).

[194] D. Leibfried, E. Knill, S. Seidelin, J. Britton, R. B. Blakestad, J. Chiaverini, D. B. Hume, W. M. Itano, J. D. Jost, C. Langer, R. Ozeri, R. Reichle, & D. J. Wineland. Creation of a six-atom 'Schrödinger cat' state. *Nature.* **438**(7068):639–642, (2005).

[195] W. B. Gao, C. Y. Lu, X. C. Yao, P. Xu, O. Gühne, A. Goebel, Y. A. Chen, C. Z. Peng, Z. B. Chen, & J. W. Pan. Experimental demonstration of a hyper-entangled ten-qubit Schrödinger cat state. *Nature Phys.* **6**(5):331–335, (2010).

[196] S. Deléglise, I. Dotsenko, C. Sayrin, J. Bernu, M. Brune, J. M. Raimond, & S. Haroche. Reconstruction of non-classical cavity field states with snapshots of their decoherence. *Nature.* **455**(7212):510–514, (2008).

[197] V. Bužek, A. Vidiella-Barranco, & P. L. Knight. Superpositions of coherent states: Squeezing and dissipation. *Phys. Rev. A.* **45**(9):6570–6585, (1992).

[198] D. F. Walls & G. J. Milburn. Effect of dissipation on quantum coherence. *Phys. Rev. A.* **31**(4):2403–2408, (1985).

[199] W. H. Zurek. Decoherence and the Transition from Quantum to Classical. *Phys. Today.* **44**(10):36–44, (1991).

[200] S. Habib, Y. Kluger, E. Mottola, & J. P. Paz. Dissipation and Decoherence in Mean Field Theory. *Phys. Rev. Lett.* **76**(25):4660–4663, (1996).

[201] E. T. Jaynes. Information Theory and Statistical Mechanics. II. *Phys. Rev.* **108**(2): 171–190, (1957).

[202] E. T. Jaynes. Information Theory and Statistical Mechanics. *Phys. Rev.* **106**(4):620–630, (1957).

[203] M. Rigol, V. Dunjko, V. Yurovsky, & M. Olshanii. Relaxation in a Completely Integrable Many-Body Quantum System: An *Ab Initio* Study of the Dynamics of the Highly Excited States of 1D Lattice Hard-Core Bosons. *Phys. Rev. Lett.* **98**(5):050405, (2007).

[204] J. M. Deutsch. Quantum statistical mechanics in a closed system. *Phys. Rev. A.* **43**(4): 2046–2049, (1991).

[205] M. Srednicki. Chaos and quantum thermalization. *Phys. Rev. E.* **50**(2):888–901, (1994).

[206] M. Rigol, V. Dunjko, & M. Olshanii. Thermalization and its mechanism for generic isolated quantum systems. *Nature.* **452**(7189):854–858, (2008).

[207] L. D'Alessio, Y. Kafri, A. Polkovnikov, & M. Rigol. From quantum chaos and eigenstate

thermalization to statistical mechanics and thermodynamics. *Advances in Physics.* **65**(3): 239–362, (2016).

[208] J. M. Deutsch. Eigenstate Thermalization Hypothesis. *Rep. Prog. Phys.* **81**(8):082001, (2018).

[209] P. Calabrese & J. Cardy. Evolution of entanglement entropy in one-dimensional systems. *J. Stat. Mech.* **2005**(04):P04010, (2005).

[210] N. Schuch, M. M. Wolf, K. G. H. Vollbrecht, & J. I. Cirac. On entropy growth and the hardness of simulating time evolution. *New J. Phys.* **10**(3):033032, (2008).

[211] J. Eisert. Entanglement and tensor network states. *Model. Simul.* **3**(520), (2013).

[212] D. N. Page. Average entropy of a subsystem. *Phys. Rev. Lett.* **71**(9):1291–1294, (1993).

[213] J. Eisert, M. Cramer, & M. B. Plenio. *Colloquium* : Area laws for the entanglement entropy. *Rev. Mod. Phys.* **82**(1):277–306, (2010).

[214] J. M. Koh, S. N. Sun, M. Motta, & A. J. Minnich. Measurement-induced entanglement phase transition on a superconducting quantum processor with mid-circuit readout. *Nat. Phys.* **19**(9):1314–1319, (2023).

[215] Google Quantum AI and Collaborators. Measurement-induced entanglement and teleportation on a noisy quantum processor. *Nature.* **622**(7983):481–486, (2023).

[216] B. Skinner, J. Ruhman, & A. Nahum. Measurement-Induced Phase Transitions in the Dynamics of Entanglement. *Phys. Rev. X.* **9**(3):031009, (2019).

[217] A. Chan, R. M. Nandkishore, M. Pretko, & G. Smith. Unitary-projective entanglement dynamics. *Phys. Rev. B.* **99**(22):224307, (2019).

[218] Y. Li, X. Chen, & M. P. A. Fisher. Measurement-driven entanglement transition in hybrid quantum circuits. *Phys. Rev. B.* **100**(13):134306, (2019).

[219] V. Khemani, A. Vishwanath, & D. A. Huse. Operator Spreading and the Emergence of Dissipative Hydrodynamics under Unitary Evolution with Conservation Laws. *Phys. Rev. X.* **8**(3):031057, (2018).

[220] T. Rakovszky, C. W. Von Keyserlingk, & F. Pollmann. Dissipation-assisted operator evolution method for capturing hydrodynamic transport. *Phys. Rev. B.* **105**(7):075131, (2022).

[221] C. Gneiting, F. R. Anger, & A. Buchleitner. Incoherent ensemble dynamics in disordered systems. *Phys. Rev. A.* **93**(3):032139, (2016).

[222] C. M. Kropf, C. Gneiting, & A. Buchleitner. Effective Dynamics of Disordered Quantum Systems. *Phys. Rev. X.* **6**(3):031023, (2016).

[223] H. B. Chen & Y. N. Chen. Canonical Hamiltonian ensemble representation of dephasing dynamics and the impact of thermal fluctuations on quantum-to-classical transition. *Sci Rep.* **11**(1):10046, (2021).

[224] S. Ruder. An overview of gradient descent optimization algorithms, arXiv:1609.04747, (2017).

[225] M. Wouters. Taming the entanglement in the dynamical theory of weakly interacting Bose gases, arXiv:2303.03230, (2023).

[226] N. N. Klausen, J. L. Bohn, & C. H. Greene. Nature of spinor Bose-Einstein condensates in rubidium. *Phys. Rev. A.* **64**(5):053602, (2001).

[227] C. K. Law, H. Pu, & N. P. Bigelow. Quantum Spins Mixing in Spinor Bose-Einstein Condensates. *Phys. Rev. Lett.* **81**(24):5257–5261, (1998).

[228] S. Yi, Ö. E. Müstecaplıoğlu, C. P. Sun, & L. You. Single-mode approximation in a spinor-1 atomic condensate. *Phys. Rev. A.* **66**(1):011601, (2002).

[229] W. Zhang, D. L. Zhou, M. S. Chang, M. S. Chapman, & L. You. Coherent spin mixing dynamics in a spin-1 atomic condensate. *Phys. Rev. A.* **72**(1):013602, (2005).

[230] L. D. Sarlo, L. Shao, V. Corre, T. Zibold, D. Jacob, J. Dalibard, & F. Gerbier. Spin fragmentation of Bose–Einstein condensates with antiferromagnetic interactions. *New J. Phys.* **15**(11):113039, (2013).

[231] J. Jie, Q. Guan, S. Zhong, A. Schwettmann, & D. Blume. Mean-field spin-oscillation dynamics beyond the single-mode approximation for a harmonically trapped spin-1 Bose-Einstein condensate. *Phys. Rev. A.* **102**(2):023324, (2020).

[232] A. Black, E. Gomez, L. Turner, S. Jung, & P. Lett. Spinor Dynamics in an Antiferromagnetic Spin-1 Condensate. *Phys. Rev. Lett.* **99**(7):070403, (2007).

[233] H. Pu, C. K. Law, S. Raghavan, J. H. Eberly, & N. P. Bigelow. Spin-mixing dynamics of a spinor Bose-Einstein condensate. *Phys. Rev. A.* **60**(2):1463–1470, (1999).

[234] B. Evrard, A. Qu, J. Dalibard, & F. Gerbier. From Many-Body Oscillations to Thermalization in an Isolated Spinor Gas. *Phys. Rev. Lett.* **126**(6):063401, (2021).

[235] R. B. Diener & T. L. Ho. Quantum Spin Dynamics of Spin-1 Bose Gas, arXiv:cond-mat/0608732, (2006).

[236] G. I. Mias, N. R. Cooper, & S. M. Girvin. Quantum noise, scaling, and domain formation in a spinor Bose-Einstein condensate. *Phys. Rev. A.* **77**(2):023616, (2008).

[237] P. Bader, S. Blanes, & F. Casas. Solving the Schrödinger eigenvalue problem by the imaginary time propagation technique using splitting methods with complex coefficients. *J. Chem. Phys.* **139**(12):124117, (2013).

[238] R. Barnett, H. Y. Hui, C. H. Lin, J. D. Sau, & S. Das Sarma. Quantum rotor theory of spinor condensates in tight traps. *Phys. Rev. A.* **83**(2):023613, (2011).

[239] L. Fernandes, M. Wouters, & J. Tempere. Gaussian trajectory description of fragmentation in an isolated spinor condensate. *Phys. Rev. A.* **105**(1):013305, (2022).

[240] B. Evrard, A. Qu, J. Dalibard, & F. Gerbier. Coherent seeding of the dynamics of a spinor Bose-Einstein condensate: From quantum to classical behavior. *Phys. Rev. A.* **103** (3):L031302, (2021).

[241] M. S. Chang, Q. Qin, W. Zhang, L. You, & M. S. Chapman. Coherent spinor dynamics in a spin-1 Bose condensate. *Nat. Phys.* **1**(2):111–116, (2005).

[242] A. Widera, F. Gerbier, S. Fölling, T. Gericke, O. Mandel, & I. Bloch. Coherent Collisional Spin Dynamics in Optical Lattices. *Phys. Rev. Lett.* **95**(19):190405, (2005).

[243] F. Gerbier, A. Widera, S. Fölling, O. Mandel, & I. Bloch. Resonant control of spin dynamics in ultracold quantum gases by microwave dressing. *Phys. Rev. A.* **73**(4):041602, (2006).

[244] Bertrand Evrard. *Dynamique Cohérente, Relaxation et Fragmentation d'un Condensat de Bose-Einstein Spinoriel*. Ph.D. thesis, Université PSL - Collège de France, Paris, (2020).

[245] J. Heinze, F. Deuretzbacher, & D. Pfannkuche. Influence of the particle number on the spin dynamics of ultracold atoms. *Phys. Rev. A.* **82**(2):023617, (2010).

[246] M. Berry, I. Marzoli, & W. Schleich. Quantum carpets, carpets of light. *Phys. World.* **14** (6):39–46, (2001).

[247] A. E. Kaplan, I. Marzoli, W. E. Lamb, & W. P. Schleich. Multimode interference: Highly regular pattern formation in quantum wave-packet evolution. *Phys. Rev. A.* **61**(3):032101, (2000).

[248] J. H. Eberly, N. B. Narozhny, & J. J. Sanchez-Mondragon. Periodic Spontaneous Collapse and Revival in a Simple Quantum Model. *Phys. Rev. Lett.* **44**(20):1323–1326, (1980).

[249] R. Robinett. Quantum wave packet revivals. *Physics Reports.* **392**(1-2):1–119, (2004).

[250] M. Serbyn, D. A. Abanin, & Z. Papić. Quantum many-body scars and weak breaking of ergodicity. *Nat. Phys.* **17**(6):675–685, (2021).

[251] E. M. Wright, D. F. Walls, & J. C. Garrison. Collapses and Revivals of Bose-Einstein Condensates Formed in Small Atomic Samples. *Phys. Rev. Lett.* **77**(11):2158–2161, (1996).

[252] E. M. Wright, T. Wong, M. J. Collett, S. M. Tan, & D. F. Walls. Collapses and revivals in the interference between two Bose-Einstein condensates formed in small atomic samples. *Phys. Rev. A.* **56**(1):591–602, (1997).

[253] M. Greiner, O. Mandel, T. W. Hänsch, & I. Bloch. Collapse and revival of the matter wave field of a Bose–Einstein condensate. *Nature.* **419**(6902):51–54, (2002).

[254] R. Horodecki, P. Horodecki, M. Horodecki, & K. Horodecki. Quantum entanglement. *Rev. Mod. Phys.* **81**(2):865–942, (2009).

[255] R. Islam, R. Ma, P. M. Preiss, M. Eric Tai, A. Lukin, M. Rispoli, & M. Greiner. Measuring entanglement entropy in a quantum many-body system. *Nature.* **528**(7580):77–83, (2015).

[256] L. M. Duan, J. I. Cirac, & P. Zoller. Quantum entanglement in spinor Bose-Einstein condensates. *Phys. Rev. A.* **65**(3):033619, (2002).

[257] B. Morris, B. Yadin, M. Fadel, T. Zibold, P. Treutlein, & G. Adesso. Entanglement between Identical Particles Is a Useful and Consistent Resource. *Phys. Rev. X.* **10**(4): 041012, (2020).

[258] M. Kitagawa & M. Ueda. Squeezed spin states. *Phys. Rev. A.* **47**(6):5138–5143, (1993).

[259] D. J. Wineland, J. J. Bollinger, W. M. Itano, & D. J. Heinzen. Squeezed atomic states and projection noise in spectroscopy. *Phys. Rev. A.* **50**(1):67–88, (1994).

[260] T. L. Ho & S. K. Yip. Fragmented and Single Condensate Ground States of Spin-1 Bose Gas. *Phys. Rev. Lett.* **84**(18):4031–4034, (2000).

[261] E. J. Mueller, T. L. Ho, M. Ueda, & G. Baym. Fragmentation of Bose-Einstein condensates. *Phys. Rev. A.* **74**(3):033612, (2006).

[262] P. Nozières & D. Saint James. Particle vs. pair condensation in attractive Bose liquids. *J. Phys. France.* **43**(7):1133–1148, (1982).

[263] B. Evrard, A. Qu, J. Dalibard, & F. Gerbier. Observation of fragmentation of a spinor

Bose-Einstein condensate. *Science.* **373**(6561):1340–1343, (2021).

[264] I. Bouchoule, B. Doyon, & J. Dubail. The effect of atom losses on the distribution of rapidities in the one-dimensional Bose gas. *SciPost Phys.* **9**(4):044, (2020).

[265] J. Berges, Sz. Borsányi, & C. Wetterich. Prethermalization. *Phys. Rev. Lett.* **93**(14): 142002, (2004).

[266] T. Mori, T. N. Ikeda, E. Kaminishi, & M. Ueda. Thermalization and prethermalization in isolated quantum systems: A theoretical overview. *J. Phys. B: At. Mol. Opt. Phys.* **51** (11):112001, (2018).

[267] B. Bertini, F. H. L. Essler, S. Groha, & N. J. Robinson. Prethermalization and thermalization in models with weak integrability breaking. *Phys. Rev. Lett.* **115**(18):180601, (2015).

[268] C. Eigen, J. A. P. Glidden, R. Lopes, E. A. Cornell, R. P. Smith, & Z. Hadzibabic. Universal prethermal dynamics of Bose gases quenched to unitarity. *Nature.* **563**(7730): 221–224, (2018).

[269] B. Misra & E. C. G. Sudarshan. The Zeno's paradox in quantum theory. *J. Math. Phys.* **18**(4):756–763, (1977).

[270] W. M. Itano, D. J. Heinzen, J. J. Bollinger, & D. J. Wineland. Quantum Zeno effect. *Phys. Rev. A.* **41**(5):2295–2300, (1990).

[271] A. Biella & M. Schiró. Many-Body Quantum Zeno Effect and Measurement-Induced Subradiance Transition. *Quantum.* **5**:528, (2021).

[272] A. Imambekov, M. Lukin, & E. Demler. Spin-exchange interactions of spin-one bosons in optical lattices: Singlet, nematic, and dimerized phases. *Phys. Rev. A.* **68**(6):063602, (2003).

[273] M. Rizzi, D. Rossini, G. De Chiara, S. Montangero, & R. Fazio. Phase Diagram of Spin-1 Bosons on One-Dimensional Lattices. *Phys. Rev. Lett.* **95**(24):240404, (2005).

[274] G. G. Batrouni, V. G. Rousseau, & R. T. Scalettar. Magnetic and Superfluid Transitions in the One-Dimensional Spin-1 Boson Hubbard Model. *Phys. Rev. Lett.* **102**(14):140402, (2009).

[275] K. V. Krutitsky & R. Graham. Spin-1 bosons with coupled ground states in optical lattices. *Phys. Rev. A.* **70**(6):063610, (2004).

[276] S. Tsuchiya, S. Kurihara, & T. Kimura. Superfluid–Mott insulator transition of spin-1 bosons in an optical lattice. *Phys. Rev. A.* **70**(4):043628, (2004).

[277] T. Kimura, S. Tsuchiya, & S. Kurihara. Possibility of a First-Order Superfluid–Mott-Insulator Transition of Spinor Bosons in an Optical Lattice. *Phys. Rev. Lett.* **94**(11): 110403, (2005).

[278] R. V. Pai, K. Sheshadri, & R. Pandit. Phases and transitions in the spin-1 Bose-Hubbard model: Systematics of a mean-field theory. *Phys. Rev. B.* **77**(1):014503, (2008).

[279] C. Becker, P. Soltan-Panahi, J. Kronjäger, S. Dörscher, K. Bongs, & K. Sengstock. Ultracold quantum gases in triangular optical lattices. *New J. Phys.* **12**(6):065025, (2010).

[280] K. W. Mahmud & E. Tiesinga. Dynamics of spin-1 bosons in an optical lattice: Spin mixing, quantum-phase-revival spectroscopy, and effective three-body interactions. *Phys.*

Rev. A. **88**(2):023602, (2013).

[281] S. S. Natu, J. H. Pixley, & S. Das Sarma. Static and dynamic properties of interacting spin-1 bosons in an optical lattice. *Phys. Rev. A.* **91**(4):043620, (2015).

[282] L. Zhao, J. Jiang, T. Tang, M. Webb, & Y. Liu. Antiferromagnetic Spinor Condensates in a Two-Dimensional Optical Lattice. *Phys. Rev. Lett.* **114**(22):225302, (2015).

[283] L. Boltzmann. On Certain Questions of the Theory of Gases. *Nature.* **51**(1322):413–415, (1895).

[284] C. Barceló, S. Liberati, & M. Visser. Analogue Gravity. *Living Rev. Relativ.* **14**(1):3, (2011).

[285] A. Einstein. Die Grundlage der allgemeinen Relativitätstheorie. *Ann. Phys. (Berl.).* **354**(7):769–822, (1916).

[286] V. P. Frolov & I. D. Novikov. *Black Hole Physics*, volume 96 of *Fundamental Theories of Physics.* Springer Netherlands, Dordrecht, (1998). ISBN 978-0-7923-5146-7 978-94-011-5139-9.

[287] A. J. S. Hamilton & J. P. Lisle. The river model of black holes. *Am. J. Phys.* **76**(6):519–532, (2008).

[288] W. G. Unruh. Experimental Black-Hole Evaporation?. *Phys. Rev. Lett.* **46**(21):1351–1353, (1981).

[289] R. Brito, V. Cardoso, & P. Pani. *Superradiance: New Frontiers in Black Hole Physics*, volume 971 of *Lecture Notes in Physics.* Springer International Publishing, Cham, (2020). ISBN 978-3-030-46621-3.

[290] W. H. Press & S. A. Teukolsky. Floating Orbits, Superradiant Scattering and the Black-hole Bomb. *Nature.* **238**(5361):211–212, (1972).

[291] S. Corley & T. Jacobson. Black hole lasers. *Phys. Rev. D.* **59**(12):124011, (1999).

[292] D. Finkelstein. Past-Future Asymmetry of the Gravitational Field of a Point Particle. *Phys. Rev.* **110**(4):965–967, (1958).

[293] J. M. Bardeen, B. Carter, & S. W. Hawking. The four laws of black hole mechanics. *Commun.Math. Phys.* **31**(2):161–170, (1973).

[294] J. D. Bekenstein. Black Holes and Entropy. *Phys. Rev. D.* **7**(8):2333–2346, (1973).

[295] J. D. Bekenstein. Generalized second law of thermodynamics in black-hole physics. *Phys. Rev. D.* **9**(12):3292–3300, (1974).

[296] S. W. Hawking. Black hole explosions?. *Nature.* **248**(5443):30–31, (1974).

[297] S. W. Hawking. Particle creation by black holes. *Commun.Math. Phys.* **43**(3):199–220, (1975).

[298] D. J. Fixsen. The temperature of the cosmic microwave background. *ApJ.* **707**(2):916–920, (2009).

[299] C. Barceló, R. Carballo-Rubio, L. J. Garay, & G. Jannes. The lifetime problem of evaporating black holes: Mutiny or resignation. *Class. Quantum Grav.* **32**(3):035012, (2015).

[300] W. G. Unruh. Origin of the particles in black-hole evaporation. *Phys. Rev. D.* **15**(2):365–369, (1977).

[301] A. Cho. Test of Hawking's Prediction on the Horizon With Mock 'White Hole'. *Science.* **319**(5868):1321–1321, (2008).

[302] I. Carusotto & R. Balbinot. Acoustic Hawking radiation. *Nat. Phys.* **12**(10):897–898, (2016).

[303] R. Balbinot, A. Fabbri, S. Fagnocchi, & R. Parentani. Hawking radiation from acoustic black holes, short distance and backreaction effects. *Riv. Nuovo Cimento.* **28**(3):1–55, (2006).

[304] W. Unruh. Dumb holes: Analogues for black holes. *Phil. Trans. R. Soc. A.* **366**(1877): 2905–2913, (2008).

[305] L. Giacomelli. *Superradiant Phenomena.* Ph.D. thesis, UniTrento, (2021).

[306] R. Balbinot, A. Fabbri, S. Fagnocchi, A. Recati, & I. Carusotto. Nonlocal density correlations as a signature of Hawking radiation from acoustic black holes. *Phys. Rev. A.* **78** (2):021603, (2008).

[307] T. Jacobson. Black-hole evaporation and ultrashort distances. *Phys. Rev. D.* **44**(6):1731–1739, (1991).

[308] W. G. Unruh. Sonic analogue of black holes and the effects of high frequencies on black hole evaporation. *Phys. Rev. D.* **51**(6):2827–2838, (1995).

[309] R. Brout, S. Massar, R. Parentani, & Ph. Spindel. Hawking radiation without trans-Planckian frequencies. *Phys. Rev. D.* **52**(8):4559–4568, (1995).

[310] L. J. Garay, J. R. Anglin, J. I. Cirac, & P. Zoller. Sonic Analog of Gravitational Black Holes in Bose-Einstein Condensates. *Phys. Rev. Lett.* **85**(22):4643–4647, (2000).

[311] I. Carusotto, S. Fagnocchi, A. Recati, R. Balbinot, & A. Fabbri. Numerical observation of Hawking radiation from acoustic black holes in atomic Bose–Einstein condensates. *New J. Phys.* **10**(10):103001, (2008).

[312] A. Recati, N. Pavloff, & I. Carusotto. Bogoliubov theory of acoustic Hawking radiation in Bose-Einstein condensates. *Phys. Rev. A.* **80**(4):043603, (2009).

[313] A. M. Kamchatnov & N. Pavloff. Generation of dispersive shock waves by the flow of a Bose-Einstein condensate past a narrow obstacle. *Phys. Rev. A.* **85**(3):033603, (2012).

[314] S. Wüster. Phonon background versus analog Hawking radiation in Bose-Einstein condensates. *Phys. Rev. A.* **78**(2):021601, (2008).

[315] O. Lahav, A. Itah, A. Blumkin, C. Gordon, S. Rinott, A. Zayats, & J. Steinhauer. Realization of a Sonic Black Hole Analog in a Bose-Einstein Condensate. *Phys. Rev. Lett.* **105** (24):240401, (2010).

[316] J. Steinhauer. Observation of self-amplifying Hawking radiation in an analogue black-hole laser. *Nat. Phys.* **10**(11):864–869, (2014).

[317] J. Steinhauer. Observation of quantum Hawking radiation and its entanglement in an analogue black hole. *Nat. Phys.* **12**(10):959–965, (2016).

[318] U. Leonhardt. Questioning the Recent Observation of Quantum Hawking Radiation. *Ann. Phys. (Berl.).* **530**(5):1700114, (2018).

[319] J. R. Muñoz de Nova, K. Golubkov, V. I. Kolobov, & J. Steinhauer. Observation of thermal Hawking radiation and its temperature in an analogue black hole. *Nature.* **569**

(7758):688–691, (2019).

[320] V. I. Kolobov, K. Golubkov, J. R. Muñoz de Nova, & J. Steinhauer. Observation of stationary spontaneous Hawking radiation and the time evolution of an analogue black hole. *Nat. Phys.* **17**(3):362–367, (2021).

[321] M. Isoard & N. Pavloff. Departing from Thermality of Analogue Hawking Radiation in a Bose-Einstein Condensate. *Phys. Rev. Lett.* **124**(6):060401, (2020).

[322] M. J. Jacquet, S. Weinfurtner, & F. König. The next generation of analogue gravity experiments. *Phil. Trans. R. Soc. A.* **378**(2177):20190239, (2020).

[323] R. Schützhold & W. G. Unruh. Gravity wave analogues of black holes. *Phys. Rev. D.* **66**(4):044019, (2002).

[324] G. Rousseaux, C. Mathis, P. Maïssa, T. G. Philbin, & U. Leonhardt. Observation of negative-frequency waves in a water tank: A classical analogue to the Hawking effect?. *New J. Phys.* **10**(5):053015, (2008).

[325] G. Rousseaux, P. Maïssa, C. Mathis, P. Coullet, T. G. Philbin, & U. Leonhardt. Horizon effects with surface waves on moving water. *New J. Phys.* **12**(9):095018, (2010).

[326] S. Weinfurtner, E. W. Tedford, M. C. J. Penrice, W. G. Unruh, & G. A. Lawrence. Measurement of Stimulated Hawking Emission in an Analogue System. *Phys. Rev. Lett.* **106**(2):021302, (2011).

[327] H. S. Nguyen, D. Gerace, I. Carusotto, D. Sanvitto, E. Galopin, A. Lemaître, I. Sagnes, J. Bloch, & A. Amo. Acoustic Black Hole in a Stationary Hydrodynamic Flow of Microcavity Polaritons. *Phys. Rev. Lett.* **114**(3):036402, (2015).

[328] M. Jacquet, M. Joly, F. Claude, L. Giacomelli, Q. Glorieux, A. Bramati, I. Carusotto, & E. Giacobino. Analogue quantum simulation of the Hawking effect in a polariton superfluid. *Eur. Phys. J. D.* **76**(8):152, (2022).

[329] M. J. Jacquet, L. Giacomelli, Q. Valnais, M. Joly, F. Claude, E. Giacobino, Q. Glorieux, I. Carusotto, & A. Bramati. Quantum Vacuum Excitation of a Quasinormal Mode in an Analog Model of Black Hole Spacetime. *Phys. Rev. Lett.* **130**(11):111501, (2023).

[330] D. Vocke, C. Maitland, A. Prain, K. E. Wilson, F. Biancalana, E. M. Wright, F. Marino, & D. Faccio. Rotating black hole geometries in a two-dimensional photon superfluid. *Optica.* **5**(9):1099, (2018).

[331] T. G. Philbin, C. Kuklewicz, S. Robertson, S. Hill, F. König, & U. Leonhardt. Fiber-Optical Analog of the Event Horizon. *Science.* **319**(5868):1367–1370, (2008).

[332] J. Drori, Y. Rosenberg, D. Bermudez, Y. Silberberg, & U. Leonhardt. Observation of Stimulated Hawking Radiation in an Optical Analogue. *Phys. Rev. Lett.* **122**(1):010404, (2019).

[333] S. Knoop, T. Schuster, R. Scelle, A. Trautmann, J. Appmeier, M. K. Oberthaler, E. Tiesinga, & E. Tiemann. Feshbach spectroscopy and analysis of the interaction potentials of ultracold sodium. *Phys. Rev. A.* **83**(4):042704, (2011).

[334] I. I. Rabi. On the Process of Space Quantization. *Phys. Rev.* **49**(4):324–328, (1936).

[335] C. Raman, M. Köhl, R. Onofrio, D. S. Durfee, C. E. Kuklewicz, Z. Hadzibabic, & W. Ketterle. Evidence for a Critical Velocity in a Bose-Einstein Condensed Gas. *Phys. Rev.*

Lett. **83**(13):2502–2505, (1999).

[336] S. Liberati, M. Visser, & S. Weinfurtner. Analogue quantum gravity phenomenology from a two-component Bose–Einstein condensate. *Class. Quantum Grav.* **23**(9):3129–3154, (2006).

[337] U. Fischer & R. Schützhold. Quantum simulation of cosmic inflation in two-component Bose-Einstein condensates. *Phys. Rev. A.* **70**(6):063615, (2004).

[338] S. Butera & I. Carusotto. Particle creation in the spin modes of a dynamically oscillating two-component Bose-Einstein condensate. *Phys. Rev. D.* **104**:083503, (2021).

[339] P. É. Larré & N. Pavloff. Hawking radiation in a two-component Bose-Einstein condensate. *Europhys. Lett.* **103**(6):60001, (2013).

[340] A. Berti, L. Giacomelli, & I. Carusotto. Superradiant phononic emission from the analog spin ergoregion in a two-component Bose–Einstein condensate. *Comptes Rendus Phys.* **24** (S3):1–20, (2023).

[341] W. C. Syu, D. S. Lee, & C. Y. Lin. Analogous Hawking radiation and quantum entanglement in two-component Bose-Einstein condensates: The gapped excitations. *Phys. Rev. D.* **106**(4):044016, (2022).

[342] W. C. Syu & D. S. Lee. Analogous Hawking radiation from gapped excitations in a transonic flow of binary Bose-Einstein condensates. *Phys. Rev. D.* **107**(8):084049, (2023).

[343] S. J. Robertson. The theory of Hawking radiation in laboratory analogues. *J. Phys. B: At. Mol. Opt. Phys.* **45**(16):163001, (2012).

[344] J. Steinhauer. Measuring the entanglement of analogue Hawking radiation by the density-density correlation function. *Phys. Rev. D.* **92**(2):024043, (2015).

[345] J. Macher & R. Parentani. Black-hole radiation in Bose-Einstein condensates. *Phys. Rev. A.* **80**(4):043601, (2009).

[346] J. Stenger, S. Inouye, A. P. Chikkatur, D. M. Stamper-Kurn, D. E. Pritchard, & W. Ketterle. Bragg Spectroscopy of a Bose-Einstein Condensate. *Phys. Rev. Lett.* **82**(23): 4569–4573, (1999).

[347] D. M. Stamper-Kurn, A. P. Chikkatur, A. Görlitz, S. Inouye, S. Gupta, D. E. Pritchard, & W. Ketterle. Excitation of Phonons in a Bose-Einstein Condensate by Light Scattering. *Phys. Rev. Lett.* **83**(15):2876–2879, (1999).

[348] J. Steinhauer, N. Katz, R. Ozeri, N. Davidson, C. Tozzo, & F. Dalfovo. Bragg Spectroscopy of the Multibranch Bogoliubov Spectrum of Elongated Bose-Einstein Condensates. *Phys. Rev. Lett.* **90**(6):060404, (2003).

[349] I. Shammass, S. Rinott, A. Berkovitz, R. Schley, & J. Steinhauer. Phonon Dispersion Relation of an Atomic Bose-Einstein Condensate. *Phys. Rev. Lett.* **109**(19):195301, (2012).

[350] I. Carusotto. Bragg scattering and the spin structure factor of two-component atomic gases. *J. Phys. B: At. Mol. Opt. Phys.* **39**(10):S211–S219, (2006).

[351] V. Cardoso, Ó. J. C. Dias, J. P. S. Lemos, & S. Yoshida. Black-hole bomb and superradiant instabilities. *Phys. Rev. D.* **70**(4):044039, (2004).

[352] L. Giacomelli & I. Carusotto. Ergoregion instabilities in rotating two-dimensional Bose-Einstein condensates: Perspectives on the stability of quantized vortices. *Phys. Rev. Re-*

search. **2**(3):033139, (2020).

[353] S. Finazzi & R. Parentani. Spectral properties of acoustic black hole radiation: Broadening the horizon. *Phys. Rev. D.* **83**(8):084010, (2011).

[354] S. Finazzi & R. Parentani. Hawking radiation in dispersive theories, the two regimes. *Phys. Rev. D.* **85**(12):124027, (2012).

[355] H. F. Trotter. On the product of semi-groups of operators. *Proc. Amer. Math. Soc.* **10** (4):545–551, (1959).